



Lee, Edward Calum (2019) *Robotic systems for exploitation of chemistry in random number generation and discovery of iron-oxo clusters*. PhD.

<https://theses.gla.ac.uk/75123/>

Copyright and moral rights for this work are retained by the author

A copy can be downloaded for personal non-commercial research or study, without prior permission or charge

This work cannot be reproduced or quoted extensively from without first obtaining permission in writing from the author

The content must not be changed in any way or sold commercially in any format or medium without the formal permission of the author

When referring to this work, full bibliographic details including the author, title, awarding institution and date of the thesis must be given

Enlighten: Theses

<https://theses.gla.ac.uk/>
research-enlighten@glasgow.ac.uk

Robotic systems for exploitation of
chemistry in random number generation and
discovery of iron-oxo clusters



Edward C. Lee

Submitted in fulfilment of the requirements of
the Degree of **Doctor of Philosophy**

School of Chemistry

College of Science and Engineering

July 2019

“There’s still much to do; still so much to learn. Mr. La Forge - engage!” Jean-Luc Picard

Abstract

Incorporation of robotic automation to chemical synthesis and discovery allows a more rapid, efficient and reliable investigation of the chemical space involved, compared to a manual approach, whilst simultaneously allowing the incorporation of inline analytics for automated real-time monitoring and recording of experimental progress. The objective of this thesis was to create a robot capable of liquid handling and inline analytics, and use these capabilities in two regards: firstly, to generate random numbers by observing outcomes of the random processes in compound synthesis and crystallisation, and secondly to discover new large iron-oxo clusters.

This thesis presents the development and results of using robotic automation and analysis in two areas. In the first, a robotic synthesis platform was used to investigate the stochasticity involved in chemical synthesis and crystallisation of polyoxometalates and coordination clusters by using observations of crystallisations to generate random numbers. In the second, a combination of a robotic synthesis platform and traditional bench methods were used to discover large iron oxide clusters.

Chapter one provides an overview of the fields studied in this thesis, beginning with an overview of polyoxometalate chemistry as an archetypal example of large molecular metal oxides. This is followed by current state of the art in large iron-oxide cluster chemistry and synthetic approaches to compound discovery. Chapter one then concludes by discussing current approaches to automation of chemistry.

Chapter two then describes the construction of a platform for automation and visual analysis of inorganic chemical synthesis and crystallisation while chapter three presents the approach used in, and results from this platform in using synthesis and crystallisation of chemical compounds to true generate random numbers.

In chapter four, the discovery and characterisation of new large iron oxide compounds is presented from both automated and traditional bench methods, including the double stranded ring $\{\text{Fe}_{16}\}$, and the large aggregates of $\{\text{Fe}_{30}\}$, $\{\text{Fe}_{34}\}$ and $\{\text{Fe}_{36}\}$.

Contents

1	Introduction.....	15
1.1	Polyoxometalates.....	16
1.1.1	Classification, synthesis and characterisation.....	16
1.1.2	Structure and bonding	20
1.1.3	Common structures.....	21
1.1.3.1	Lindqvist	21
1.1.3.2	Evans-Anderson	22
1.1.3.3	Keggin	23
1.1.3.4	Dawson	28
1.2	Iron oxide chemistry	29
1.2.1	Iron Aqueous chemistry	30
1.2.2	Large iron -oxo clusters.....	32
1.2.2.1	Lindqvist and Super-Lindqvist.....	33
1.2.2.2	Keggin and Kegginoids	34
1.2.2.3	High nuclearity ferric wheels and cages.	36
1.2.2.4	High nuclearity Fe- containing POMS	40
1.3	Automation in chemistry	41
1.3.1	Synthetic devices	42
1.3.1.1	Iterative synthesis devices	42
1.3.1.2	Micro and milli-fluidic devices.....	42
1.3.1.3	Automated batch reactors	43
1.3.1.4	Reactionware.....	43
1.3.2	Discovery Devices.....	44
1.3.2.1	Droplet automation	44
1.3.2.2	Networking chemical robots	45
1.3.2.3	Humans vs robots	45
1.3.2.4	Chemical computing.....	46
1.4	Random number generation.....	46

2	Aims	48
3	Crystalbot platform.....	49
3.1	Hardware	49
3.1.1	Robot frame	49
3.1.1.1	Mechanical Design	50
3.1.1.2	CNC kit	50
3.1.1.3	Crystallization platform	51
3.1.1.4	Imaging support system.....	52
3.1.1.5	Stirring apparatus.....	54
3.1.1.6	Fluid handling structure	54
3.1.2	Liquid Handling	55
3.1.2.1	Pumps	55
3.1.2.2	Syringes, Valves and Tubing.....	55
3.1.2.3	Outlet Support	56
3.1.3	Electronics.....	57
3.1.3.1	Axis control	57
3.1.3.2	Pump control	58
3.1.4	Bill of Materials	58
3.2	Method 2: Software implementation	59
3.2.1	Mechanical operation	59
3.2.1.1	Experiment controller.....	60
3.2.1.2	Data Management	61
3.2.1.3	Input files	61
3.2.1.4	Robot activation	61
3.2.1.5	Pumps	62
3.2.1.6	Camera	62
3.2.1.7	Arduino.....	63
3.2.1.8	Firmware.....	63
3.2.1.9	Experimental Procedure	64

3.2.2	Analytical Procedure	64
3.2.2.1	Vial detection	65
3.2.2.2	Crystal detection	68
3.3	Conclusions and future work	70
4	Random number generation from crystallisation	72
4.1	Introduction	72
4.2	Chapter objectives	72
4.3	Chemistry investigated	73
4.4	Methods and Results.....	74
4.4.1.1	Binary Salt Crystallisation	75
4.4.1.2	Oxide cluster compounds.....	76
4.4.1.3	Ligated cluster compound.....	79
4.4.2	Deployment.....	81
	CuSO ₄	82
	{W ₁₉ }.....	82
	{Co ₄ }.....	83
4.4.3	Crystal Detection	83
4.4.4	Binarization and Randomness assessment	83
4.4.4.1	Theory and Method development	83
4.4.4.2	Results from experiments	90
4.4.5	Encryption	96
4.5	Discussion and Future work	98
5	Discovery of iron clusters	100
5.1	Synthetic approaches	100
5.1.1	Robotic automation	100
5.2	Iron compound discovery in aqueous systems	101
5.2.1	Methodological development	102
5.2.2	Ligand substitution	103
5.2.3	Bismuth substitution	103

5.2.4	Reducing agent.....	104
5.3	Iron compound discovery in organic systems	107
5.3.1	Fe ₁₇ in concentrated pyridine.....	109
5.3.1.1	Ligand substitution	109
5.3.1.2	Organic reducing agents	110
5.3.2	Facilitation of growth by dilution	111
5.3.3	Large iron oxo-aggregate molecules: {Fe ₃₄ }, {Fe ₃₀ } and {Fe ₃₆ }.....	111
5.3.3.1	{Fe ₃₄ }	113
5.3.3.2	{Fe ₃₀ }	118
5.3.3.3	{Fe ₃₆ } - structural description.....	122
5.3.4	Templated iron cluster synthesis.....	130
5.3.5	Diazino compounds	132
5.3.5.1	Pyrimidine	132
5.3.5.2	Phthalazine	133
5.3.6	Alcohol-pyridines	134
5.3.6.1	2-pyridinemethanol	134
5.3.6.2	Chiral {Fe ₁₇ } using 2-pyridineethanol	136
5.3.7	Reducing Agents	137
5.3.7.1	Chains	138
5.3.7.2	Ferric ring molecule: {Fe ₁₆ }	139
5.4	Conclusions and Future work	144
6	Conclusions.....	146
7	Experimental	149
7.1	Materials	149
7.2	Instrumentation	149
7.3	Method of Crystal Growth	150
7.4	Synthesis of Compounds	150
7.4.1	Synthesis of 2Na·[FePb ₃ O(C ₆ H ₄ O ₇) ₃]·3H ₂ O (1).....	150
7.4.2	Synthesis of [Fe ₁₇ O ₁₆ (OH) ₁₂ (C ₇ H ₉ N) ₁₂ Br ₄]·3Br·5(C ₇ H ₉ N) (2)	151

7.4.3	Synthesis of $[\text{Fe}_{17}\text{O}_{16}(\text{OH})_{13}(\text{C}_5\text{H}_5\text{N})_{12}\text{Br}_3] \cdot 3\text{Br} \cdot 2(\text{C}_5\text{H}_5\text{N})$ (3)	151
7.4.4	Synthesis of $[\text{Fe}_{17}\text{O}_{16}(\text{OH})_{12}(\text{H}_2\text{O})_6(\text{C}_5\text{H}_5\text{N})_{12}\text{Br}_2] \cdot [\text{Fe}_{17}\text{O}_{16}(\text{OH})_{12}(\text{H}_2\text{O})_3(\text{C}_5\text{H}_5\text{N})_{12}\text{Br}_3] \cdot 6\text{Br} \cdot 2(\text{C}_5\text{H}_5\text{N})$ (4)	151
7.4.5	Synthesis of $[\text{Fe}_{34}\text{O}_{38}(\text{OH})_{12}\text{Br}_{12}(\text{C}_5\text{H}_5\text{N})_{18}] \cdot [\text{Br}_6\text{Fe}_2\text{O}]$ (5)	152
7.4.6	Synthesis of $[\text{Fe}_{34}\text{O}_{38}(\text{OH})_{12}\text{Br}_{12}(\text{C}_5\text{H}_5\text{N})_{18}] \cdot 2\text{Br}$ (6)	152
7.4.7	Synthesis of $[\text{Fe}_{34}\text{O}_{38}(\text{OH})_{12}\text{Br}_{12}(\text{C}_{12}\text{H}_{11}\text{N})_{18}] \cdot 2\text{Br}$ (7).....	153
7.4.8	Synthesis of $[\text{Fe}_{34}\text{O}_{38}(\text{OH})_{12}\text{Br}_{12}(\text{C}_4\text{H}_4\text{N}_2)_{18}] \cdot 2\text{Br}$ (8).....	153
7.4.9	Synthesis of $[\text{Fe}_{30}\text{O}_{31}(\text{OH})_{16}\text{Br}_9(\text{C}_5\text{H}_5\text{N})_{15}]_{0.9} \cdot [\text{Fe}_{34}\text{O}_{38}(\text{OH})_{12}\text{Br}_{12}(\text{C}_5\text{H}_5\text{N})_{18}]_{0.1} \cdot 9\text{Br}$ (9)	153
7.4.10	Synthesis of $[\text{Fe}_{30}\text{O}_{31}(\text{OH})_{16}\text{Br}_9(\text{C}_6\text{H}_7\text{N})_{15}]_{0.9} \cdot [\text{Fe}_{34}\text{O}_{38}(\text{OH})_{12}\text{Br}_{12}(\text{C}_6\text{H}_7\text{N})_{18}]_{0.1} \cdot 9\text{Br}$ (10).....	154
7.4.11	Synthesis of $[\text{Fe}_{36}\text{O}_{30}(\text{OH})_{34}\text{Br}_8(\text{C}_6\text{H}_7\text{N})_{24}] \cdot 6\text{Br}$ (11)	154
7.4.12	Synthesis of $[\text{Fe}_{36}\text{O}_{30}(\text{OH})_{34}\text{Br}_8(\text{C}_7\text{H}_9\text{N})_{24}] \cdot 6\text{Br}$ (12)	155
7.4.13	Synthesis of $[\text{Fe}_{36}\text{O}_{38}(\text{OH})_{12}\text{Br}_{12}(\text{C}_7\text{H}_9\text{N})_{24}] \cdot 6\text{Br}$ (13).....	155
7.4.14	Synthesis of $[\text{Fe}_{36}\text{O}_{38}(\text{OH})_{12}\text{Br}_{12}(\text{C}_7\text{H}_9\text{N})_{24}] \cdot 6\text{Br}$ (14).....	155
7.4.15	Synthesis of $[\text{Mo}_{10}\text{O}_{27}(\text{C}_7\text{H}_9\text{N})_7]$ (15)	156
7.4.16	Synthesis of $[\text{Fe}(\text{C}_4\text{H}_4\text{N}_2)_2\text{Br}_2]$ (16).....	156
7.4.17	Synthesis of $[\text{Fe}_4\text{O}(\text{OH})(\text{C}_8\text{H}_6\text{N}_2)_6\text{Br}_5] \cdot [\text{Br}_6\text{Fe}_2\text{O}] \cdot 5(\text{H}_3\text{C}_2\text{N})$ (17).....	156
7.4.18	Synthesis of $[\text{Fe}_8\text{O}_4(\text{C}_6\text{H}_6\text{ON})_8\text{Br}_8]$ (18)	156
7.4.19	Synthesis of $[\text{Fe}_{17}\text{O}_{16}(\text{C}_7\text{H}_8\text{ON})_{12}\text{Br}_4] \cdot \text{Br} \cdot (\text{Br}_6\text{Fe}_2\text{O})$ (19)	157
7.4.20	Synthesis of $n\text{-}[\text{Fe}_2(\text{C}_5\text{H}_5\text{N})_2\text{Br}_2(\text{C}_2\text{O}_4)\text{O}]$ (20)	157
7.4.21	Synthesis of $n\text{-}[\text{Fe}(\text{C}_5\text{H}_5\text{N})_4(\text{SO}_4)]$ (21)	157
7.4.22	Synthesis of $[\text{Fe}_{16}\text{O}_8(\text{ox})_{16}\text{Br}_4(\text{py})_{12}] \cdot 4(\text{C}_5\text{H}_6\text{N}) \cdot 2(\text{C}_5\text{H}_5\text{N})$ (22).....	157
8	Crystallographic Data.....	159
8.1	$2\text{Na} \cdot [\text{FePb}_3\text{O}(\text{C}_6\text{H}_4\text{O}_7)_3] \cdot 3\text{H}_2\text{O}$ (1).....	160
8.2	$[\text{Fe}_{17}\text{O}_{16}(\text{OH})_{12}(\text{C}_7\text{H}_9\text{N})_{12}\text{Br}_4] \cdot 3\text{Br} \cdot 5(\text{C}_7\text{H}_9\text{N})$ (2)	161
8.3	$[\text{Fe}_{17}\text{O}_{16}(\text{OH})_{12}(\text{H}_2\text{O})_9(\text{C}_5\text{H}_5\text{N})_{12}\text{Br}_1] \cdot 5\text{Br} \cdot 2(\text{C}_5\text{H}_5\text{N})$ (3).....	162

8.4	$[\text{Fe}_{17}\text{O}_{16}(\text{OH})_{12}(\text{H}_2\text{O})_6(\text{C}_5\text{H}_5\text{N})_{12}\text{Br}_2] \cdot [\text{Fe}_{17}\text{O}_{16}(\text{OH})_{12}(\text{H}_2\text{O})_3(\text{C}_5\text{H}_5\text{N})_{12}\text{Br}_3] \cdot 9\text{Br} \cdot 5$ ($\text{C}_5\text{H}_5\text{N}$) (4)	163
8.5	$[\text{Fe}_{34}\text{O}_{38}(\text{OH})_{12}\text{Br}_{12}(\text{C}_5\text{H}_5\text{N})_{18}] \cdot (\text{Br}_6\text{Fe}_2\text{O})$ (5)	164
8.6	$[\text{Fe}_{34}\text{O}_{38}(\text{OH})_{12}\text{Br}_{12}(\text{C}_5\text{H}_5\text{N})_{18}] \cdot 2\text{Br}$ (6)	165
8.7	$[\text{Fe}_{34}\text{O}_{38}(\text{OH})_{12}\text{Br}_{12}(\text{C}_{12}\text{H}_{11}\text{N})_{18}] \cdot 2\text{Br}$	166
8.8	$[\text{Fe}_{34}\text{O}_{38}(\text{OH})_{12}\text{Br}_{12}(\text{C}_4\text{H}_5\text{N}_2)_{18}] \cdot 2\text{Br}$	167
8.9	$[\text{Fe}_{30}\text{O}_{31}(\text{OH})_{16}\text{Br}_9(\text{C}_6\text{H}_7\text{N})_{15}]_{0.9} \cdot [\text{Fe}_{34}\text{O}_{38}(\text{OH})_{12}\text{Br}_{12}(\text{C}_5\text{H}_5\text{N})_{18}]_{0.1} \cdot 2 \cdot 9\text{Br}$...	168
8.10	$[\text{Fe}_{30}\text{O}_{31}(\text{OH})_{16}\text{Br}_9(\text{C}_6\text{H}_7\text{N})_{15}]_{0.9} \cdot [\text{Fe}_{34}\text{O}_{38}(\text{OH})_{12}\text{Br}_{12}(\text{C}_6\text{H}_7\text{N})_{18}]_{0.1} \cdot 2 \cdot 9\text{Br}$...	169
8.11	$[\text{Fe}_{36}\text{O}_{30}(\text{OH})_{34}(\text{C}_7\text{H}_9\text{N})_{24}\text{Br}_8] \cdot 6\text{Br}$	170
8.12	$[\text{Fe}_{36}\text{O}_{30}(\text{OH})_{34}(\text{C}_7\text{H}_9\text{N})_{24}\text{Br}_8] \cdot 6\text{Br}$	171
8.13	$[\text{Fe}_{36}\text{O}_{30}(\text{OH})_{34}(\text{C}_6\text{H}_7\text{N})_{24}\text{Br}_8] \cdot 6\text{Br}$	172
8.14	$[\text{Fe}_{36}\text{O}_{30}(\text{OH})_{34}(\text{C}_7\text{H}_9\text{N})_{24}\text{Br}_8] \cdot 6\text{Br}$	173
8.15	$[\text{Mo}_{10}\text{O}_{27}(\text{C}_5\text{H}_5\text{N})_7]$	174
8.16	$n\text{-}[\text{FeBr}_2(\text{C}_4\text{H}_4\text{N}_2)]$	175
8.17	$[\text{Fe}_4\text{O}_2\text{Br}_5(\text{C}_8\text{H}_8\text{N}_2)_6] \cdot (\text{Br}_6\text{Fe}_2\text{O}) \cdot 6(\text{C}_2\text{C}_3\text{N})$	176
8.18	$[\text{Fe}_8\text{O}_4(\text{C}_6\text{H}_6\text{NO})_8\text{Br}_8]$	177
8.19	$[\text{Fe}_{17}\text{O}_{16}(\text{C}_7\text{H}_8\text{ON})_{12}\text{Br}_4] \cdot 3\text{Br} \cdot 0.5(\text{Br}_6\text{Fe}_2\text{O})$	178
8.20	$n\text{-}[\text{Fe}_2(\text{C}_5\text{H}_5\text{N})_2\text{Br}_2(\text{C}_2\text{O}_4)\text{O}]$	179
8.21	$n\text{-}[\text{Fe}(\text{C}_5\text{H}_5\text{N})_4(\text{SO}_4)]$	180
8.22	$[\text{Fe}_{16}\text{O}_8(\text{C}_2\text{O}_4)_{16}(\text{C}_5\text{H}_5\text{N})_{12}\text{Br}_4] \cdot 4(\text{C}_5\text{H}_6\text{N}) \cdot 4(\text{C}_5\text{H}_5\text{N}) \cdot (\text{C}_2\text{H}_3\text{N})$	181
9	References	182

Acknowledgements

The work presented in this thesis was undertaken between the groups of Professor Lee Cronin at the University of Glasgow and of Professor Euan Brechin at the University of Edinburgh between October 2015 and June 2019. It is a result of both direct and indirect contributions from many people and I have a great deal of gratitude to each and every one, even those not listed below. However, I would particularly like to mention my thanks the following people:

Professor Lee Cronin for offering support and guidance during my PhD, and aiding my development to gain a large number of skills in chemistry and robotics. I'd also like to thank him for provoking thoughtful discussions on science and philosophy.

Professor Euan Brechin for supporting me with a unique insight into chemical synthesis and an opportunity to perform research in his lab.

Dr. Nancy Watfa for being an especially supportive mentor, who aided me with both professional and personal development. She continually excelled as team leader and I am very grateful for her scientific discussions, guidance and support.

Dr. Deliang Long for sharing excellent chemistry and x-ray diffraction knowledge, as well as aiding with difficult x-ray structural solutions. **Dr. Weimin Xuan** and **Dr. Qi Zheng** for chemistry discussions and structure solutions, as well as karaoke sessions. **Dr. Ross Winter**, **Dr. Yousef Abul-Haija**, **Dr. Harry Miras** and **Dr. Alon Henson** and **Dr. Juan Manuel Parrilla Gutierrez** have all provided a great deal of support with getting through difficult patches of this PhD and their chemistry and programming knowledge has been invaluable.

Thanks are also due to the many support and technical staff that have helped my both my PhD and the Cronin group to run smoothly. Particularly, I'd like to think **Jim McIver** whose practical knowledge seems unbounded and has been invaluable, **Dr. Maria Diana Castro-Spencer** who has both provided help with mass spectrometry and made the laboratory run smoothly, as well as **Amanda McGarvey**, **Dr. Laia Vila-Nadal**, **Stuart Marshall** and **Stuart MacKay** for providing, administrative, organisational and IT support.

I'd also like to extend my thanks to my many other co-workers who have helped created a supportive, stimulating, and exciting environment to work, whether our acquaintance was long or brief. In particular, I'd like to mention **Dr. Mercé Martin**,

Dr. Jamie Purcell, Dr. Vasilis Duros, Dr. Hector Fraser, Naomi Johnson, Danny Salley, Robert Pow, Edu Garrido Ribo, Marcus Tze-Kiat Ng, Zoe Sinclair, David Lockey, Daniel Tague, Noel de Kler and Maxence Lion.

I'd also like to thank my family **Phil Lee and Jen Lee, Liz Lee, Mike Lee and Cath Mitchell, Dave Lee and Alice Lee**, and **Lisa Boyden and Richard Boyden** for their ongoing understanding and support during my studies. Lastly, my final thanks go to my wife **Sarah Adams** who has been an incredible support over the past years, helped me through all the ups and downs, and shared many fantastic experiences over the years. I hope I can provide as much support as you progress through and complete your degree.

Thesis contributions

Some of the work detailed in this thesis was performed in collaboration with others, whilst other parts have built upon the previous work of former group members. I would like to specifically acknowledge the following:

Danny Salley for designing and building the robotic platform clusterbot which was used as an additional platform for compound discovery.

Dr. Hector Fraser for synthetic procedure in the discovery of $\{\text{Fe}_{34}\}$. Also, David Lockey for helping with reproduction and characterisation of several iron clusters discovered in this work, specifically Fe_{16} , Fe_{30} , Fe_{34} , and Fe_{36} .

Publications

The following publication was a direct result of work undertaken in this thesis:

‘Exploring the stochasticity of chemical processes in an automated robotic crystallization platform to generate random number’. Lee, E., Gutiérrez, J.M.P., Henson, A., Brechin, E.K. and Cronin, L., *manuscript under consideration*

The following publications are currently under preparation as a direct result of work undertaken in this thesis:

Synthesis and Magnetism of a new double stranded iron ring molecule: Fe₁₆

Lee, E., Lockey, D., Fraser, H., Long, D.L, Brechin, E., Cronin, L., *manuscript in preparation*

An [FeIII₃₄] molecular metal oxide, Alice E. Dearle, Daniel J. Cutler, Hector W. L. Fraser, Sergio Sanz, Edward Lee, Sourav Dey, Ismael F. Diaz-Ortega, Gary S. Nichol, Hiroyuki Nojiri, Marco Evangelisti, Gopalan Rajaraman*, Jürgen Schnack*, Leroy Cronin, and Euan K. Brechin, *manuscript in preparation*

Conferences attended

The following conference presentations were undertaken over the course of this PhD program:

Automation for discovery of new polyoxometalate compounds.

Frontiers in Metal Oxide Cluster Science (FMOCS) 2016, Newcastle

Design and formation of large, magnetic iron oxide clusters- Fe₃₀ and Fe₃₄.

International conference on coordination chemistry (ICCC) 2018, Sendai

Abbreviations

bdma	1,3-benzenedimethanamine
bgr	blue, green, red
bpy	benzylpyridine
CMOS	Complementary Metal-Oxide Semiconductor
CNC	Computer Numeric Control
COCO	Common Objects in Context
dbm	dibenzoylmethane
DCM	dichloromethane
dmf	dimethyl formamide
ep	ethylpyridine
ESI-MS	Electrospray Ionisation Mass Spectroscopy
FEP	fluorinated ethylene polypropylene
FT-IR	Fourier Transform Infrared
GooF	Goodness of Fit
ox	oxalate
thbd	1,2,3,4-tetrahydroxybutane-1,1-dicarboxylate
heia	2-(hydroxyethyl)iminoacetate
hmp	hydroxymethylpyridine
hmta	hexamethylenetetraamine
ICP-OES	Inductively Coupled Plasma Optical Emission Spectroscopy
ipp	isopropylpyridine
LED	Light Emitting Diode
lut	lutidine
MeCN	acetonitrile
MMT	2-mercapto-5-methyl-1,3,4-thiadiazole
MOF	Metal Organic Framework
MONC	Metal Oxide Nano Capsule
MS	Mass Spectroscopy
MT	Mersenne Twister
NIST	National Institute of Standards and Technology
PEEK	polyether ether ketone
PgC6	c-hexylpyrogallol[4]arene
ph	phenol

phth	phthalazine
pic	picoline
pmd	pyrimidine
POM	Polyoxometalate
PRNG	Pseudorandom Number Generator
PTFE	Polytetrafluoroethylene
pXRD	Powder X-ray Diffraction
py	pyridine
pye	pyridineethanol
pyph	2-pyridylphosphonate
RAMPS	Rep-rap Arduino Mega Pololu Shield
RCNN	Region-based convolutional neural network
tart	tartaric acid
tca	trichloroacetate
tea	triethanolamine
TGA	Thermogravimetric Analysis
THF	tetrahydrofuran
thme	tris(hydroxymethyl)ethane
thmp	tris(hydroxymethyl)propane
TMSP	Transition Metal Substituted Polyoxometalate
TRNG	Truly Random Number Generator
XOR	exclusive OR operation

1 Introduction

This thesis lies at the intersection between traditional manual discovery methods and scientific discovery made possible as a result of robotic automation. It investigates new rapid synthetic and analytical techniques to explore ‘difficult to predict’ chemical reaction systems, where a single reaction pathway has multiple steps which all occur in one mixture along one of many possible reaction trajectories. Such systems are typically very sensitive to reaction conditions, and require tight control in order to achieve reproducible results, making them ideal for testing the limits of automation.

One aspect of this is in the discovery of new functional molecular metal oxide clusters, whose final structures result from the formation and combination of various building blocks which result from dissolution of metal salts in solution. One classic example where structure formation in this way occurs is with polyoxometalates,¹ but can also occur in other classes of chemistry.² In particular, recent results indicate that there are similarities between polyoxometalates and molecular iron oxide chemistry,³ and this will be explored in this thesis, both with and without automation.

A second aspect of this complex and sensitive chemistry is that the underlying processes are chaotic in nature, meaning that small fluctuations in initial conditions may cause large macroscopic differences between samples,⁴ and may plausibly be used as an entropy source in the generation of random numbers.⁵ This thesis combines the synthesis and crystallisation processes of complex molecular metal oxide clusters with the rapidity and repeatability of automation to create a new type of random number generator.

The themes of the thesis are discovery and synthesis of iron compounds, automation of chemistry, and application of complex chaotic syntheses in the generation of random numbers. As such, the introduction is split into three sections:

- Section 1.1 - Polyoxometalates. This section introduces and describes our current understanding of polyoxometalates (POMs), as an example of a complex chaotic chemical system.

- Section 1.2 - Iron oxide chemistry. This section details the chemical processes involved in the growth of iron oxide clusters, with comparison between this and equivalent processes in POMs. It also describes the state of the art and common features of groups of iron oxide clusters.
- Section 1.3 - Automation in chemistry. This section describes recent developments in applying automation to various applications in chemistry, such as synthesis and analysis.

1.1 Polyoxometalates

Polyoxometalates (POMs) are a class of discrete inorganic molecular oxide clusters. Specifically, they are comprised of multiple connected $\{MO_6\}$ and $\{MO_4\}$ polyhedra, where M can be at least one of several different elements, most commonly Mo, W and V. Interest in POMs is based on two aspects of the molecules in the class. First, there exists a tremendous degree of structural diversity which may form by variation of only a few synthetic parameters. The ability to explain this is desirable from a purely inquisitive point of view in which our understanding of the chemistry involved is enhanced. Secondly, the chemical modifiability of these structures allows molecules to be created with tailored properties desirable for specific applications. Examples of useful properties include magnetism, catalytic activity, redox activity and bioactivity. These allow the possibility for application in a huge number of areas, such as spintronics, memory devices, catalysis, energy storage and medicine.⁶⁻¹⁴

1.1.1 Classification, synthesis and characterisation

POM clusters are primarily composed of oxo-verticed tetrahedra and octahedra of one element, and particular atoms of this are distinguished as *addenda* atoms, commonly Mo, W, V, Nb and Ta.¹⁵ However, almost any element capable of forming $\{MO_4\}$ or $\{MO_6\}$ polyhedra can be incorporated into POM frameworks as *heteroatoms*, and organic fragments may also be attached to POM structures.¹⁶ Characteristic of all POMs is the formation of oxide bridges between polyhedra to form a stable fixed molecular structure and the presence of shorter, relatively inert terminal M=O double bonds to stabilise the structure with respect to the environment.¹⁷ This bridging allows for a huge number of different structural

frameworks to exist, which, when considered with the elemental diversity in POMs, permits the potential for a tremendous number of distinct molecules.¹⁵

According to Louis C. W. Baker,¹⁶ there are certain criteria that atoms should fulfil to function as *addenda* in POMs. These are: 1) have the ability to change their coordination to oxygen between 4 and 6 as they polymerise during a change in pH; and 2) have high positive charge and be amongst the smallest ions capable of octahedral packing.¹⁶ By this classification, the only species capable of acting as *addenda* are $\text{Mo}^{5+/6+}$, W^{6+} , V^{5+} , Nb^{5+} , Ta^{5+} , Re^{7+} and I^{7+} , however, an increasing number of compounds composed primarily of other elements are being discovered and referred to as POMs.¹⁷ These fall into one of two categories of POM-like clusters, namely, those stabilised by a strong terminal triple *yl* oxide bond (mainly uranium) and those stabilised by organic capping ligands (mainly transition metals).¹⁷ This second group extends the number of possible *addenda* metals to include elements such as Sn, Al¹⁸ and Ti¹⁹ (alkoxides), and Fe^3 , Mn^{20} , Cu^{21} , Gd^{22} and Pd^{23} (carboxylates).

POMs are generally synthesised in a one-pot reaction from a simple metal(ate) salt by the polymerisation of $\{\text{MO}_x\}^{n-}$ polyhedra (where $x = 4-7$). This occurs due to the introduction of a large change in the pH environment (high to low in the case of Mo and W, and vice versa for Nb and Ta),¹⁷ which causes the metal group anions to condense as they grow towards the newly thermodynamically favoured solid state for the particular new environmental conditions. This can be represented as moving from right to left on a Pourbaix Diagram (Figure 1.1), from MO_4^{2-} to MO_3 or MO_2 . However, the kinetic route to this involves the formation of semi-stable intermediates, which can themselves react to form kinetically stable isolable structures. The presence of other species in solution, such as other inorganic-oxo group anions, simple salts, and organic structures may also allow their incorporation into the final POM structure. This process can be directed by varying one or more of several parameters, including pH, temperature, reactant ratio, reactant concentration, ionic strength and the presence of other directing agents such as oxidants, reducing agents or organic ligands. Although the synthetic process is straightforward, POMs often have a very narrow synthetic window in which they will form. As such, POM chemists must be precise in how experiments

are conducted and recorded to assure reproducibility, which is a relatively common problem in the field.^{24,25}

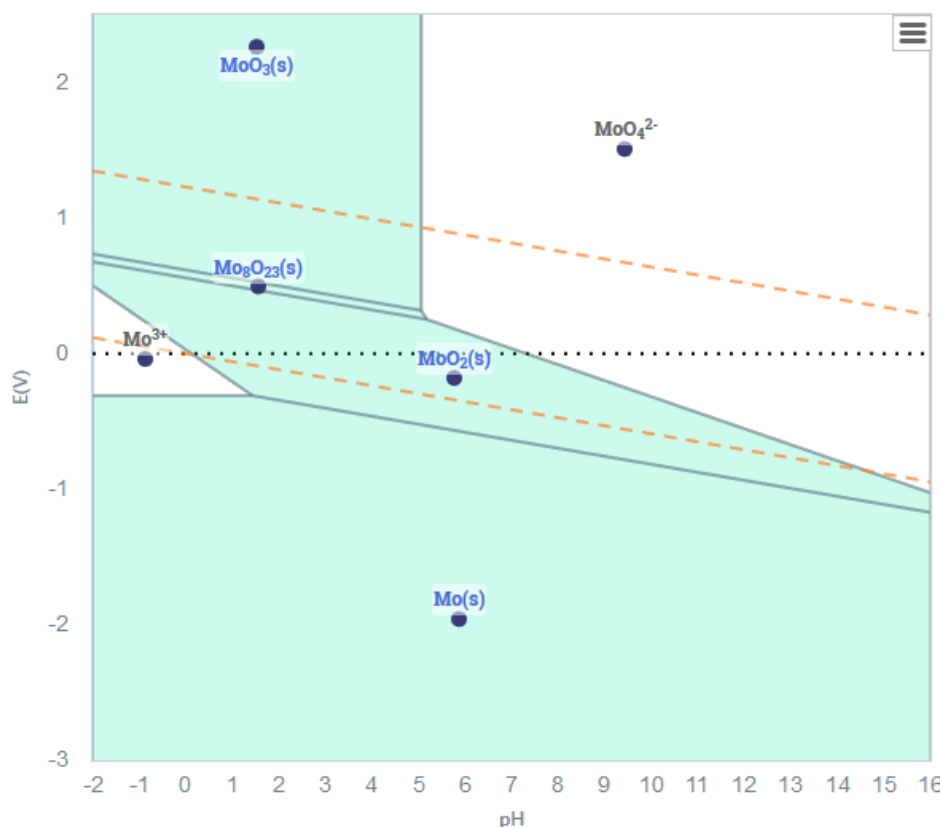


Figure 1.1 Pourbaix diagram of Mo, with different phases separated by solid lines, solid phases coloured in cyan, and aqueous phases in white. Water reduction and oxidation conditions are shown as dashed orange lines²⁶

Alternative methods for POM synthesis include using hydrothermal (or solvothermal) techniques in which the one-pot reaction is performed at high temperatures and pressures. Such reactions create conditions which are far from equilibrium and allow for the formation of meta-stable structures. One other common synthetic procedure is to use POMS obtained from one-pot reactions and react them in further one-pot reactions, allowing for modifications of the original POM.²⁵

Isolation and purification of POMs are usually achieved via crystallisation from the reaction solution. Crystallisation conditions and techniques, therefore, are important factors to consider in the experimental methodology. Techniques commonly employed to facilitate crystallisation can involve slow evaporation of

solvent, layering of co-solvent, or vapour diffusion. Further, parameters such as environmental temperature, humidity and vibrations, as well as crystallisation vessel size, shape and defects affect the rate of crystal growth and crystal quality. As such, reproduction of POM compounds often difficult, as crystallisation conditions, such as room temperature, vary throughout day/year, across one laboratory room, and between laboratories in countries with different climates. In addition, random factors, such as accidentally ‘jolting’ a crystallising sample may either enhance crystallisation, or prevent it entirely.

The primary technique for characterisation of POMs is crystallography, with single crystal x-ray diffraction most commonly utilised. This allows for an absolute structural assignment of atoms in a molecule, providing a high confidence for features such as bond distances, bond angles and oxidation states of metals. However, single crystal crystallography alone may be insufficient for an unambiguous characterisation. For instance, it struggles to deal with disordering of elements within a molecule, disordering of molecules within a crystal, and uncertainty in the quantity of solvent molecules observed. Further, the crystal chosen for x-ray analysis is not necessarily identical to those in the rest of the sample. As such, several complementary techniques are often employed to remove any structural ambiguity and prove sample purity. These include Thermogravimetric Analysis (TGA), which can be used to quantify solvent content of a crystal, Fourier Transform infrared spectroscopy (FT-IR), which is useful for confirming the presence of structural motifs (such as organic fragments or metal-oxo-metal bonds) via observation of characteristic vibrational bands, mass spectroscopy (MS), which can be used to identify a parent ion and characterise any fragmentation of this, powder X-ray Diffraction (pXRD) is sometimes used if a single crystal cannot be obtained, Inductively Coupled Plasma-Optical Emission Spectroscopy (ICP-OES) may be used to quantify amount of particular elements in a sample, and nuclear magnetic resonance (NMR) to determine the presence and bonding state of elements. Some (or all) of these techniques are usually reported along with a crystal structure when a new compound is produced.²⁷

1.1.2 Structure and bonding

As mentioned, POMs are synthesised by changing pH in order to facilitate polymerisation of metal oxide polyhedra. The vast majority of polyhedra formed by *addenda* atoms such as Mo and W are octahedral. However, these units are always greatly distorted due to the short terminal M=O double bond, a long M-O single bond *trans* to it, and intermediate M-O single bonds *cis* to each of these, as shown in Figure 1.2. This is due to the *trans*-effect, in which the ligands geometrically *trans* to one another utilise the same central metal orbital, and as such the strengthening of one M-O bond results in the weakening of the other. A terminal oxo ligand is a better electron donor to the d^0/d^1 central metal than a bridging oxo ligand, and as such exerts a geometric distortion via the structural *trans*-effect.²⁸ This has an effect on the reactivity of each site in that the terminal oxo ligands, whose electrons are polarised towards the metal centre, are more positive and thus are less basic than typical oxo-ligands. POMs can be categorised into three types based on the number of external M=O bonds in each octahedron in a structure.²⁹ Type I POMs contain only one terminal M=O bond whereas as Type II POMs contain two *cis*-related terminal M=O bonds. Finally, Type III POMs contain a mixture of octahedra with one and two terminal M=O bonds.

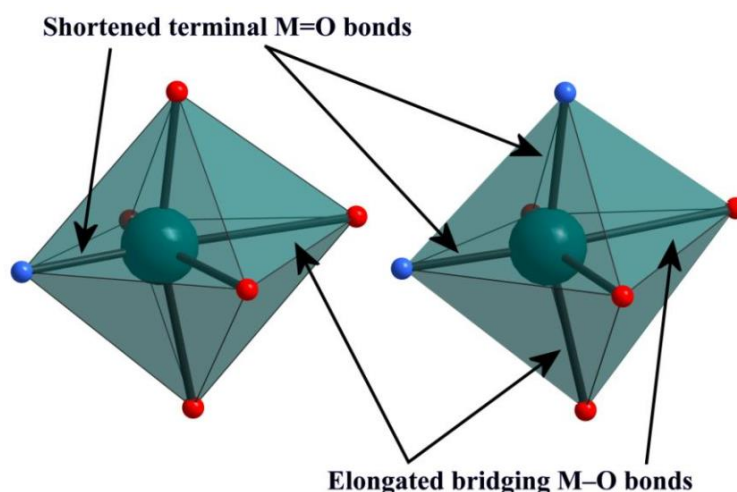


Figure 1.2 Shortening and lengthening of M-O bonds in *trans* positions in $\{MO_6\}$ octahedra due to the *trans* effect. (Colour scheme: M=teal, O(terminal)=blue, O (bridging)=red)

Complete POM structures are formed by sharing of oxide ligands through three different geometries - corner sharing, edge sharing and occasionally face sharing

(Figure 1.3).³⁰ In this way, gigantic structures of up to 368 metal centres can be formed.³¹ However, while structures can contain octahedra with one or two terminal oxo ligands, no cluster has been observed that contains octahedra with three or more terminal oxo ligands. This is due to the Lipscomb rule, which states that in order for the high positive charge of addenda to be stabilised, oxygen atoms should be shared throughout the cluster, and additional terminal oxides may be displaced to achieve this.³²

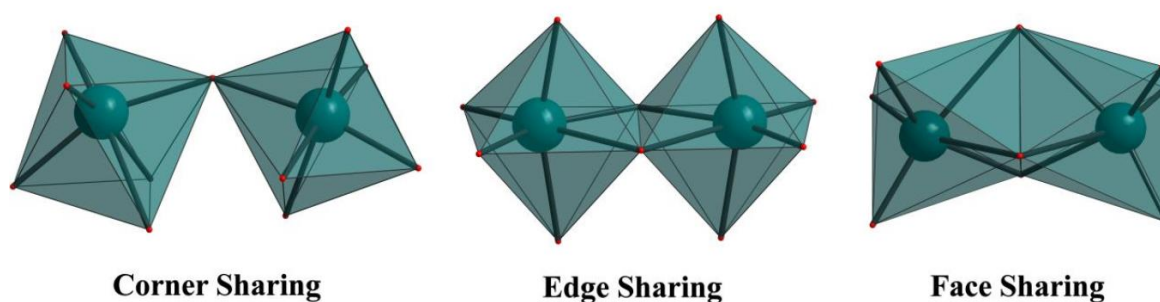


Figure 1.3 Different oxide sharing geometries of POM $\{MO_6\}$ octahedra (Colour scheme: M=Teal, O=red)

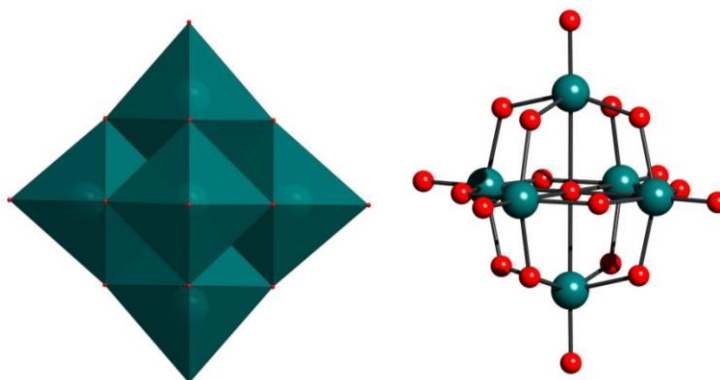
1.1.3 Common structures

There exists a handful of basic POM structural motifs that have been well studied in the literature. This is due to their high reproducibility and stability as independent structures, but also they are highly modifiable, and act as the basis for fragments of many other compounds. In addition, different metal *addenda* are able to form these same structures. Described below are the Lindqvist ($[M_6O_{19}]^{n-}$), the Evans-Anderson ($[XM_6O_{24}]^{n-}$), the Keggin ($[XM_{12}O_{40}]^{n-}$), and the Wells-Dawson ($[X_2M_{18}O_{62}]^{n-}$), where M = the addenda metal atom, X = the heteratom and n = the charge of the ion.³³

1.1.3.1 Lindqvist

The Lindqvist anion, $[M_6O_{19}]^{n-}$, (shown in Figure 1.4) is structurally similar to a fragment of a cubic close packed metal oxide. It consists of an octahedral arrangement of 6 metal addenda atoms, which all exist in edge sharing octahedra with four neighbouring octahedra. It contains 19 oxygen atoms: 6 of which (one from each metal) are terminal double bonded making this a Type I POM; a further

12 form bridges between two addenda centres; and the final oxygen is at the molecule's centre and is coordinated to all 6 addenda atoms. Lindqvist POMs have



been discovered for W^{34} , Mo^{33} , Nb^{35} and Ta^{36} , however several other elements, such as V, Cr and Fe can form this structure if some of the terminal oxo groups are substituted,³⁷ or if stabilised by another organometallic fragment.³⁸ Lindqvist structures may be reacted with organic molecules to form large structures, or even be incorporated into metal organic frameworks (MOFs).

Figure 1.4. The Lindqvist ($[M_6O_{19}]^{n-}$) anion, with polyhedral (left) and ball and stick (right) representations.

1.1.3.2 Evans-Anderson

Like the Lindqvist, the basic Evans-Anderson structure, $[XM_6O_{24}]^{n-}$, (Figure 1.5) consists of six edge sharing $\{MO_6\}$ octahedra. However, the 6 $\{MO_6\}$ octahedra are arranged in a single plane, and all contain two terminal $M=O$ bonds making this a Type II POM. In addition, the structure contains one central X atom, also in an octahedral coordination environment. This atom may be one of several first row transition metals (e.g. $Fe^{II/III}$, Mn^{II} , Co^{II} , Cr^{III})^{39,40}, a p-block element (e.g. Al^{III} , Te^{IV})^{41,42}, or another addenda atom (e.g. Mo^{VI} , W^{VI})^{43,44}. Two Anderson isomers exist depending on whether the X atom is out of the M_6 plane (α -isomer, with C_{3v} symmetry), which occurs when X is an addenda atom, or whether X is in the same plane (β -isomer, with D_{3h} symmetry), which occurs with p-block and other transition metal elements. Addenda elements for the Evans-Anderson can be Mo and W, however, this structure has also been seen with elements such as Bi⁴⁵ in which the oxo-groups are replaced by I atoms. Also like the Lindqvist, organic molecules can be reacted with the Evans-Anderson to form hybrid molecules.⁴⁶

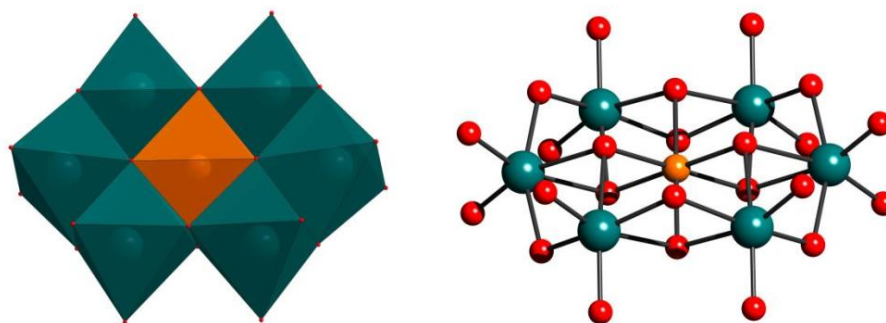


Figure 1.5 Structure of the Anderson cluster, $[XM_6O_{24}]^{n-}$, with polyhedral (left) and ball-and-stick (right) representations (Colour scheme: M=teal, X=orange, O=red).

1.1.3.3 Keggin

The Keggin anion, $[XM_{12}O_{40}]^{n-}$, (Figure 1.7) consists of four $\{M_3O_{13}\}$ triads (Figure 1.6) clustered around a central tetrahedral heteroatom, and as such are often described using $\{(XO_4)@M_{12}O_{36}\}$ notation. Each $\{MO_6\}$ octahedron within a triad shares edges with the other two, and each triad is connected through sharing of two of the three octahedra in a triad. Keggin anions are an example of Type I POMs as they only contain one terminal $M=O$ bond per octahedron.

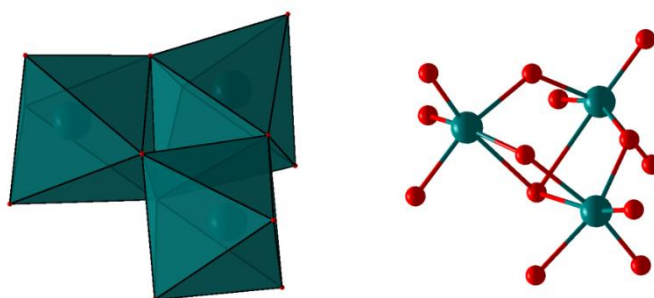


Figure 1.6 Structure of the $\{M_3O_{13}\}$ triad which forms the basis of each Keggin cluster in polyhedral (left) and ball and stick (right) representations (Colour scheme: M=teal, O=red).

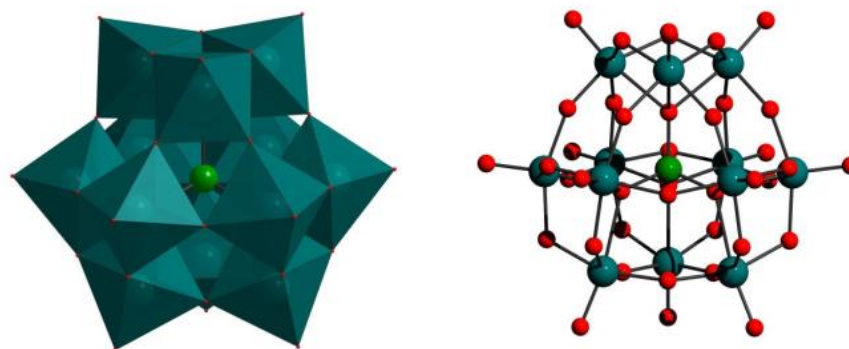


Figure 1.7 Structure of the α -Keggin cluster $[XM_{12}O_{40}]^{n-}$ which is formed from four $\{M_3O_{13}\}$ triads around a central X heteroatom in polyhedral (left) and ball and stick (right) representations (Colour scheme: M=teal, O=red).

Five different isomeric Keggin structures (α , β , γ , δ , and ϵ , Figure 1.8) can be formed due to the potential for a 60° rotation of each triad around its C_3 axis.³² Each isomer can be distinguished based on the geometry of each triad with respect to the central heteroatom tetrahedron. This can exist in either a staggered or eclipsed arrangement, which are interchangeable through a 60° rotation, as shown in Figure 1.9.

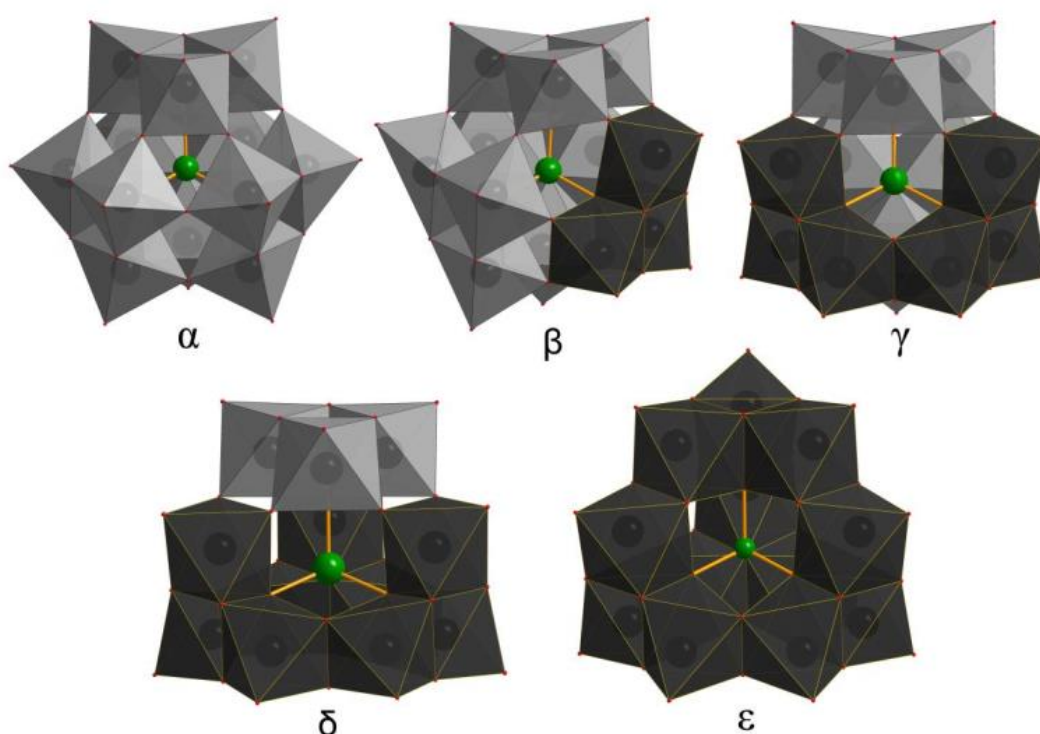


Figure 1.8 Polyhedral representations of the five Keggin isomers, α - ϵ , which result from sequential 60° rotations of the $\{M_3O_{13}\}$ triad around the central tetrahedron. (Colour scheme: heteroatom (X) = green, oxygen = red, metal (M) = grey - staggered face = pale grey, eclipsed face = dark grey)

Recently, several Keggin-like structures have been discovered with frameworks composed of non-traditional POM addenda elements (eg $\text{Mn}^{\text{III/IV}}$, Ga^{III} , Al^{III} , Mn^{II} , Fe^{III} , Zr^{II} , and Ti^{IV})⁶⁴⁻⁶⁶ with slightly different Keggin architectures. This has led to the introduction of the term ‘kegginoidal’ structures to describe a generalised clathrate structure with a single ion core and twelve-membered shell.⁵⁸ In this view, there are two main kegginoidal metal-oxo skeletons: the ‘classical’ $\{\text{XM}_{12}\text{O}_{36}\}/\{\text{XM}_{12}\text{O}_{24}\}$ Keggin structures, which contains each of the α - ϵ isomers, and a more recent ‘extended’ $\{\text{XM}_{18}\text{O}_{42}\}$ framework (Figure 1.10). The latter group can be conceptualised as having additional $\{\text{MO}_x\}$ groups located distally with respect to each of the six unoccupied square faces of the outer Keggin shell formed by 24 bridging oxo ligands. Examples of the extended kegginoidal type include Cu, Pd, Co and Ni.⁶⁷⁻⁷⁰

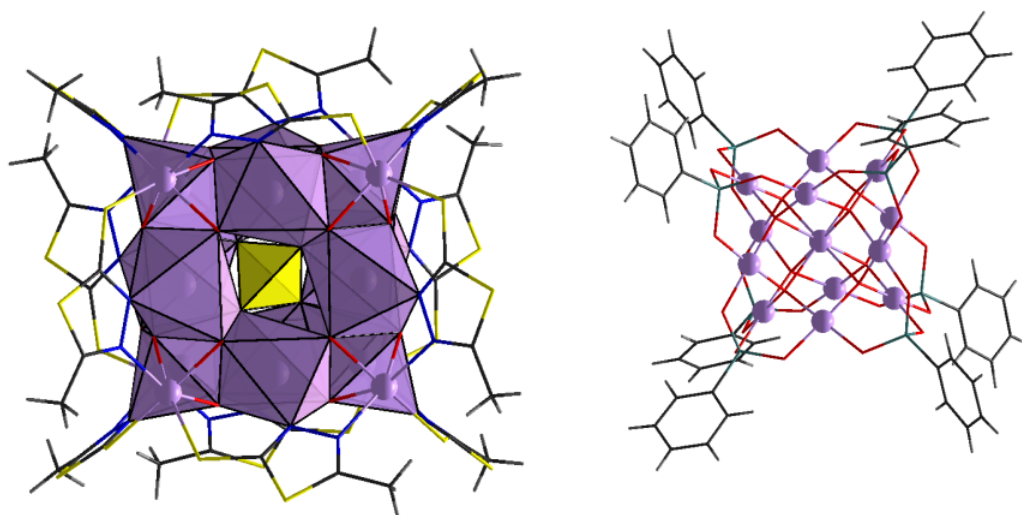


Figure 1.10 Representation of two non-classic kegginoids. Left) polyhedral representation of $[\text{Co}_{20}(\text{OH})_{24}(\text{MMT})_{12}(\text{SO}_4)]^{2+}$ (MMT=2-mercapto-5-methyl-13,4-thiadiazole) which contains the kegginoid substructure of $\{(\text{SO}_4)@\text{Co}_{12}\text{O}_{24}\}$. Right) Ball and stick representation of $\{\text{Pd}_{13}(\text{AsPh})_8\text{O}_{32}\}$ (Ph=phenol) which contains the kegginoid $\{(\text{PdO}_8)@\text{Pd}_{12}\text{O}_{24}\}$. (Colour scheme: S = yellow, O = red, Co/Pd = lavender, N = blue, C = teal, C = black, H = grey)

Interesting first row transition metal kegginoids include the $\{\text{Mn}_{13}\}$ and $\{\text{Fe}_{13}\}$ classical Kegginoids, respectively. The former, discovered in 2011, is synthesised in methanol using one pot reaction of $\text{Mn}(\text{NO}_3)_2 \cdot 6\text{H}_2\text{O}$ with 2,6-bis[*N*-(2-hydroxyethyl)iminomethyl]-4-methylphenol (H_3bemp) acting as a ligand. The cluster contains an inner MnO_6 octahedron within the Mn_{12} clathrate shell, and is

capped by six bemp ligands: each capping two Mn centers. This compound was found to be able to undergo four reversible one-electron redox processes. Three of the five redox states from this process were isolated, and ground state molecular spins determined as $S=9/2$, $10/2$ and $11/2$ for the $\{\text{Mn}^{\text{III}}_{11}\text{Mn}^{\text{IV}}_2\}$, $\{\text{Mn}^{\text{III}}_{10}\text{Mn}^{\text{IV}}_3\}$ and $\{\text{Mn}^{\text{III}}_{12}\text{Mn}^{\text{IV}}\}$, clusters, respectively.⁷¹

The latter Kegginoid is the ‘iron Keggin’, initially prepared by Nyman, et al in 2015. This kegginoide, consists of an inner $\text{Fe@Fe}_{12}\text{O}_{36}$ Keggin classical, Keggin, but contains six bismuth atoms in above each of the Fe_3 triad caps. This makes the structure resemble an inverted heteroatom extended Keggin, where the 18 metal centers are split between Fe^{III} and Bi^{III} . This structure is interesting in that Bi is the only element capable of stabilising the compound, and while the trichloroacetic acid ligand can be removed and replaced with another O- donor ligand, removal of the Bi causes the structure to decompose. This compound will be discussed further in section 1.2.2.2.⁷²

Keggin structure isomers can also be seen in some metal-oxide solid state crystal structures. For example, two forms of iron (oxy)hydroxide, ferrihydrite and magnetite, contain the δ and ϵ Keggin motifs (Figure 1.10),^{73,74} respectively, and there is evidence that a discrete Fe_{13} ion forms as a precursor to both of these minerals.^{75,76} These are highlighted within the bulk structure of Ferrihydrite and hematite in figure 1.11

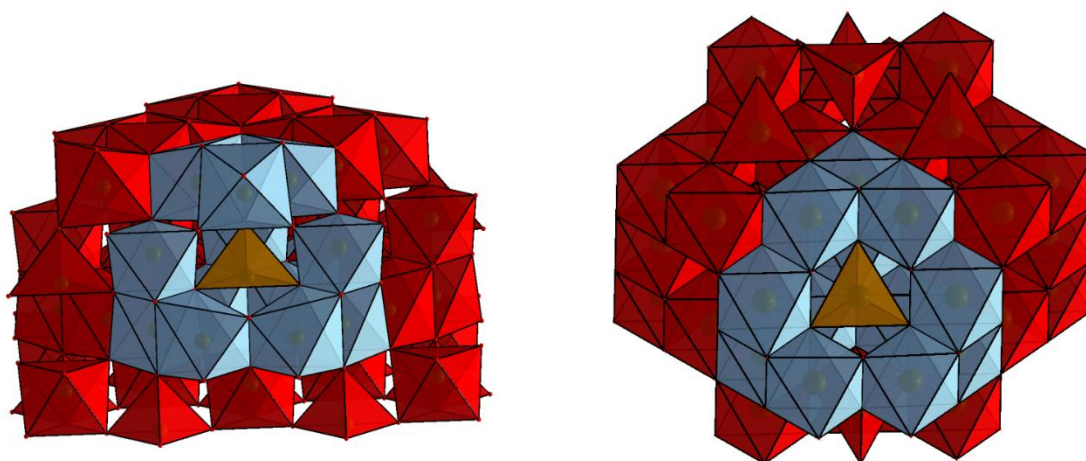


Figure 1.11 Polyhedral representations of 6-line Ferrihydrite (left) and magnetite (right), with δ and ϵ Keggin structures highlighted, respectively. (Colour scheme: Fe bulk = red, Fe Keggin shell = light blue, Fe Keggin core = orange)

1.1.3.4 Dawson

The Dawson anion, $[X_2M_{18}O_{62}]^{n-}$, (Figure 1.12) consists of 18 addenda-centred shell forming octahedra and two inner heteroatom-centred tetrahedra. The structure resembles the combination of two α -Keggin units with three addenda sites removed from each. The removed addenda come from neighbouring sites of three different trimer units in each Keggin. This allows the two fragments to bond together *via* corner sharing of the newly accessible bridging oxo ligands, which creates a belt region with 12 addenda atoms. The final 6 addenda atoms arise from the two $\{M_3O_{13}\}$ units at opposite sides (poles) of the belt region (Figure 1.11) giving an overall oval shaped closed framework.⁷⁷ The increased ratio of bridging M-O bonds to bridging X-O bonds in the Dawson compared with that of the Keggin results in a greater overall stability of the Dawson.⁷⁸

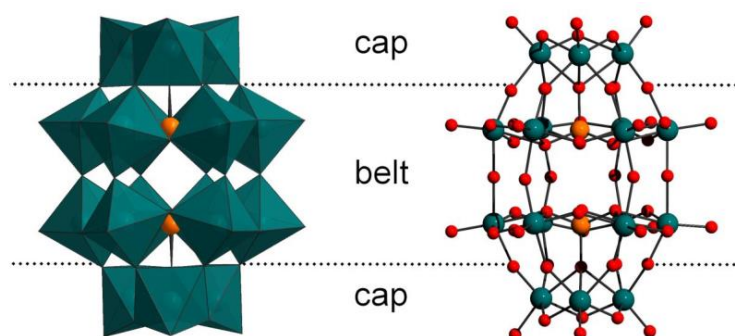


Figure 1.12 Representations of the Dawson structure $\{X_2M_{18}O_{62}\}^{n-}$ in (left) polyhedral and (right) ball-and stick representation. (Colour scheme: M = teal, W orange, O = red)

Like with Keggin clusters, multiple isomers of the Dawson ion exist. These result from a combination of 60° rotations around the capping triads (resulting in α , β , and γ isomers), and an additional 60° rotation around the belt region, transforming the original isomers to α^* , β^* and γ^* , respectively as shown in Figure 1.13

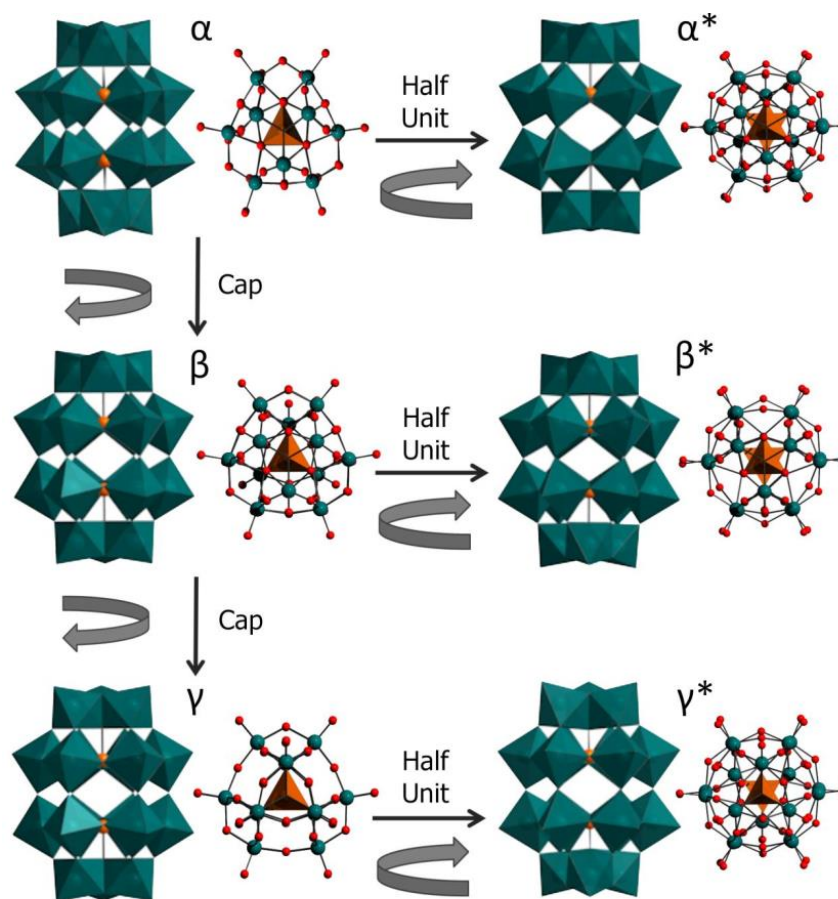


Figure 1.13 Polyhedral and ball and representations of the six Dawson isomers permissible by 60° rotation of cap and belt regions.

Examples of Dawson isomers exist for the α , β , γ and γ^* isomers, but not for β^* and α^* .^{14,77,79-81} This is likely due to the theoretical stability of each structure decreasing along this sequence, which is a consequence of increasing structural distortion from the heteroatom and a greater number of eclipsed versus staggered conformations.⁸²

1.2 Iron oxide chemistry

Iron oxides and hydroxides, which make up around 5% of the minerals in earth's crust,⁸³ are an important class of compounds both in nature and in human society.⁸⁴ Over a dozen natural polymorphs exist, including ferrous compounds (e.g. wüstite, FeO),⁸⁵ ferric compounds, (e.g. hematite, α -Fe₂O₃; and maghemite, γ -Fe₂O₃)^{86,87}, mixed ferrous/ferric (e.g. magnetite, Fe₃O₄),⁸⁸ as well as a host of hydroxides (e.g. goëthite, α -FeOOH; lepidocrocite, γ -FeOOH; and ferrihydrite, 5.Fe₂O₃.9H₂O)^{84,89,90}. In the human body, iron is found in proteins (haemoprotein),

as haem compounds (haemoglobin or myoglobin), as well as in various enzymes, and is mainly responsible for oxygen transport and electron transfer processes.^{91,92} The main transport mechanism for iron in the body is via the protein ferritin, which stores up to 4,500 iron atoms in the form of ferrihydrite.⁹³ Iron deficiency is associated with diseases such as anaemia, hypothyroidism and celiac disease.^{94,94}

In society, iron oxides have been in use since prehistoric times as pigments⁹⁵ and later as objects of philosophical interest, with Thales of Miletus (624-546 B.C.) reasoning that lodestone (magnetite) must contain a soul due to its ability to cause motion.⁹⁵ Today, iron oxides are of great importance in catalysis (e.g. water treatment, hydrogen peroxide decomposition, carbon monoxide removal, ammonia synthesis),⁹⁶⁻⁹⁹ propellants,¹⁰⁰ medicine (e.g. MRI contrast agents)^{101,102} and magnetic materials (e.g. single molecular magnets and adiabatic coolants).^{103,104} As such there is an impetus to develop new iron oxide materials. Because many high nuclearity iron oxides arise from clustering and trapping of iron nuclei in water, the following sections describe the behavior of iron in aqueous solution, growth of iron clusters, and examples of high nuclearity clusters.¹⁰⁵

1.2.1 Iron Aqueous chemistry

The equilibrium state of iron in water is described by a Pourbaix diagram which shows the thermodynamically favoured state of iron in certain conditions. A Pourbaix diagram is a two dimensional plot of electrical potential against pH, at a specified temperature and elemental concentration. Often, the region of water stability to reduction and oxidation are also marked. The Pourbaix diagram for iron¹⁰⁶ (Figure 1.14) shows two stable aqueous phases, namely Fe^{3+} at very low pH and oxidising electrical potential, and Fe^{2+} in weakly to strongly acidic solutions and weakly reducing electrical potential. Solid phases (Fe_2O_3 , Fe_3O_4 , and FeO) are found in more alkaline conditions. Metallic iron is found in very reducing conditions, whereas FeO_4^{2-} is found in very oxidising conditions, however neither of these phases are stable in water. Thus, many cluster synthesis reactions begin in either Fe^{2+} or Fe^{3+} regions.

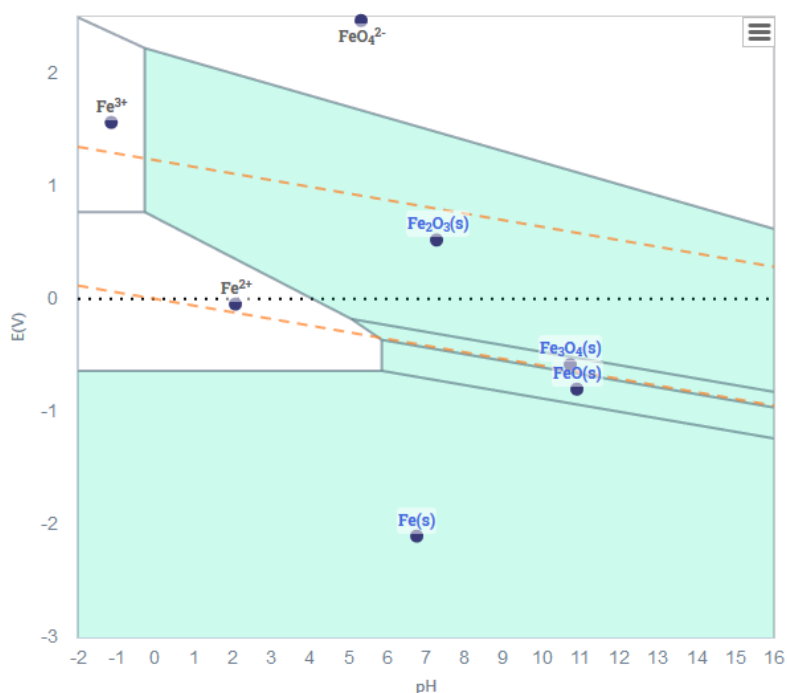


Figure 1.14 Iron Pourbaix Diagram, showing regions of thermodynamic stability for different phases of iron(hydr)oxide

However, iron cations form hexacoordinate aquo complexes, $[\text{Fe}(\text{H}_2\text{O})_6]^{z+}$ ($z=2$ and 3 for $\text{Fe}(\text{II})$ and $\text{Fe}(\text{III})$, respectively) in water, which undergo sequential deprotonation as pH increases. Further, the relative concentrations of individual $\text{Fe}(\text{II}/\text{III})$ aquo complexes can be shown in a speciation diagram. Speciation diagrams for Fe^{2+} and Fe^{3+} are shown in Figure 1.15, which show that deprotonation begins at a much lower pH for Fe^{3+} compared with Fe^{2+} .¹⁰⁷ This is due to the charge and size of the cation, which makes the ferric aquo complex more acidic than the ferrous species.¹⁰⁸

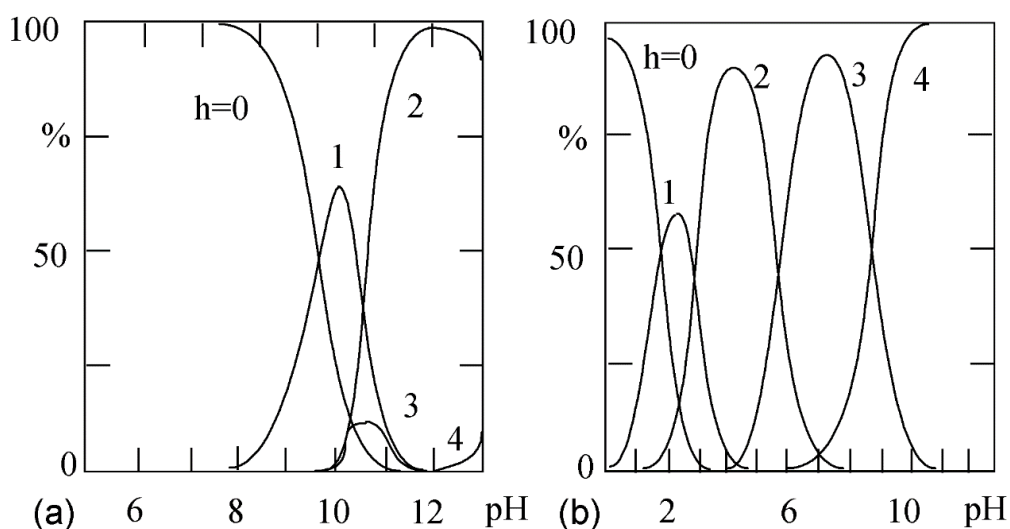


Figure 1.15. Speciation of $[\text{Fe}(\text{OH})_h(\text{H}_2\text{O})_{6-h}]^{z-h}$ complexes of a) Fe^{2+} and b) Fe^{3+} (Taken from Jolivet, et al¹⁰⁸)

Deprotonation of ferric aquo complexes by addition of base also leads to a rapid drop in solubility. This is due to the reduced Coulombic repulsion between the high charges of each individual complex. Aggregation of larger clusters then proceeds by one of two mechanisms depending on the coordination sphere of each cation. Aquohydroxo complexes react through a single step by olation with elimination of water, and the formation of a hydroxo bridge (Figure 1.16, taken from Jolivet, et al¹⁰⁸). Oxohydroxo complexes, however, have no leaving water group and require a two-step associative mechanism, followed by proton transfer from the bridging hydroxyl group to the terminal hydroxyl group. This forms an oxo-bridge and terminal water, which is eliminated in the final reaction stage.¹⁰⁹

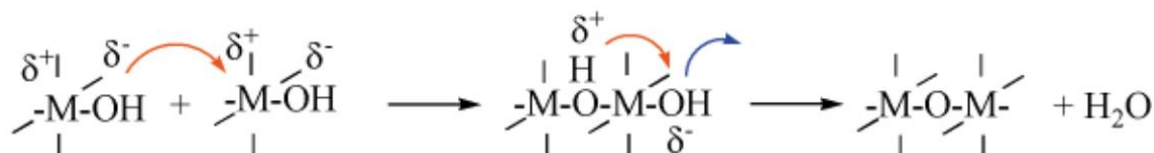


Figure 1.16 Condensation of iron aquohydroxo complexes by a single step olation¹⁰⁸

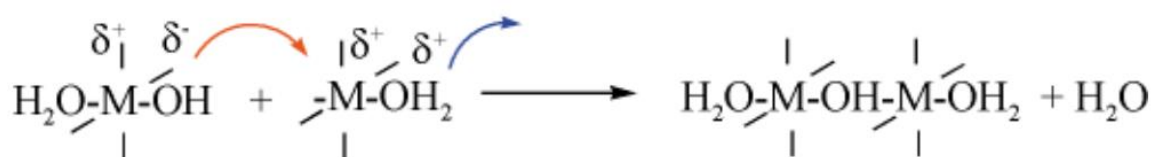


Figure 1.17 Condensation of iron oxohydroxo complexes via two step oxolation¹⁰⁸

Therefore, it is possible, in principle, possible to grow and stabilise iron oxide clusters in a similar way to polyoxometalates, namely by applying a pH change to facilitate condensation reactions. However, the lack of the formation of a terminal $\text{M}=\text{O}$ bond means that growing clusters lack kinetic stability and will continue growth until an infinite polymer is reached. In the first instance, this is often ferrihydrite, which will eventually decompose to form hematite.

1.2.2 Large iron -oxo clusters

Over the past few decades, and especially since the discovery of single molecular magnets, hundreds of iron oxo-clusters have been synthesised, with dozens of distinct architectures existing. Unlike polyoxometalates, which are stabilised by

terminal M=O bonds, each of these structures are stabilised by organic ligands, particularly alkoxide, carboxylate and halogens. These compounds are of interest for their magnetic, catalytic and bio-inorganic relevance. The following section reviews current literature of large iron-oxo clusters based on dimensionality, and if possible, compares them to known structures of polyoxometalates. Often, these reactions are performed in organic solvents to prevent rapid uncontrolled aggregation of iron (oxo)hydroxo complexes.

1.2.2.1 Lindqvist and Super-Lindqvist

The Lindqvist structure, $\{M_6O_{19}\}$ was described in section 1.1.3.1. The first iron Lindqvist analogue, $[OFe_6(\text{THME})_6]^{2-}$ (THME = tris(hydroxymethyl)ethane) was discovered in 1990¹¹⁰ using THME as tridentate ligand and FeCl_3 as iron source in methanol, with a second, $[Fe_6O(\text{OCH}_3)_{18}]^{2-}$, being produced 2 years later in 1992 in similar conditions but using methoxide as ligand.¹¹¹ These compounds are unusual in that they contain a long Fe- μ_6 O bond of 2.3 Å. Additionally, the authors of the former note that stopped flow kinetic studies suggest that multiple species are present in solution, and suggest this compound may not be the major solution component.¹¹⁰

In 2000, the Lindqvist structure was expanded upon with a decametalate ($\{M_{10}O_{28}\}$) analogue, $[Fe_{10}O_2Cl_8(\text{THMP})_6]$ (THMP = tris(hydroxyl methyl)propane).¹¹² This was synthesised by reacting FeCl_2 with THMP in acetonitrile and using solvothermal conditions. Structurally, 8 of the terminal oxo ligands replaced by chloride, and the metal framework is extended by one layer in one direction. More recently, in 2015,¹¹³ solvothermal reactions were used to take this one step further with the synthesis of an iron ‘super-Lindqvist’ aggregate, $[Fe_{19}O_{13}(\text{OH})(\text{OEt})_{30}]$. Synthetically it involves the solvothermal reaction of $[Fe_2(\text{O}^t\text{Bu})_6]$ with ethanol in the presence of tetrabutylammonium ethoxide. The structure is based on the Lindqvist, but with an addition layer of iron octahedra extending from four of the eight Lindqvist faces. It is reminiscent of ‘keggins’ mentioned in section 1.1.3.3 as it contains an outer polyhedral shell and inner metal octahedron. These four Lindqvist-like compounds are shown in Figure 1.18.

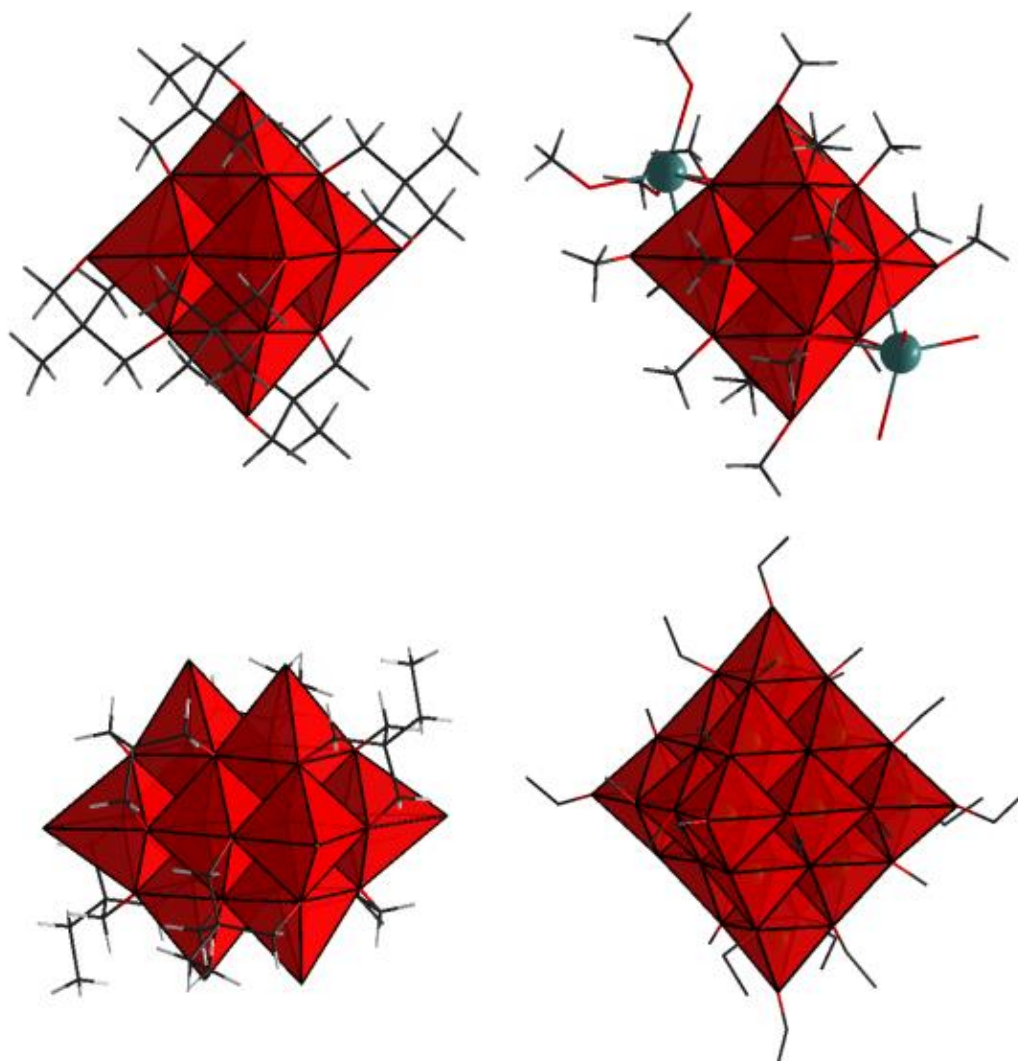


Figure 1.18 Lindqvist-like iron clusters. Top left) THME stabilised $\{\text{Fe}_6\}$ Lindqvist. Top right) methoxide and Na^+ stabilised Lindqvist. Bottom left) THMP stabilised $\{\text{Fe}_{10}\}$ decametalate. Bottom right) ethoxide stabilised Fe_{19} super-Lindqvist

1.2.2.2 Keggin and Kegginoids

The Keggin structure $\{(\text{XO}_4)\text{M}_{12}\text{O}_{36}\}$, described in section 1.1.3.3, is particularly interesting for iron clusters as it forms the basis of both magnetite and ferrihydrite and is thought to be a precursor to growth of the solid state. Four ferric Kegginoid structures are known (shown in Figure 1.19). The first iron Kegginoid cluster, $[(\text{FeO}_4)\text{Fe}_{12}\text{F}_{24}(\text{OMe})_{12}]^{5-}$ was discovered in 2002.¹¹⁴ It exhibits an α -Keggin structure with $\text{X}=\text{Fe}$ in the XO_4 tetrahedron. It is synthesised from FeF_3 in methanol by simply stirring with heat in the presence of pyridine. Interestingly, while the core oxo ligands are retained, each of the bridging oxo groups between M_3 triads of a classic Keggin have been replaced by an F^- bridge, while the intra triad bridges

are replaced with methoxy groups and the terminal oxo group replaced by additional fluoride.¹¹⁴

Later, in 2004, two structures were published which are structural fragments of magnetite: $[\text{Fe}_9\text{O}_4(\text{OH})_5(\text{heia})_6(\text{Hheia})_2]$ and $[\text{Fe}_{17}\text{O}_{16}(\text{OH})_{12}(\text{py})_{12}\text{Cl}_4]^{4+}$ (heia = (2-hydroxyethyl)iminoacetate, py = pyridine).¹¹⁵ The former is similar to a lacunary ϵ -Keggin, with three octahedra removed, disrupting the M_3 triads, and was synthesised by reacting $\text{Fe}(\text{NO}_3)_3 \cdot 9\text{H}_2\text{O}$ with H_2heia in methanol in the presence of tetramethylammonium hydroxide. The latter is similar to a complete ϵ -Keggin with an additional four FeO_3Cl tetrahedra in the hexagonal 'windows', and was synthesised using FeCl_3 in pyridine. Interestingly, this compound has a large molecular spin ground state of $35/2$ due to antiferromagnetic coupling between the 12 octahedral Fe(III) centres in the Keggin shell and the 5 tetrahedral Fe(III) centres in the core and caps of the molecule. Several analogues of this have been created by replacing the pyridine with other aromatic amines, and the chlorine with bromide.¹¹⁶

The most recent iron Kegginoid to be synthesised was by Nyman et. al.³ in 2015: $[(\text{FeO}_4)\text{Fe}_{12}\text{O}_{12}(\text{OH})_{12}(\text{tca})_{12}]$ (Htca = trichloroacetic acid). This compound, which forms an α -Keggin is synthesised in water from $\text{Fe}(\text{NO}_3)_3 \cdot 9\text{H}_2\text{O}$, $\text{Bi}(\text{NO}_3)_3 \cdot 5\text{H}_2\text{O}$ and tca in the presence of NaHCO_3 . This was the first example of a large purely iron oxo-cluster being stabilised in water, which usually drives the reaction towards uncontrolled polymerisation of ferrihydrite. Stabilisation was likely due to the presence of the strongly acidic tca ligands and high charge of the Bi^{3+} which is (possibly) uniquely able to interact with prenucleation trimer clusters at a pH below which uncontrolled aggregation normally occurs.^{117,118}

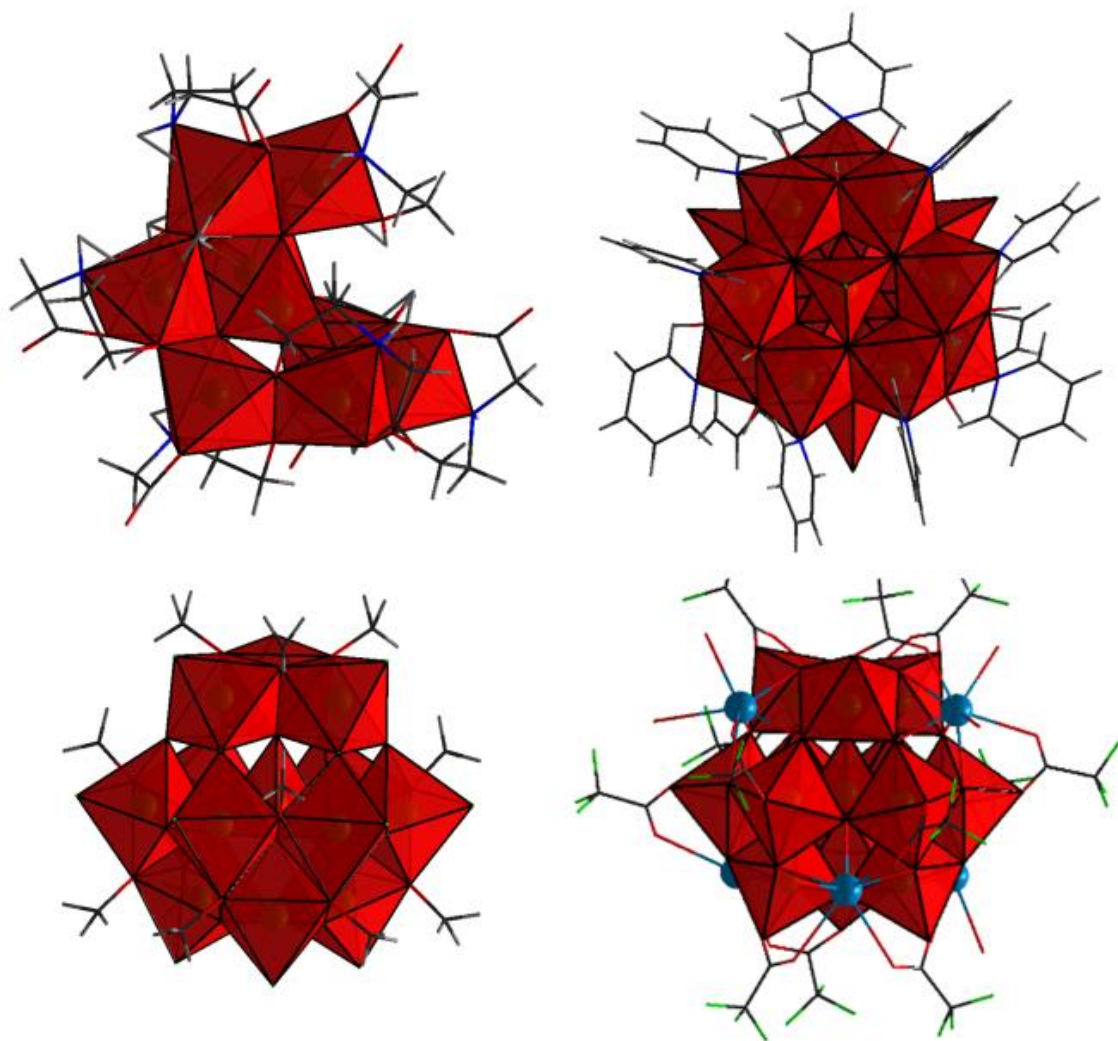


Figure 1.19 Iron kegginooids. Top left) heia stabilised Fe_9 lacunary ϵ -Kegginoid. Top right) pyridine stabilised Fe_{17} 'bromide capped ϵ -Kegginoid. Bottom left) methoxide and fluoride stabilised Fe_{13} α -Kegginoid. Bottom right) tca and Bi^{3+} stabilised α -Kegginoid.

1.2.2.3 High nuclearity ferric wheels and cages.

Another common type of high nuclearity iron cluster is that which forms macrocycles, or molecular wheels. In addition to the magnetic and biological relevance of these structures, wheels and cages have the additional capability to encapsulate guest molecules, providing additional functionality to this class. Wheels and cages exhibit the highest nuclearity iron clusters due to the ability of organically stabilised building clusters to aggregate into larger stable structures. Currently, ferric wheels range in size from 6 to 28 iron atoms, while cages can

grow up to a nuclearity of 168.¹¹⁹ The first ferric wheel was discovered in 1988 as $[\text{Na}_2\text{Fe}_{18}\text{S}_{30}]^{8-}$.¹²⁰ Interestingly, this contained only tetrahedral iron environments, contained no terminal ligands and was stabilised solely by sulfide bonds. It is formed by reaction of FeCl_3 with Li_2S in methanol in the presence of $\text{Na}[\text{PhNC}(\text{O})\text{Me}]$ and tetrapropylamine bromide followed by ether diffusion into acetonitrile.¹²⁰ However, the first iron oxo ring was discovered shortly after in 1990 as $[\text{Fe}_{10}(\text{OMe})_{20}(\text{O}_2\text{CCH}_2\text{Cl})_{10}]$ by reaction of iron acetate with iron nitrate in methanol which shows a ground spin state of 5/2. This 10-member ring is stabilised by bridging trichloroacetate ligands, and forms a cavity of 2-3 Å.¹²¹ These wheels are shown in Figure 1.20.

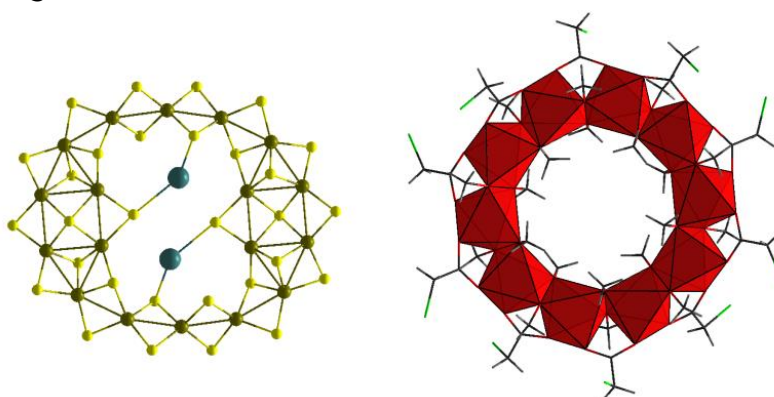


Figure 1.20 Early Ferric rings. Left) $[\text{Na}_2\text{Fe}_{18}\text{S}_{30}]^{8-}$, Right) $[\text{Fe}_{10}(\text{OMe})_{20}(\text{O}_2\text{CCH}_2\text{Cl})_{10}]$

Following this came a several smaller hexanuclear rings whose internal cavity hosted (and was supported by) an alkali metal cation (Eg, Li^+ , Na^+) and ligands such as dibenzoylmethane (dbm), with a molecular ground spin state of 5/2 (Figure 1.21, left).¹²²⁻¹²⁴ This structures is akin to that of the Anderson POM, but with a ligand stabilised ring, and the central transition metal replaced with an alkali metal. By using this approach with a larger alkali metal cation, such as Cs^+ , a larger $\{\text{Fe}_8\}$ ring could also be stabilised (Figure 1.21, right) with a molecular spin state of 5/2.¹²⁵

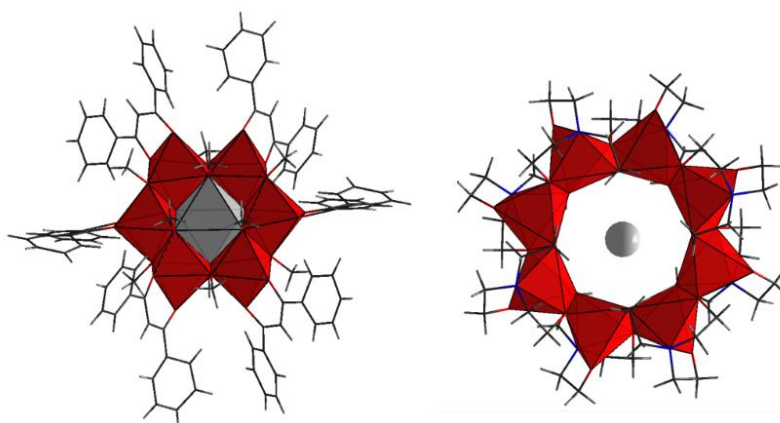


Figure 1.21 Small rings template by an alkali metal cation. Left) alkali metal template $\{\text{Fe}_6\}$ ring, $[\text{NaFe}_6(\text{OCH}_3)_{12}(\text{dbm})_6]^+$,¹²³ right) $[\text{CsFe}_8\{\text{N}(\text{CH}_2\text{CH}_2\text{O}_3)_8\}]^{+125}$

Following this, many larger rings were described including the twisted dodecameric ring, $[\text{Fe}_{12}(\text{OCH}_3)_{24}(\text{dbm})_{12}]^{126}$, hexadecameric ring $[\text{Fe}_{16}(\text{EtO})_4(\text{PhCOO})_{16}(\text{Hthme})_{12}]^{127}$ and the octadecameric ring $[\text{Fe}_{18}(\text{OH})_6(\text{bdma})_6(\text{OCH}_3)_{18}(\text{O}_2\text{CCH}_3)_{12}]^{128}$ (bdma = 1,3-benzenedimethanamine), which is currently the largest single stranded ferric wheels bridged only by oxygen atoms. Recently, in 2017, an $\{\text{Fe}_{18}\}$ wheel has been extended into a 24-unit wheel by the incorporation of a series of lanthanide cations to form $\{\text{Fe}_{16}\text{Ln}_6\}$ rings ($[\text{Fe}_{18}\text{M}_6(\text{O}_2\text{CCHMe}_2)_{12}(\text{Htea})_{18}(\text{tea})_6(\text{N}_3)_6]$, where M = Dy, Gd, Tb, Ho, Sm, Eu and Y, and H_3tea =triethanolamine).¹²⁹

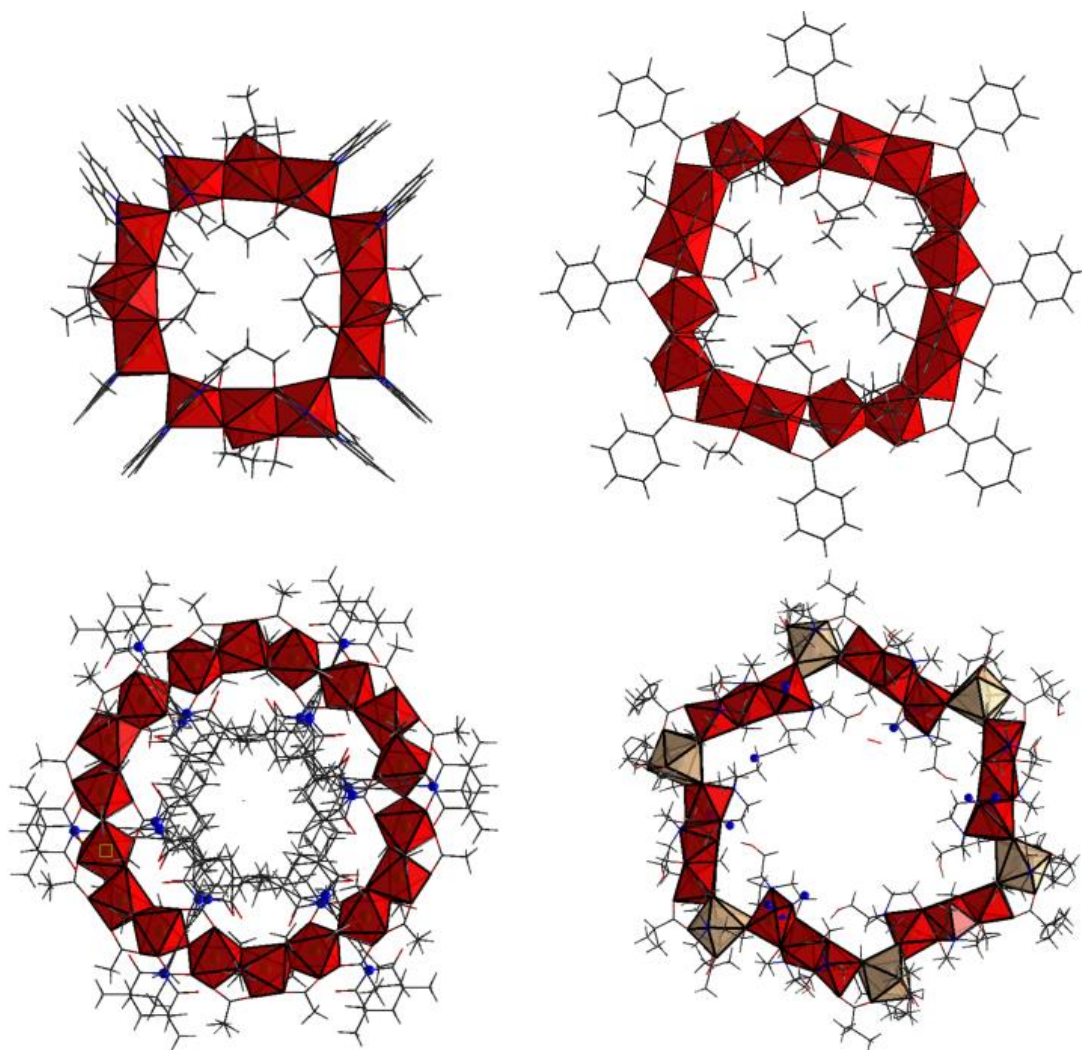


Figure 1.22 Large ligand stabilised ferric rings. Top left) $\{\text{Fe}_{12}\}$, Top right) $\{\text{Fe}_{16}\}$, Bottom left) $\{\text{Fe}_{18}\}$. Bottom right) $\{\text{Fe}_{18}\text{Ln}_6\}$.

The largest iron oxide ring structure known to date is $\{\text{Fe}_{28}\}$, $([\text{Fe}_{28}\text{O}_8(\text{tart})_{16}(\text{CH}_3\text{COO}_{24})])^{20-}$ (tart = L-/D- tartrate, Figure 1.23, middle) and was discovered in 2009.¹³⁰ This molecule consists of four discrete $\{\text{Fe}_7\}$ subunits (Figure 1.23, left), which are linked by tartrate molecules into a ring. The metal centres within a subunit are held together by a combination of shared oxygen atoms arising from both the five tartrate molecules, six carboxylate molecules and two $\mu_3\text{O}$ atoms. The synthesis of this molecule is possible using both L- and D- tartaric acid, and the result is an enantiomerically pure, chiral L- $\{\text{Fe}_{28}\}$ or D- $\{\text{Fe}_{28}\}$, depending on which tartaric acid isomer was used. This compound exhibits an S=0 ground spin state due to the presence of strong antiferromagnetic interactions.

Shortly after this discovery, the $\{\text{Fe}_{28}\}$ structure was itself used as a building unit for an even larger molecule, $\{\text{Fe}_{168}\}$ $([\text{Na}_{24}\text{Fe}_{168}(\text{tart})_{96}\text{O}_{48}(\text{HCOO})_{144}]^{96-})$, which is composed of 6 $\{\text{Fe}_{28}\}$ molecules or 42 $\{\text{Fe}_7\}$ units.¹³¹ It forms a roughly cubic cage of length 38.7 Å, with NbO topology.¹³²

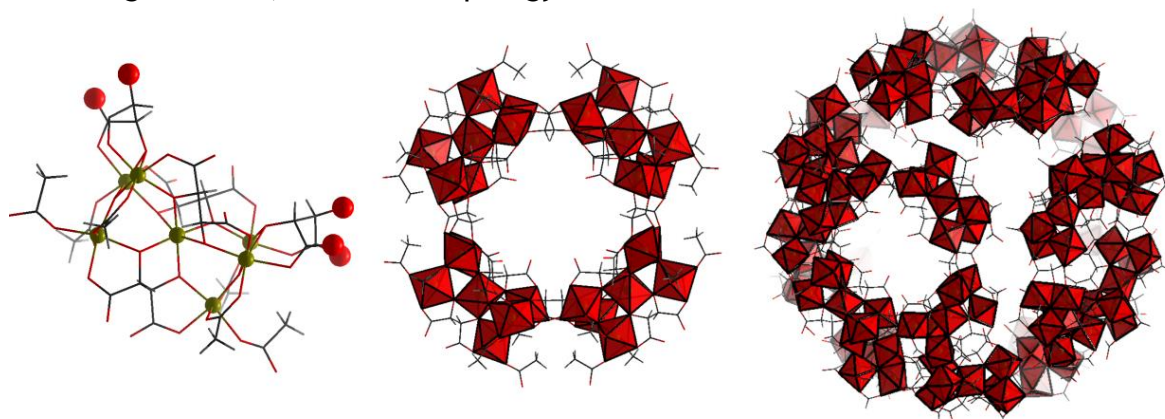


Figure 1.23 Chiral ferric compounds formed using tartaric acid. Left) Stick representation of $\{\text{Fe}_7\}$ building unit found in $\{\text{Fe}_{28}\}$ and $\{\text{Fe}_{168}\}$. Iron atoms are shown as gold balls, and oxygen atoms that link between $\{\text{Fe}_7\}$ units are shown as red balls. Middle) polyhedral representation of $\{\text{Fe}_{28}\}$ which forms by linking of four $\{\text{Fe}_7\}$ units through tartrate molecules. Right) Polyhedral representation of $\{\text{Fe}_{168}\}$ which is formed by linking of 6 $\{\text{Fe}_{28}\}$ units through Na^+ cations.

Only three other large ferric cages have been reported to date. The largest of these $\{\text{Fe}_{64}\}$, $[\text{Fe}_{64}\text{O}_{24}(\text{tea})_8(\text{Htea})_{24}(\text{HCOO})_{24}]^{12+}$, was discovered in 2008,¹³³ and like $\{\text{Fe}_{164}\}$, contains multiple discrete subunits: eight $\{\text{Fe}_8\text{O}_3(\text{tea})(\text{Htea})_3(\text{HCOO})_6\}$ at the corners of a cube linked by 12 carboxylate anions. In 2013, came the discovery of $\{\text{Fe}_{36}\}$,¹³⁴ $[\text{Fe}_{36}(\text{pyph})_{44}(\text{H}_2\text{O})_{48}]^{20+}$ (pyph = 2-pyridylphosphonate), which, unlike $\{\text{Fe}_{164}\}$ and $\{\text{Fe}_{64}\}$ was formed as an entirely interconnected, discrete

cage connected through phosphate ligands, rather than chains of $\{\text{Fe}_n\}$ units. The most recent large cage structure to be discovered is $\{\text{Fe}_{32}\}$,¹³⁵ $\text{Fe}_{32}(\text{PgC}_6)_6(\text{Cl})_{16+n}(\text{DMF})_{12}(\text{H}_2\text{O})_{20-n}$ ($n = 0-8$, DMF = dimethylformamide, PgC_6 = C-hexylpyrogallol[4]arene), which forms a mixed-valence iron metal oxide nanocapsule (MONC) with an internal cavity of around 1470 Å.

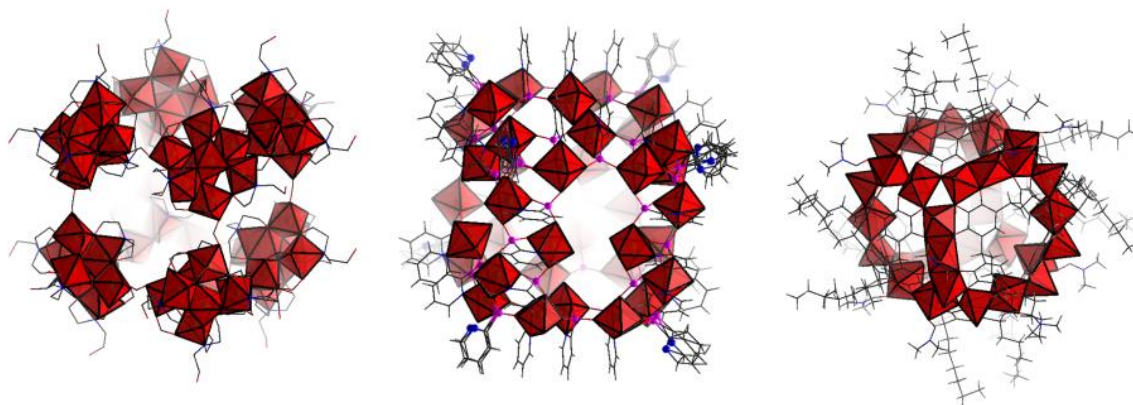


Figure 1.24. Left) $\{\text{Fe}_{64}\}$, middle) $\{\text{Fe}_{36}\}$, right) $\{\text{Fe}_{32}\}$

1.2.2.4 High nuclearity Fe- containing POMs

The final group of high nuclearity iron containing compounds are those found in transition metal substituted polyoxometalates (TMSPs). Substitution of iron into lacunary POM sites is common, and these are often used to connect different POM fragments into larger structures, although the iron nuclearity of these compounds is generally relatively low.¹³⁶⁻¹³⁸ There are a number of interesting exceptions to this, including the Fe-substituted Keplarate structure $\{\text{Mo}_{72}\text{Fe}_{30}\}$, $[\text{Mo}_{72}\text{Fe}_{30}\text{O}_{252}(\text{H}_2\text{O}(\text{MeCO}_2)_{15})]$, which contains single iron octahedra bridging between $\{\text{Mo}_5\}$ pentagonal units to form a stable MONC;¹³⁹ the ring structure $\{\text{W}_{48}\text{Fe}_{16}\}$, $[\text{P}_8\text{W}_{48}\text{O}_{184}\text{Fe}_{16}(\text{OH})_{28}(\text{H}_2\text{O})_4]^{20-}$, which is composed of four W_{12} lacunary Dawson units surrounding a double stranded $\{\text{Fe}_{16}\}$ ring;¹⁴⁰ a tetrahedral cluster $\{\text{W}_{60}\text{Fe}_{14}\}$, $[\text{Fe}_{14}(\text{OH})_{13}\text{O}_6\{\alpha\text{-P}_2\text{W}_{15}\text{O}_{56}\}_4]^{31-}$, which contains an 14-centred iron core trapped within four lacunary Dawson clusters, with a disordered tetrahedral core;¹⁴¹ and finally $\{\text{W}_{48}\text{Fe}_{27}\}$, $[\text{H}_{45}\text{P}_8\text{W}_{48}\text{Fe}_{27}\text{O}_{248}]^{28-}$.¹⁴²

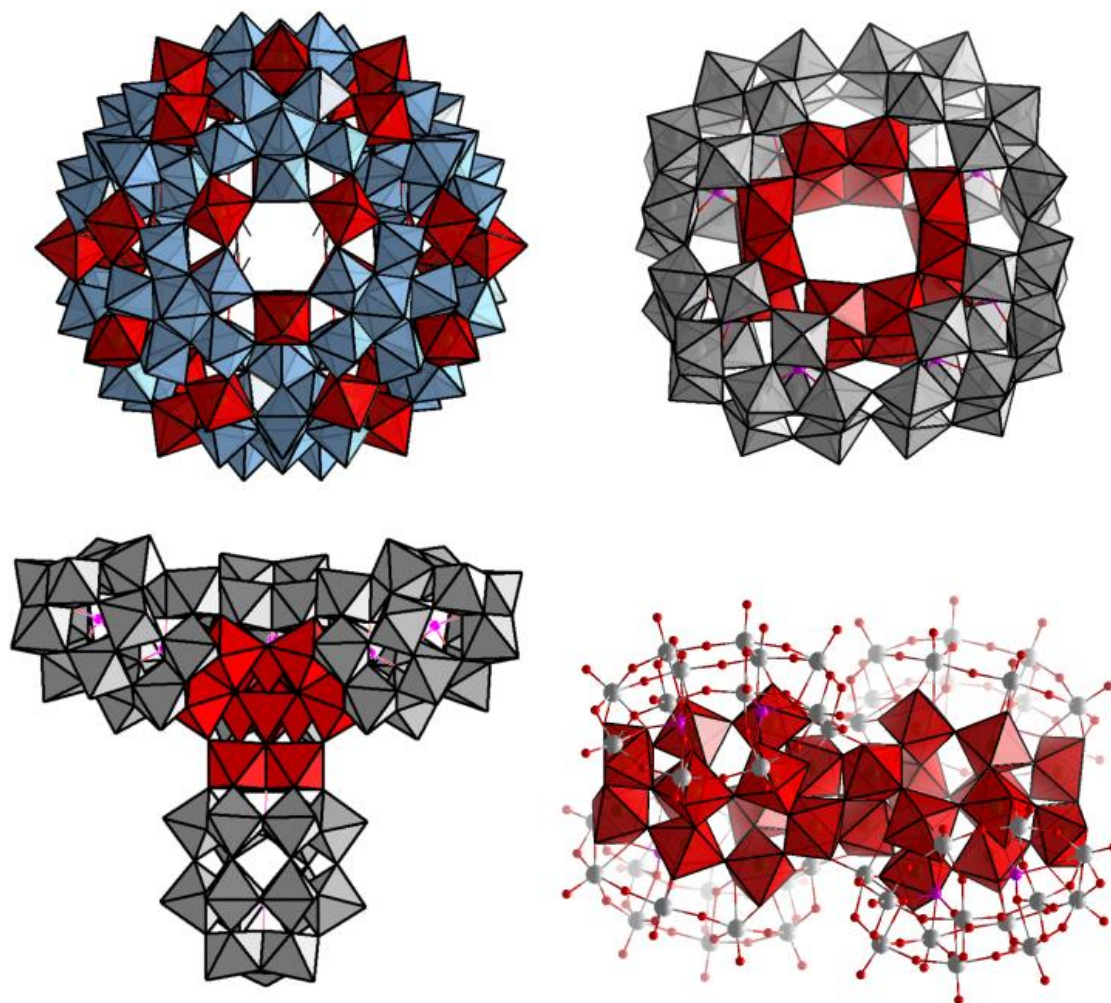


Figure 1.25 Top Left) $\{\text{Mo}_{72}\text{Fe}_{30}\}$ Keplarsite. Top Right) $\text{W}_{48}\text{Fe}_{16}$ ring. Bottom Left) $\{\text{W}_{60}\text{Fe}_{14}\}$ tetrahedra cluster. Bottom right) $\{\text{W}_{48}\text{Fe}_{28}\}$

1.3 Automation in chemistry

The introduction of automation to chemistry is likely to result in a transformation in approaches to chemical synthesis and analysis. It is currently commonplace for labour-intensive and (occasionally) risky procedures using potentially hazardous chemicals to be performed manually by highly trained and educated workers. Automation of such procedures offers many benefits, such as increased time efficiency and output per worker, increased through-put of experiments, increased safety of those working with chemicals, increased reliability and reproducibility of results, and the possibility of a digital standard procedure to avoid ambiguity in data reporting. Additionally, there is the possibility of incorporation of in-line analytics to allow continuous, real-time monitoring of

experiments. There currently exist three main types of automation technologies to aid in synthesis and analytics: iterative synthesis, flow chemistry and batch synthesis.¹⁴³ The following sections explore the advantages and disadvantages of some of these technologies.

1.3.1 Synthetic devices

1.3.1.1 Iterative synthesis devices

Iterative synthesis is used in the synthesis of oligomers that must be sequence controlled and function by sequentially coupling protected monomers to longer and longer chains. This technology, which uses solid state resins as growth matrices is currently used in the synthesis of peptides,¹⁴⁴ oligonucleotides,¹⁴⁵ and oligosaccharides¹⁴⁶.

This type of automation was initially developed in the mid-1960s, where protected amino acids were de-protected and coupled with further protected amino acids to allow controlled peptide growth. Within a decade, such synthesisers could produce proteins up to 124-amino acids long.¹⁴⁷ By the 1980s, nucleotide coupling chemistry had developed, and the use of silica as an alternative support to resin were sufficient for the introduction of a fully automated DNA synthesiser.¹⁴⁵ Currently, synthetic DNA fragments with up to 10,000 base pairs are possible through such automated synthesisers.¹⁴⁸ The first fully automated oligosaccharide synthesisers were introduced in around 2000.¹⁴⁹ The reason for this development was due to the difficulty in controlling chemoselective protection and deprotection of condensation sites as well as possible isomerism of the glycosidic bond. Currently automation of oligosaccharides can reach up to 50 units.¹⁵⁰ These devices are very reliable, but are necessarily specialised to one function, or type of reaction.

1.3.1.2 Micro and milli-fluidic devices

Micro and milli-fluidic devices are used in continuous flow chemistry - an automated process which allows reactions to take place within the confines of flowing solvent in tubing. This allows a much lower quantity of reagents to be used, improving safety, as well as providing much more efficient mixing and heat

transfer due to the narrow tubules and high surface-to-volume ratio.¹⁵¹ This technique also allows some highly hazardous chemicals, such as diazomethane and hydrogen cyanide to be generated, used and denatured *in situ*.^{152,153} Further, due to the efficient mixing and potential for high pressures in the narrow tubules, reactions may be carried out using less harsh reagents or conditions, and shorter timescales, making this a potentially green route for product synthesis.¹⁵⁴ Finally, multistep syntheses are also possible in flow, with both natural products and pharmaceutical products being synthesised entirely in flow.^{155,156} Flow reactors have been used for inorganic compound discovery, with a good deal of success.¹⁵⁷⁻¹⁶⁰ However, these devices cannot handle solids, and precipitation of solid material during a reaction can cause mechanical issues such as blocking. Additionally, scale up of flow reactions into batch does not translate directly, usually requiring further method development.¹⁶¹

1.3.1.3 Automated batch reactors

Automated batch reactors, which have been in use since the 1970s,¹⁶² generally consist of a mechanism (such as a pump) to deliver reagents from a stock source to a reactor, and are usually attached to some analytical equipment to allow automated data processing.¹⁶³ Batch reactors also have the capability to perform multistep reactions or processes by transferring reaction contents between different experimental modules, allowing for automation of procedures such as liquid/liquid separation and evaporation to be performed without manual intervention to the reaction system.¹⁶⁴ Batch reactors have recently been used for the automated discovery of new inorganic compounds via condition screening and search networking algorithms, and organic compounds via active learning algorithms, as well as total synthesis of multistep pharmaceutical products.¹⁶⁵⁻¹⁶⁸

1.3.1.4 Reactionware

A recent development on the automated batch reactor is a technique involving 3D printed apparatus in which entire reaction sequences can be performed, also known as Reactionware. This involves the printing of several cartridges composed of polypropylene, each of which is designed to facilitate a specific chemical transformation, such as reagent coupling, crystallisation and filtration. This

technique was introduced in 2012, with the synthesis of the inorganic polyoxometalates $\{W_{19}Mn_2\}$ and the phenanthridine-based heterocycle $C_{22}H_{20}N_2O$ (Figure 1.26).

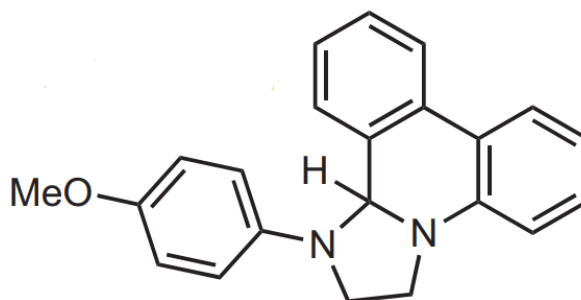


Figure 1.26. $C_{22}H_{20}N_2O$ synthesised in Reactionware

Later, pharmaceutical compounds were targeted using the synthesis and purification of ibuprofen as a proof of concept. The setup here involved three interconnected reaction vessels to allow a Friedal-Crafts acylation, followed by a 1,2-aryl migration, and finally base hydrolysis to produce crude ibuprofen. Acid workup and column chromatography were then performed manually to obtain purified ibuprofen in yields of around 30%.

1.3.2 Discovery Devices

In recent years, robotic systems and optimisation algorithms have been coupled with chemical research for purposes other than automated synthesis of organic and inorganic compounds. The aim of such research is to observe new chemical phenomena by applying an evolutionary algorithm to data obtained from reactions on an automated platform.

1.3.2.1 Droplet automation

In 2014, Gutierrez et. al, developed an automated platform for discovery of novel behaviour in oil droplets by altering the droplet composition. The system consisted of three main stages which were repeated: composition selection, behaviour observation and evaluation, and composition mutation. The composition selection stage involved choosing the proportions of each reagent (1-octanol, diethyl phthalate, 1-pentanol and either octanoic acid or dodecane) to be used in an experiment. The automated system would then dispense this composition into a Petri dish of water and a camera would observe the motion of the droplets for the

duration of the experiment. Depending on the initial reagent composition, varying degrees of droplet behaviour (eg, motion, division, explosion, vibration) could be observed and quantified. An evolutionary algorithm was then performed on the data in order to predict compositions required for enhancement of a particular behaviour. By selecting the outputs of the evolutionary algorithm as compositions for the initial stage, behaviours could be seen to increase in magnitude. For instance, optimising for motion caused the average droplet motion of the next generation to increase.

1.3.2.2 Networking chemical robots

In 2018, Caramelli et. al, produced a system in which two low-cost chemistry performing robots could perform reactions simultaneously and update each other via Twitter with observations gained from the systems they were investigating. These systems included the optimisation of synthetic conditions required for the formation of the polyoxometalates $\{W_{19}\}$, discovery of conditions required to produce azo-dyes of different colours from an aniline derivative precursor. In these systems, it was found that chemical space, and also optimal synthetic conditions could be determined more rapidly when the robots were collaborating than when the robots were performing reactions independently.

1.3.2.3 Humans vs robots

In 2017, Duros, et. al, produced a system in which an automated platform was allowed to explore chemical space for the crystallisation of the polyoxometalates $\{Mo_{120}Ce_6\}$ using an evolutionary algorithm. However, the aim of this algorithm was to obtain as complete an understanding of the crystallisation space as possible, rather than precise identification of successful crystallisation conditions. Thus, the approach was to identify conditions of highest uncertainty of outcome in each generation, so that the overall uncertainty of the system was decreased. Further, the researchers wanted to compare the ability of the robot to decrease uncertainty with that of human researchers. The results showed that while both humans and robots were better at decreasing system uncertainty than choosing conditions at random, the robot proved better at doing this than the human test subjects. A later article published using a similar system showed that when a

human was allowed to select conditions from a list generated by the robot, crystallisation space could be explored more effectively than the human or robot could alone.

1.3.2.4 Chemical computing

In 2019, Gutierrez et. al, developed a device which utilised the Belousov-Zhabotinsky (BZ) reaction to produce a chemical computing system. The BZ reaction, which involves the reversible redox reaction of $[\text{Fe}(\text{Bpy})_3]^{2/3+}$ and undergoes colour oscillations when stirred, was performed on a 5x5 cell grid in which the contents of each cell can freely diffuse to neighbouring cells. In this system, colour oscillations in a cell could be initiated by activating a magnetic stirring bar in the appropriate cell, and these oscillations would influence the oscillations of neighbouring cells in a spatiotemporal manner, and allow oscillations to propagate. As such, application of specific cells by stirring would result in the production of a specific oscillation pattern across the 5x5 cell array. By training a neural network to recognise this pattern, the robotic system could observe a pattern and deduce the input stirrer activation required to achieve this pattern. It was noted that one application of this computing capability could be encoding of data, in which the 2^{25} different stirrer states are encoded as a specific oscillating pattern that cannot be decoded without in identical device.

1.4 Random number generation

Random numbers are used extensively in many applications where their non-deterministic properties and unpredictability are essential, such as cryptography,¹⁶⁹ scientific modelling¹⁷⁰ and lotteries.¹⁷¹ As such, both generation and validation of random numbers are important to ensure that all output is as desired and devoid of systematic determinism or predictability, which could affect the quality of the output.⁵ There are two approaches for generation of random numbers: computationally generated (pseudorandom) and generation via a non-deterministic physical process (true random).⁵ Pseudorandom number generators (PRNGs), which create an arbitrarily long string of binary integers from an input seed using a mathematical algorithm, such as the Mersenne Twister,¹⁷² suffer from being deterministic and show long range correlations making them inappropriate

for many applications. In contrast, the binary strings produced by true random number generators (TRNGs) are inherently unpredictable and non-deterministic, increasing their quality but at the cost of resources required for their generation.¹⁷³

True random numbers cannot be generated computationally and must instead be harvested and distilled from a physical entropy source which exhibits nondeterministic behaviour. For the purposes of random number generation, a binary integer (bit) sequence that results from any system can be considered random if it meets the following criteria: 1) it exhibits statistical properties of an ideal random number, 2) subsequent bits cannot be predicted from prior bits, and 3) it cannot be reliably reproduced.¹⁷⁴ Many true random number generators exist such as, cosmic background radiation,¹⁷⁵ lava lamps,¹⁷⁶ and radioactive decay¹⁷⁷ with recent developments including quantum entanglement¹⁷⁸, electronic noise¹⁷⁹ and social media¹⁸⁰.

Many processes in chemistry are understood to be stochastic in nature. Phenomena controlling reaction kinetics such as molecular diffusion and collision rates, as well as thermodynamic phenomena such as chemical equilibria and phase changes can be modelled parsimoniously from stochastic assumptions.^{181,182} Inspired by the notion of chemical computing described in section 1.3.2.4, it was considered plausible that an automated platform could be created which utilised chemical reaction and crystallisation as an entropy source to create random numbers for encryption of data. This is discussed further in chapters 3 and 4.

2 Aims

The accessibility and capabilities of robotic automation has been increasing greatly in recent years, giving rise to the development of rapid and reproducible procedures; however, the application of automation to chemistry has been limited due to the difficulty in building and programming devices capable of the required procedures.

In particular, inorganic cluster chemistry has been under-developed due to the difficulty in handling reagents and performing reactions, as well as the difficulty in controlling the outcomes of such reactions in a reproducible way.

The first aim of this research is to create an automated robotic platform capable of reliably performing several types of inorganic cluster reactions in batch with the capability of filming reaction progress in real time and to explore the capabilities of such a device.

One aspect of this is in using the inherent stochasticity of these reactions to generate random numbers. In this aim, automated reactions will be developed to produce crystals which can be monitored remotely and used to generate random numbers. In doing so, it would also create a system from which code can be used to generate reproducibility in chemical reaction outcomes.

The second capability investigated using the robotic device is in the discovery and synthesis of new inorganic cluster compounds. In particular, cluster compounds involving iron will be explored due to the potential for such compounds to exhibit useful magnetic and electrochemical properties.

A third aim of this thesis is to discover large iron clusters using traditional manual synthesis should discovery by automated means prove problematic or slow.

3 Crystalbot platform

The following two chapters will document the work done on the project known as 'crystalbot'. The name crystalbot was given because its aim was to be able to perform inorganic reactions, capture images of the crystallizations and identify these automatically using a robot.

The robotic platform described in this document, was built by combining prior developments of the RepRap 3D printer project with a commercially available Computer Numeric Control (CNC) platform. It was designed to perform a large array of batch reactions in parallel, vastly speeding up screening of experimental conditions in compound discovery. The open-source nature and large amount of available documentation facilitated prototyping, development and implementation of the platform. This section is intended to give a complete methodology for recreating the random number generator. Section 3.2 describes the mechanical frame work, section 3.3 describes the methods used to perform chemistry, and section 3.4 specifies the electronic setup employed.

3.1 Hardware

The following sections describe the hardware required to create the platform, including the platform specifications and materials used in its construction.

3.1.1 Robot frame

The rationale for platform design was that firstly, as many identical reactions should be performed as close to simultaneously as possible, secondly that it should be possible to reliably produce images subsequent crystallizations, and thirdly that costs should be minimized. To achieve this, the main body of the platform consisted of an OX CNC Mechanical Kit, with dimensions of 500x750mm, giving a large area for multiple automated reactions and control of reagent output in the X, Y and Z dimensions. Reaction vials were then located on a supported glass sheet, below which a mobile camera was implemented on a set additional linear axes. A single mobile camera was incorporated (as opposed to an array of multiple fixed cameras) in order to prevent excess costs, and the delay in imaging between separate vials was considered not significant for data acquisition. All v-slot beam

connections were made using 90 Degree Angle Corners. Every mobile axis had an end stop attached at the end in order to define the zero position of the axis. The complete platform is shown in Figure 3.1.

3.1.1.1 Mechanical Design

The final platform design used for all experiments in this publication is shown in Figure 1. This consists of the i) CNC kit, which positions where reagents are to be dispensed; ii) a crystallization platform, which supports reaction vials and maintains their positions; iii) an imaging support system, which moves a camera to locations below vials in order to capture images; and iv) a fluid handling system which controls reagent transfer from stock solutions to reaction vial.

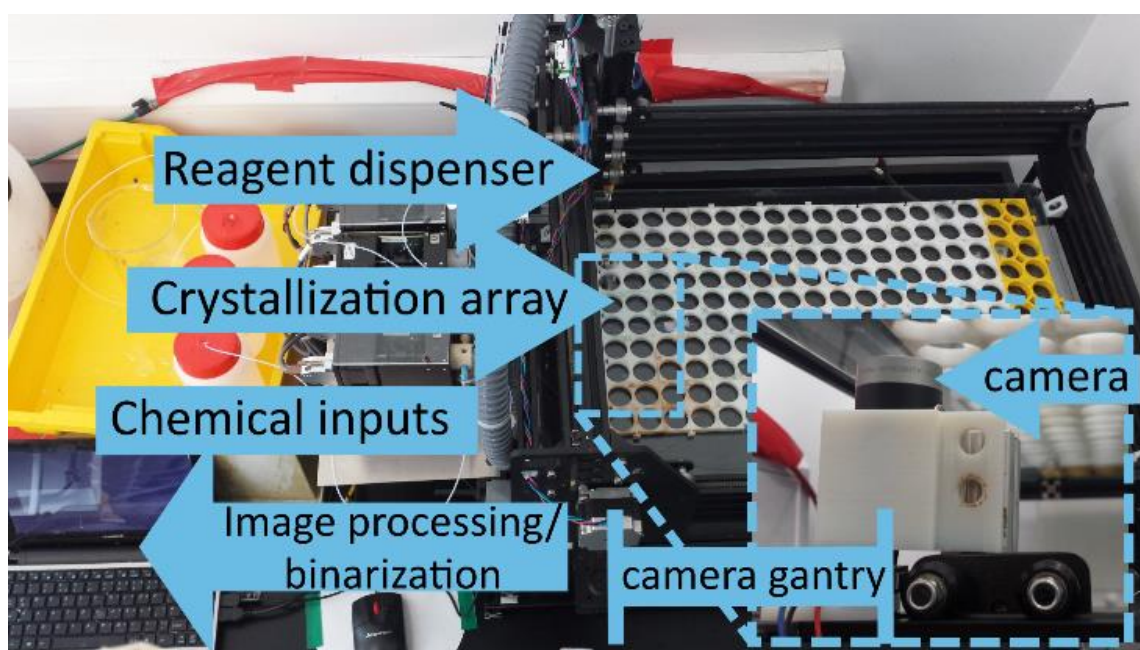


Figure. 3.1. Setup of the robotic system. Photograph showing the crystallization array inside the CNC framework and its relative position to the input stock solutions, pumps, camera and controlling computer.

3.1.1.2 CNC kit

The CNC kit used was an OX CNC Mechanical Kit with dimensions 500 x 750mm, and four NEMA23 - 175 oz - 2.0A stepper motors. It was constructed as directed in the manual.

3.1.1.3 Crystallization platform

The crystallization platform consisted of a sheet of glass with dimensions 350 x 400 x 3 mm (Figure 3.2). To support this, four 20 x 20 x 100mm v-slot aluminium beams were attached to the underside of the CNC Kit Y-frame: 50mm from each end of both sides and directed in towards the device in parallel with the X-frame. The vials used were made of glass, with a 14ml capacity and 12mm radius. An array of these vials was created on the glass surface held in place using interlocking 3D printed vial holders (Figure 3.3). An array of 10 x 10 vials was used to create experiments with 100 vials in them, although there was space available for more.

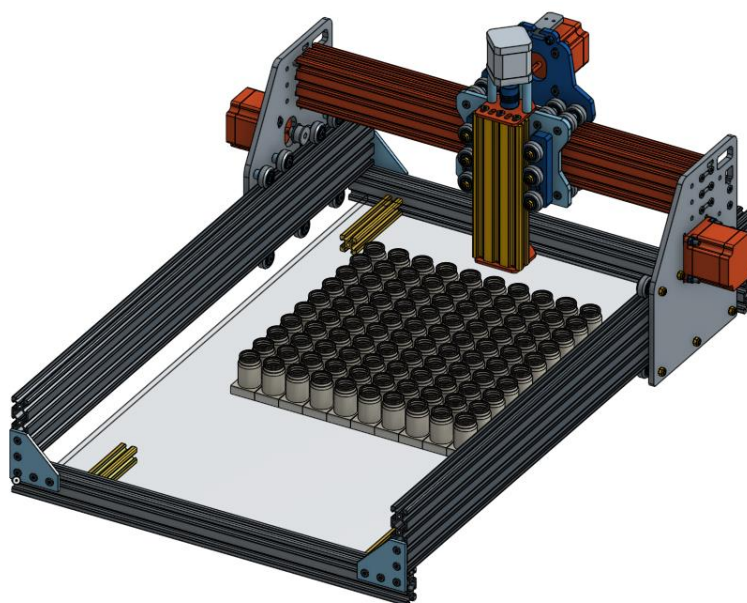


Figure. 3.2. Setup of the reagent dispensation, reaction and crystallization part of the robotic system.

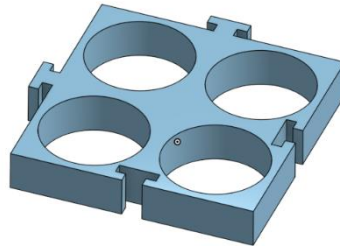


Figure. 3.3. 3D printed configurable vial holder.

3.1.1.4 Imaging support system

The platform was raised using four vertical 20x20x300mm v-slot aluminium beams connected at each corner of the CNC kit, and secured at the base using two horizontal 20x20x500mm V-slot aluminium beams and two horizontal 20x20x750mm V-slot aluminium beams running parallel with the Y and X axes, respectively (Figure 3.4). Two further horizontal 20x20x500mm were attached to the vertical beams along the Y axis 200mm below the CNC kit.

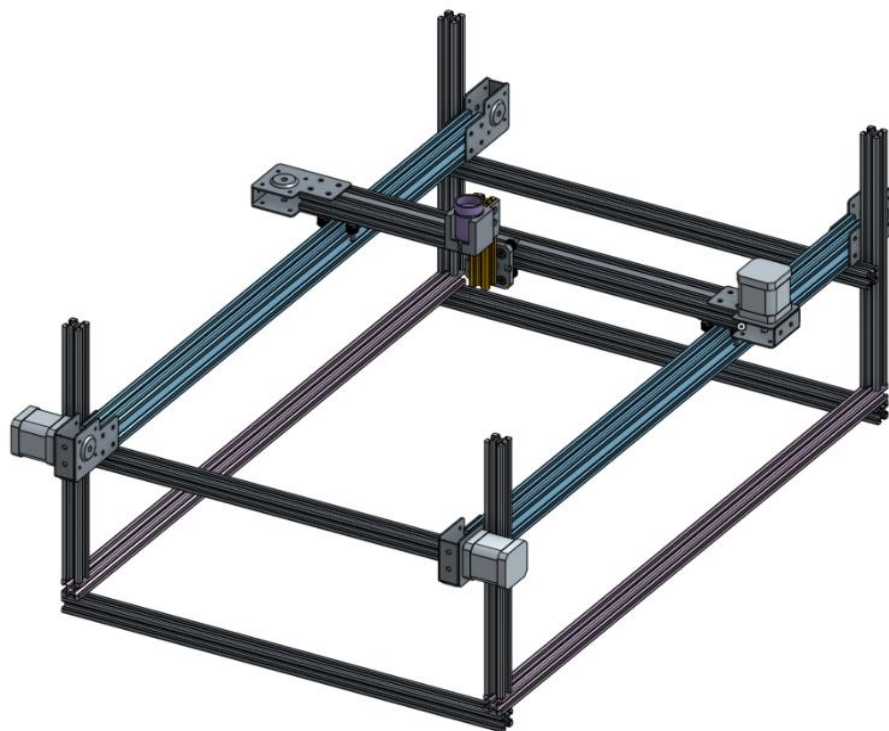


Figure. 3.4. Robot frame and underside camera cantry.

Initially, the camera mobility was provided by attaching a screw driven axis to the underside of the main X axis via an extension built from 20x20x200mm V-slot beams (Figure 3.5). Camera X mobility was provided by moving the main X-axis as

normal, and Y mobility as provided by positioning the camera on a small cart fixed on the screw driven axis. This allowed accurate control of camera position, however precision was too low to consistently obtain a full vial image.

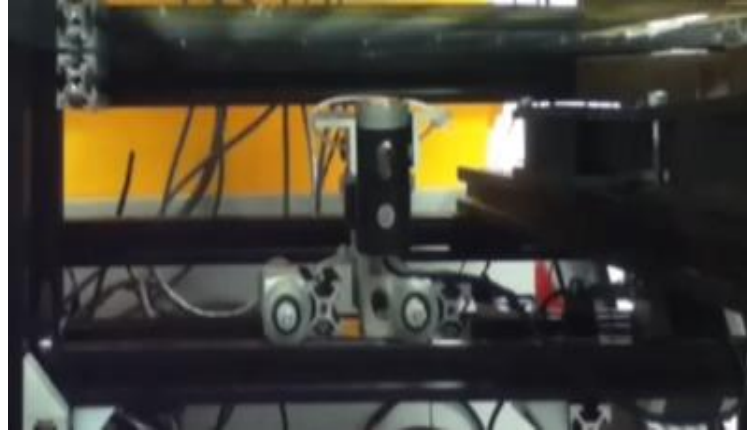


Figure. 3.5. Image of initial camera mobility devices composed of a screw driven axis attracted to the main X axis.

Instead, this system was replaced, and the camera mobility was enabled using a set of belt driven linear actuators, each containing small four wheeled gantries, a 20 x 40 mm extrusion profile, black anodise colour and NEMA23 - 175 oz - 2.0A stepper motors. Two of these of length 750mm were attached at either side of the platform to the horizontal beams 200mm below the main framework in parallel with the X axis of the platform, forming the cY axis. A third actuator of length 500mm was fixed at either end to the gantries of the two 750mm linear axes and ran in parallel to the Y axis. Vertically attached to the cY axis gantry was a 20x20x100mm v-slot aluminium beam which acted as a support for the camera

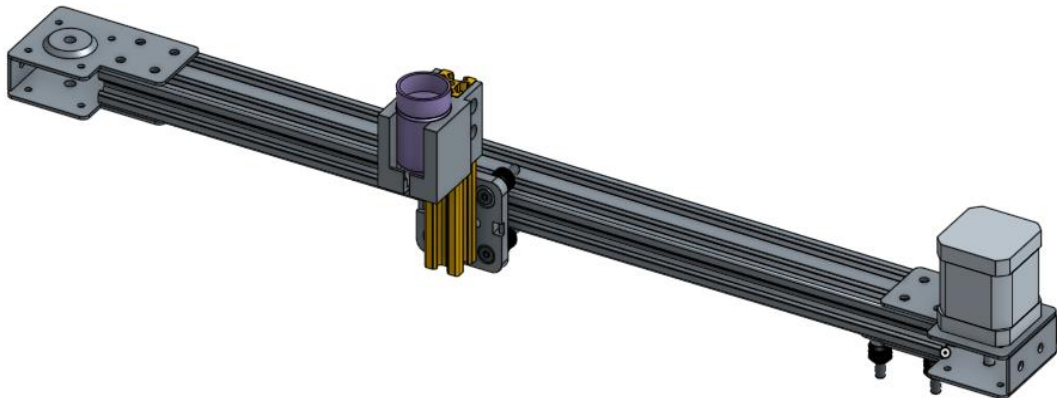


Figure. 3.6. Schematic of camera mobility device composed of a linear belt driven axis

holder. A webcam was placed in the holder pointing up towards the crystallization platform. This was connected to a laptop via USB. A schematic of the mobile camera gantry alone and 3D printed camera holder are shown in Figures 3.6 and 3.7

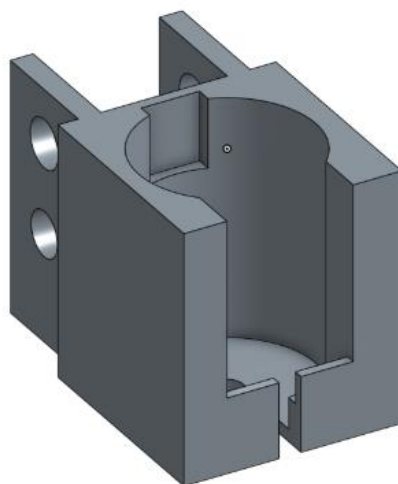


Figure. 3.7. 3D printed configurable camera holder.

3.1.1.5 Stirring apparatus

The initial iteration of the platform contained an array of magnetic stirrer bars attached to a corresponding array of 4x4cm cooling fans below half of the reaction vials and was both controlled and powered by the Arduino. This allowed reactions to be performed in one vessel and decanted to a clean vial for filming of crystallisation. However, during operation, it was noted that several of the reactions being performed did not require stirring in order to produce crystals, and that precipitate could be avoided after optimising reaction conditions. Since the project was now moving in the direction of filming crystallisations for the production of random numbers, rather than for compound discovery, the stirring apparatus was removed so as to provide more space for crystallisations and to remove the complexity involved in reaction transfer.

3.1.1.6 Fluid handling structure

The fluid handling system consisted of a simple aluminium support of dimensions 250 x 120 x 5 mm attached distally to the back of the Y-axis of the CNC kit. It was supported by two 20 x 20 x 100mm v-slot aluminium beams. The sheet contained

drilled holes for attaching five Tricontinent C series syringe pumps. The reagent stock solutions were located in a secondary containment tray adjacent to the platform and were not fixed.



Figure. 3.8. Setup of pumps used to dispense reagent

3.1.2 Liquid Handling

3.1.2.1 Pumps

Different volumes of a variety of reagents, with different properties, needed to be pumped quickly, accurately and reliably. Additionally, it was desirable that the pump was easy to set up, use and troubleshoot. The type of pump chosen was the Tricontinent C3000 Series syringe pump, which provides support for multi-distribution valves, pumping resolution of 24,000 microsteps allowing a precision and accuracy of at least 99.95% and 99% respectively. In addition, this type of pump was the standard pump used in our group, so support could be provided in installing and solving errors with the pump. Another benefit was that some software had already been developed by our group to control multiple pumping functions. As such five were attached to an aluminium sheet described in section 3.3.3 and fitted with with 5 or 12.5ml syringes.

3.1.2.2 Syringes, Valves and Tubing

The primary concerns with the syringes, values and tubing for transfer of reagents to reaction vial was chemical compatibility, and lack of leakages. These components needed to be resistant to a large range of solvents, oxidative

environments and pH ranges, and have long enough lifespans that only limited maintenance was required. The syringes chosen were those recommended by the pump manufacturer and composed of borosilicate glass and polytetrafluoroethylene (PTFE), which are widely known for their excellent chemical compatibility across a wide range of conditions.

Similarly, the valves used were those recommended by the pump manufacturer. These were composed of a combination of PTFE and polyetherether ketone (PEEK) for the valve housing and plug, respectively. The latter component also has excellent chemical compatibility for many substances, however, some mineral acids such as concentrated nitric acid and sulphuric acid should be avoided.

The tubing used to connect the stock solutions to the pumps, and the pumps to the reaction vials was 1/16 inch fluorinated ethylene propylene (FEP), which also has excellent chemical resistance. This material was cut to desired lengths so that it could connect the reactions to the pumps (~300mm) and the pumps to the reaction vials (~1200mm). The latter tubing section was connected to the body of the platform at the y-axis, and directed down the z-axis so that the final outlet would discharge its contents at the intended location.

3.1.2.3 Outlet Support

A 3D printed support device was attached to the end of the tubing at the base of the Z axis in order to direct the outlets of the tubing. The device was a cylinder with 20mm length, 10mm diameter and contained 5 holes of radius 1.58mm to snugly accommodate the tubing.

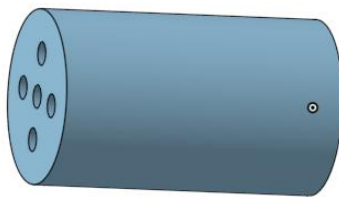


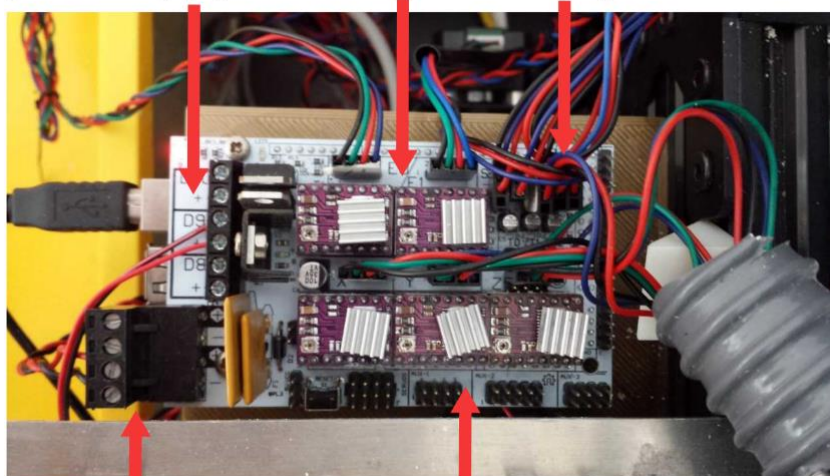
Figure. 3.9. 3D printed component to control reagent outflow.

3.1.3 Electronics

3.1.3.1 Axis control

Axis positioning was controlled by an Arduino 2560 Mega attached to a RepRap Arduino Mega Pololu Shield v3.4 (RAMPS) and connected to a laptop. This was powered by an ATX 500W power supply and connected to the motors and end stops of 5 linear axes. Three of the axes (X, Y and Z) controlled the reagent output location via the X, Y and Z RAMPS pins, and the other two (cX, and cY) control the location of the camera via the E0 and E1 RAMPS pins. Both the X and cX axes consisted of two rails at either side of the platform and were connected electronically so that they were powered by the same source. Five of the six end stop pins were attached to each of the axes- one for each axis.

Cooling Fan power supply
Camera motor
Axis drivers
Axis end stops



12V DC power input
Dispensing Arm Axis motor drivers

Figure. 3.10. Photograph of Arduino used to control motors of robotic axes

3.1.3.2 Pump control

The pumps mentioned in subsection 3.2.1 were daisy chained together and controlled via USB. Power was sourced from the same ATX 500W power supply mentioned in section 3.3.3.

3.1.4 Bill of Materials

- The device body was constructed from an Ooznest OX CNC mechanical kit of dimensions: 500x750mm.
- The platform was raised using four 300mm (20x20mm) V-slot linear rails. Further linear rails (2x 500mm (20x20mm) and 2x 750mm (20x20mm)) were used to secure the base of the frame using 90-degree angle corner brackets.
- Two 750mm Mini V Linear Actuator Kits were attached to the vertical V-slot-linear rails in parallel along the length of the platform. One 500mm Mini V Linear Actuator Kit was positioned perpendicularly to this and fixed to the gantries of the 750mm Linear Actuator kits.
- The syringe pumps used were “TriContinent C-Series”. Each of them used 5ml syringes connected to identical 3-way PEEK valves
- An Arduino Mega 2560 and was used to control arm motors
- A RepRap Arduino Mega Polulu Shield was used to house the stepper drivers for motor arm control
- The stepper driver used to power the arm motors were Pololu a4988.
- “IDEX Health Science FEP Ora 1/16 x 0.20” tubing was to connect the stock reagents to the syringe pumps, and from the pumps to the vials.
- Flangeless fitting nuts, 1/16" OD Tubing, PEEK, were used to connect these tubes to the syringe pumps and device, with corresponding cone shaped fitting.
- “Microsoft LifeCam Cinema Webcam (H5D-00014)” was used to record images of the crystallizations.
- 3D printed objects were composed of polylactic acid (PLA)

3.2 Method 2: Software implementation

The robotic platform was controlled using code written in a combination of Python and C++ programming languages. Python was used to define the experiment controller, in which experimental procedures, experimental inputs and logic of the platform were defined. This was run in parallel to image analysis using computer vision. C++ was used solely in the Arduino firmware in order to convert instructions written in Python to physical output to the motors on the axes. The software was initially all written in one file, due to inexperience with the programming languages. However, this was difficult to maintain and was eventually separated into several files and classes. During development, a graphical user interface was added, however this was later removed in favour of entirely command line interface as testing was much faster via this method.

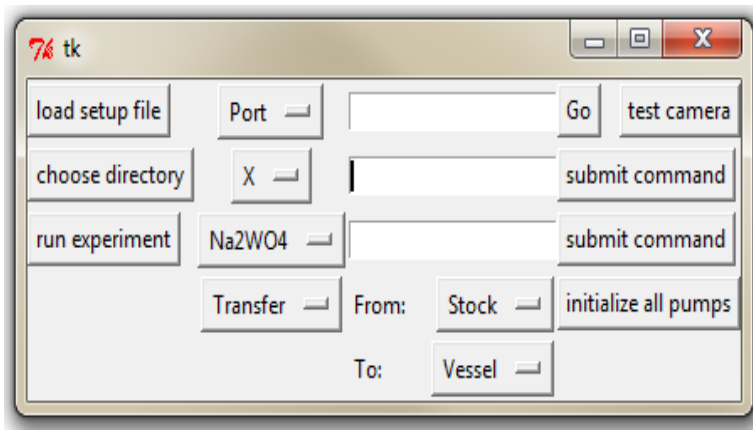


Figure. 3.11. Initial development of a user interface to control the robotic platform

3.2.1 Mechanical operation

Mechanical operation of the platform could be performed in two ways: experimental run and interactive environment. Both modes allowed use of all robotic components via the Experiment class (section 3.3.1.1), so that the entire robot could be given commands as desired. An experimental run required that an experiment name was given, and then the robot would proceed to perform a pre-defined set of steps that resulted in pump and motor activation to perform reactions and imaging, and image processing, as described in a configuration file. On the other hand, interactive mode was accessed using the interactive python ('ipython') environment, and allowed for individual testing of all experimental

components. Here, each component could be loaded and tested simultaneously, or discrete units, such as the pumps could be tested in isolation. Both the experimental run and the interactive environment used the same ‘platform’ object for all procedures.

3.2.1.1 Experiment controller

The experiment controller was the central task scheduler and contained all of the operations and hardware that the robot had access to, such as the pumps, Arduino and webcam. It also contained information on the experimental procedure to employ, such as reaction routines and imaging routines, as well as the physical properties of the robot, such as dimensions, and vial locations. The controller was coded as a class named Experiment which accepted the name of the target compound as an argument. Instantiation of the class would initially define attributes such as compound name, paths to save data and location of analytical files, then go on to load experimental conditions, create necessary data directories, load the robotic components and prepare the experimental routines. The architecture and decisions for the input files, robot control and procedures are described in the following sections.

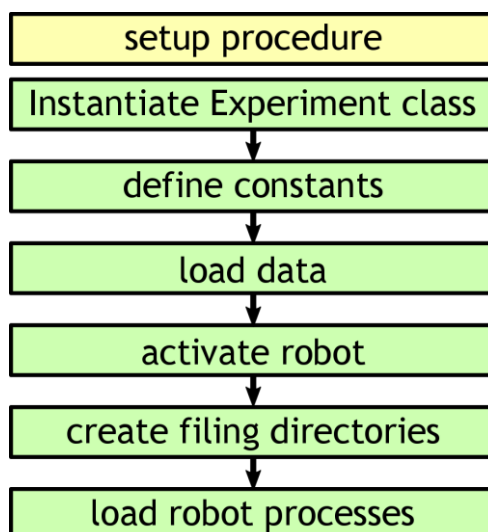


Figure. 3.12. Flow diagram for activation of robotic platform.

3.2.1.2 Data Management

The instantiation of the Experiment class also allowed the creation of two directories for storage of results: one directory was located locally on the hard disc of the laptop being used while the other was located in the group's remote server called 'Orkney1'. This latter server was used to securely handle the large amounts of data being produced, whilst also being regularly backed up to multiple devices at regular intervals. The former directory was used as a temporary location in case the connection to Orkney1 failed or was interrupted during an experiment. Data could be transferred if a connection drop ever occurred. Data stored included the initial configuration data file used to define the experimental parameters in order to allow exact replication of the experiment, as well as each image of the reaction taken which was given its own sub directory in the results folder.

3.2.1.3 Input files

The experiment input file type is that of a json file. From this, each reaction and experimental parameter could easily be specified and changed if needed. Experimental parameters included number of reactions, images per reaction, time between images and reagents. For each reagent, the json format was used to specify the contents of each input solution in terms of chemical name and quantity of reagent. This was in the format for a list of strings so that stock solutions with multiple reagents could be defined. The was formatted so that the chemical name and the quantity separated delimited by an underscore. For instance, a stock solution containing 300ml of H₂O and 10g of CuSO₄ would have the format {"contents": ["CuSO4_10g", "H2O_300ml"]}. In addition, for each reagent, a volume to dispense, time to dispense and a dispense flag were specified. All of these data were loaded using Python's native json module and stored as in a dictionary format, as well as being set as attributes to the experiment object.

3.2.1.4 Robot activation

Activation of the robot, whether in experimental or interactive mode was achieved by the instantiation of a 'Robot' class. This class was able to activate and control each piece of hardware used in the robot's operation including, the

pumps, camera and components attached to the Arduino. Upon instantiation, the robot would run code to instantiate a 'Platform' class, which took information about the physical system, such as position, size, and number of vials from a configuration file, and generated x,y,z co-ordinates for every vial relative to the origin of the mobile axes. This allowed an easy referencing system to access the accurate location of every vial in the platform. After this, separate methods (for pumps, camera and Arduino) could be used to activate different pieces of hardware individually, or simultaneously. Once activated, they were accessed as attributes to the Robot class, and each contained specific methods for different functions. The software controlling the pumps, camera and Arduino are described in the following sections.

3.2.1.5 Pumps

Pump control was achieved using the python module called pycont. This module was written in-house for serial control of Tricontinent pumps, which were used in this project. Pumps were accessed through the Controller class which accepts a configuration file as an argument, in which variables such as pump name, switch number, syringe volume and speed, and communication port are defined. Specific pumps could then be accessed as an attribute of the created class directly, and from within a dictionary of the 'pumps' attribute of this class. Each individual pump object contained methods for syringe motion of specified pumps, such as pump, deliver and transfer, which accepted arguments for volume, valve direction, and scheduling flags such as 'wait until finished pumping'. Every time the pumps were activated on the robot, a protocol to ensure pump initialisation was run.

3.2.1.6 Camera

Camera control was achieved using the standard python computer vision module called Opencv. This was implemented in the software as a 'Camera' class, which was instantiated with the camera port number. This allowed the camera to be accessed as an attribute to this class. In addition, image resolution was defined here and could be changed if required.

3.2.1.7 Arduino

The Arduino, which regulated power to the motors used to position the robot axes, was controlled using a python module called `commanduino` and was also written in-house. Axes were registered through the `CommandManager` class which accepts a configuration file as an argument, in which variables such as axis name, speed and direction, as well as communication port were defined. This allowed each axis to be accessed as an attribute attached to the manager object. For high level control, the `commanduino` module also contained classes called `Axis` and `MultiAxis`. Individual axes could then be instantiated by creating a new object representing an axis (e.g. X-axis) with the `Axis` class by accepting the corresponding axis attribute of the command manager, movement rate (in mm per motor step), minimum position and maximum position. The physical motors of axis each could then be communicated with by accessing the methods of each `Axis` object. Such methods included commands like `'move'`, `'move_to'` and `'home'`, which caused the axis to move a certain distance (in mm), move to a certain distance from the axis origin, and return to the axis origin, respectively. In this way, a separate attribute for the X, Y, Z, CX and CY axes were defined and accessible from the `Robot` class. Further, the `MultiAxis` class, which took in predefined `Axis` objects was used to combine them into a new `MultiAxis` object. This was done to allow single attribute control of the X and Y axes (`XY`), the CX and CY axes (`CXY`), the X, Y, CX and CY axes (`XY_CXY`) and every axis including the Z axis (`BOT`). From this a simple command, such as `'BOT.home()'` would result in the motion of every axis to its origin position.

3.2.1.8 Firmware

One extra layer of code was required for Arduino control: the firmware installed on the actual Arduino Board. This code was written in C++ as this is the native language for Arduino development. Two in-house written code libraries, `CommandHandler` and `CommandTools`, were used to link output pins to specific motors. The former allowed low-level handling of commands from serial, string, or character by character while the latter allowed higher level commands for specific pieces of hardware. This project used the `CommandManager`, `AccelStepper` and `CommandLinearAccelStepperActuator` to control the motors.

CommandManager is the generic function manager for all hardware, while the latter two were specific for assigning axes through their driver PINs and end stop PINs.

As standard with Arduino programs, the firmware consisted three sections: an initial definitions section to import libraries, assign Arduino PINs and function types; a setup() function, where serial communication is established, devices are registered to the Command Manager and the Arduino is initialised; and a loop() function, which continually updated the command manager.

3.2.1.9 Experimental Procedure

After setup of all experimental components, it was then possible for the platform to undergo all reactions as described in the input configuration file for that experiment. Reactions were conceptualised as class called Reaction, and were instantiated by accepting the Experiment object itself to allow the reaction access to all attributes of the Experiment, such as motor access and pumping access. The reaction class also contained a 'run()' method, which accepted an integer as an argument corresponding to the reaction number. This allowed the reaction object to move platform arm axis to the corresponding vial and deliver reagents as determined in the configuration file. Using infrastructure, reactions were actualised by simply performing a loop over the number of reactions required, and performing the 'run()' method taking in the loop iteration number (reaction number) as an argument. Once all reactions had been performed, the imaging route could be performed in a similar manner. A class named Image was defined which accepted the Experiment as an object, and a method called 'run()' was used to move the camera axis to the correct location and take an image of the underside of the reaction vial. Imaging was then scheduled so that images of each crystallisation vial could be taken a set number of times and at intervals defined in the experiment input configuration file. Each image could then be analysed and processed for features such as crystals and reaction vial.

3.2.2 Analytical Procedure

The aim of the analytic procedure using visual images was to be able to define regions of the crystallisation vial corresponding to crystals. Here, it was important

to obtain suitably high precision and recall (minimise type I and type II errors). This achieved using a combination of computer vision and machine learning packages available in the Python programming language.

3.2.2.1 Vial detection

Small variations in camera position relative to each vial within and between experiments meant that vials would be in marginally different locations when taking images. However, the exact vial location was required in order to define the boundaries of possible crystallisation. Instead, the vial in each image was detected using computer vision techniques alone. Initially, it was reasoned that the rim, being circular, would be detected using the Hough Circle Transform. This approach eventually proved difficult because, in addition to being relatively slow, a high number of circles were detected, each with slightly different centres and radii, when different parameters were tried. The effect of this was that it was impossible to reliably assign the correct circle representing the vial using this method.

Instead, a method that relied on the detection of contours in the image was employed. Images were loaded using `opencv` as an array with dimensions `1200x800x3`, where the former two dimensions correspond to the width and height of the images, and the latter dimension corresponds to the number of colour channels in each pixel at a particular row and column index. In `opencv` these three channels are ordered as blue, green and red (*bgr*) and can have values between 0 and 255. The three channels can undergo colour space transformation in order to group features more effectively. For example, the *hsv* colour space converts each channel to represent the pixel's hue, saturation and value, respectively. Here, value is defined as the highest maximum number in any of the *bgr* channels, saturation is defined as the pixel's value - the lowest minimum of any of the *bgr* channels divided by its value. By applying the *bgr* to *hsv* colour transformation, the vial rim was reliably isolated from the rest of the image through its *value* channel. A threshold was then applied to the image on this channel, such that any pixel with a *value* below a certain limit was assigned a new value of 255, and any pixel with a *value* above this limit was assigned a 0. This allowed the construction of a new black and white image with the vial interior clearly

separated from the exterior. From here it was simple to locate all contours in the image, select the largest circular one nearest the centre of the image, and calculate the minimum enclosing circle of this contour. This provided an accurate and reliable method of ascertaining the vial parameters of central (x,y) pixels, and vial radius. The accuracy was judged by how many rim pixels were included in the detected vial (type I error) and how many vial pixels were omitted (type II error). This ended up being less than 0.5% of image pixels in both cases. The threshold value for the *value* channel was individually chosen for each reaction chemistry tried to optimise the detection reliability.

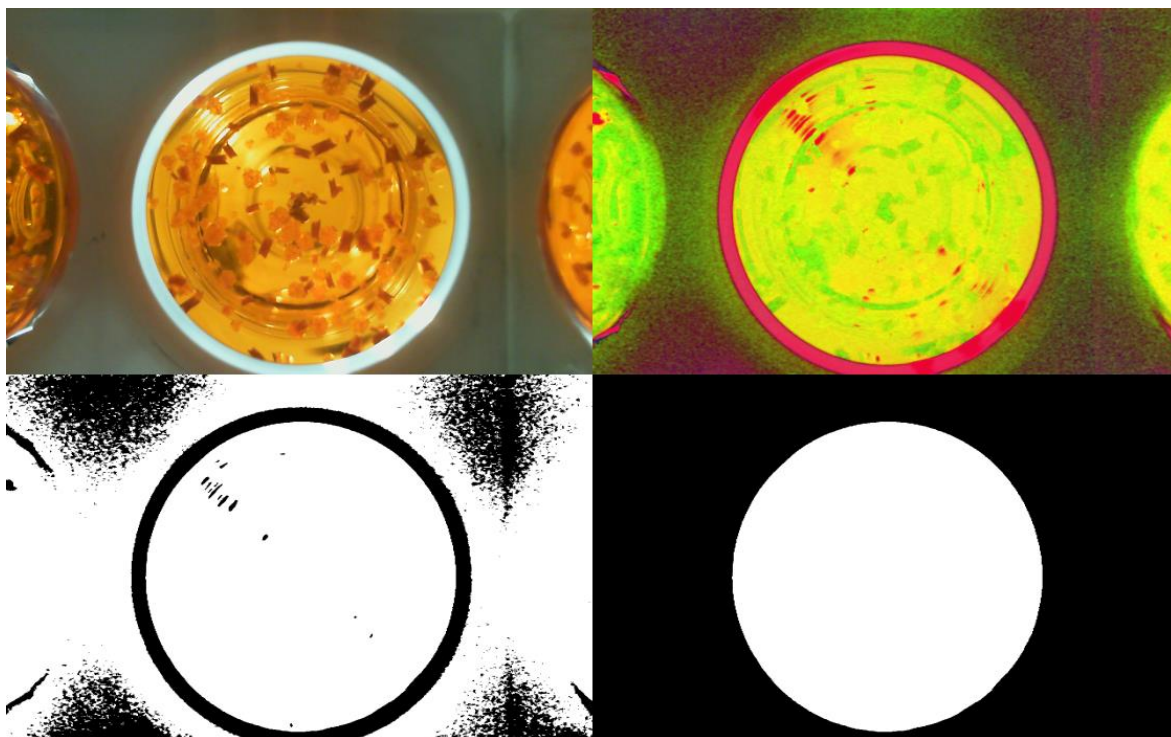


Figure. 3.13. Steps in determining vial inner diameter. **Top left:** original image. **Top right:** *hsv* representation of original image. **Bottom left:** Mask showing all pixels with value less than 200. **Bottom right:** contour of largest central contour. Calculation of minimum enclosed circle results in values for central pixel and circle radius.

Two further attempts were used to try to improve this so that individual settings would not need to be manually chosen. The first was a vector quantisation technique called *k*-means clustering, which can be employed from a module native to *opencv*. *K*-means clustering is a method of partitioning observations into a pre-determined number of clusters, *k*, in which different observations are grouped

into the cluster with the nearest mean. For instance, it was reasoned that if k was set as 3, then the vial, vial rim and outer vial holder would be separated due to their differences in colour properties. However, it was found that clustering didn't occur as expected. For instance, the rim would often be grouped with both pixels in the background and inside the vial, and the vial area would be split into two different groupings. In addition, the k -means clustering problem is computationally difficult, and slow to implement when testing different parameters during optimisation. The second approach was to use another machine learning technique called Mask Region-based Convolutional Neural Networks (Mask R-CNN). Mask R-CNN is used to detect and segment all objects in an image by combining classical computer vision object detection, which is able to classify and provide a bounding box for objects with semantic segmentation, which classifies each pixel without differentiating object instances to create an image mask. Initial training weights were provided by a model trained using the Common Objects in Context (COCO) dataset by Microsoft, which contains 1.5 million labelled and segmented objects in 80 different classes. Further training required an additional dataset containing multiple labelled images containing the feature of interest. This was created by manually labelling images of vials using VGG image annotation software. A deep neural network model was then trained in inference mode using ResNet101 backbone with the classes of 'background' and 'vials'. This

method identified the vial region with high accuracy, but less precision than the colour thresholding method, so was not used.

3.2.2.2 Crystal detection

The main purpose of using a camera in this system was to be able to detect features of crystals, such as presence, location, morphology and classification identity. Crystal detection was found to be non-trivial when applying computer vision techniques. This was a result of two main factors: the colour similarity between the mother solution and crystals, and the presence of noisy background features such as vial lip. This meant that applying colour space transformations such as *bgr* to *hsv* were unreliable, especially when crystal edges blurred into the background solution, or the presence of shadow meant that no definitive hue threshold could be used to separate the crystals. An example of this is shown in Figure 3.15, where all pixels identified lay within a specific *hsv* range. Further,

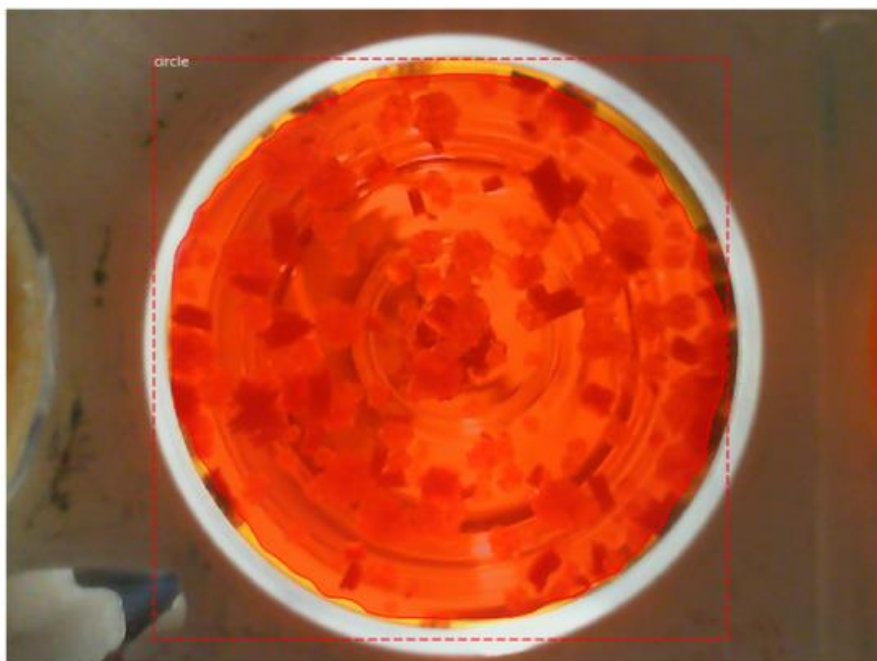


Figure. 3.14. Example of vial detection using model generated using Mask RCNN technique.

feature detection software such as Canny edge detection and Hough Lines Transform was unusable due for similar reasons.

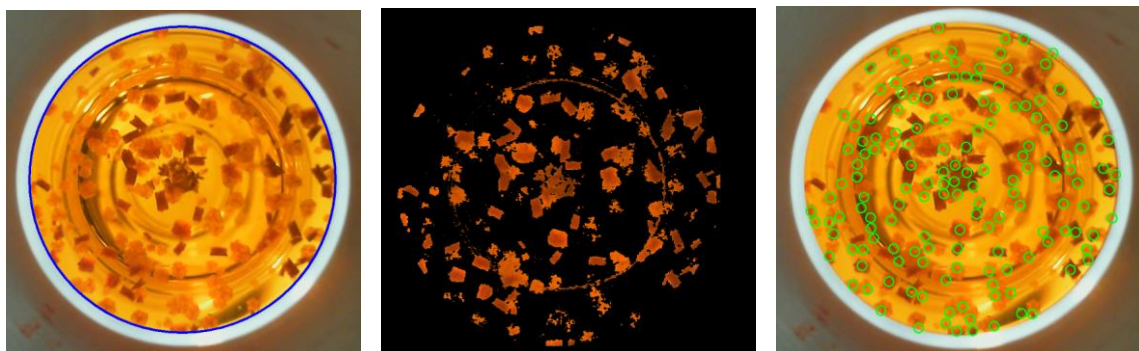


Figure. 3.15. Crystal detection on image using computer vision techniques

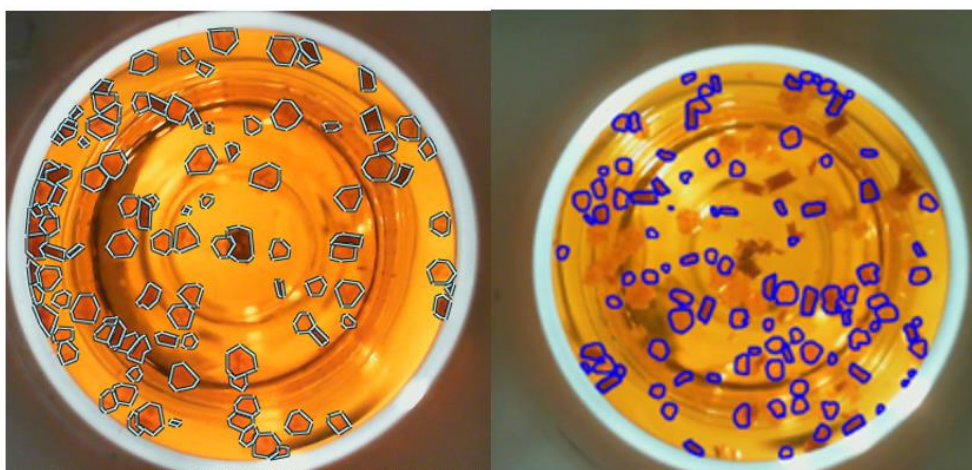


Figure. 3.16. Manual labelling of crystals using VGG software (left) and result of applying a trained image classifier (right).

As with vial detection algorithms, Mask R-CNN was used to attempt to segment and classify crystals in images. However, in this case, the approach was much more successful. The initial weights used here were also those obtained from a model trained on the coco dataset. Training of the datasets was achieved using vgg image annotator, in which images containing crystals were manually labelled with the polygons designating the location of crystals. These data were then stored in a .csv file for use in training (Figure 3.17). In order to increase the size of the crystal dataset, the image augmentation techniques of mirror reflection, rotation, brightness multiplication and blurring were applied randomly. The head branches were then trained using learning rate of 0.001 over one epoch. All layers were then trained using a learning rate of 0.0001 over 30 epochs. The resultant crystal detection model was able to detect close to 90% of crystals in a vial

containing around 80 crystals, while avoiding detection of false positives as shown in Figure 3.18.

	A	B	C	D	E	F	G	H	I	J	K
1	#fil	file	file	reg	reg	region_shape_attributes	region_attributes				
2	000	###	{}	94	0	{"name":"polygon","all_points_x":[698,680,69	{"object_name":"crystal","object_color":"orange"}				
3	000	###	{}	94	1	{"name":"polygon","all_points_x":[637,631,61	{"object_name":"crystal","object_color":"orange"}				
4	000	###	{}	94	2	{"name":"polygon","all_points_x":[651,639,63	{"object_name":"crystal","object_color":"orange"}				
5	000	###	{}	94	3	{"name":"polygon","all_points_x":[566,555,57	{"object_name":"crystal","object_color":"orange"}				
6	000	###	{}	94	4	{"name":"polygon","all_points_x":[569,576,58	{"object_name":"crystal","object_color":"orange"}				

Figure. 3.17. Format of data storage for crystal locations after labelling by hand



Figure. 3.18. Example of crystal detection using model generated using Mask RCNN technique

3.3 Conclusions and future work

This platform was created to be reliable in positioning and pumping of chemical reagents to perform chemical reactions, and to have the ability to take images of events in the vial, such as crystallisation, in real time. Further, it contains automated crystal and vial recognition software, and can also detect features such as colour changes. As this was the first iteration of its kind, it could still be optimised in a number of ways. A subsequent version of this would likely include a higher resolution camera so that smaller crystals could be detected. This would

allow the nucleation times and positions to be specified more accurately. Another modification would be to improve the image recognition capability which suffered from a relatively high false negative detection rate. It is also a possibility that a user interface could be incorporated. Further, continuation of this project could allow the incorporation of a heater, allowing for temperature controlled reactions and crystallisations. Finally, the ability to stir reactions was initially included, but was included in order to optimise data collection for experiments in chapter 4, where the platform was used to convert data from crystallisations into random binary sequences.

4 Random number generation from crystallisation

This chapter leads on from the previous chapter by focussing on results obtained when exploring the generation of random numbers from crystallisation of chemical compounds using the platform. It begins with a brief introduction of the area, followed by the rationale behind the chemistry and how this was applied in the platform. Then, it will show the main results obtained, including how different algorithms affect the randomness of the number produced. Finally, it will be concluded with a discussion and suggestion of future work.

4.1 Introduction

As mentioned in Chapter 1, several liquid handling robots have been developed to search reaction and crystallisation space. However, one broader approach of how such devices may be used is to consider what other applications are possible with such an automated device. It is from this angle that the project of random number generation using chemistry and automation was conceived.

It was hypothesised that by creating an automated device to observe a stochastic chemical process as a source of entropy, such as crystallization, it could be possible to generate sequences of truly random numbers which both pass standard tests for randomness and securely encrypt data. In this regard this project involved the development of a totally automated platform capable of performing chemical reactions and following the subsequent growth of the products as crystals using a webcam, and convert this data into binary strings that could be assessed for randomness as shown schematically in Figure 4.1.

4.2 Chapter objectives

As the platform has been described in the previous chapter, the current section will describe the results obtained in application of the platform to the generation of random numbers. This would require that the platform is able to run autonomously for long periods of time and show highly reproducible results in terms of chemistry performed. Conversely, it would also have to show some feature which could not be controlled despite identical inputs. In addition, it would also require that enough data could be gathered to produce random

numbers. Ultimately the aim of this chapter is to investigate whether truly random numbers can be obtained from chemical processes, and whether different chemical processes could affect the result of the random number obtained.

4.3 Chemistry investigated

Chemical inputs were screened primarily such that they would produce macroscopically observable crystals in a timescale of minutes to hours without the formation of precipitate. A further consideration was that different reactions which exhibit multiple random chemical processes were investigated, namely (1) crystallisation, (2) cluster formation and (3) ligand attachment to cluster. While each process can be modelled reliably, the exact outcome, such as location of crystallisation cannot be predicted. It was hypothesized that by increasing the number of random events prior to observation of crystallization, the likelihood of the final output being random would increase. As such, three reactions were chosen: recrystallization of the inorganic salt $\text{CuSO}_4 \cdot 5\text{H}_2\text{O}$, the synthesis and crystallization of the polyoxometalate $[\text{W}_{19}\text{Mn}_2\text{O}_{61}\text{Cl}(\text{SeO}_3)_2(\text{H}_2\text{O})_2]^{9-}$, hereafter referred to as $\{\text{W}_{19}\}$,¹⁸³ and the synthesis and crystallization of the coordination cluster $[\text{Co}_4(2\text{-pyridinemethanol})_4(\text{MeOH})_4\text{Cl}_4]$, hereafter referred to as $\{\text{Co}_4\}$.¹⁸⁴ Snapshots of these crystallizations at different times are shown in Figure 4.2. These reactions involve the stochastic processes of (1), (1 and 2), and (1, 2 and 3), respectively. To test the hypothesis that by increasing the number of random events prior to observation of crystallization, the likelihood of the final output

being random would increase, the resultant binary sequences were assessed using the tests available in NIST SP-800 22a.

4.4 Methods and Results

The apparatus used to perform crystallisations was discussed in detail in chapter 3. This section of this chapter will first describe how specific chemical reactions were developed for application in the platform (Section 4.4.1), then describe the procedure used in, and results obtained from generation and analysis of the crystal images (Section 4.4.2). It will then go on to describe the procedure used to convert these images into binary sequences (Section 4.4.3), and the assessment of these sequences to detect the existence of correlations indicating that the sequences are not random (Section 4.4.4). Finally, it will report the outcomes of using numbers generated to encrypt messages and compare these to those encrypted using a common pseudo random number generator, the Mersenne Twister.



Figure. 4.2. Crystallisation progression of {CuSO₄}, {W₁₉} and {Co₄} (left to right) at times after crystallization of 0, 40 and 150 minutes (top to bottom).

4.4.1.1 Binary Salt Crystallisation

Crystallisation of a binary salt involved the dissolution of a preformed ionic compound, and evaporation to allow recrystallization. The first set of compounds considered were alkali metal halogen salts. Experiments were initially performed with LiCl, NaCl and KCl and RbCl, because one possibility was to investigate the effect of incommensurate ion size on the random number produced. Bench recrystallisations looked promising, however, when adapted to the automated platform, it became apparent that the lack of contrast between the white crystals and white ceiling made crystal identification very difficult (Figure 4.3).

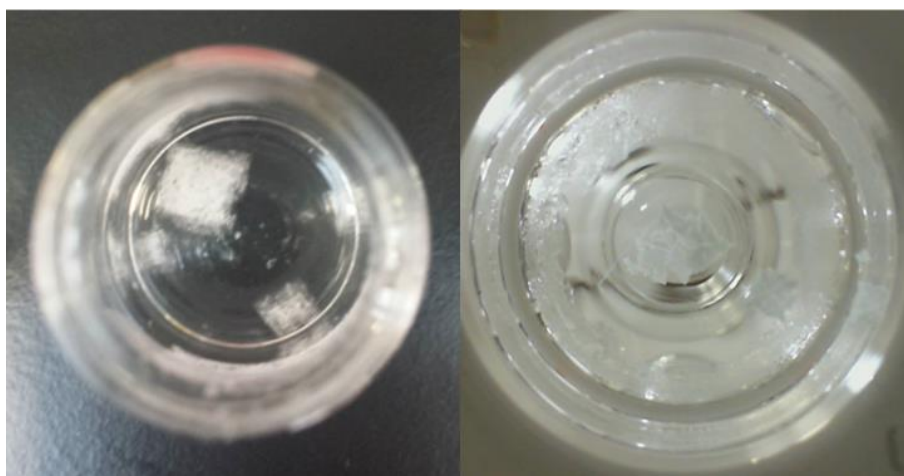


Figure 4.3 Crystallisation of KCl was easily identifiable on the bench (left), but hard to distinguish on the automated platform (right) due to ceiling colour.

Eventually, this approach was replaced using crystals which showed contrast against the background. The compound chosen was the crystallisation of $\text{CuSO}_4 \cdot 5\text{H}_2\text{O}$, (Figure 4.4). This compound readily dissolves in water, and its crystallisation rate could be controlled by varying the amount of acetone added as crystallising agent.

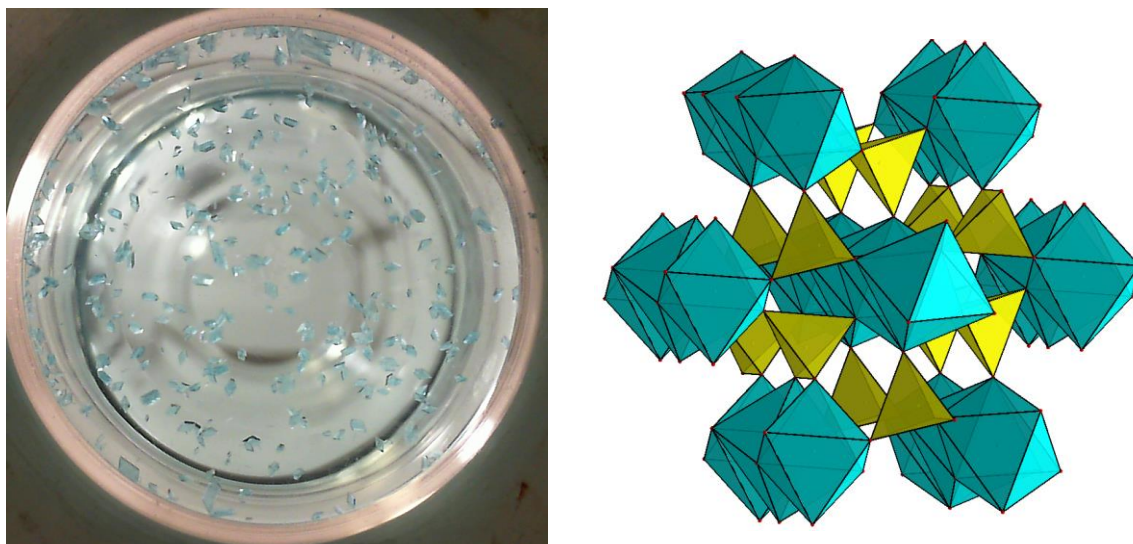


Figure. 4.4. Left) Crystallisation of $\text{CuSO}_4 \cdot 5\text{H}_2\text{O}$ and Right) polyhedral representation of the packing structure of $\text{CuSO}_4 \cdot \text{H}_2\text{O}$ (Colour scheme: CuO_6 polyhedra = cyan, SO_4 tetrahedra = yellow)

4.4.1.2 Oxide cluster compounds

The compounds considered for this process were all polyoxometalates as these form the majority of metal oxide clusters. However, polyoxometalate synthesis is often difficult to perform reliably, and as it was important that crystallisation would occur without fail, a well-tested facile polyoxometalate synthesis was sought. Previous literature¹⁸³ had shown that two tungsten POMs in particular were suitable candidates as they had been used in automated POM synthesis via an automated ‘printing’ method, namely $(\text{C}_2\text{H}_8\text{N})_m\text{Na}_n[\text{W}_{19}\text{M}_2\text{O}_{61}\text{Cl}(\text{SeO}_3)_2(\text{H}_2\text{O})_2]\text{Cl}_2 \cdot x\text{H}_2\text{O}$, ($\{\text{W}_{19}\text{M}_2\}$) where $\text{M} = \text{Co}(\text{II})$ or $\text{Mn}(\text{II})$.

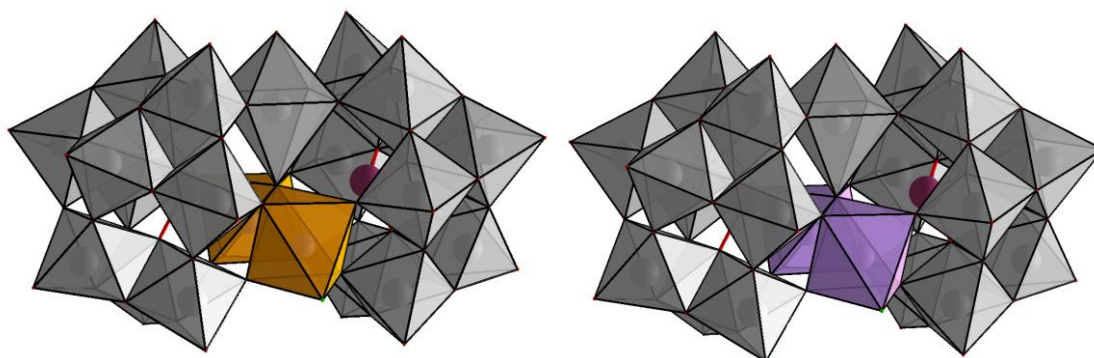


Figure. 4.5. polyhedral representation of $[W_{19}M_2O_{61}Cl(SeO_3)_2(H_2O)_2]$ where $M=Mn(II)$ (left) and $Co(II)$ (right). (Colour scheme: WO_6 octahedra = grey, MnO_5Cl octahedra=orange, CoO_5Cl octahedra = lavender and Se = burgundy)

For the case of $\{W_{19}Co_2\}$, the reaction consisted three aqueous solutions at the concentrations given in the original article¹⁸³, and shown in Figure 4.4.2: A) containing the cobalt source ($CoCl_2 \cdot 6H_2O$); B) containing the tungsten source ($Na_2WO_4 \cdot 2H_2O$), selenium source (Na_2SeO_3) and an organic cation (dimethylamine hydrochloride); and C) containing HCl to acidify the reaction to around pH 3.5. The reagents were mixed by addition of C to A, then this solution to B, with stirring for 10 minutes. The reaction was then transferred to a secondary crystallisation vessel without filtration and left to crystallise. This was done both on the bench by hand, and on the robotic platform automatically. Light pink crystals began to appear from the pink solution after around 20 minutes, consistent with the original article, and continued for around 5 hours. The identity of the crystals was confirmed using X-ray diffraction. Repeating this without stirring also produced crystals in the of the same type in a similar timeframe. This approach was promising, however, the crystals that formed were not ideal for image detection due to the faintness of colour of the crystals, and the similarity in colour between the crystals as the mother liquor. As this was at the start of the project, and our image analysis technique hadn't been developed it was decided that a system with more easily identifiable crystals would be investigated in addition.

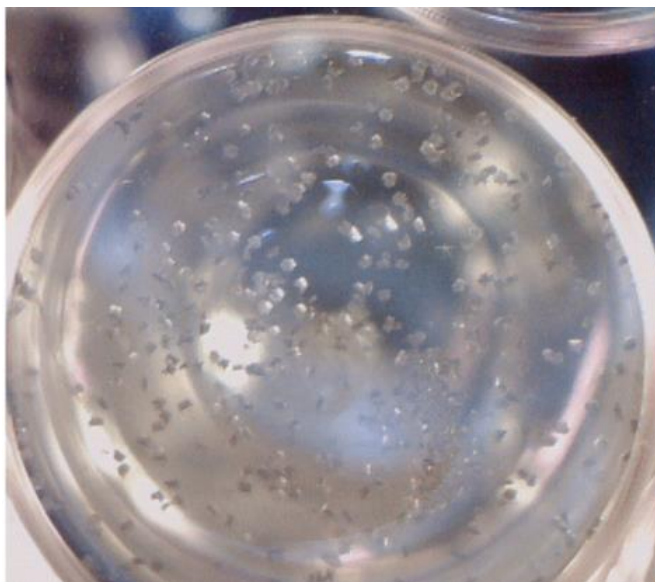


Figure. 4.6. Crystallisation of $\{W_{19}Co_2\}$.

The reaction and conditions to form $\{W_{19}Mn_2\}$ were very similar to that of the cobalt analogue. The only difference was the solution A) contained a manganese source ($MnCl_2 \cdot 4H_2O$) instead of cobalt. Again, both on the bench and on the platform, this reaction produced crystals that were dark orange-brown against a yellow mother solution within 15 minutes, and crystal growth continued for around 5 hours. Again, x-ray diffraction was used to confirm the identity of these crystals. However, under the conditions initially tested, the crystals that formed were small and difficult to distinguish by camera. As such, variations in reaction conditions were tested to try to grow larger crystals that could be analysed more easily using a webcam. It was found that by adding a varying volume of water, crystallisation rate and size could be controlled, with small but numerous crystals being found at small volumes (Figure 4.7, left), and large but fewer crystals being found in more dilute samples (Figure 4.7, right). In addition, it was noted that volume of HCl added had a large affect in all cases, and slight variations would form either precipitate (too much HCl) or leave the solution totally clear (too little HCl).

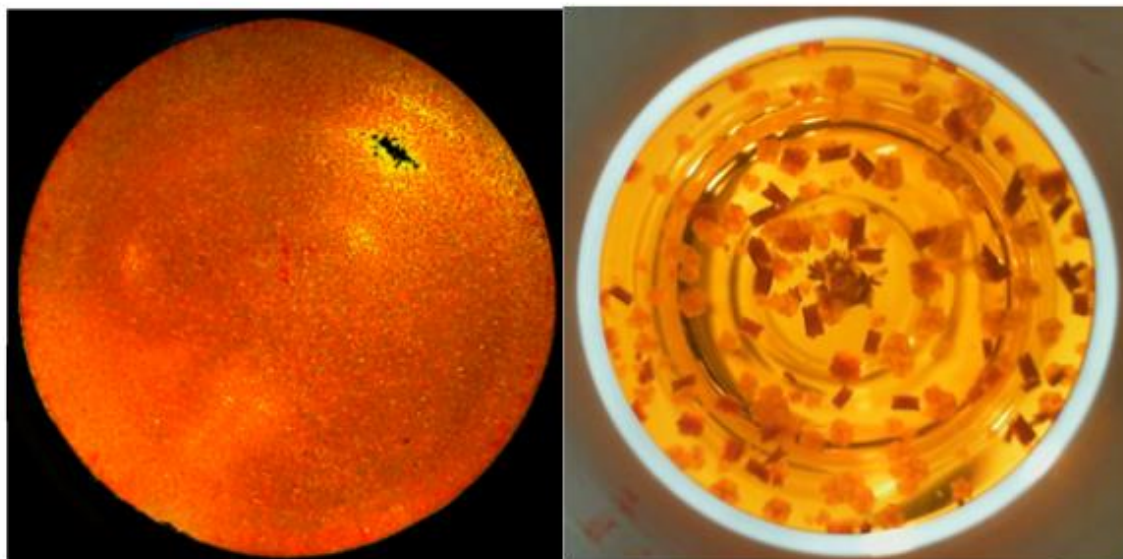


Figure. 4.7. Comparison of crystallization of $\{W_{19}Mn_2\}$ in concentrated solution (left) and dilute solution (right).

4.4.1.3 Ligated cluster compound

To identify the effect of ligand attachment in addition to cluster formation and crystallisation, several compounds were considered as candidates. The preferred candidate was the recently discovered iron kegglin compound $\{Fe_{13}Bi_6O_{40}(tfa)_{12}\}^{72}$ (Htfa = trifluoroacetic acid) which contains one tfa ligand for every outer iron atom ligands surrounding an α -Keggin of iron oxide. The published synthetic route ⁷²requires mixing iron nitrate nonahydrate with bismuth nitrate pentahydrate at 150°C until a clear red solution is obtained, then adding a mixture of Htfa and sodium bicarbonate in an ice bath. The resulting orange solid would then be filtered and dissolved in acetone for recrystallization over three days. However, as described in section 5.2, this reaction was one of the systems under investigation in parallel in order to discover new iron oxide compounds. In this capacity it had been discovered that the reaction procedure could be simplified by adding nitric acid to the iron nitrate and bismuth nitrate solution at room temperature to form a clear, colourless solution. To this the corresponding amount of Htfa was added, and the pH raised to around pH 1.5, at which point the solution would turn dark red. Via this method, crystals of the target compound formed after one hour and were verified by x-ray diffraction. Unfortunately, when tested on the platform the lack of stirring prevented sufficient mixing of the base

and precipitate formed around the dispensed liquid, leaving the rest of the reaction clear. In addition, attempts to change the order and speed of addition resulted in a large amount of foam being produced by CO₂ released from the reaction. Crystals would not form in any of these circumstances. The stirrer system was briefly re-installed to see if the reaction could work with stirring. This setup allowed sufficient mixing of the base and a homogenous red colour appeared in the reaction. However, crystallisation did not occur over a period of five days, which was unexpected. To test whether a problem with inaccurate reagent dispensation had developed, the reaction was performed on a 300ml scale on the bench and directly pumped into vials separately. Surprisingly, the result of this was that crystallisation from the remaining mother liquor in the stock solution beaker was successful, but crystallisation in the reaction vials was unsuccessful, despite cleaning with hydrochloric acid and water. Investigation to find an explanation of this observation was not pursued as it was likely to take up too much time, and hold back the rest of the project. One possible explanation for this is that the crystallisation vials being used were new and unlikely to have the rougher surfaces of well used laboratory equipment such as the beaker containing the mother liquor.

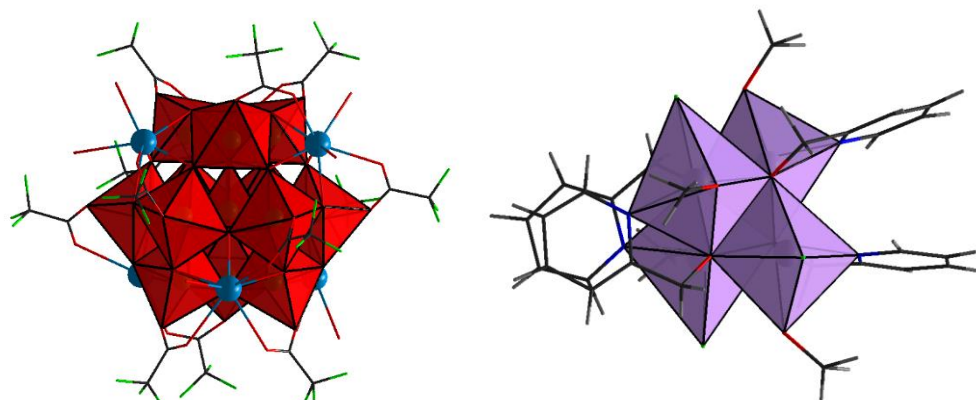


Figure. 4.8. Polyhedral representation of {Fe₁₃} (left) and Co₄ (right). Colour scheme: FeO₆/FeO₄ polyhedra = red, CoO₄ClN octahedra = lavender, Bi = light blue, O=red sticks, N=dark blue, Cl=green, C=black

Instead, a different coordination cluster, {Co₄} ([Co₄(hmp)₄(MeOH)₄Cl₄)]¹⁸⁴, was selected for synthesis and crystallisation. The synthetic and crystallisation route for this was simple and was prepared by reacting Co(H₂O)₆Cl₂, sodium methoxide

(MeONa), and hydroxymethylpyridine (1:1:1 ratio) in methanol. This was first attempted on the bench with by mixing two solutions: A) $\text{CoCl}_2 \cdot 6\text{H}_2\text{O}$ in methanol and B) sodium methoxide and hydroxymethylpyridine in methanol. This reaction could be achieved simply by dispensing the two solutions simultaneously, and crystallisation began within 30 minutes. Crystals would continue grow for around 3 hours, but would eventually shrink as the solvent evaporated due to instability in air.

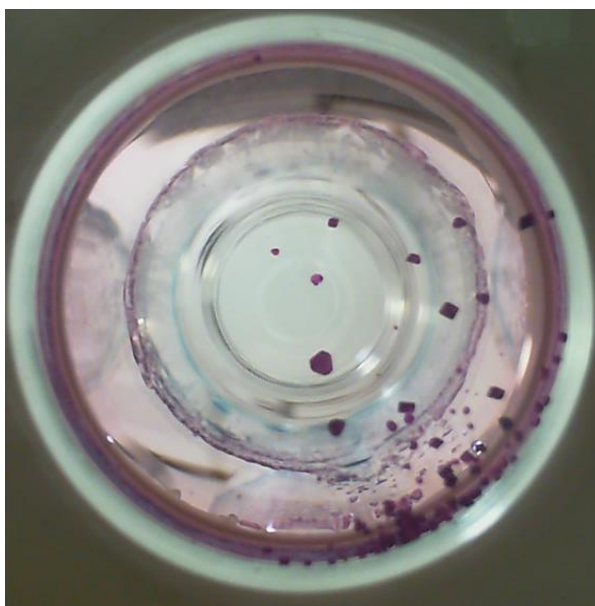


Figure. 4.9. Crystallisation of $\{\text{Co}_4\}$.

4.4.2 Deployment

Stock solutions were prepared by hand, and connected to the robot using 1.6mm tubing. The final optimised input files for each reaction were as shown below, which specify the number of reactions to perform, number of images to take per reaction, and interval between images, as well as the volume and contents of each reagent solution.

CuSO₄

```
{
  "number_of_reactions": 100,
  "images_per_reaction": 200,
  "time_between_images": 600,
  "reagents":
  {
    "Cu":
    {
      "contents":["CuSo4_10g", "H2O_300ml"],
      "dispense": true,
      "volume": 4,
      "time": 0
    },
    "Acetone":
    {
      "contents":["Acetone", "300_ml"],
      "dispense": true,
      "volume": 2.0 ,
      "time": 2
    }
  }
}
```

Figure. 4.10. Input file for generation of random numbers using CuSO₄.{W₁₉}

```
{
  "number_of_reactions": 100,
  "images_per_reaction": 200,
  "time_between_images": 600,
  "reagents":
  {
    "W":
    {
      "contents":["Na2WO4.2H2O_50g", "Na2SeO3_4g", "DMA.HCl_20g", "H2O_300ml"],
      "dispense": true,
      "volume": 3,
      "time": 2
    },
    "Mn":
    {
      "contents":["MnCl2.6H2O_6.48g", "HCl_27ml", "H2O_408ml"],
      "dispense": true,
      "volume": 2,
      "time": 0
    },
    "H2O":
    {
      "contents": ["H2O"],
      "dispense": true,
      "volume": 3,
      "time": 5
    }
  }
}
```

Figure 4.11 Input file for generation of random numbers using {W₁₉}

{Co₄}

```
{
  "number_of_reactions": 100,
  "images_per_reaction": 200,
  "time_between_images": 600,
  "reagents":
  {
    "Co":
    {
      "contents":["CoCl2.6H2O_1.925g", "MeOH_200ml"],
      "dispense": true,
      "volume": 1,
      "time": 0
    },
    "hmpH":
    {
      "contents":["NaOMe_0.407g", "hmpH_0.780ml", "MeOH_200ml"],
      "dispense": true,
      "volume": 1,
      "time": 2
    }
  }
}
```

Figure. 4.12. Input file for generation of random numbers using {Co₄}.

4.4.3 Crystal Detection

The general method used to detect crystals was described in section 3.2.2.2. This section describes how effective the crystal detection was on each of the three compounds investigated.

4.4.4 Binarization and Randomness assessment

4.4.4.1 Theory and Method development

The output binary strings were evaluated for randomness using the tests for randomness published in NIST SP-800-22a Rev.1a.¹⁷⁴ These identify features of an ideal random binary string, such as an equal number of 0s and 1s, and assesses the probability that an input test binary sequence exhibits those features. The rationales, bases and procedures for each test used is not fully described here but can be found in the NIST SP-800-22a document. However, a summary of the purpose of each test is presented in Table 4.1. For each test a feature (such as equal bit frequency) is identified and a null hypothesis (that the feature is present,

H_0) and alternative hypothesis (that the feature is not present, H_a) are generated. Applying the test to the string generates a p-value representing the likelihood that the null hypothesis is true. Typically, the null hypothesis should only be rejected if the p-value is below a specified threshold, often set as 0.01.

Typically, the first test to be applied is the Frequency (Monobit) Test as all other tests rely on this being passed before they can be run. In this case, the specific null hypothesis is that in a sequence of independent identically distributed Bernoulli random variables, the probability of ones is 0.5. Further, in a large number of trials, the normalised (by \sqrt{n}) binomial sum of the sequence is approximated by a standard normal distribution. A p-value can be assigned using the complementary error function (erfc), which gives the probability of this the resultant value occurring assuming a normal distribution of mean 0 and variance 0.5. The procedure for running this is as follows:¹⁷⁴

- 1) Convert all 0s to -1s and obtain the sum of this new, n length sequence, S_n .
- 2) Obtain the test statistic, $s_{obs} = |S_n|/\sqrt{n}$
- 3) Compute the p-value = $\text{erfc}(s_{obs}/\sqrt{2})$

Once a string has undertaken a test, two further levels of assessment must be passed to ensure that the generator indeed produces random strings. The second level requires that the first level of each test is carried out many times, with the p-values for each test being recorded. Then a confidence interval can be assigned for the expected pass rate when running each test. The third level, also known as the p-value of p-values, assesses the uniformity of p-values obtained from running each test multiple times. In this case, the p-values are plotted in a histogram with 10 bins, a further p-value is generated based on how likely it is that the histogram originated from a uniform distribution. Sequences can be considered uniformly distributed if the observed p-value is much greater than 0.0001.¹⁷⁴

To convert images of crystals in a vial into random binary sequences required consideration of several variables. For instance, the strings generated needed to be based on physical observations of the crystals, and not on other sources of noise in the image. Also, any algorithm employed needed to be able to produce a sufficiently large number of bits such that the sequences produced long enough to

obtain valid results from the applied randomness tests. By the standards set out by the National Institute of Standards and Technology (NIST), in the Special Publication 800-22 Rev. 1a,¹⁷⁴ assessment of random number generator using their tests is only statistically valid for very large sample sizes. In order to be suitably long enough to undergo the most rigorous tests, each of the three test levels (pass basic test, obtain sufficient pass rate, and obtain pass-rate uniformity), a sequence would have to contain a minimum of 55 million bits. As such, this was the target minimum sequence length for output from this platform. However, it may be noted that many of the tests could be and statistically meaningful results obtained with far fewer sequence lengths. Finally, the binarization algorithm needed to be able to produce sequences that passed each of the tests for randomness applied.

Several methods for converting raw images and crystallisation data into binary sequences were considered. As a starting point, the result of direct pixel binarization on the entirety of a grey scale image taken with crystals in it was investigated. The strategy for this was to convert the image to grey scale using Opencv, iterate through pixels in every row and column and apply binary division in order to return the modulo 2 of the pixel value. This will then result in a 0 for even pixel values and a 1 for odd pixel vales. By creating one bit per pixel, the length of sequences created per image would be the same as the camera resolution, which was $1280 \times 800 = 1,024,000$. Thus, an experiment with greater than 55 images could be assessed for randomness by the NIST barrage.

Test name	Purpose
Monobit	To assess whether overall ratio of 0s and 1s is as expected for a random bitstring.
BlockFrequency	To assess whether ratio of 0s and 1s in multiple substrings is as expected for a random bitstring.
Runs	To assess whether number of uninterrupted sequences of identical bits ('runs') is as expected for a random bitstring
LongestRunOfOnes	To assess whether longest uninterrupted sequence of 1s is as expected for a random bitstring
Rank	To assess whether the number of long-range repetitive patterns throughout its sequence is as expected for a random bitstring.
DFT	To assess whether the number of short-range repetitive patterns throughout its sequence is as expected for a random bitstring.
NonOverlapping TemplateMatching	To assess whether the number of sequences without showing repetition is as expected for a random bitstring
Universal	To assess whether the compressibility of the bitstring is as expected for a random bitstring
LinearComplexity	To assess whether the complexity of the bitstring is as expected for a random bitstring
Serial	To assess whether the frequency of different bit patterns of different lengths is as expected for a random bitstring
Approximate Entropy	To assess whether the frequency of different overlapping bit patterns of different lengths is as expected for a random bitstring
Cusums	To assess whether any maximum extent of the cumulative sum of the bitstring (treating 1 as +1 and 0 as -1) is as expected for a random bitstring
RandomExcursions	To assess whether the number of a particular cusum values is as expected for a random bitstring. Note that substrings in which the cusum crosses 0 less than 500 times are rejected.
RandomExcursions Variant	To assess whether the number of deviations from a particular cusum value is as expected for a random bitstring

Table 4.1. Summary of tests in NIST barrage for random number testing

Before running the NIST barrage, the data could be inspected visually by converting the binary sequences into a binary image in the same dimensions as the original image. This was useful to identify from where any source of bias in the binary sequence may arise. An example of this, in the case of $\{W_{19}\}$, is shown in Figure 4.13, which also shows the binarization method mentioned above. Here, it can be seen that in particularly bright areas the pixel values reach their maxima of 255 and this results in several features that would be expected in a perfectly random sequence, such as more unequal than expected monobit frequencies and longer than expected runs consisting of only one digit. This is reflected clearly in both the pass rates and uniformity of p-value resulting from running the NIST barrage onto this binary sequence, with a majority of the tests being easily failed. This indicates that the strings generated by this method are not random. It also shows why the second and third level tests are necessary: on some occasions each individual test may be passed without the test sequence being random.

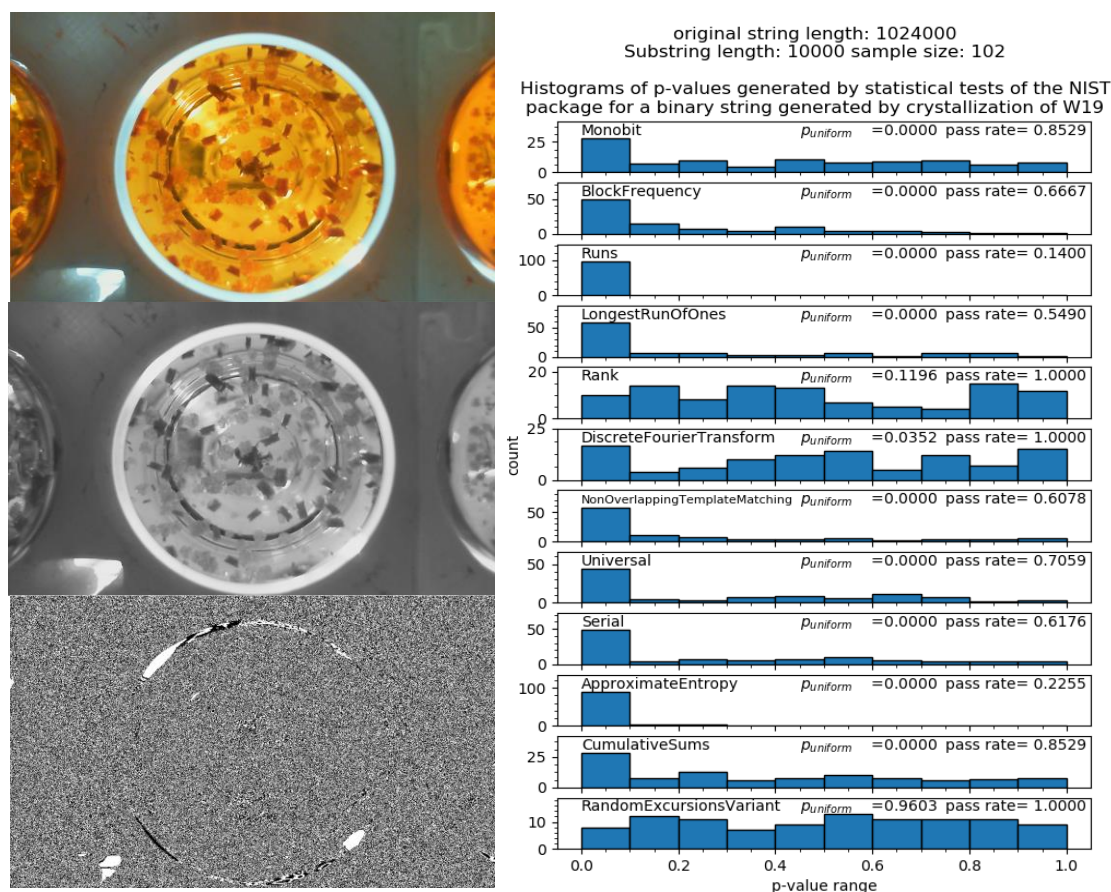


Figure. 4.13. Left) Visualisation of binarisation algorithm by obtaining the parity of each pixel in a black and white image. Right) Results of running the NIST barrage onto binary sequence generated by this algorithm. Results show failure of multiple tests.

A second approach to binarization was to apply the same greyscale binary division but only on the vial region, which itself could be isolated using the procedure described in section 3.2.2.1. Using this method of binarization (illustrated in Figure 4.14), more tests from the NIST barrage were passed at each level than in the one incorporating the entire image. This suggested that the statistical properties of the sequences more closely resembled that of a truly random sequence. In particular, the tests now showed the correct distribution for the *Monobit*, *Universal*, *Serial* and *Cusum* tests. However, several of the other tests were still failed. Notably, the failure of the *Runs* and *Longest Run of Ones* tests is likely to be due a smooth brightness gradient across the image which will introduce correlations between neighbouring pixel which are then detected by the test. Another issue was that the length of sequences was reduced by around two thirds compared with the whole image binarization method. One attempted solution to this was to apply binary division onto each colour channel of the original image and concatenate the result. However, this suffered from the same problems of correlation between pixels.

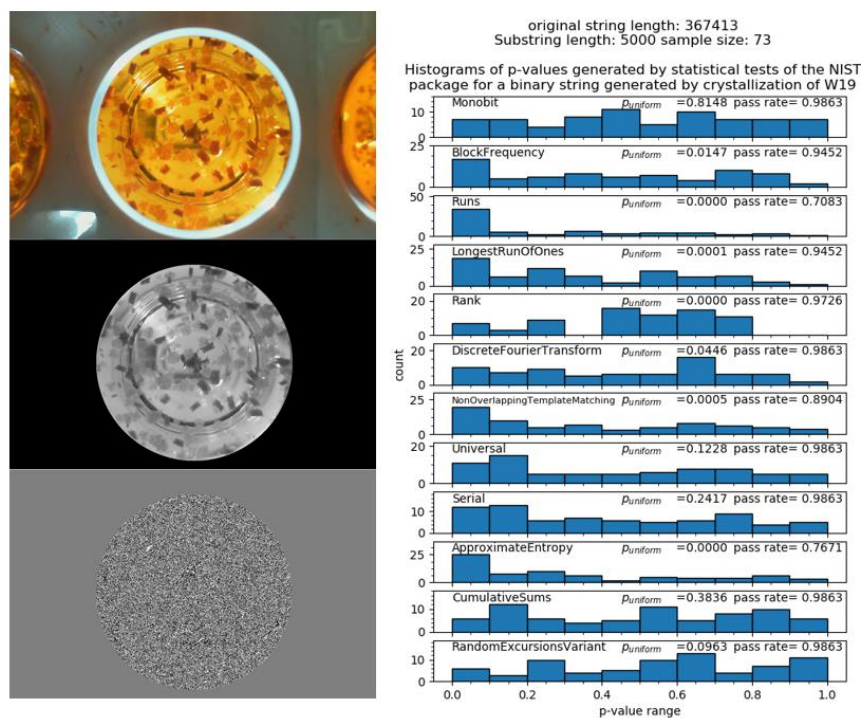


Figure. 4.14. Left) Visualisation of binarisation algorithm by obtaining the parity of each pixel in a black and white image within a crystallisation vial. Right) Results of running the NIST barrage onto binary sequence generated by this algorithm. Results show failure of multiple tests.

A more promising binarization strategy was to use the location of crystals in the vial, rather than the colour. Initially, this was done by iterating through pixels in the vial region and assigning a 0, 1 or no number based on whether the centre of a crystal was detected in the left half of the image, right half of the image, or not detected at that pixel, respectively.

This approach was promising as each of the tests for which there was enough data showed the strings were random. However, only up to around 60 crystals were detected per image, and concatenation of these across different reactions in an experiment amounted to sequences of only around 6,000 bits - a number still too short to obtain statistically reliable results. Because of this, a binarization procedure that incorporated the (apparent) random properties of crystal location with the large sequences possible using pixel colour values was developed.

This new method involved iterating through crystal masks to find crystal pixels that are within the radius of the vial circle. This was followed by a calculation of the crystal width and height at that pixel, as well as the distance from vial centre to the pixel. These values are multiplied and the modulo of 256 taken from this in order to obtain an 8-bit sequence from this pixel. The original image is then converted to greyscale, and the colour intensity value of that pixel (which is in the range of 0-255) is taken as a second 8-bit sequence. Finally, an exclusive OR (XOR) operation is applied between the two 8-bit sequences and the output is taken as the random sequence for that pixel. XOR was used because it maintained the ratio of 0s and 1s seen in the original sequence, whereas other logical operations would result in an excess of either 0s or 1s, and result in failure of most, if not all, of the statistical tests. From this, longer random sequences were then built up by concatenating sequences obtained from crystals of one image, and images of each reaction at synchronous times in an experiment. The procedure is summarised below and represented diagrammatically in Figure 4.15:

1. Search each row of the image for a pixel inside the vial which has been classified as belonging to a crystal.
2. Count the number of adjacent crystal pixels in this row and this column (P_r , and P_c , respectively); calculate the distance of this pixel from the vial centre (P_d); and determine the greyscale value of the pixel (P_v).

3. Calculate an 8-bit location component for the pixel (P_L) by multiplying P_r , P_c and P_d modulus 256.
4. Apply the exclusive OR operator between P_L and P_v to obtain the final 8-bit sequence resulting from a crystal pixel.

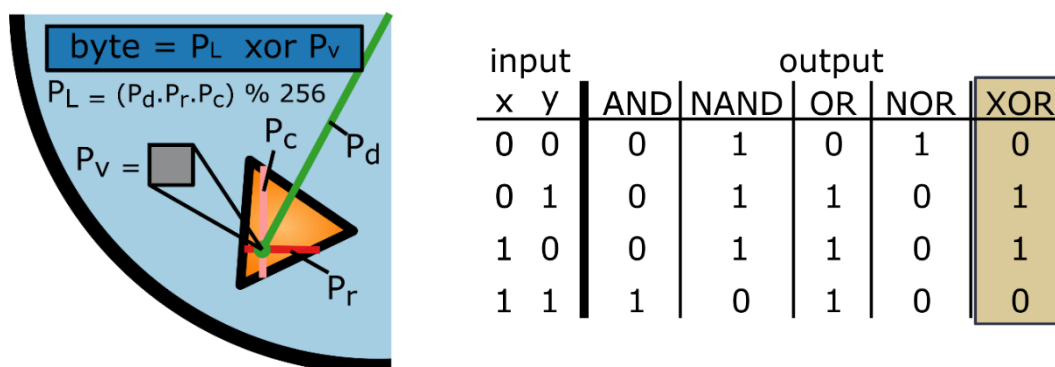


Figure. 4.15. Left) Schematic of the binarization procedure. Right) Output of applying different logical operators to two binary inputs

By applying this method to experiments, long sequences could be built up as the crystallisations progressed. Due to processing considerations, testing of sequences was done at specific time indices, namely, the points at which crystal growth had proceeded for long enough that crystal size was constant between images. This ensured generation of the longest possible sequences, and therefore the most reliable statistical results from applying the NIST barrage.

4.4.4.2 Results from experiments

CuSO₄.5H₂O

An example of crystallisation over time and image detection for CuSO₄.5H₂O is shown in Figure 4.16. Here it can be seen that the image recognition model is very successful in avoiding false positive. Typically, only one or two crystals would be identified in the initial images without any crystals. The number of false positives did not increase during crystallisation, nor at the end point of the crystallisation, when a large number of crystals were present. This is important because detection of the vial may introduce bias into the sequences generate. On the other hand,

although the true positive rate was lower than desired, it was high enough for generation of long sequences based entirely on crystal data.

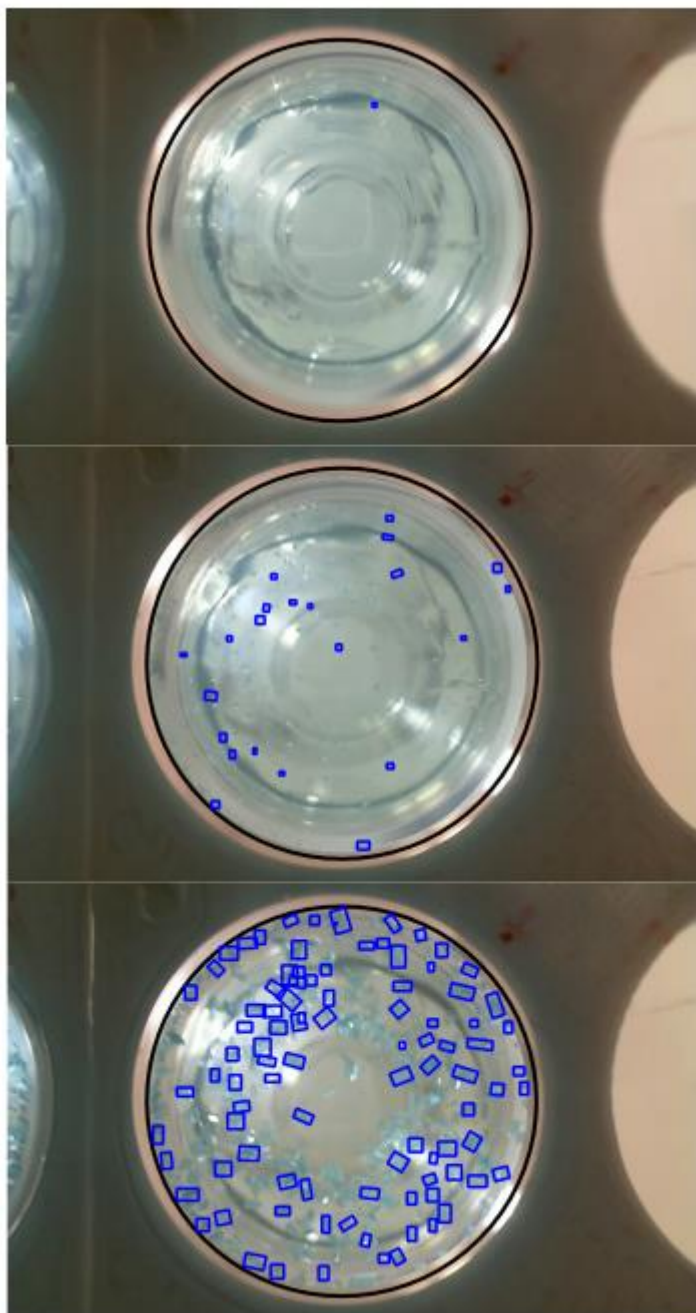


Figure. 4.16. Crystal detections for $\text{CuSO}_4 \cdot 5\text{H}_2\text{O}$ at time intervals of 0, 60 and 150 minutes

When the sequences of $\text{CuSO}_4 \cdot 5\text{H}_2\text{O}$ were assessed for randomness using the method described above, it was seen that each test was passed easily at each level, as shown in Figure 4.17. The pass rate for each test was comfortably within the range expected, and the uniformity of p-values, which ranged between 0.1 and 1 was well above the minimum specified in the NIST guidelines by several orders of magnitude. As such, this shows that binary sequences generated from the $\text{CuSO}_4 \cdot 5\text{H}_2\text{O}$ crystals are random, and this implies that the crystallisation pattern itself is a source of randomness.

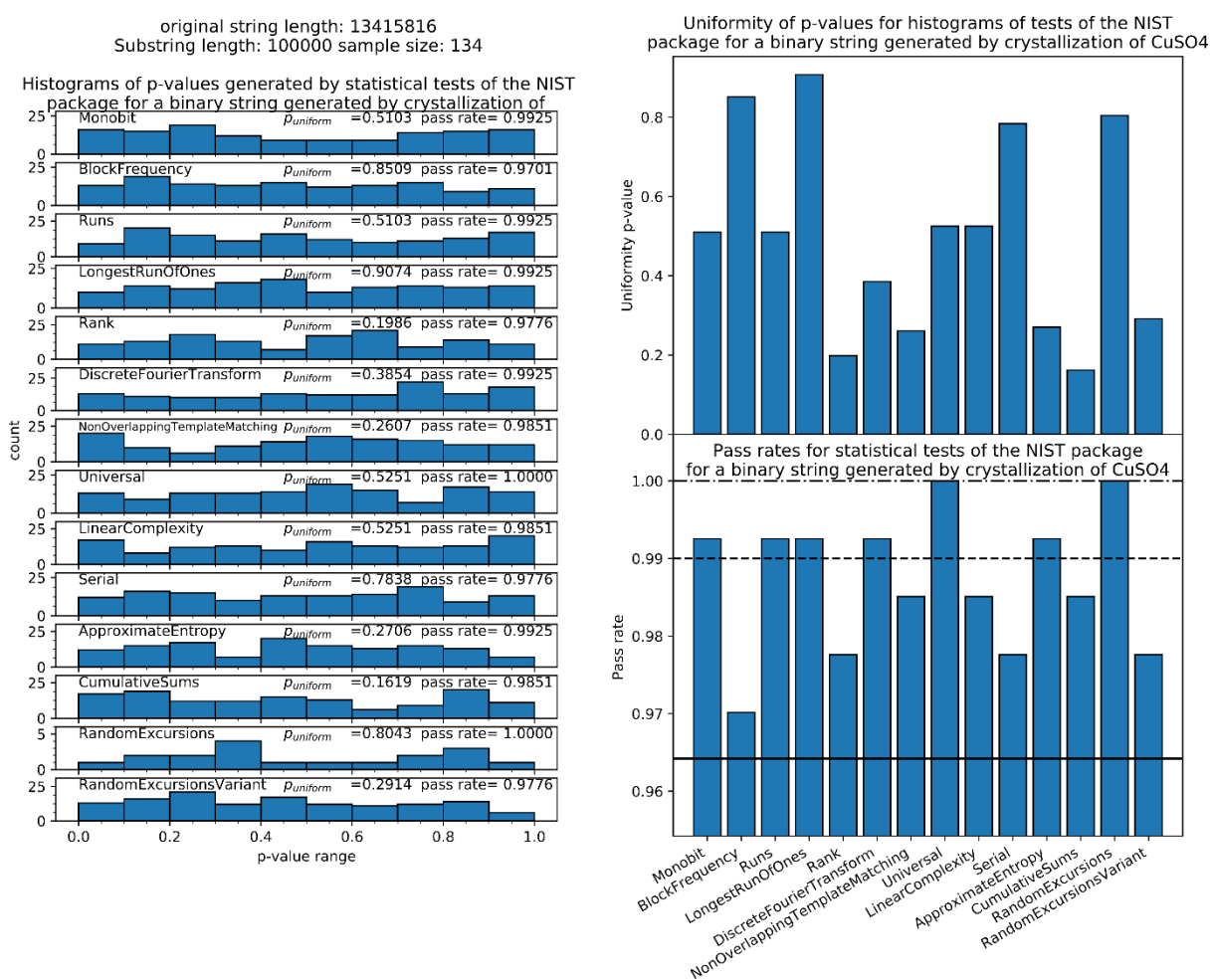


Figure. 4.17. Results from running the NIST barrage on binary sequences generated by CuSO_4 crystallisations. Left) histograms of p-values for each test in the barrage. Top Right) bar chart of p-values for level 3 NIST test (uniformity). Bottom right) bar chart level 2 NIST test (pass rates), showing minimum pass rate (unbroken line), expected mean pass rate (dashed line) and maximum pass rate (broken dashed line)

{W₁₉}

Crystallisation progression and crystal detection for the {W₁₉} reaction is shown in Figure 4.18. The crystal detection ability in this case was similar to that of CuSO₄·5H₂O, in that while some crystals were missed, very few were assigned incorrectly. The results from the NIST barrage (Figure 4.19) show that each level of each test is passed, indicating the binary sequences generated from this compound were also random.

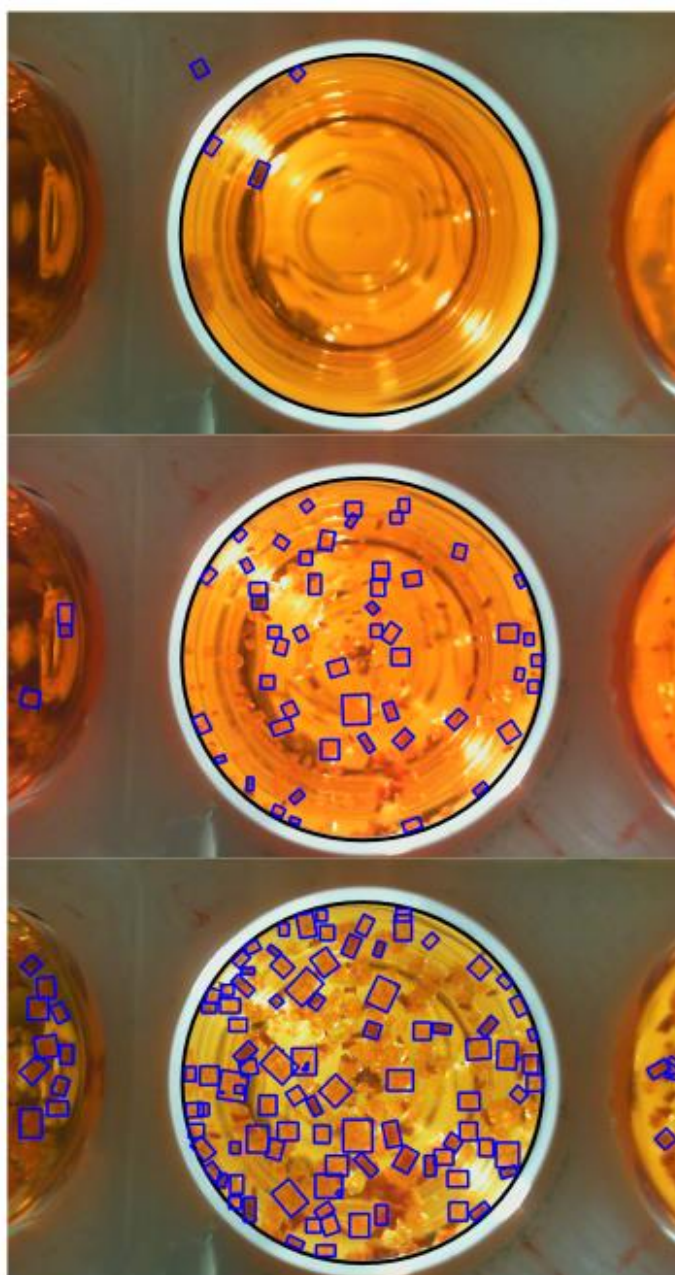


Figure. 4.18. Crystal detections for {W₁₉} at time intervals of 0, 60 and 150 minutes.

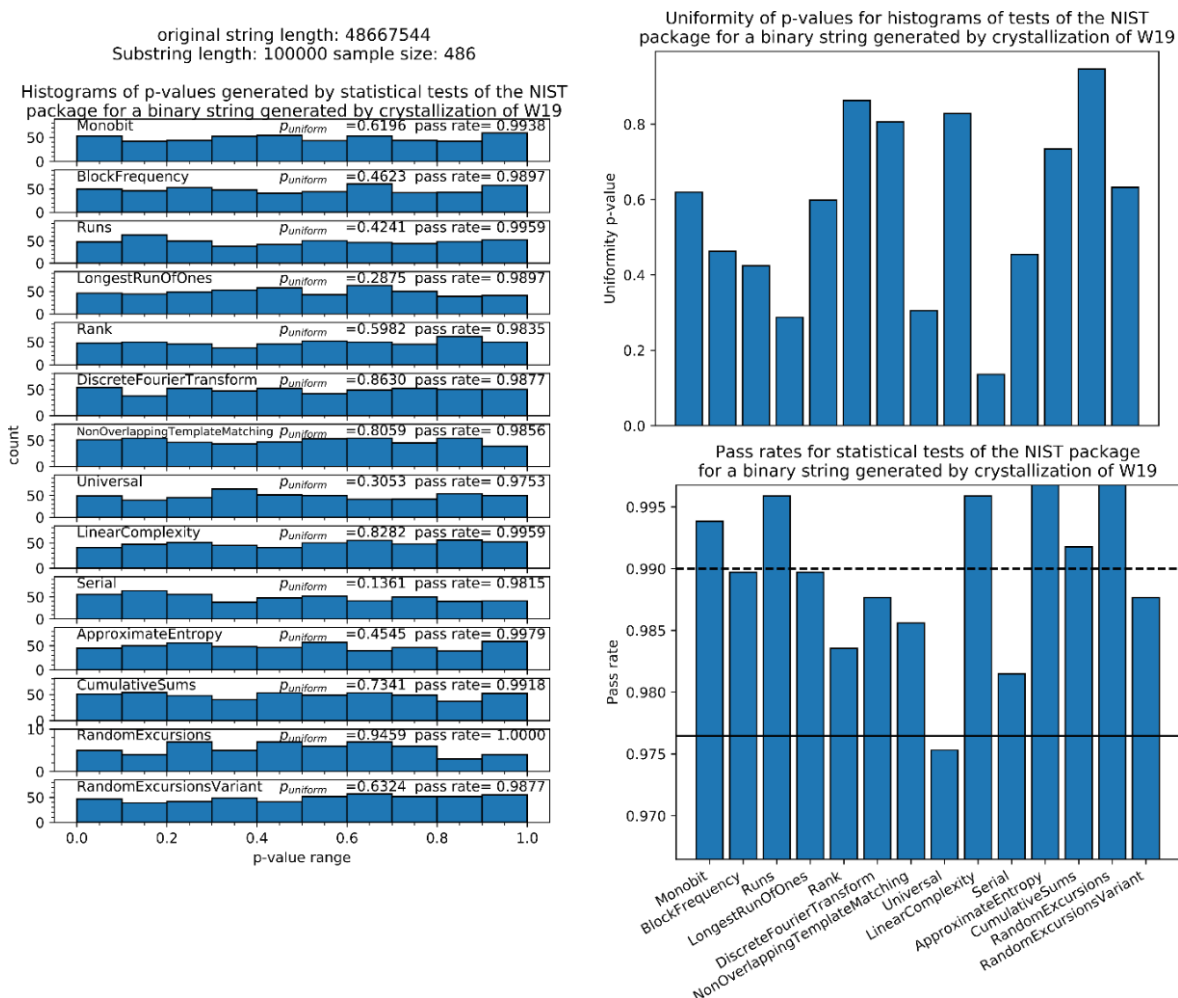


Figure. 4.19. Results from running the NIST barrage on binary sequences generated by $\{W_{19}\}$ crystallisations. Left) histograms of p-values for each test in the barrage. Top Right) bar chart of p-values for level 3 NIST test (uniformity). Bottom right) bar chart level 2 NIST test (pass rates), showing minimum pass rate (unbroken line), expected mean pass rate (dashed line) and maximum pass rate (broken dashed line)

Co4

Crystallisation progression and crystal detection for Co_4 reaction is shown in Figure 4.20. The crystal detection ability in this case was similar to that of $CuSO_4 \cdot 5H_2O$ and W_{19} , in that while some crystals were missed, very few were assigned incorrectly. The results from the NIST barrage (Figure 4.21) show that each level

of each test is passed, indicating the binary sequences generated from this compound were also random.

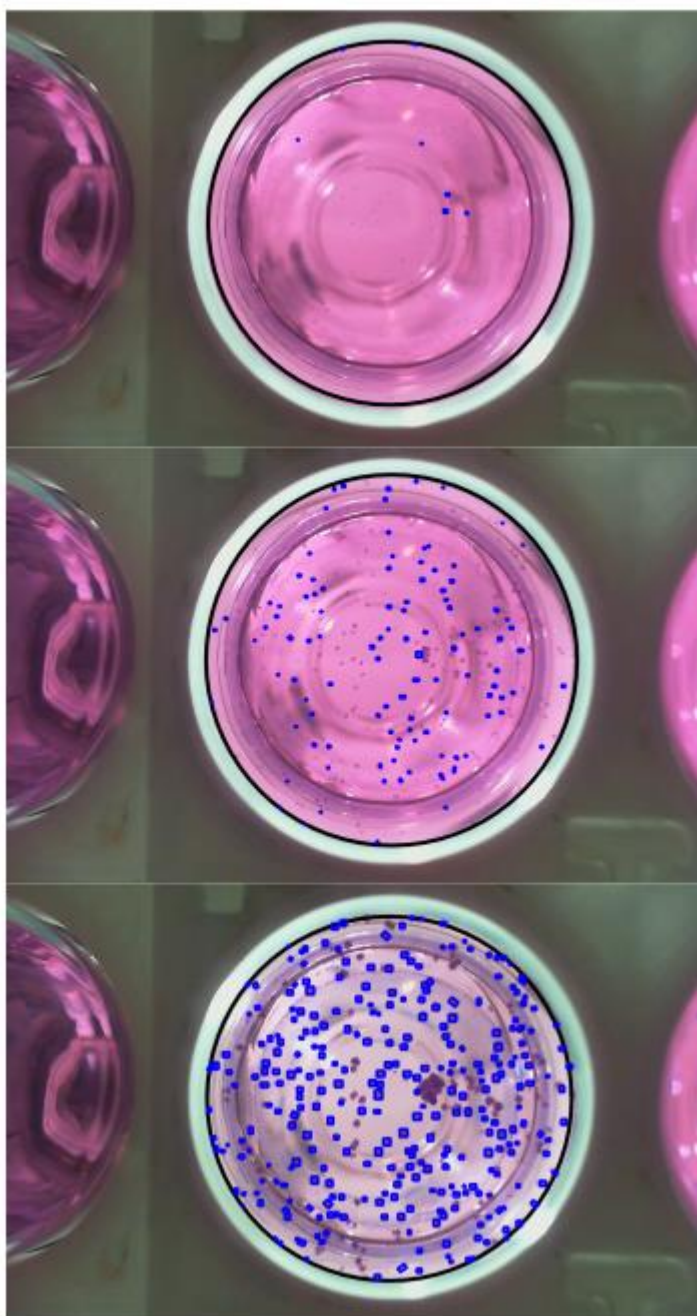


Figure. 4.20. Crystal detections for $\{Co_4\}$ at time intervals of 0, 60 and 150 minutes.

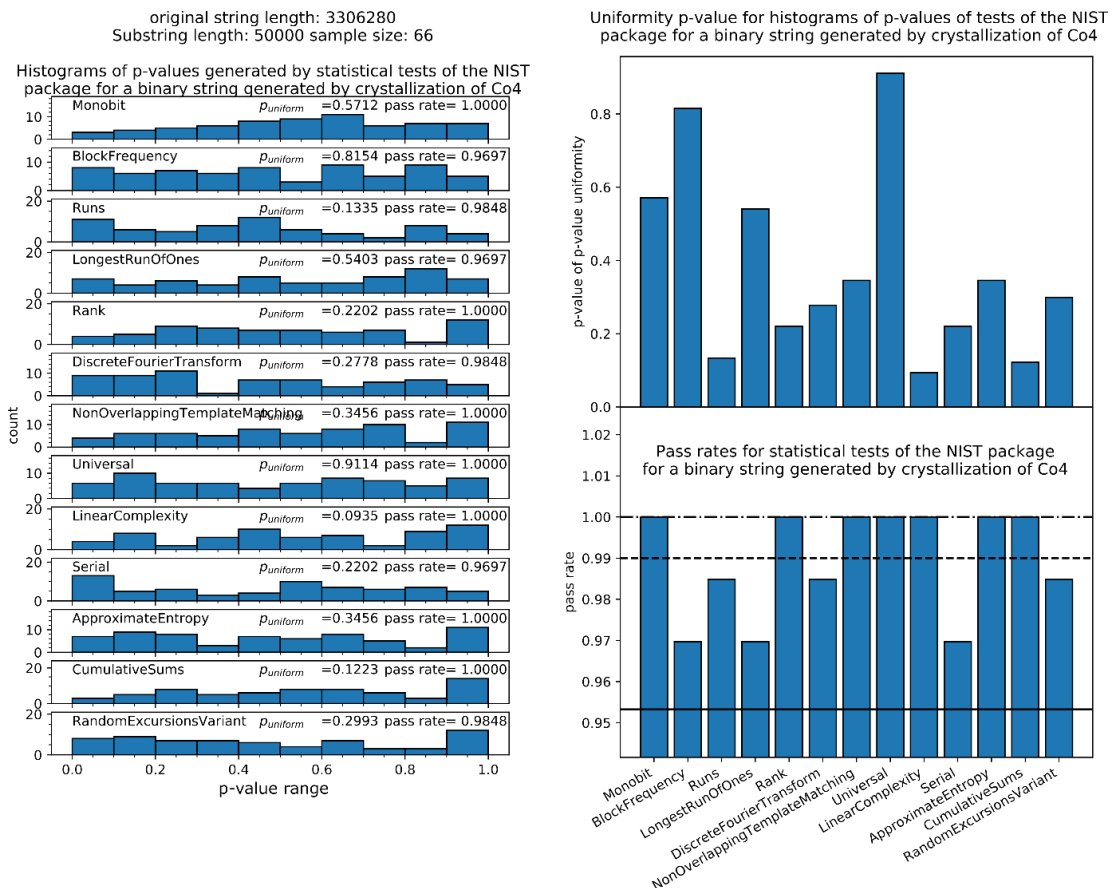


Figure. 4.21. Results from running the NIST barrage on binary sequences generated by $\{Co_4\}$ crystallisations. Left) histograms of p-values for each test in the barrage. Top Right) bar chart of p-values for level 3 NIST test (uniformity). Bottom right) bar chart level 2 NIST test (pass rates), showing minimum pass rate (unbroken line), expected mean pass rate (dashed line) and maximum pass rate (broken dashed line).

4.4.5 Encryption

True random numbers have an advantage over pseudo-random numbers in that they are non-deterministic and therefore cannot be predicted with greater (or less) than 50% certainty. One benchmark of this platform is to use this feature to compare the encryption strength of our numbers to that of a pseudo-random number generator. The Mersenne Twister (MT)¹⁷² is a pseudo random number generator used as the default random number generator in several applications including Microsoft Excel, Python, R and MATLAB. It algorithmically generates a number based on its current state, which contains 624 32-bit numbers. Once this state is determined, its output can be determined with a high degree of accuracy.⁵ This feature was used to compare the encryption strength achievable using both

the MT and crystallisation as random number generators to provide encryption

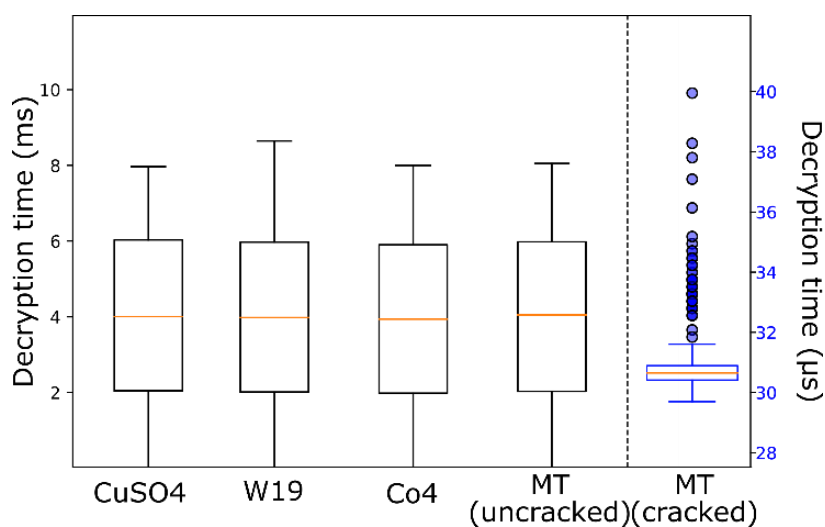


Figure. 4.22. Boxplots of times for the message ‘crystal’ to be decrypted after encryption using 8-bit keys generated by different methods. Keys generated using the crystallization random number generator on average take as long to crack as those produced using the uncracked Mersenne Twister (MT), however, once the state of the MT is determined, the average decryption time for this method is substantially shorter than the crystallization method.

keys. This was done by having each generator produce 12800 8-bit sequences (keys) and use these to encrypt the text string ‘crystal’ with each key. Encryption was done by applying the XOR operation between the keys and each letter (which also contains 8-bits) in the string. The resulting encrypted string was then decrypted using a brute force method of iteratively checking every possible key (any applying the XOR operation with it) in order to obtain the original message back out. In the case of the keys generated by the crystal random number generator, this took approximately 4 ms of time to crack each key. In the case of the MT, the initial time to crack each key was the same as the crystal random number generator, however, once sufficient keys had been deciphered the internal state of the MT was known and subsequent output could be determined. As such, the keys were decrypted orders of magnitude faster than corresponding keys generated by the crystal generator, illustrating the practical importance of such as generator. The results from this test are shown in Figure 4.22

4.5 Discussion and Future work

Using this platform, it was possible to show that crystallization of chemical compounds can be used to create sequences of numbers which conform to statistical distributions expected from truly random bit sequences. The randomness in each of these bit sequences originate from the stochasticity inherent in crystallisation as an entropy source. However, this method did not link detection of any relation between number of prior stochastic processes and degree of randomness produced between different crystallizations. There are several possible explanations for this. In order to obtain large enough bit sequences, the binarization algorithm needed to incorporate data from the size, shape, position and colour of every crystal formed. It is possible that by combining fewer of these parameters, or combining them in a different way, differences between the systems could be observed. In addition, the true positive rate detection rate was lower than desired, and as such, if more data was included some of the tests may have affected the results. However, it is likely that crystallisation alone is able to provide enough entropy to randomise the results, and as such the randomness of these systems cannot be distinguished in this method.

Finally, it was shown that numbers produced in this manner are superior to those produced by the Mersenne Twister, a common pseudo random number generator in terms of encryption strength, as the latter can easily be cracked.

Although the bit generation rate is significantly lower than other methods, this new method represents the first of a new class of true random number generation. Future optimisation of this process will likely permit much greater bit-production rates. One approach to do this would be increase the size of the platform so that more crystallizations may be undertaken simultaneously. Alternatively, compounds with faster crystallization rates may be used to speed up generation rates, or a more efficient binarization technique may be found. Another approach could be to create a simplified monolithic fully sealed device, such as that depicted in Figure 4.23, in which crystallisation is temperature controlled, allowing for repeated cycles of random number generation and reducing the setup and disposal costs of the chemicals involved. Such a sealed device could also be embedded in conventional electronic computers allowing true-random number

generation on demand on the desktop. A continuation of this work may also involve using properties of crystallization, such as the Poisson distribution of crystallization over time in order to produce random numbers with exponential distributions as opposed to uniform.

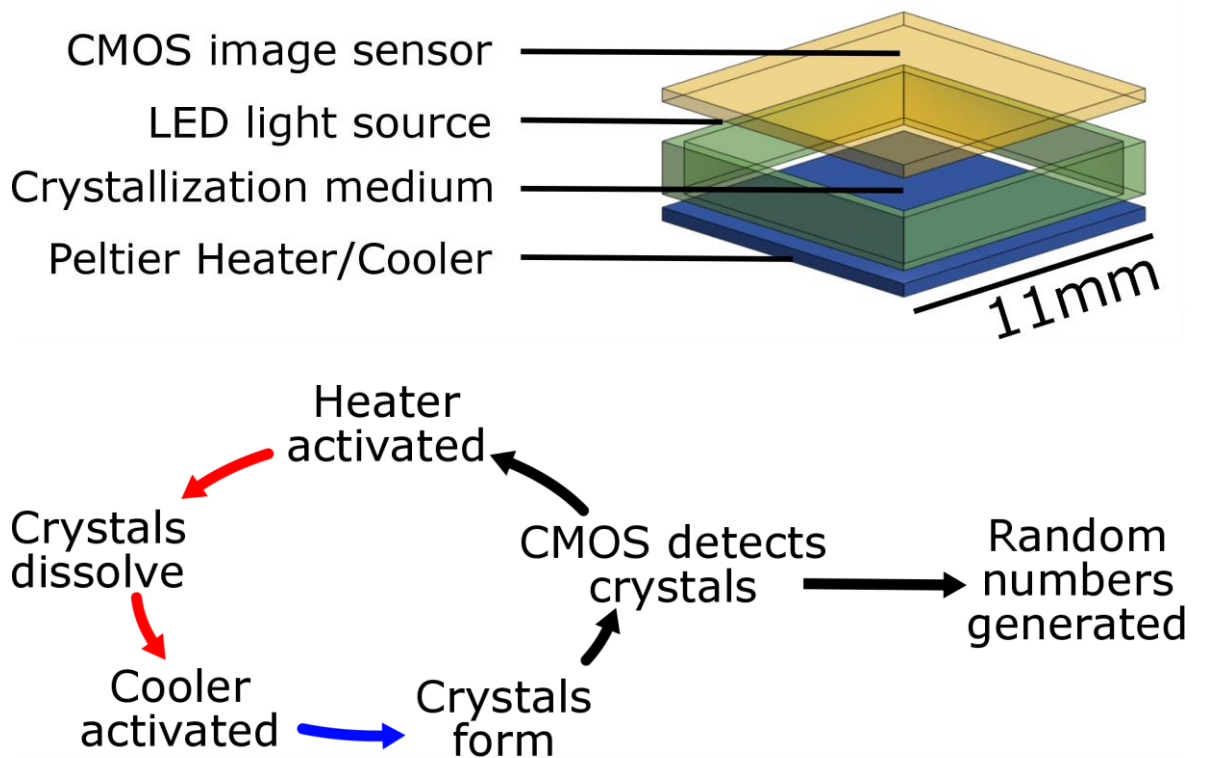


Fig. 4.23. Conception of miniaturised component for generation of random numbers. Top) A microchip-sized sealed device containing a crystallization medium is combined with a heating/cooling source (Peltier) and ceramic metal-oxide semiconductor (CMOS) image sensor, and is illuminated by light emitting diodes (LEDs). Bottom) Procedure for bit generation using crystallization. Cycles of heating and cooling allows dissolution and crystallization. Detection of crystallization using CMOS image sensor allows generation of random numbers.

5 Discovery of iron clusters

This chapter describes the work done to discover and characterise new large iron-oxo clusters. It will describe the methodology and reasoning behind synthetic decisions made. The synthetic aim of this chapter was to build upon the two compounds recently reported in the literature: the Fe₁₃ Keggin³ and the Fe₁₇ molecular magnetite¹¹⁵. As such, the structure of this chapter will describe the effects of changing various synthetic conditions and search strategies, and present new compounds and observations results from these experiments.

The work in this chapter forms the basis of two papers, which are currently under preparation.

5.1 Synthetic approaches

Although the main goal of this was the discovery of new iron clusters on an automated system, most of the new compounds described here were discovered by conventional bench synthesis, with only a few being discovered using an automated approach. This was initially because reactions were done in parallel to the construction of the automated platform described in sections 3 and 4. However, there were some compounds discovered on the bench, such as Fe₃₄, where replication and further exploration on an automated platform was difficult for various reasons, and as such new compounds derived from this were also discovered on the bench. The following sections will be clear as to whether the compounds synthesised were discovered by manual or automatic means.

5.1.1 Robotic automation

In the final year of this project, a second robotic platform was developed for use in rapid automated cluster synthesis. This was for three main reasons: 1) the robotic system described in Section 3 was still being used to collect data for random number generation described in chapter 4, 2) synthetic interest had shifted to focus on reactions involving pyridine and prevented use of the platform outside of a fumehood, and this meant that space limitations required use of a smaller platform, and 3) an underside camera was not required for this project, so this allowed a decrease in platform size.

The design of this platform was achieved by another group member in work yet to be published and incorporated a Geneva wheel to position vials below a stationary reagent point and replaced the syringe pumps with peristaltic pumps. These features had the effect of reducing the overall cost of the platform, but decreased the overall reaction throughput, and speed of reagent dispensing.

Additionally, an automatically updated database was incorporated into the code, so that all reaction conditions, observations and compound formation, would be digitally collated with the intention of performing machine learning to aid prediction of compound reactivity. This platform and its features will be part of a forthcoming publication.

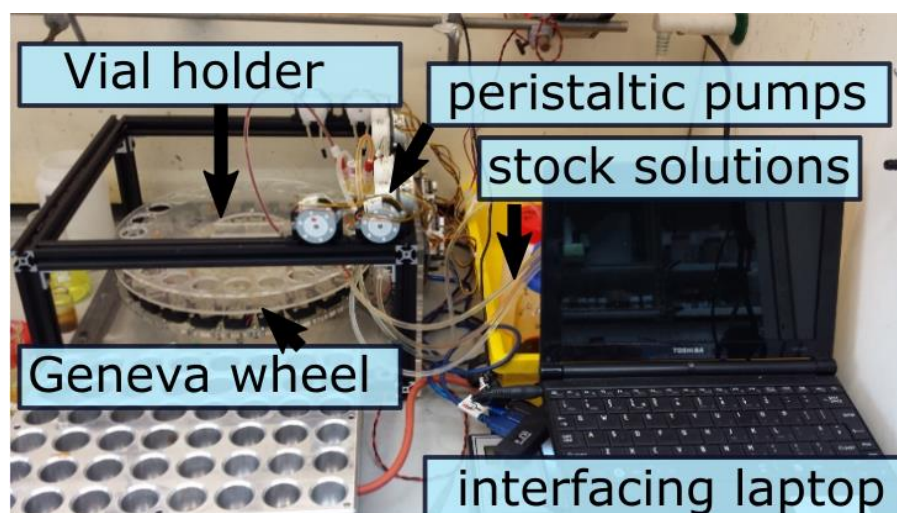


Figure 5.1 Platform used to automate discovery of several iron oxo compounds

5.2 Iron compound discovery in aqueous systems

As mentioned in Chapter 4, the published synthetic route for create Fe₁₃-TCA requires mixing iron nitrate nonahydrate with bismuth nitrate pentahydrate until boiling until a clear red solution is obtained then adding a mixture of trichloroacetic acid and sodium bicarbonate. The resulting orange solid would then be filtered and dissolved in acetone for recrystallization over three days. Although the synthetic pathway of this compound was unknown, it seemed reasonable that aggregating iron hydroxo units were being coordinated by the strongly acidic carboxylate ligands and stabilised by Bi³⁺ ions. As such, a plausible approach for expanding on this structure was to change the ligand to produce either an analogue of Fe₁₃, or an entirely new structure. It also seemed likely that

replacement of Bi^{3+} with another similarly sized cation may also allow trapping of the Keggin structure, or alternatively replacement with a smaller cation may allow a new structure to form. Thirdly, as iron aqueous chemistry and aggregation is affected by electrochemical environment, the addition of a reducing agent was also considered. Other factors, such as identity of base, counter anion of the iron salt, temperature and reaction time were considered, but not explored in this system. However, the first approach was to make the synthetic procedure more facile as described in the following section. Each of the following reactions were performed manually by traditional methods.

5.2.1 Methodological development

Reproduction of the reported synthesis had several issues. The first problem was that boiling of the iron and bismuth source to form a clear red solution required over an hour rather than the stated 5 minutes in the literature (although this was later solved after a second publication specifying that 150°C was needed). Secondly, combining this solution with a boiling solution of trichloroacetic acid and NaHCO_3 produced a huge amount of gas and needed to be done over a long period to prevent bubbling. Thirdly, recrystallization from THF, although successful resulted in low yield with crystal of poor quality.

As such, this method was relatively slow, and difficult to control factors such pH. Instead, it was discovered that the initial heating of the iron and bismuth solution to form a clear solution could be formed by adding around 1% volume of 70% nitric acid. Further, by adding the organic ligand first, the pH could be easily controlled using an aqueous solution of base (e.g. 1M sodium carbonate). Below pH 0.8 the solution was clear and colourless, but above this a clear dark red solution formed. Further pH increase above 2.5 resulted in beige precipitate, similar to that observed in the original synthesis. Typically, the reaction was left to proceed at room temperature for 2-3 hours in the pH range 0.9-2. Crystallisation of Fe_{13} could then be observed in high yield within 4 hours by slow evaporation from the dark red solution. This method, with varying concentrations of each of the reagents was used for each of the following experiments within this pH range investigated.

5.2.2 Ligand substitution

Because the Fe₁₃ Keggin had been reported with both trichloroacetate (*tca*) and trifluoroacetate (*tfa*), one first approaches to build on the original synthesis to replace this with another ligand able to cap the iron octahedra in a similar manner. Indeed, the authors noted that the organic ligand could be replaced in solution (by tetrahydrofuran, *thf*), and its role is likely to aid crystallisation rather than in cluster stabilisation. One of the first ligands tried was that of trifluorobutyrate, as this maintained the fluorinated component of the original ligands. However, this only resulted in an Fe₃ triangle compound, whose type had been well documented.¹⁸⁵ Other ligands attempted were benzoic acid and 4-nitrobenzoic acid because the bulky aromatic group may sterically promote the growth of a larger cluster. However, this formed a further Fe₃ triangle in the former case, and evaporation to dryness in the latter. Another approach was to use a tri-ligating acid, such as iminodiacetic acid, but this resulted in precipitation of amorphous material during the reaction, even at elevated temperature. Other ligands attempted were those with rigid structures (squaric acid and oxalic acid) and one inorganic acid (phosphoric acid), however, none of these resulted in the formation of crystals for analysis. It is possible, that these results were due to pKa being an important factor in the formation of Fe₁₃, as all the compounds used had pKa values between 1.5 and 4, whereas those of Htca and Htfa are 0.7 and 0.2, respectively. On returning to this, choosing ligands that are also in this range, such as difluoroacetic acid, may be more promising.

5.2.3 Bismuth substitution

A second approach was to find other inorganic cations capable of stabilising the cluster with the same ligands. It was noted that although the absence of Bi³⁺ prevented cluster formation in favour of polydisperse spherical particles, it was uncertain whether other metals could fulfil the role of cluster stabilisation. It was suspected that the high cation charge of bismuth was responsible for neutralising the high anionic cluster charge (-17) and preventing precipitation of iron oxyhydroxide.

As such cations with high charge and similar ionic radius as bismuth were selected and investigated, including Ce³⁺, La³⁺ and Pb²⁺, however none of these were able

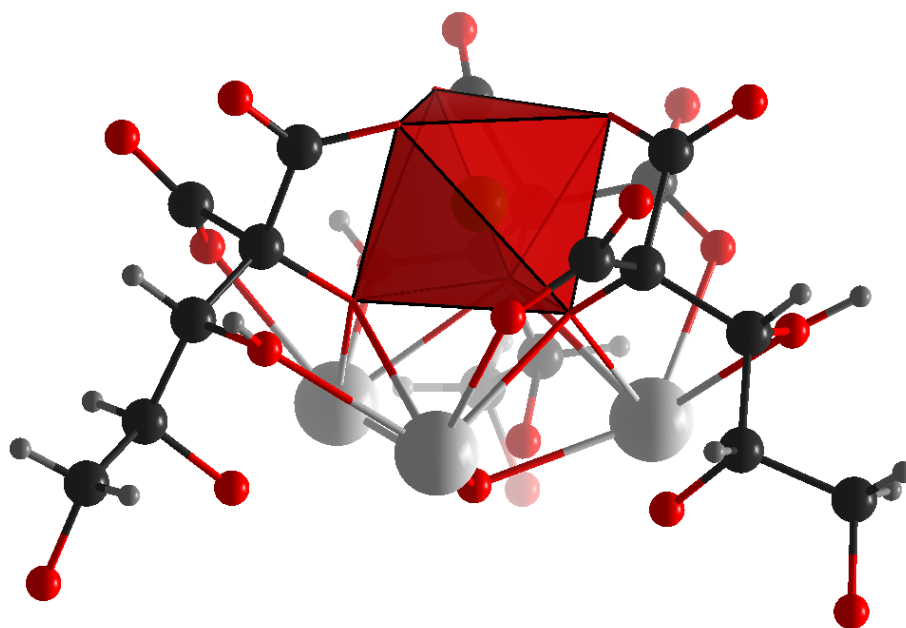
to stabilise any iron cluster under the conditions investigated. Similarly, when smaller transition metals Co^{2+} , Mn^{2+} , Cr^{3+} were tried, no new compounds could be isolated.

In a later paper Nyman *et al.*¹¹⁷, reported they had undertaken a similar approach and also failed to stabilise any cluster using p-block and f-block metals, and eventually concluded that this kind of cluster stabilisation was unique to bismuth. Interestingly, they also report the formation and stabilisation of a potential precursor of BiFe_3 at pH 0.7, whereas the complete Fe_{13} cluster forms at pH 0.05 and requires heating. As such, they suggest that the presence of Bi^{3+} is essential to drive olation at low pH, and increasing pH promotes formation of smaller clusters. This hypothesis is inconsistent with the observation that by changing the reaction procedure (described in section 5.1.1), the Fe_{13} cluster can form at higher pH (up to pH 2).

5.2.4 Reducing agent

A final approach to manipulating the aggregation pathway and produce a new cluster was to change the electric potential environment of the reaction. For this, the organic reducing agent of ascorbic acid was primarily investigated as it could also act as ligand to direct structure formation. Whilst no new clusters were formed using the original reagents, by replacing bismuth nitrate with lead nitrate AND incorporating ascorbic acid, a new cluster, $\{\text{Pb}_3\text{FeL}_3\text{O}\}$, $(2\text{Na}\cdot[\text{FePb}_3\text{O}(\text{cpa})_3]\cdot 3\text{H}_2\text{O})$ (cpa =2-carboxypentonate)) (1), formed and could be crystallised. This contains one Fe(III) atom in an octahedral oxygen environment trapped by three Pb(II) atoms and three *cpa* ligands. The oxidation states of these atoms were confirmed by BVS calculations. Overall, the structure (Figure 5.2) shows C_3 symmetry, with the iron atom located on the C_3 axis. Each *cpa* ligand donates a total of four oxygen atoms to stabilise the structure. Two oxygen atoms are donated to the octahedral environment of the iron atom: one from a carboxylate group and the other from the alkoxide group of the carbon at the start of the butyl chain. This latter oxygen also bridges between two of the lead atoms. Further connections between the *cpa* ligand and lead atoms are formed by donation from the second carboxylate group the alkoxide group on the position 2 carbon forms a μ_2 bond to two separate lead atoms. The last structure stabilising

oxygen forms a μ_3 bond between the three lead atoms is located on the rotation axis. The three lead atoms are crystallographically identical and are pentacoordinated and *hemidirected*. In the crystal structure (Figure 5.2) the molecules are linked *via* two sodium atoms, which are also located on the rotation axis. One of these is entirely coordinated by one of the two oxygen atoms in each of the carboxylate groups of three *cpa* ligands from three different molecules. The other sodium shares three of the same oxygen atoms, but has its coordination shell completed by water molecules. Multinuclear lead-oxo compounds are relatively



rare in the literature, and this iron-substituted lead cubane is unique.

Figure 5.2. Ball and stick representation of a section of the packing structure of $\{\text{Pb}_3\text{FeL}_3\text{O}\}$. (Colour Scheme: Fe polyhedra = red polyhedra, Pb = white, O = red balls, C=black *cpa*⁻

The decomposition of ascorbic acid into H_3cpa has been seen in both basic and acidic conditions.^{186,187} In fact, this process of decomposition and ligand attachment has been observed in the formation of another coordination complex $[\text{Cu}_9\text{Cl}_2(\text{cpa})_6(\text{H}_2\text{O})_3]^{2-}$.¹⁸⁶ The decomposition mechanism involves the oxidation of ascorbic acid into dehydroascorbic acid followed by the facile lactone ring opening to form 2,3-hexodiulosonic acid. This then undergoes a rearrangement to form the branched chain, *cpa*, as illustrated in figure 5.4.

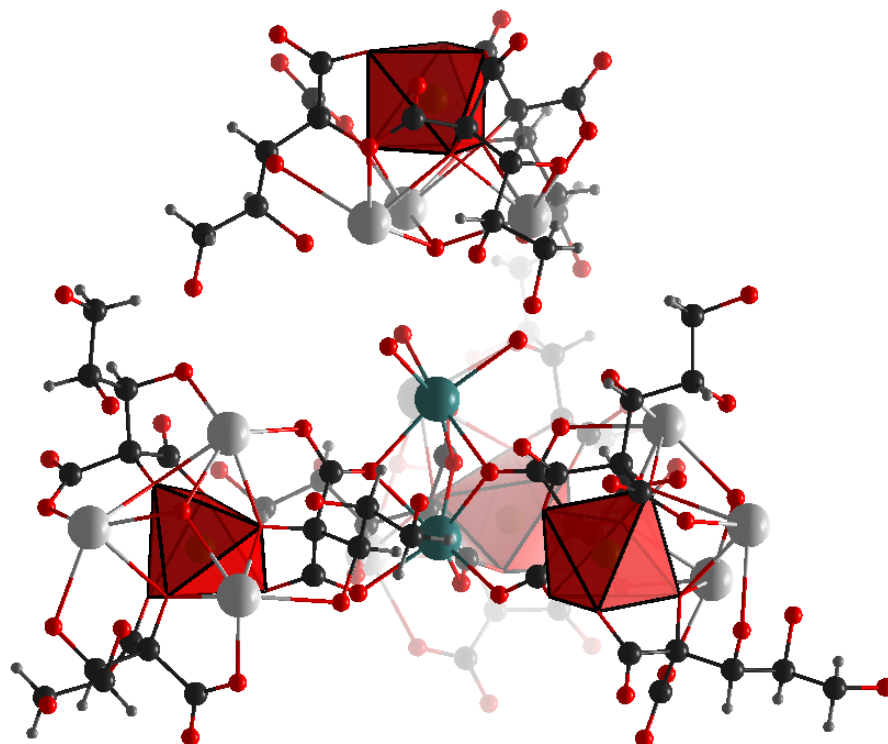


Figure 5.3 Ball and stick representation of a section of the packing structure of $\{Pb_3FeL_3O\}$. (Colour Scheme: Fe polyhedra = red polyhedra, Pb = white, O = red balls, C=black)

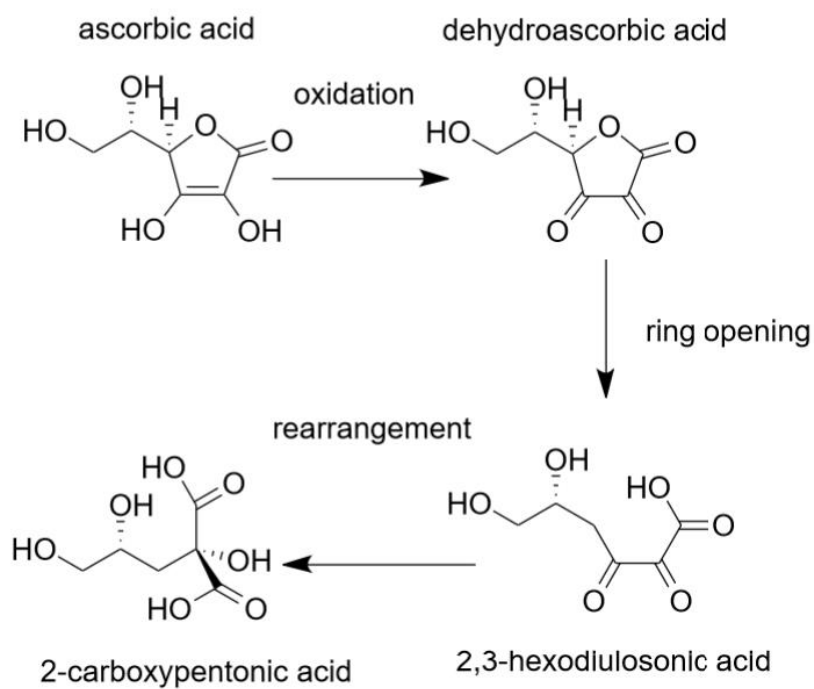


Figure 5.4 Processes and compound involved in the *in situ* transformation of ascorbic acid to 2-carboxypentonic acid.

It is worth noting that this molecule may have direct biological relevance. In the past few decades, multiple studies have reported an inverse correlation between lead and ascorbic acid in biological systems in humans and rats, particularly in blood, brain and bone.¹⁸⁸⁻¹⁹¹ Additionally, one study showed that the presence of ascorbic and iron together prevent adverse effects of lead ingestion in rats.¹⁹¹ This is believed to be because of the high chelating capability ascorbic acid which has been shown to have similar Pb removal capability as EDTA in lead exposed rats.¹⁸⁹ However, neither the molecular interaction responsible for, nor the molecular species resulting from this are known. As this is a mixed iron-lead chelation compound resulting from the decomposition of ascorbic acid, it would be interesting to investigate whether this structure is involved in this process and its detection in biological systems may have implications for the prevention of lead toxicity. However, a study of this kind is beyond the scope of this thesis.

5.3 Iron compound discovery in organic systems

A second approach for iron compound discovery was to perform reactions in organic solvents. This has the advantage that the uncontrolled aggregation of iron oxide particles in aqueous systems as pH increases is limited due to decreased concentration of water. However, on the other hand, the lack of water can also act as a limiting factor for particular growth and prevent the formation of high nuclearity compounds.

The starting point for synthetic exploration in this system was the iron-oxo compound Fe₁₇ (Figure 5.5, left), initially discovered in 2004.¹¹⁵ This compound is synthesised by reacting either FeCl₃ or FeBr₃ with an aromatic nitrogenous base, where the base acts as solvent and trapping ligand. Examples of aromatic nitrogenous bases, for which this has been reported include pyridine, 3-picoline, 4-picoline, 3,5-lutidine and isoquinoline. Reactions can occur at room temperature and are completed after as little as 30 minutes of stirring, with crystal formation after around 3 days. As mentioned in section 1.2, the structure resembles that of magnetite, albeit with the iron atoms all existing as Fe(III), with the outer octahedral and tetrahedral irons being capped by the base and halide, respectively. This structure can also be described as an ϵ -Keggin, with the four hexagonal 'windows' being filled with FeO₃Cl tetrahedra. The basic iron

arrangement consists of three parts as shown in Figure 5.6: an outer capping region formed by four FeO_3Cl tetrahedra which act as the vertices of a 5.66 \AA tetrahedron, an outer framework region formed by 12 $\text{FeO}_5(\text{py})$ octahedra which act as the vertices of an inverted truncated tetrahedron, and a core consisting of a single iron atom. The 28 oxygen atoms in the structure, which are all thought to arise from water impurity in the solvent, allow for fast aggregation of oxo-coordinated iron atoms, but limited due to the large excess of mixed oxo-base-halogen coordinated iron centred groups. As such, it can be surmised that such a solution contains a large number of different iron species in equilibrium, and controlling this may allow for the formation of other, larger structures.

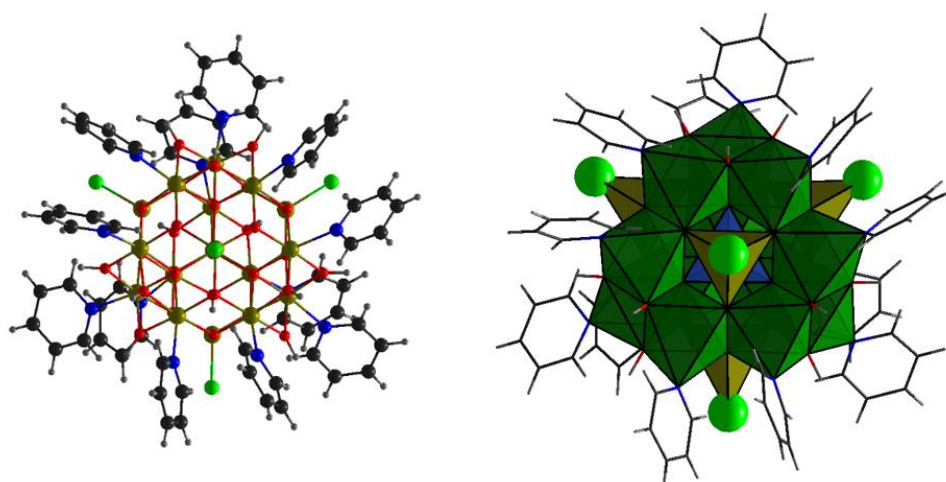


Figure 5.5. Left) Ball and stick representation of $\{\text{Fe}_{17}\}$. Right) Polyhedral representation of Fe_{17} . Cl ligands shown as bright green balls for clarity

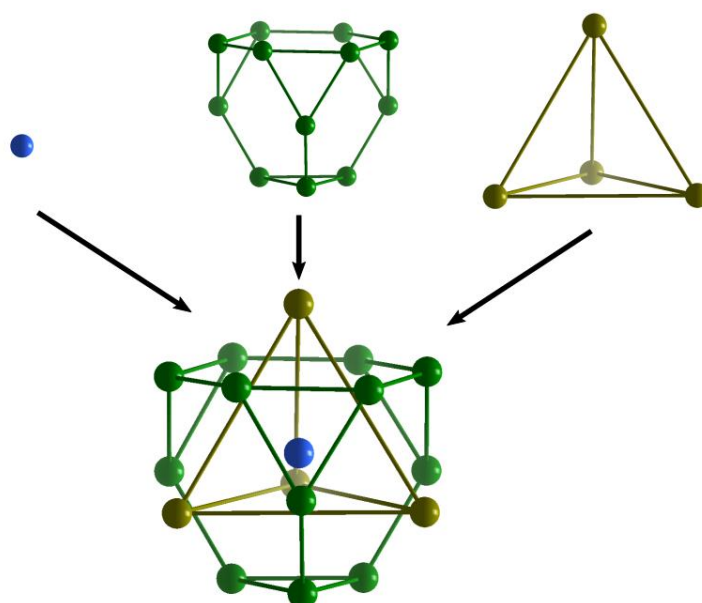


Figure 5.6 Ball and stick model of the iron framework of Fe_{17} . Top left) Central $\{\text{Fe}\}$ atom. Top middle) Inner $\{\text{Fe}_{12}\}$ framework. Top right) Outer Fe caps.

5.3.1 Fe₁₇ in concentrated pyridine

Initial investigations in this system involved retaining the use of the aromatic base as solvent and ligand, and focussed on modifying conditions such as adding a templating group, changing groups on the ring, and adding a reducing agent.

5.3.1.1 Ligand substitution

Based on the literature mentioned, there were some obvious gaps in the ligands tried, namely other mono- or di- methylated pyridine ligands. Reactions were then tried using the same conditions but using 2-picoline, 2,x-lutidine (x=3,4,5,6) and 3,4-lutidine. Out of these only 3,4-lutidine formed a new compound, Fe₁₇ (Figure 5.7), and was structurally analogous to the previous Fe₁₇ compounds reported in the literature. The general formula for this compound is [Fe₁₇O₁₆(OH)₁₂Br₄(3,4-lut)₁₂]·3Br·5(3,4-lut) (**2**). The three bromide counter anions reside in the gaps above three of the four Fe₃ triads, and are stabilised by hydrogen bonds to the bridging hydroxyl groups. The gap above the fourth Fe₃ triad is occupied by a molecule of 3,4-lutidine. Interestingly, each of the ligands in a Fe₂ couple have the 3-methyl group staggered with respect to each other to minimise steric hindrance, with one exception where they are eclipsed as shown in Figure 5.7. Overall, this has the effect of reducing the molecular symmetry from T_d to C₁.

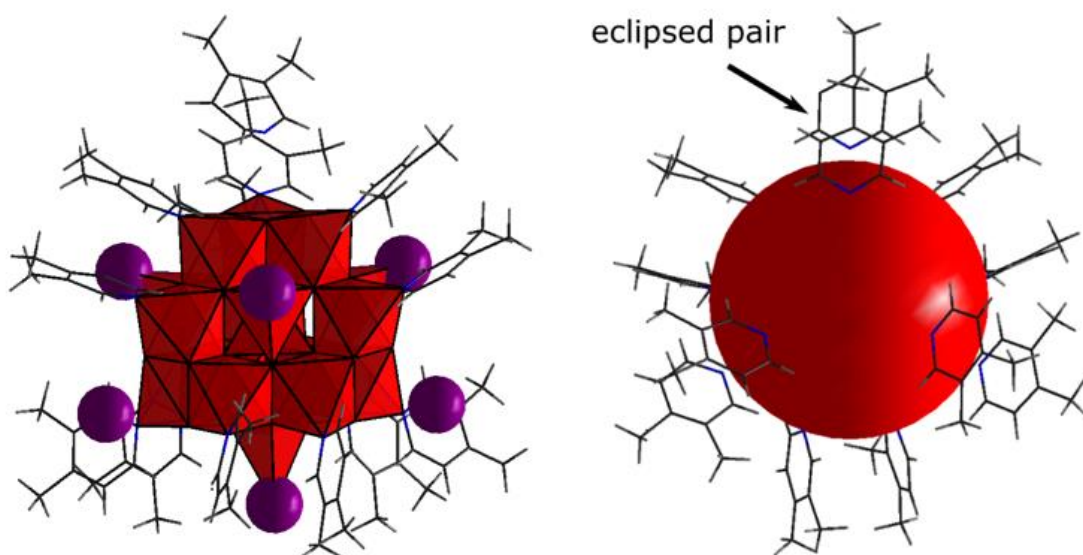


Figure 5.7. Structure of [Fe₁₇O₁₆(OH)₁₂Br₄(3,4-lut)₁₂]³⁺. Left) Polyhedral representation of {Fe₁₇(3,4-lut)₁₂}, with 3,4-lut ligands shown in wireframe, and Br⁻ ligands enlarged for clarity. Right) Fe₁₇ with eclipsed ligands highlighted. Core is shown as a single sphere for clarity.

Modified pyridine rings were also tested such as 4-bromopyridine, 4-pyridine carbonitrile, and 3-nitropyridine by using ethanol as a solvent since these molecules exist as solids. However, none of these were successful in creating new structures. Larger pyridine-based ligands acting also as solvent, including 4-ethyl pyridine, 4-benzylpyridine were not tried, and remain a gap in this family of compounds. These are, however, discussed in section 5.3.3.

5.3.1.2 Organic reducing agents

As noted in section 5.2.4, different iron compounds may form based on the electrical potential of the solution. Thus, it was hypothesised that adding a reducing agent to the reaction solution may have an effect on the structure. To test this, the Fe₁₇ reaction was tested with the addition of a small amount of ascorbic acid to the previous reaction conditions using pyridine. This resulted in a series of modifications to the original Fe₁₇ structure, namely the conversion of some of the outer capping Fe tetrahedra to hydroxyl terminated iron centred octahedra. The first in the series, of {Fe₁₇Br₃} [Fe₁₇O₁₆(OH)₁₂(C₇H₉N)₁₂Br₃] (**3**) has one of these groups substituted and arises from the addition of 0.05-0.2 equivalents of ascorbic acid. This modification changes the overall symmetry of the molecule to C_{3v}. The latter two compounds, of {Fe₁₇Br₂} [Fe₁₇O₁₆(OH)₁₂(C₇H₉N)₁₂Br₂] and of {Fe₁₇Br₂} [Fe₁₇O₁₆(OH)₁₂(C₇H₉N)₁₂Br₂] (**3**) (**4**), arise together and co-crystallise when around 0.5 equivalents of ascorbic acid are used. The first of these has two octahedra replaced, lowering its symmetry again to C_{2v}, while the symmetry of the final compound with three substitutions, returns to a symmetry of C_{3v}. Although it wasn't observed, a cluster with all four tetrahedra replaced would have a symmetry returned to T_d. This symmetry transition sequence is also seen when iterating through α - ϵ Keggin of traditional POMs.

Further investigation may be done by replacing ascorbic acid with other reducing agents, and also replacing pyridine with other aromatic nitrogenous bases. In addition, it may be possible to functionalise the compounds by reacting the newly accessible hydroxyl-capped octahedra with a tri-chelating ligand such as tris(hydroxymethyl)aminomethane (TRIS). This system with ascorbic acid was also investigated using dilute concentrations of pyridine and a solvent of acetonitrile, and this is discussed in section in section 5.3.7.

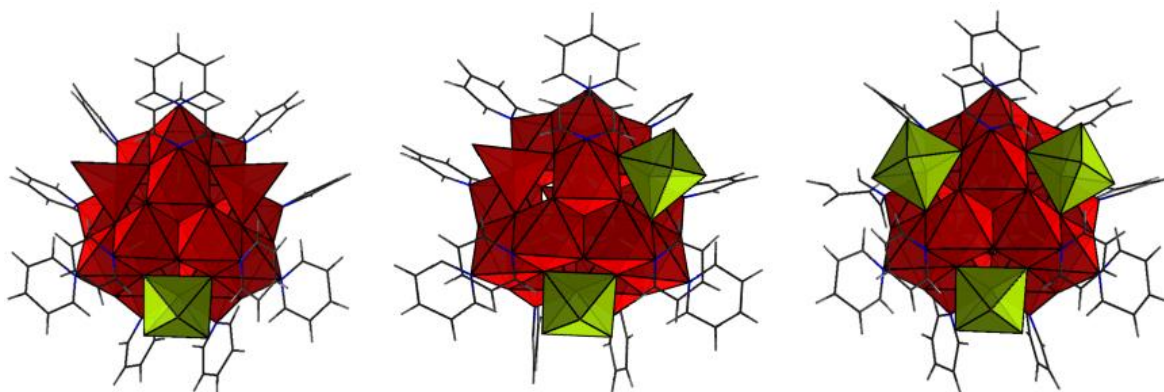


Figure 5.7. Polyhedral representations of $\{\text{Fe}_{17}\}-(\text{H}_2\text{O})_{3n}(\text{Br})_{4-n}$ ($n=1,2,3$) Left) $n=1$, middle) $n=2$. Right) $n=3$. Original $\{\text{FeBr}\}$ tetrahedra are shown in red, substituted $\{\text{O}_3\text{-Fe}(\text{H}_2\text{O})_3\}$ octahedra shown in yellow.

5.3.2 Facilitation of growth by dilution

A second, more general approach to cluster synthesis was to either increase the concentration of H_2O in the solution (providing an O^{2-} source for cluster growth) or to decrease the concentration of aromatic base in the solution. Addition of small amount of water to the solution resulted in the formation of only the original cluster, until around 3% volume H_2O , when all that could be formed was an insoluble precipitate. However, dilution of the aromatic base was a much more successful strategy, and resulted in the discovery of three entirely new structures, with several analogues of each type achieved by changing the ligand. In addition, by slightly increasing the functionality of the aromatic base, a further series of novel compounds were discovered. Another approach taken was to try to introduce inorganic templates in order to interrupt the aggregation pathway and potentially create mixed metal compounds. Finally, the incorporation of a reducing agent in this system was also successful in creating novel molecular compounds. The following sections all involve dilution of an aromatic nitrogenous base-ligand in discovery of new high nuclearity iron-oxo clusters.

5.3.3 Large iron oxo-aggregate molecules: $\{\text{Fe}_{34}\}$, $\{\text{Fe}_{30}\}$ and $\{\text{Fe}_{36}\}$

The first discoveries of new iron-oxo compounds under these conditions were $\{\text{Fe}_{34}\text{L}_{18}\}$ ($[\text{Fe}_{34}\text{O}_{28}(\text{OH})_{12}\text{Br}_{12}\text{L}_{18}]^{2+}$), $\{\text{Fe}_{30}\text{L}_{15}\}$ ($[\text{Fe}_{30}\text{O}_{31}(\text{OH})_{16}\text{Br}_9\text{L}_{15}]^{3+}$), and $\{\text{Fe}_{36}\text{L}_{24}\}$ ($[\text{Fe}_{36}\text{O}_{30}(\text{OH})_{34}\text{Br}_8\text{L}_{24}]^{6+}$), where L is a pyridine or pyridine derived ligand (see Table 5.2 for a summary of relationship between L and Fe_n structure) which are

the largest iron-oxo aggregate compounds known. They are prepared using the same method as Fe₁₇, except that the solvent is polar aprotic, the aromatic base is present in around 5 % volume, and pH is held around pH 5. The solvent used for almost every successful reaction was acetonitrile (**5**, **7-14**), however, Fe₃₄ was also seen to grow in dichloromethane (**6**). However, no polar protic or non-polar solvents yielded any of these compounds. The measured pH was important in this system, with Fe₃₀ only forming below pH 4.5, and Fe₃₄ mainly forming above this. However, more important than this for determining which structure formed was identity of ligand used. Fe₃₄ would only form when using pyridine, pyrimidine and 4-benzyl pyridine, whereas only Fe₃₆ would form when using 3-picoline, 4-picoline, 3,4-lutidine, 3,5-lutidine and 4-ethylpyridine. Fe₃₀, on the other hand, was found to form using pyridine and 4-picoline. The following subsections describe the structures and characterisation of these compounds.

Ligand	Cluster framework			
	{Fe ₁₇ }	{Fe ₃₀ }	{Fe ₃₄ }	{Fe ₃₆ }
pyridine	Powell <i>et al.</i> ¹¹⁵	9	5, 6	-
3-picoline	Gass <i>et al.</i> ¹¹⁶	-	-	12
4-picoline	-	10*	10*	11
3,4-lutidine	2	-	-	13
3,5-lutidine	Gass <i>et al.</i> ¹¹⁶	-	-	14
4-ethylpyridine	-	-	-	15
4-benzylpyridine	-	-	7	-
pyrimidine	-	-	8	-
2-pyridineethanol	19	-	-	-

Table 5.1 Summary of large iron-oxide aggregate structures reported in literature and discovered in this work. *These compounds were discovered when an inorganic template was added to the reaction conditions, and did not form in its absence.

5.3.3.1 {Fe₃₄}

The general formula of {Fe₃₄} is [Fe₃₄O₃₈(OH)₁₂Br₁₂(lig)₁₈]²⁺, where lig is an aromatic base (pyridine (**5**) and (**6**), pyrimidine (**7**), 4-benzylpyridine (**8**)). Synthetically, it is prepared by the reaction between FeBr₃ and the aromatic base. When using pyridine as a ligand, this was achieved in both acetonitrile (**5**) and dichloromethane (**6**), which resulted in a different crystal packing structure, namely P-1 and Pnma, respectively as shown in Figure 5.8. The compound could be formed in a pH range of 4.6-5.2, and was initially discovered using hexamethylenetetramine (*hmta*) as base. However, this was later replaced successfully with morpholine so that the reaction could be performed entirely by a liquid handling robot as *hmta* has low solubility in organic solvents suitable for this reaction.

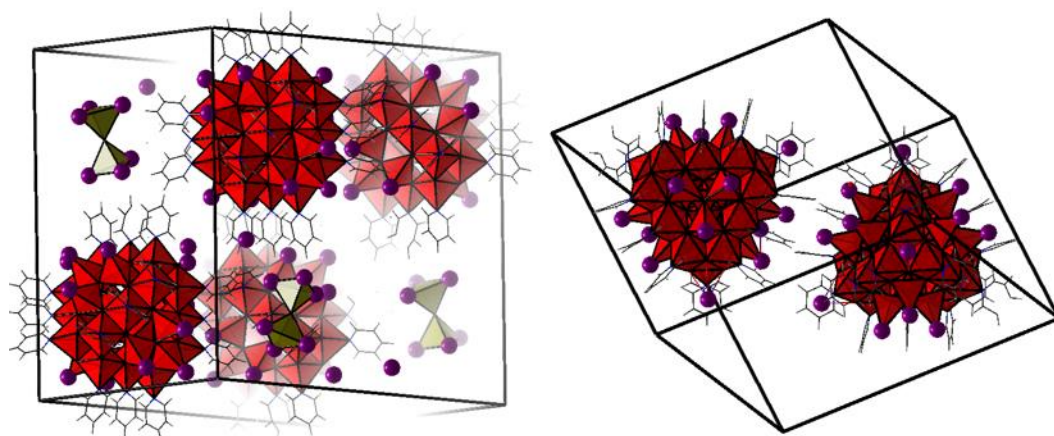


Figure 5.8 Packing structure of Fe₃₄ grown in Left) acetonitrile, Right) DCM

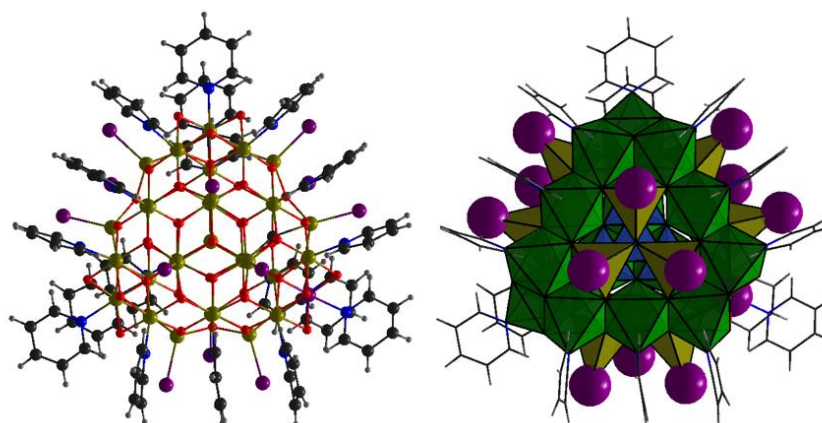


Figure 5.9 Two different representations of {Fe₃₄}. Left) Ball and stick representation (colour scheme: Fe=gold, O =red, Br = purple, N=blue, C=black, H=grey). Right) Polyhedral representation of Fe framework, with wireframe representation of ligands and ball representation of Br. (Colour scheme: Core Fe polyhedra = blue, outer Fe framework polyhedra = green, outer capping Fe polyhedra = gold, Br= purple, C=black, H=grey).

The crystals which formed were morphologically different for each of the ligands used. Those with pyridine (**5**) were large black blocks which and produced very good x-ray diffraction patterns. However, those of 4-benzylpyridine (**8**) were small, red, produced much worse diffraction, and were obtained in much lower yield. The maximum crystallographic resolution obtained for (**8**) was only around 1.3 Å, so only the frame work could be resolved. The ligands were then inferred based on the known structure of $\{\text{Fe}_{34}(\text{py})_{18}\}$. Crystals obtained using pyrimidine were more similar to those of pyridine being large black blocks. However, the yield of these low, with only a few of these crystals being produced per reaction. Interestingly, reactions involving pyrimidine also produced a second type of crystal simultaneously with $\{\text{Fe}_{34}\}$. These were large and light orange in colour with a much larger yield. X-ray analysis revealed these as a novel metal-organic framework, which is discussed in section: 5.3.5.

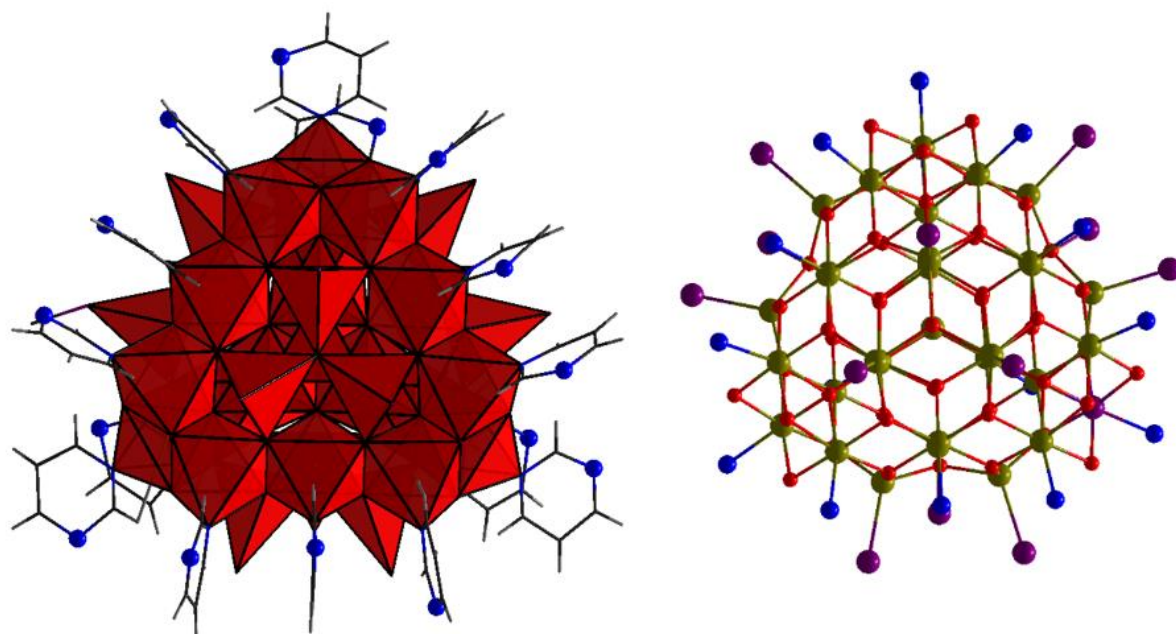


Figure 5.10 Molecular representation obtained from crystal structure of $\{\text{Fe}_{34}\}$ with ligands: Left) pyrimidine (N of pyrimidine enlarged for clarity. Right) 4-benzylpyridine (ligands could not be resolved).

Each of the $\{\text{Fe}_{34}\}$ molecules were structurally almost identical, so the following description, although based on the pyridine version ($\{\text{Fe}_{34}(\text{py})_{18}\}$), closely follows those formed using other ligands. The general structure of $\{\text{Fe}_{34}\}$ consists of a 34 Fe(III) framework divided into three main regions - a tetrahedral core with 4 iron atoms (blue in Figure 5.11, top left), a truncated tetrahedron outer framework with 18 iron atoms (green in Figure 5.11, top middle) and a distorted

cuboctahedron outer capping region with 12 iron atoms (gold in Figure 5.11 top right). The combination of these three constituents is shown in Figure 5.11 (bottom) and results in the overall T_d symmetry of the molecule. As such, it contains the same general features as an ϵ -Keggin structure, but contains an additional layer along each edge, making this a ‘super-Kegginoid’, akin to that of the previously reported ‘super-Lindqvist’¹¹³.

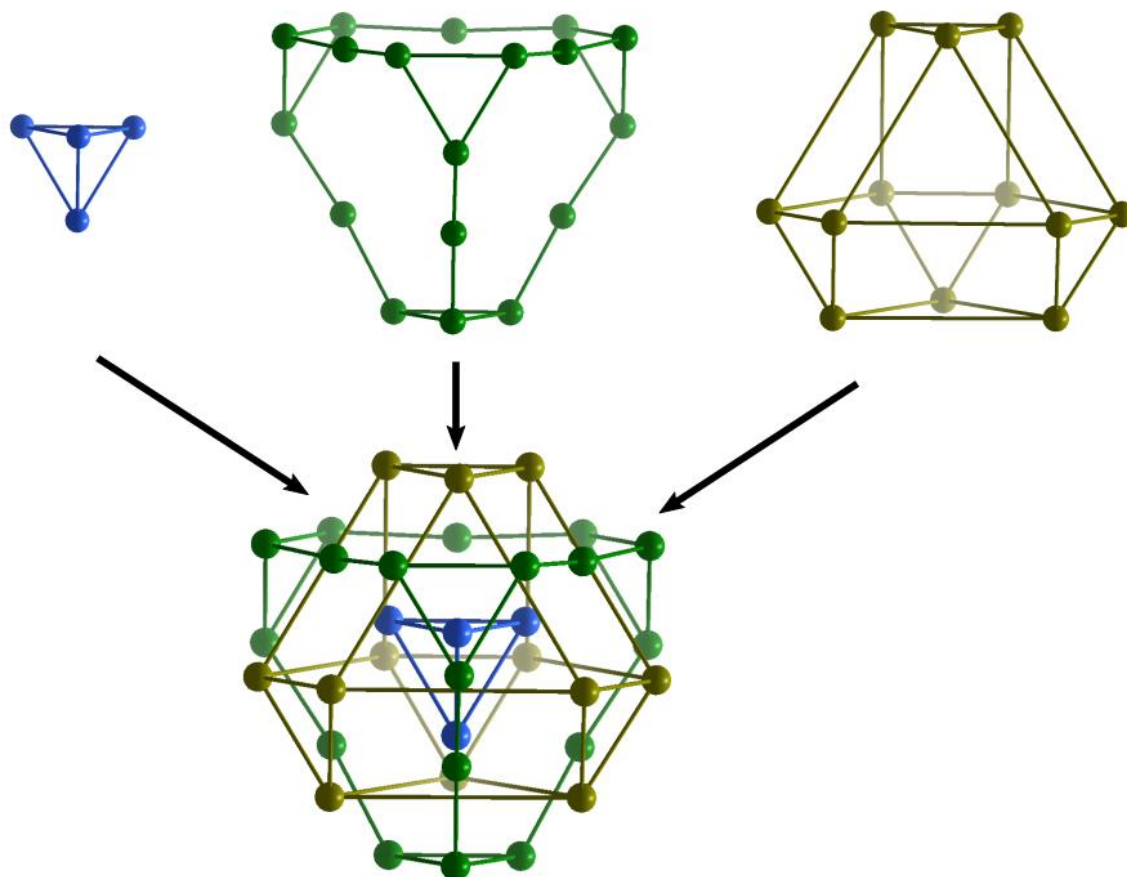


Figure 5.11 Ball and stick model of the iron framework of Fe_{34} . Top left) Core $\{\text{Fe}_4\}$ tetrahedron. Top middle) Inner $\{\text{Fe}_{18}\}$ truncated tetrahedral framework. Top right) Outer $\{\text{Fe}_3\}$ caps linked into a distorted cuboctahedron. Bottom) Overlap of the three components of the $\{\text{Fe}_{34}\}$ structure.

The iron atoms in the outer capping region (gold in Figure 5.11) lie at the vertices of a distorted cuboctahedron. The small triangular faces of this sub-structure are very close to equilateral, with internal angles of 60.0° and Fe-Fe distances of 3.33 \AA . The centres of these faces lie on each of the molecule’s trigonal axes. The larger triangular faces are, likewise, also very close to equilateral with internal angles of 60.0° side and lengths of 5.88 \AA . The centres of these faces lie on each

of the molecule's tetrahedral axes. The quadrilateral faces are rectangles with two edges shared with each type of adjacent triangle. The angles of the rectangle are very close to 90° , and the centres of each rectangle lie on each of the molecule's C_2 axes. Each of the iron atoms in the outer capping region lies between 4.62 Å and 4.72 Å from the centre of the molecule.

Interlaced with the cuboctahedral iron framework of the outer capping region is a truncated tetrahedral framework, with iron atoms located at each of the vertices and in the centre of each edge of the resultant hexagon (green in Figure 5.11). Here, the triangular faces are around 10 % smaller than the corresponding triangles of the cuboctahedral sub-framework, with Fe-Fe distances of 3.06 - 3.09 Å. However, these lengths match well with the corresponding triads of the $\{Fe_{17}\}$ structures, which are 3.02 - 3.06 Å in length. The centres of each of these triangles lie on the molecule's tetrahedral axis and are coplanar with the large triangular faces of the outer capping region. The planes are separated by a distance of 1.56 - 1.64 Å, with the inner framework actually being located distal to the outer capping region here. The large, distorted hexagonal faces of this sub-framework have internal angles of very close to exactly 120° and are coplanar with the small triangular faces of the outer capping region (plane separation is 1.91-1.93 Å). Each of the long sides are 5.84 - 5.86 Å in length, and are shared with adjacent hexagonal faces, while the shorter sides are shared with the adjacent triangular faces. The long edges are composed of three Fe atoms, with a shorter Fe-Fe distance along these edges than that in the triangular faces, at 2.92-2.94 Å. The central atom resides 0.16 Å away from the hexagon's edge towards the centre of the molecule, which results in an Fe-Fe-Fe angle of 174.0° . These central atoms lie directly distal to the centre of each outer-capping region's rectangular faces, and is offset by 0.82-0.84 Å. The distance between the centre of the molecule and an edge iron atom is 4.07-4.10 Å while the distance between a vertex iron atom and the centre is 5.14-5.16 Å.

The core of this compound consists of a tetrahedron of iron atoms (blue in Figure 5.11) which are each separated by distances of 3.16-3.18 Å and angles of 60.0° . This tetrahedron is orientated in the same way as the outer framework, with a separation of 1.71-1.73 Å between the faces of the two structures.

The connectivity between the iron atom at each of these vertices and the iron triad at each corner of the outer framework bears the relationship between the central atom of an $\{\text{Fe}_{17}\}$ molecule and each of its corner triads, i.e through a single $\mu_3\text{O}$ atom (Figure 5.12). The Fe-Fe distances in each case are very similar, being 3.38-3.41 Å in the former and 3.46-3.49 Å in the latter. These similarities suggest they may arise from the same meta-stable building units in solution.

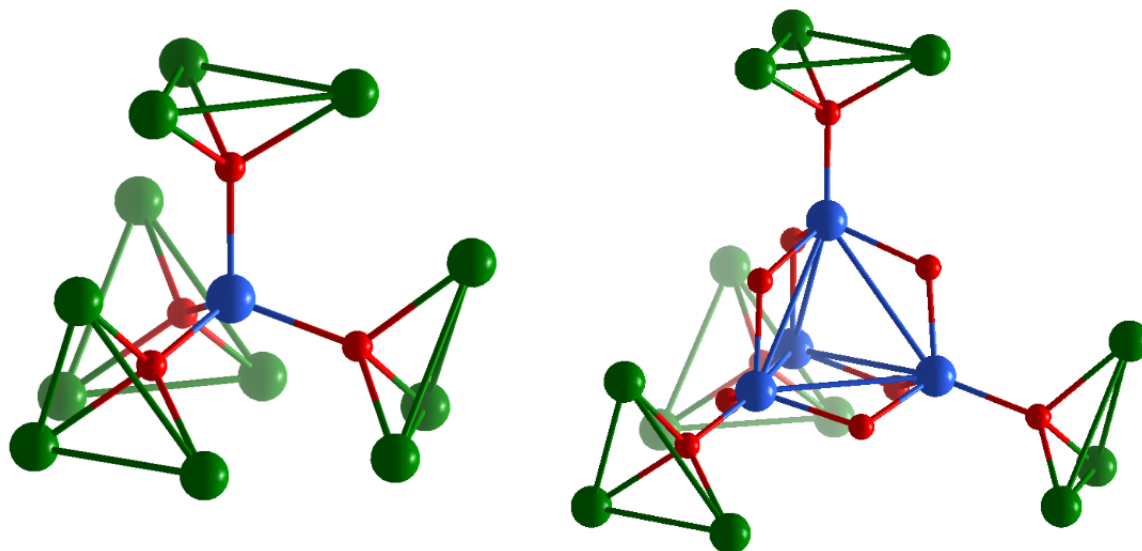


Figure 5.12 Connectivity between inner core atom(s) of with outer framework via a single $\mu_3\text{O}$ atom in $\{\text{Fe}_{17}\}$ (left) and $\{\text{Fe}_{34}\}$ (right).

Magnetic Data

Preliminary magnetic susceptibility and low field magnetisation curves were obtained for $\{\text{Fe}_{34}\}$ and are shown below in Figures 5.13 and 5.14. These indicate the presence of antiferromagnetic exchange interactions between the Fe centres, however, a complete understanding of these data is currently pending.

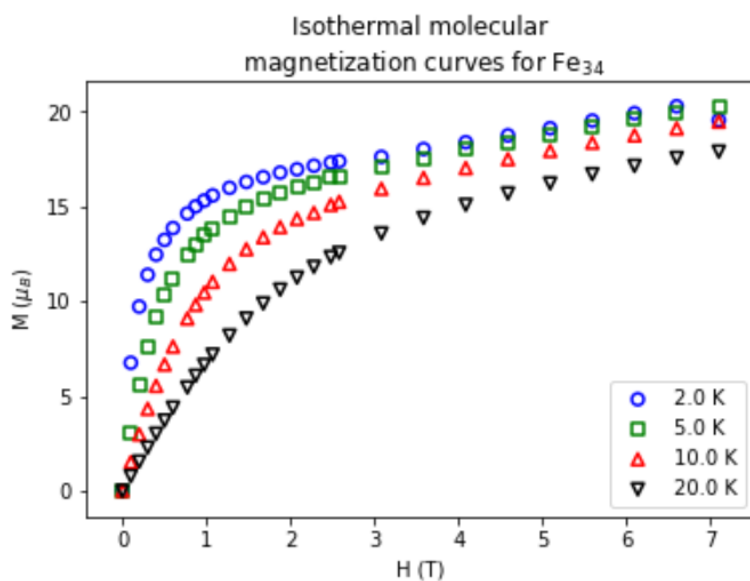


Figure 5.13. Magnetic susceptibility curves for $\{\text{Fe}_{34}\}$.

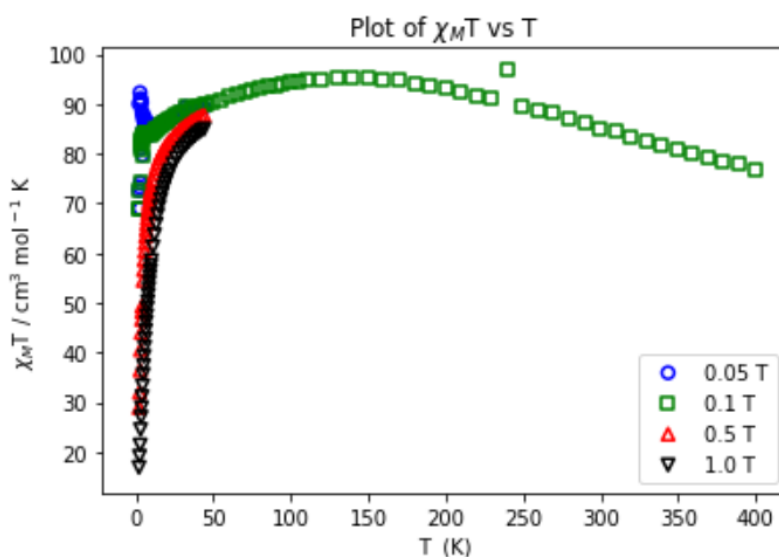


Figure 5.14. Low-field magnetisation curves for $\{\text{Fe}_{34}\}$

5.3.3.2 $\{\text{Fe}_{30}\}$

The general formula of $\{\text{Fe}_{30}\}$ is $[\text{Fe}_{30}\text{O}_{31}(\text{OH})_{16}\text{Br}_9(\text{lig})_{15}]^{3+}$, where lig is an aromatic base (pyridine (**9**), 4-picoline (**10**)). Synthetically, it is prepared by an almost identical reaction to that of Fe_{34} between FeBr_3 and the aromatic base in acetonitrile. The compound could only be formed in a pH range slightly lower than that of $\{\text{Fe}_{34}\}$ between 4.5-4.7, and was initially discovered using

hexamethylenetetramine (hmta) as base to control the pH. In this case, the crystals for each ligand looks similar, being dark black and hexagonal. Interestingly, in both cases, the crystal structure was disordered and showed that both $\{\text{Fe}_{30}\}$ and $\{\text{Fe}_{34}\}$ were present, although in a 9:1 ratio. Attempts were made to separate these by recrystallization, but unfortunately, no suitable conditions could be found to achieve this. Synthesis of this compound using ligands other than pyridine required the addition of a metal templating ion, such as BiBr_3 . Although this doesn't feature in the crystal structure, reactions which did not include this resulted in the formation of a different compound, $\{\text{Fe}_{36}\}$ (see section 5.3.3.3).

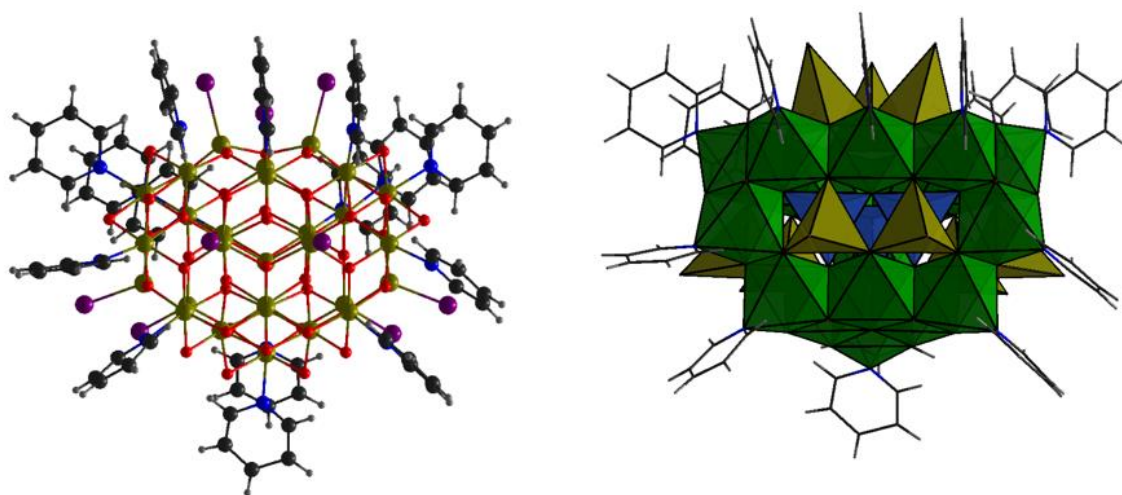


Figure 5.15 Two different representations of $\{\text{Fe}_{30}\}$. Left) Ball and stick representation (colour scheme: Fe=gold, O = red, Br = purple, N=blue, C=black, H=grey). Right) Polyhedral representation of Fe framework, with wireframe representation of ligands and ball representation of Br. (Colour scheme: Core Fe polyhedra = blue, outer Fe framework polyhedra = green, outer capping Fe polyhedra = gold, Br= purple, C=black, H=grey).

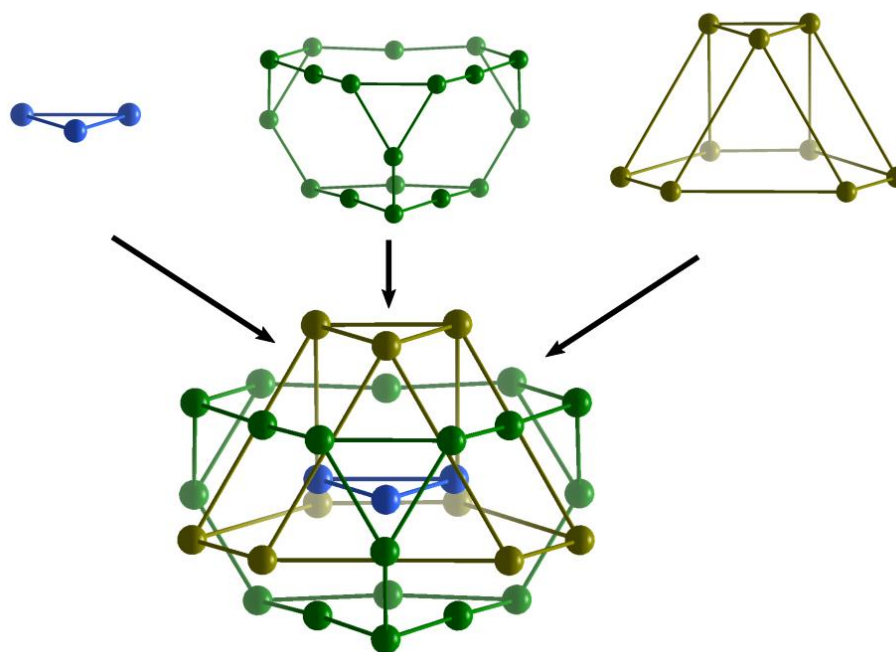


Figure 5.16 Ball and stick model of the iron framework of Fe_{30} . Top left) Core $\{\text{Fe}_3\}$ tetrahedron. Top middle) Inner $\{\text{Fe}_{18}\}$ framework. Top right) Outer $\{\text{Fe}_3\}/\{\text{Fe}_2\}$ caps. Bottom) Overlap of the three components of the $\{\text{Fe}_{30}\}$ structure.

The general structure of $\{\text{Fe}_{30}\}$ is directly related to that of Fe_{34} , as it also contains an outer capping region, outer framework and inner region, but is truncated in one axis which reduces the molecular symmetry from T_d to C_{3v} . Compared with Fe_{34} , the Fe_{30} core is reduced from a 3-dimensional tetrahedral arrangement to a 2-dimensional triangular arrangement by removal of one iron atom. This has the effect on the outer framework that one of its axes is truncated one layer earlier than the other three. Three further iron oxo octahedra then fill the gap left to complete this layer. Finally, this has the effect that three of the four windows created by the outer framework are reduced in size, and can only accommodate two capping iron tetrahedra. The final window is unaffected and hosts three capping iron tetrahedra, as in Fe_{34} .

Overall, both the outer framework and outer capping region remain as truncated tetrahedra, however, with one axis truncated earlier than the other three. This results in three core tetrahedra, 6 outer capping tetrahedra, and 18 outer framework octahedra. The major chemical difference lies in that of the three extra iron octahedra in the truncated layer of the outer framework: the

coordination environment of each of these is purely oxo-based ($\text{Fe}(\mu_4\text{O})_2(\mu_3\text{O})(\mu_3\text{O}-\text{H})(\mu_2\text{O}-\text{H})$) unlike those in Fe_{34} , which contain pyridine in the coordination environment.

Initial magnetic data for this compound was collected but has not yet been interpreted.

Magnetic Data

Preliminary magnetic susceptibility and low field magnetisation curves were obtained for $\{\text{Fe}_{30}\}$ and are shown below. These indicate the presence of antiferromagnetic exchange interactions between the Fe centres, however, a complete understanding of these data is currently pending.

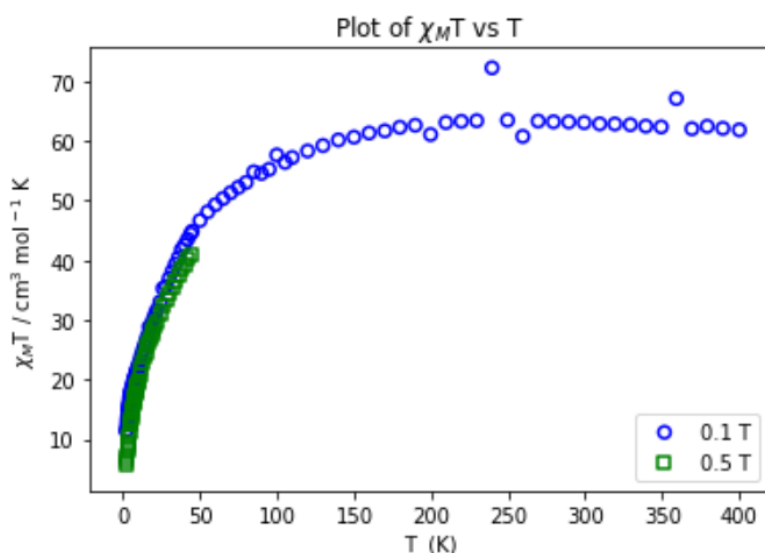


Figure 5.17. Magnetic susceptibility curves for $\{\text{Fe}_{30}\}$.

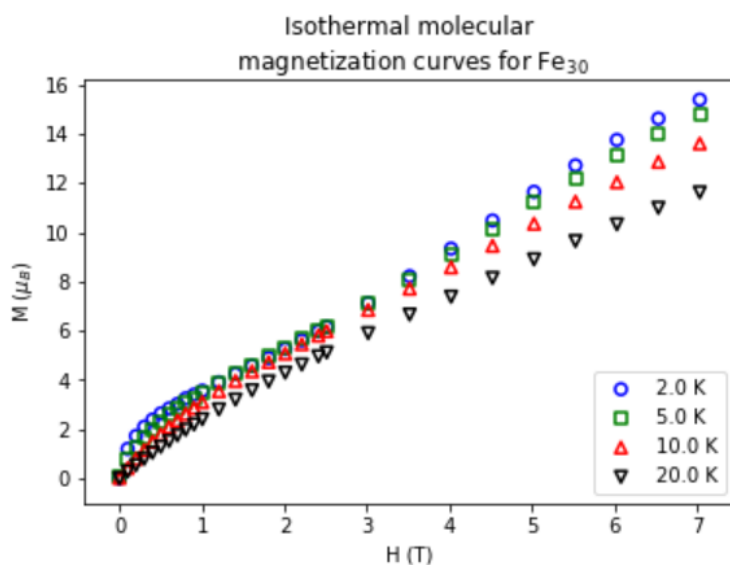


Figure 5.18. Low-field magnetisation curves for $\{\text{Fe}_{30}\}$

5.3.3.3 {Fe₃₆} - structural description

The general formula of {Fe₃₆} is [Fe₃₆O₃₀(OH)₃₄Br₈(lig)₂₄]·6Br, where lig is an aromatic base (4-picoline (11), 3,4-lutidine (12), 3,5-lutidine, (13), 4-ethylpyridine, (14)). The 4-picoline version is shown in Figure 5.17 using ball and stick, polyhedral and space filling representations. It consists of a 36 Fe(III) framework divided into three main regions - a tetrahedral core with 4 iron atoms (blue in Figure 5.19), a distorted truncated octahedral outer framework with 24 iron atoms (green in Figure 5.19) and a distorted cubic outer capping region with 8 iron atoms (gold in Figure 5.19). The overall symmetry of the molecule is close to O_h but is lowered to T_d due to distortions in the outer framework and the tetrahedral arrangement of the core.

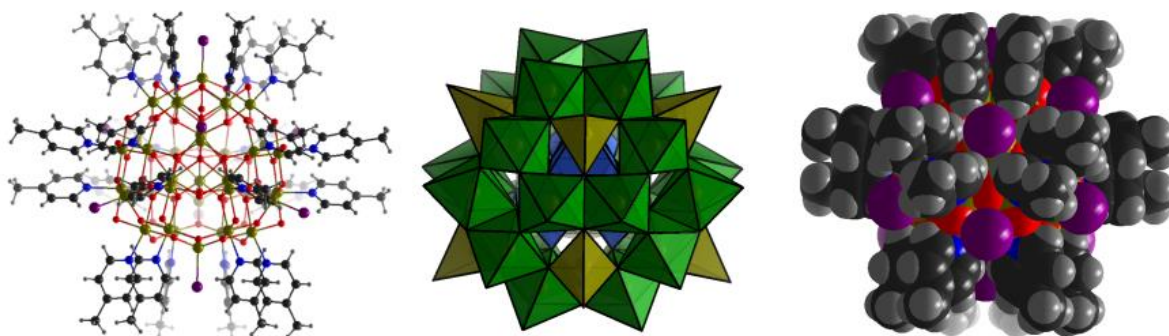


Figure 5.19 Three different representations of {Fe₃₆}. Left) Ball and stick representation (colour scheme: Fe=gold, O =red, Br = purple, N=blue, C=black, H=grey). Centre) Polyhedral representation of Fe framework, with ligands omitted for clarity. (Colour scheme: Core Fe polyhedra = blue, outer Fe framework polyhedra = green, outer capping Fe polyhedra = gold, Br= purple, C=black, H=grey). Right) Space filling model (colour scheme: Fe=gold, O=red, Br=purple, N=blue, C=black, H=grey)

The outer diameter of the structure, from the final carbons in the alkyl chain on opposite sides of the structure is 23.1 Å and 25.1 Å for Fe₃₆ with a methyl group. Unlike with Fe₃₄ and Fe₃₀, each Fe₃₆ analogue packs with cubic crystal symmetry. Additionally, the crystal morphology (a tiny hexagon) was identical in each case,

but with very low yield - only a few crystals per sample. The following structural description is based specifically on the 4-picoline analogue, however, each compound with the other ligands showed only very slight differences in the atomic distances and angles of the molecule's framework.

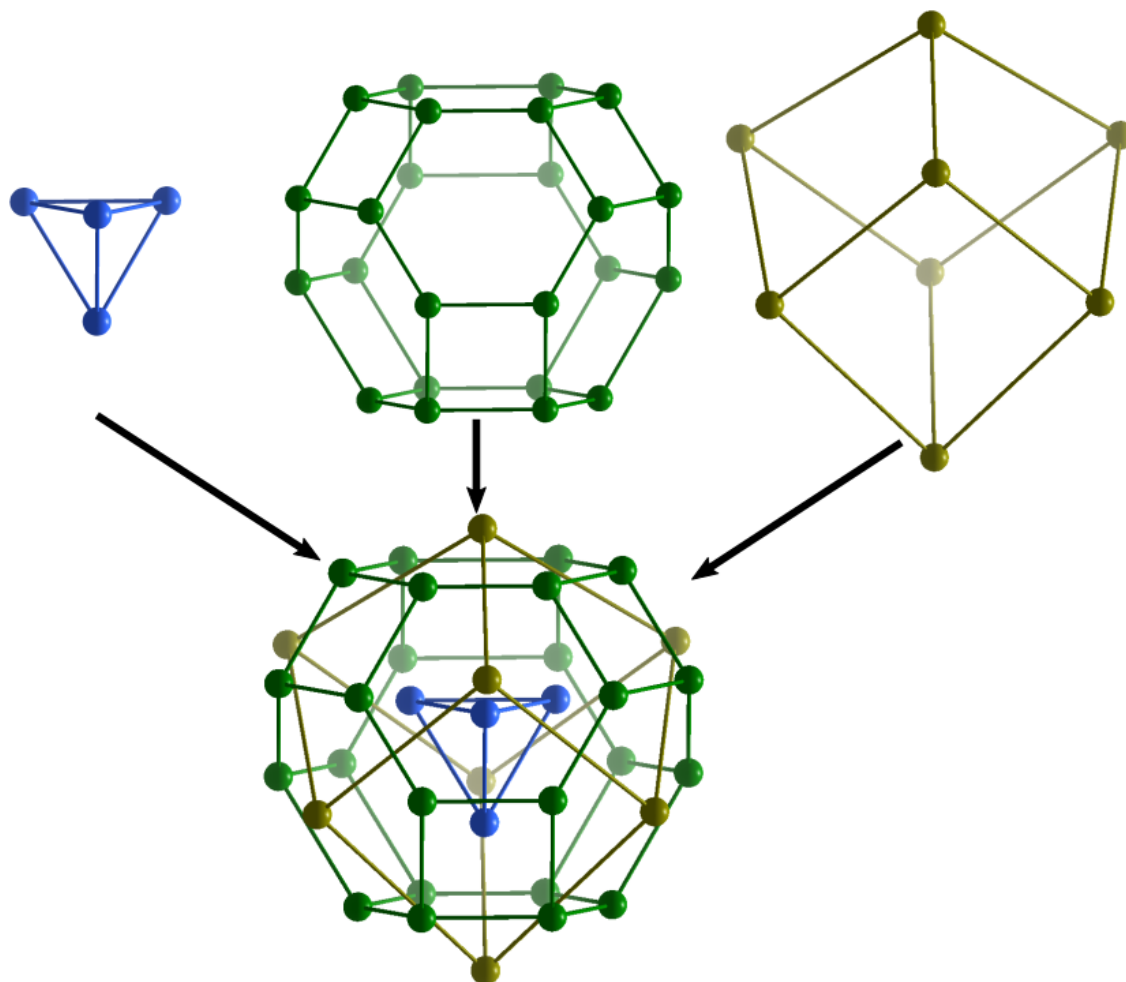


Figure 5.20 Ball and stick model of the iron framework of Fe₃₆. Top left) Core {Fe₄} tetrahedron. Top middle) Inner {Fe₂₄} framework. Top right) 6 Outer {Fe} caps. Bottom) Overlap of the three components of the {Fe₃₆} structure.

The irons in the outer capping region lie at the corners of a distorted cube with Fe-Fe distance of 6.1237 Å and angles 97.685° and 81.754° at adjacent vertices. This distortion results in half of these irons being significantly further away from the core of the molecule at 5.6467 Å compared with 4.9082 Å of the other half. Each of these Fe atoms reside in a distorted tetrahedral coordination environment consisting of a capping Br atom and three O atoms connecting to the rest of the framework. The bond lengths to these for each Fe type are similar with Fe-Br

distances being 2.3452 Å and 2.4420 Å for the distal and proximal irons, respectively, and Fe-O distances being 1.8640 Å and 1.8422 Å, likewise.

The 24 Fe atoms are all crystallographically identical, and together form a distorted truncated octahedron. Unlike the distortion in the outer capping region, whose distortion was due to deviations in angle, the angles forming the geometry of this region are ideal, with 120.0° between atoms in each hexagonal face, and 90.0° between atoms in each quadrilateral face. However, distortions arise from the distances between adjacent vertices. The edges of the six quadrilateral faces are rectangles with a short edge of 3.1013 Å and a long edge of 3.6924 Å. Each edge is shared with one of the structure's six distorted hexagons. Each of the six hexagon then shares three of its edges with an adjacent rectangular face, and three with an adjacent hexagon. This results in alternating hexagons of two different sizes: the smaller one exclusively sharing the short edge of three rectangular faces, and the larger one exclusively sharing the longer edges. The inter-hexagon edge is identical in every case, with a length of 2.9453 Å.

Each iron atom in this region resides in a distorted octahedral environment and is connected to a terminal nitrogen (of the capping aromatic base), and five bridging oxygen atoms. Two of those, which are equatorial, have μ_2 coordination and form the edges of the rectangular faces. The remaining three have μ_3 coordination, with two equatorial atoms bridging the short hex-hex edge and also connecting the outer capping region to the outer framework. The final atom is apical and bridges between vertices of the long rectangular edge and a vertex of the inner core region. The apical Fe-N bond is longest of these at 2.1898 Å with the Fe-O bonds being 5-10% shorter. The Fe- μ_2 O bonds are 2.0001 Å and 1.9873 Å on the long and short rectangular edge, respectively, and the equatorial Fe- μ_3 O bonds are 1.9790 Å and 1.9613 Å when bonding towards the large and small hexagons, respectively. The apical Fe- μ_3 O is substantially larger than the other four at 2.0953 Å.

The Fe- μ_2 O-Fe bond angles are 102.574° and 134.757° along across the short and long rectangular edges, respectively. The remaining equatorial Fe- μ_3 O-Fe bond angles between the short hex-hex edges are much lower at 97.332° and 96.171°. The Fe- μ_3 O-Fe bond angle between the capping tetrahedral Fe and framework octahedral Fe is 125.292° and 131.801° for the distal and proximal tetrahedron,

respectively. The latter, therefore, is almost exactly planar with the three connecting iron atoms. This plane is also shared with the six equatorial oxygen atoms directly coordinated to the iron atoms located at the short hex-hex edge.

The inner core consists of 4 iron atoms arranged in an ideal tetrahedron with edges of length 3.4537 Å, and internal angles of 60.0°. However, the coordination environment of these atoms, and location of oxygen ligands is ambiguous from the crystallographic data. For each iron atom, the three distal $\mu_3\text{O}$ which are connected bonded to the outer framework make up part of the coordination environment. The strongest peaks correspond to oxygen positions which reside directly between the iron positions at a distance of 2.231 Å, and Fe-O-Fe angle of 101.750°. This creates an octahedral environment for each of the four iron centres, and so the core would be structured as a tetrahedron of octahedra (Figure 5.17, left). This arrangement can be seen in the core of an iron cluster (albeit half occupied) in the TMSP cluster $[\{\text{Fe}^{\text{II}}_{1.5}\text{Fe}^{\text{III}}_{12}(\mu_3\text{-OH})_{12}(\mu_4\text{-PO}_4)_4\}(\text{B-}\alpha\text{-PW}_9\text{O}_{34})_4]$ (Figure 5.18, top left). A similar cubane core is also seen in the cluster $[\text{Fe}_8\text{O}_4(\text{pz})_{12}\text{Cl}_4]$, (pz=pyrazolate), but few other true examples exist in the literature.¹⁹² A similar core with a tetrahedron of octahedra is seen the TMSP $[\text{H}_{45}\text{P}_8\text{W}_{48}\text{Fe}_{28}\text{O}_{248}]$ (Figure 5.22, top right), although the polyhedra here are corner, rather than edge sharing.

However, there also exists a crystallographic peak in the direct centre of the cluster. Assigning this as an oxygen requires that the previously described oxygen atoms should be removed in order to be chemically reasonable. This creates a tetrahedral environment for each of the core iron atoms, which together form a tetrahedron of tetrahedra. Interestingly this type of arrangement is seen in another TMSP structure $[\text{Fe}_{14}\text{O}_6(\text{OH})_{13}(\text{P}_2\text{W}_{15}\text{O}_{56})_4]$ (Figure 5.18 bottom), although again with some differences. In addition to being half occupied, each tetrahedra in this structure is rotated by 60°.¹⁴¹

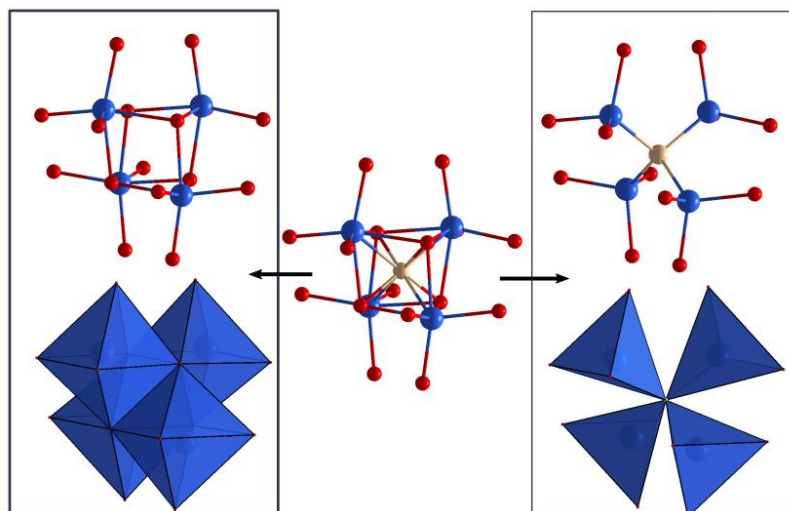


Figure 5.21 Potential crystallographic core structures for $\{\text{Fe}_{36}\}$: Left) edge sharing tetrahedron of octahedra with ball and stick (top) and polyhedral (bottom) representations. Middle) Crystallographic peaks which are observed after x-ray crystallography. Right) corner sharing tetrahedron of tetrahedra with ball and stick (top) and polyhedral representations (bottom).

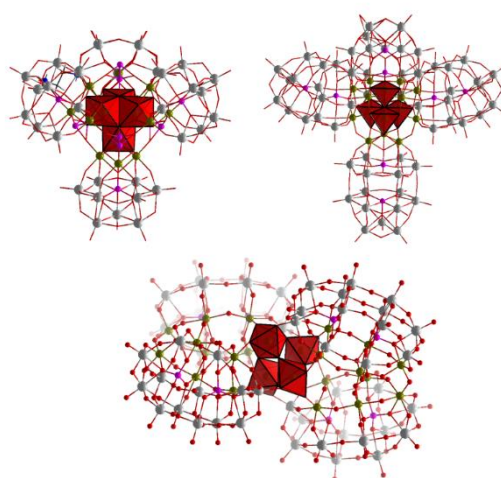


Figure 5.22 TMSP structure that exhibit Fe-O motif possibilities for the core of $\{\text{Fe}_{36}\}$. Top) partially occupied core of (left) edge sharing tetrahedron of octahedra in $[\{\text{Fe}^{\text{II}}_{1.5}\text{Fe}^{\text{III}}_{12}(\mu_3\text{-OH})_{12}(\mu_4\text{-PO}_4)_4\}(\text{B-}\alpha\text{-PW}_9\text{O}_{34})_4]$ and (right) corner sharing tetrahedron of tetrahedra in $[\text{H}_{45}\text{P}_8\text{W}_{48}\text{Fe}_{28}\text{O}_{248}]$. Bottom) Fully occupied corner sharing tetrahedron of octahedra found in $[\text{Fe}_{14}\text{O}_6(\text{OH})_{13}(\text{P}_2\text{W}_{15}\text{O}_{56})_4]$

Mass Spec studies

In order to try to identify the central structure of the $\{\text{Fe}_{36}\}$, ion mobility mass spectroscopy was used to compare the spectra of the 4-picoline (11) and 4-

ethylpyridine (**14**) clusters. Both compounds showed similar fragmentation patterns when using methanol as solvent (Figure 5.24, 5.25) The spectra of these are composed of two main regions separated by drift time and m/z : 1) a low m/z region across a wide envelope, ranging from around 1080 to 1300 m/z . Ions in this region have a charge of 3+, giving the total mass of the species to be in the range of 3000-3900 g/mol; and 2) a high m/z region across a wide envelope ranging from 1500-2050 m/z . Ions in this region have a charge of +2 giving the total mass of species in this region to be in the range of 3000-4100 g/mol. As such, the molecular ions for (**11**) and (**14**), with molecular weights of 5943.37 and 6279.61, respectively, were not observed. These features make the spectra obtained difficult to interpret. One possible explanation for this is that the aromatic ligands were replaced by solvent molecules when dissolved in methanol. Replacement of each ligand with methanol gives a molecular mass of 4476.73 g/mol, which is much closer to the upper limit of species observed in each envelope. The observable envelopes would then be due to successive loss of constituent atoms and groups down to a relatively stable cluster with a molecular weight of around 3500 g/mol. However, the identity of this structure is unknown. One possibility is a structure composed of only the core outer capping region and inner framework without any ligands (i.e. loss of the core cubane group). This would give a molecular formula of $[\text{Fe}_{32}\text{O}_{30}(\text{OH})_{26}\text{Br}_8]^{2+}$ weight of 3348.37, charge of +2 and m/z of 1674.2. Loss of a further hydroxyl group would then give a molecular weight of 3331.37, charge of +3 and m/z of 1110.46. Both of these values fit the observed peaks in both envelopes for each compound reasonably well. Larger peaks would then be explained by incomplete loss of ligand (solvent), while lower peaks can be explained by less stable structures arising from loss of Fe and Br. Evidence for this is that it explains the observation that the position of each envelope doesn't depend on ligand present, and that the spectrum of very low m/z shows a large peak that can be assigned to the ligand being used (shown in Figure 5.19)

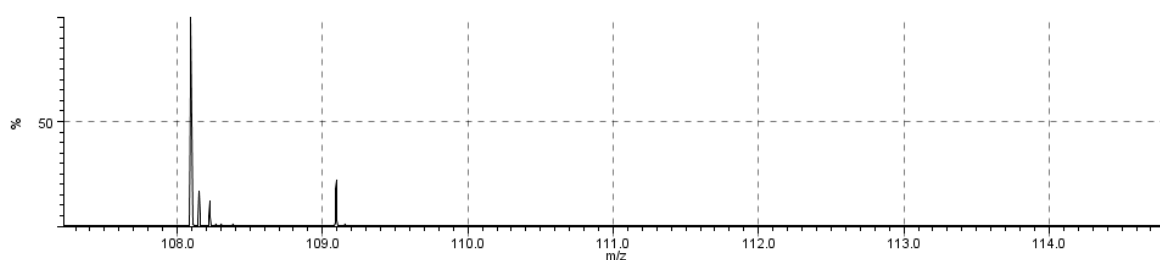


Figure 5.23. Mass spectrum of (**14**) at low m/z showing presence of 4-ethylpyridine

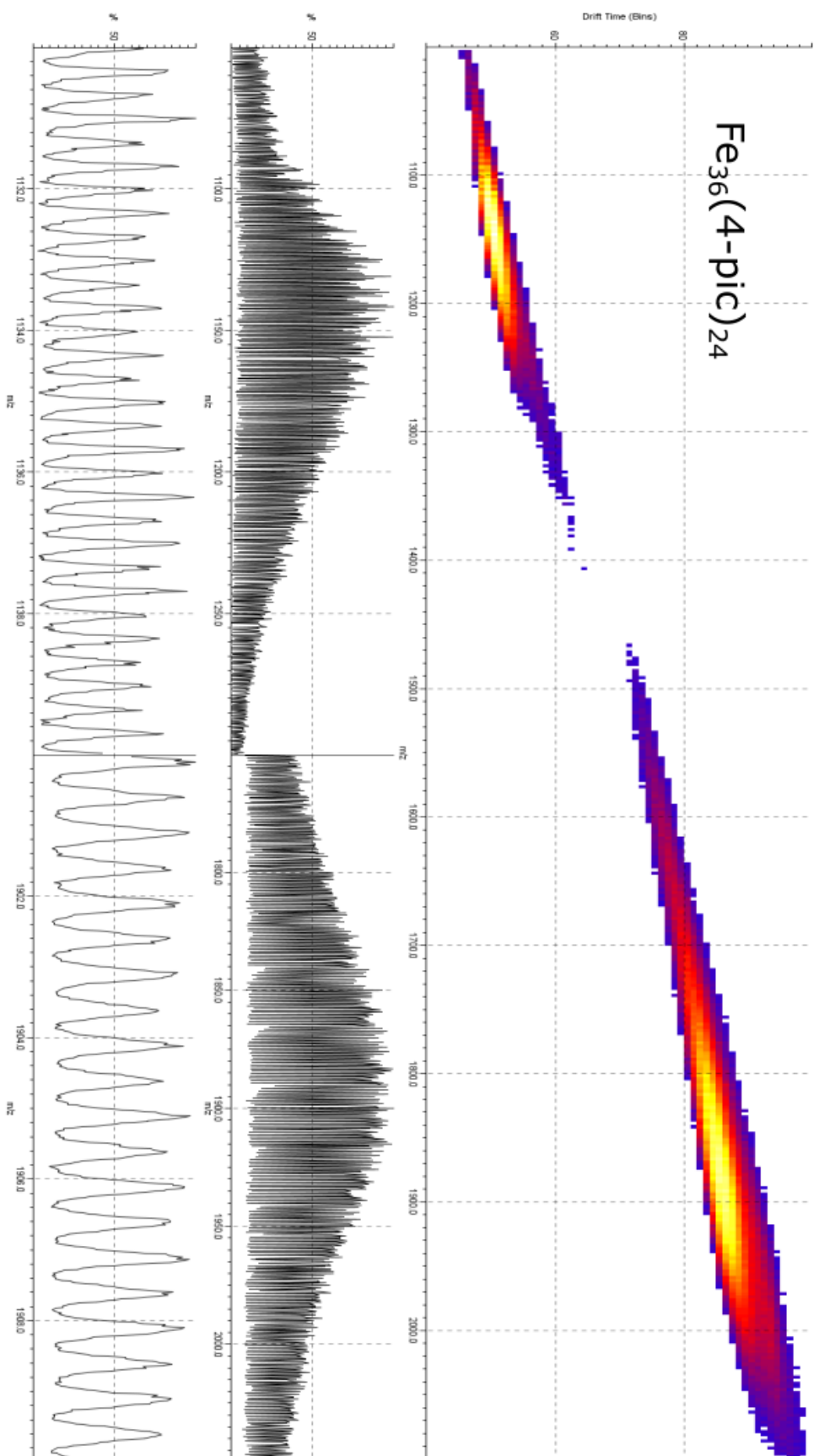


Figure 5.20 Ion mobility mass spectrum of $\text{Fe}_{36}(\text{4-pic})_{24}$. Top) plot of m/z vs drift time showing two distinct regions centred around 1140 and 1890. Middle) Envelope shapes for the lower (left) and higher (right) m/z regions. Bottom) Shape of peaks within an envelope for the lower (left) and higher (right) m/z regions.

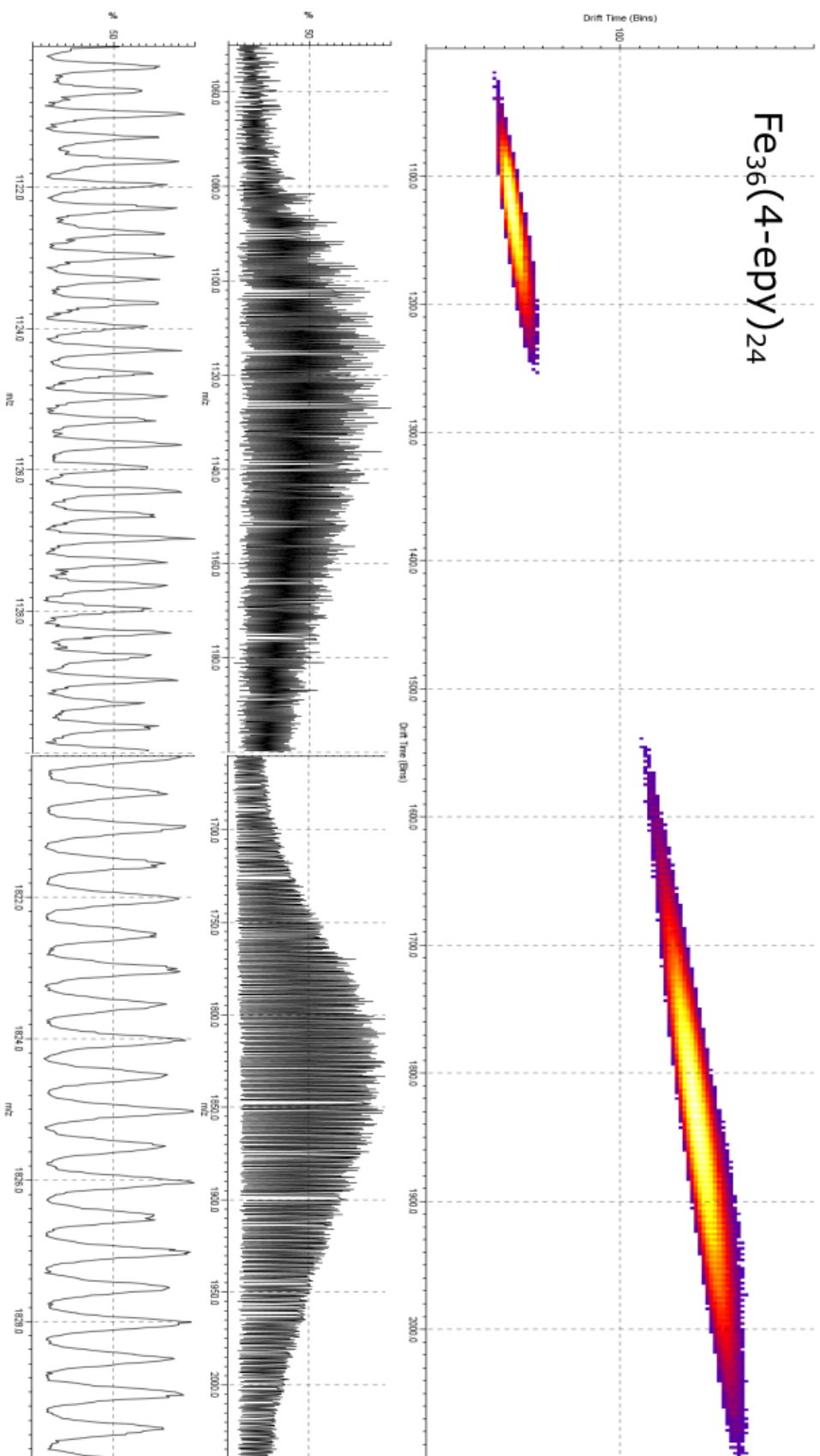


Figure 5.21 Ion mobility mass spectrum of $\text{Fe}_{36}(4\text{-epy})_{24}$. Top) plot of m/z vs drift time showing two distinct regions centred around 1130 and 1840. Middle) Envelope shapes for the lower (left) and higher (right) m/z regions. Bottom) Shape of peaks within an envelope for the lower (left) and higher (right) m/z regions.

Inspection of the structure of $\{\text{Fe}_{36}\}$ also shows similarities with haematite, as shown in Figure 5.26, where a hexameric ring similar to that on the outer framework of $\{\text{Fe}_{36}\}$ can be seen in the crystal structure of haematite. This indicates that by changing the ligand, a growth pathway can be redirected from one akin to that of magnetite to that of haematite.

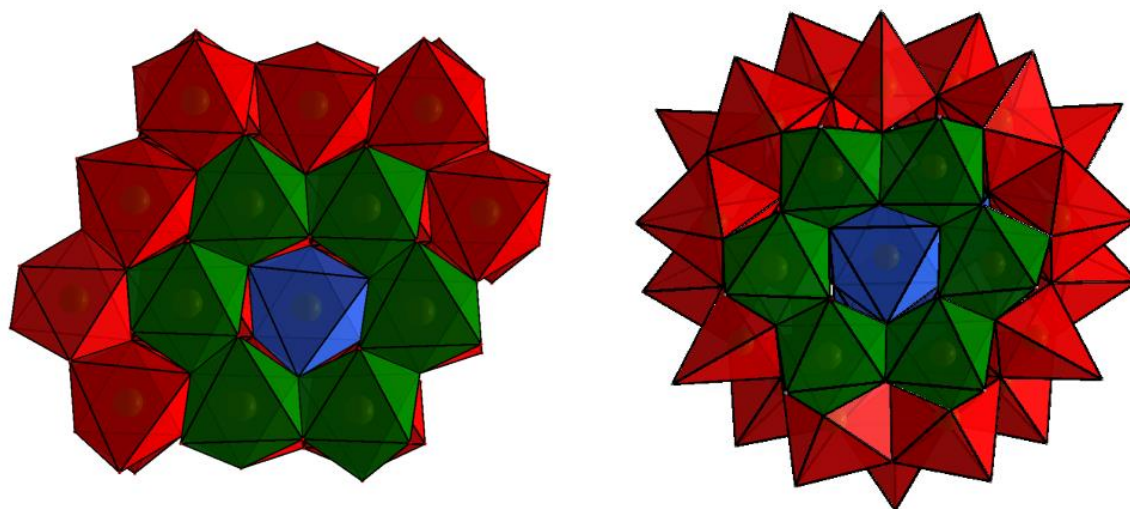


Figure 5.26. Polyhedral representations of: Left) crystal structure of haematite (Fe_2O_3), where the hexagonal Fe-O ring is composed of green polyhedra, a central, lower Fe-O polyhedron is highlighted in blue, and the ‘bulk’ Fe polyhedra are shown in red. Right) structure of $\{\text{Fe}_{36}\}$ with one capping Fe-Br tetrahedron removed to reveal a lower Fe-O polyhedron (highlighted in blue), a hexagonal Fe-O ring highlighted in green polyhedra and the ‘bulk’ Fe polyhedra shown in red.

5.3.4 Templated iron cluster synthesis

Another approach to generate large iron-oxo compounds was to incorporate small inorganic groups, which could act as templates around which new clusters could form. This approach was chosen since it is found ubiquitously in POMs made from elements such as tungsten and molybdenum where anionic template formed by hetero atoms such as phosphorus, tellurium and manganese are hugely important in the structural diversity of heteropolyoxometalates. Analogously to HPOMs, because structures such as $\{\text{Fe}_{17}\}$, $\{\text{Fe}_{13}\}$ and those described in section 5.3.4 contain templating tetrahedra and octahedra in their cores, it was hypothesised that addition of a group anion such as phosphate may also act as a template to iron cluster formation. As such as range of other metal salts were incorporated into the synthetic procedure of $\{\text{Fe}_{17}\}$, including MoCl_5 , P_2O_7 , several first row transition metal (Mn, Cr, Cu, Co) chlorides and bromides, periodic acid, selenic

acid and telluric acid. The search strategy involved adding between 0.1 to 2 equivalents of the heteroatom and modifying the pH with hmta between 4.3 and 5.5. The volume of pyridine, acetonitrile and mass of FeBr_3 were not varied in these experiments.

Unfortunately, templating of iron compounds was not achieved using this strategy and no new iron based compounds were discovered. However, this did allow the discovery of a new molybdenum oxo compound, $\{\text{Mo}_{10}\} [\text{Mo}_{10}\text{O}_{27}(\text{3,4-lut})_7]$ (**15**) which is shown in Figure 5.29. The compound exists as a 6 member Anderson-like ring made of four $\text{MoO}_5(\text{3,4-lut})$ octahedra and two MoO_6 octahedra. but instead of having a central hetero group, the centre of the ring is empty. Two further $\text{MoO}_5(\text{3,4-lut})$ octahedra lie directly above and below the ring's cavity, bound by sharing of three of the ring's bridging oxide anions. Two further molybdenum octahedra are bound between the MoO_6 octahedra and one of the out of plane octahedra on each side of the ring. Interestingly, one of these is a purely MoO_6 octahedron while the other is a $\text{MoO}_5(\text{3,4-lut})$ octahedron. In addition, BVS shows that the molybdenum atoms in the compound exist in either +5 or +6 state, and this gives results in an overall neutral compound.

The compound arises through a series of transformation beginning with the replacement of chloro ligands of MoCl_5 before dimerization into $\text{Mo}_2\text{O}_4^{2+}$ groups with a single metal-metal bond and combination of these into a ring and the final compound. In the final structure contains eight of the ten Mo centres are involved in Mo dimers with Mo-Mo bond distances of around 2.56 Å. The distance between non-dimer edge sharing adjacent Mo atoms is much longer at around 3.45 Å.

This compound is similar to a small group of compounds described in the literature, with general formula $[\text{Mo}_{10}\text{O}_{26}(\text{lig})_8]$ (lig = 3,5-lutidine, 3-picoline, 4-isopropylpyridine).^{193,194} However, whereas these compounds all contain an inversion centre, the different types of octahedra in the face-sharing positions results in the loss of this and a reduction in symmetry to C_1 .

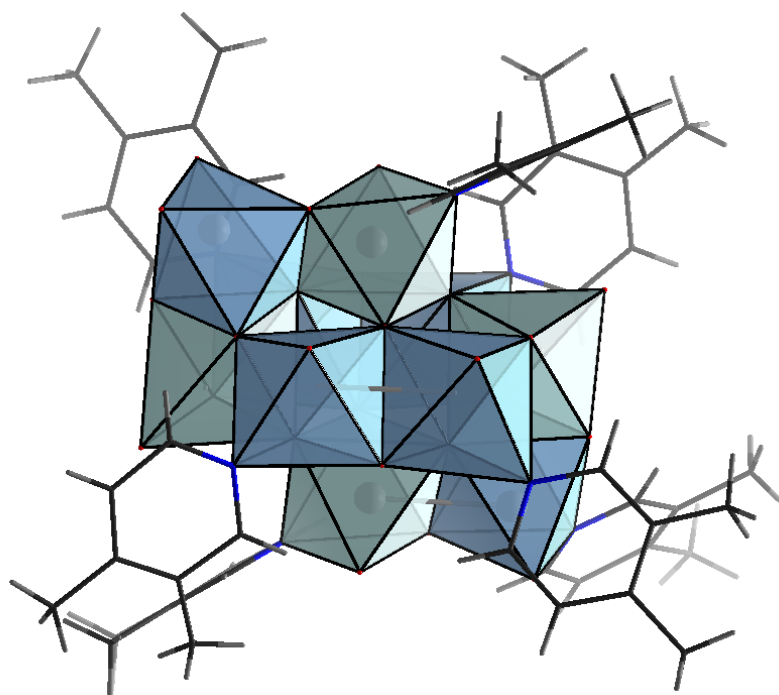


Figure 5.29 Polyhedral representation of $[\text{Mo}_{10}\text{O}_{27}(\text{3,4-lut})_7]$. Darker polyhedra represent Mo^{VI} , whereas lighter ones represent.

5.3.5 Diazo compounds

As it had been observed that by changing the number and type of alkyl chains to the pyridine ring a large number of new compounds and compound types could be synthesised, a natural step was to investigate the effect of adding different functionality to the pyridine ring. One approach was to use a range of di-azo compounds under the same conditions.

5.3.5.1 Pyrimidine

The replacement of pyridine with pyrimidine using the same reaction schemes gave two new compounds. One of these, as described in section 5.3.3.1 was Fe_{34} which was anticipated based on previous reactions. However, in the same reaction, a second type of compound formed which was revealed by x-ray analysis to be a type of metal organic framework material based on octahedra $\text{FeBr}_2(\text{pmd})_4$ (**16**) units (Figure 5.30, left) and crystallised in the $I4$ space group. Here, the Fe-Br bonds are both 2.5788 Å and the Fe-N bonds are around 2.253 Å. This results in a calculated oxidation state of the iron centre of +2. Each pmd unit forms a bridge

between neighbouring iron centres and forming 6 member closed rings (Figure 5.26, middle). Each iron centre is separated from neighbouring iron centres by around 6.3210 Å. The ring itself adopts a distorted ‘chair’ conformation, with the distorted axis running parallel with the longer c axis of the unit cell (Figure 5.22, right).

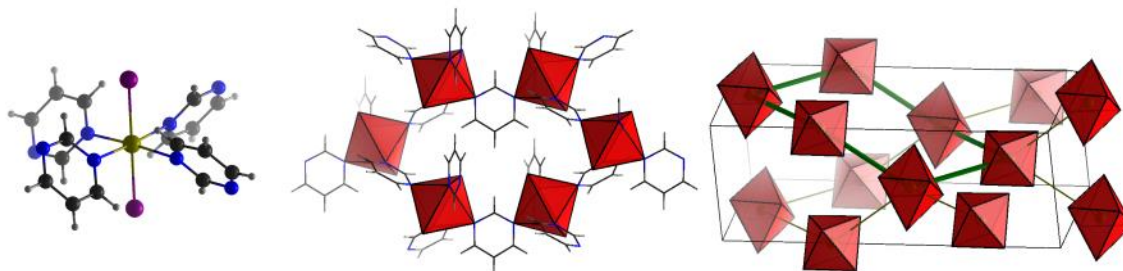


Figure 5.30 Left) Monomer unit of $\{\text{FeBr}_2(\text{pmd})_4\}$, middle) Ring formation formed by 6 monomer units, right) 3D structure arrangements of interlocking 6 unit rings in the crystal structure.

5.3.5.2 Phthalazine

The rationale behind the use of phthalazine was also to try to produce a large Fe-oxo aggregate, but with a double aromatic ring system. Although, no such compound was obtained, a novel iron triangle compound, $[\text{Fe}_4\text{O}(\text{OH})(\text{phth})_6\text{Br}_5]^{2+}$ (**17**) was produced, and is shown in Figure 5.31. This iron triangle is unusual in that the outer bridging atoms are purely nitrogen bridged. Only a few examples of this exist in the literature, and only one other di-chelating ligand (4-nitropyrazolate)¹⁹⁵ has been seen to stabilise this structure. Secondly, while two of the three terminal groups on the iron octahedra are bromide atoms, the third is a FeBr_3O tetrahedron, linked by the O group.

As with other compounds of this type, the Fe_3O groups are in the same plane, with the phthalazine 6 ligands all at an angle of approximately 45° with respect to this plane and Fe-Fe distances of 3.233 Å. The Fe-N bonds are all around 2.22 Å, whereas the Fe- $\mu_3\text{O}$ bonds range between 1.8 and 1.9 Å and the N-N bonds are around 1.36 Å, which is consistent with the literature for this type of compound.¹⁹⁶ The terminal Fe-Br bonds in the triangle plane are all 2.50 Å, while the Fe-Br bonds in the terminal Fe-tetrahedron are shorter at around 2.39 Å. The Fe-O-Fe

bond between the triangle and terminal group is slightly bent at 173° with the O atom positioned slightly closer to the Fe tetrahedron (1.848 \AA vs 1.727 \AA).

The crystal structure of this compound packs in $P2_1/n$ and also contains two $[\text{Fe}_2\text{OBr}_6]^{2-}$ counter anions and five acetonitrile solvent molecules per $\{\text{Fe}_4\}$ molecule. Within the unit cell, the planes of the triangles are arranged perpendicularly to each other, with a gap of 5.8126 \AA between the tetrahedral iron atom and the plane of the neighbouring triangle.

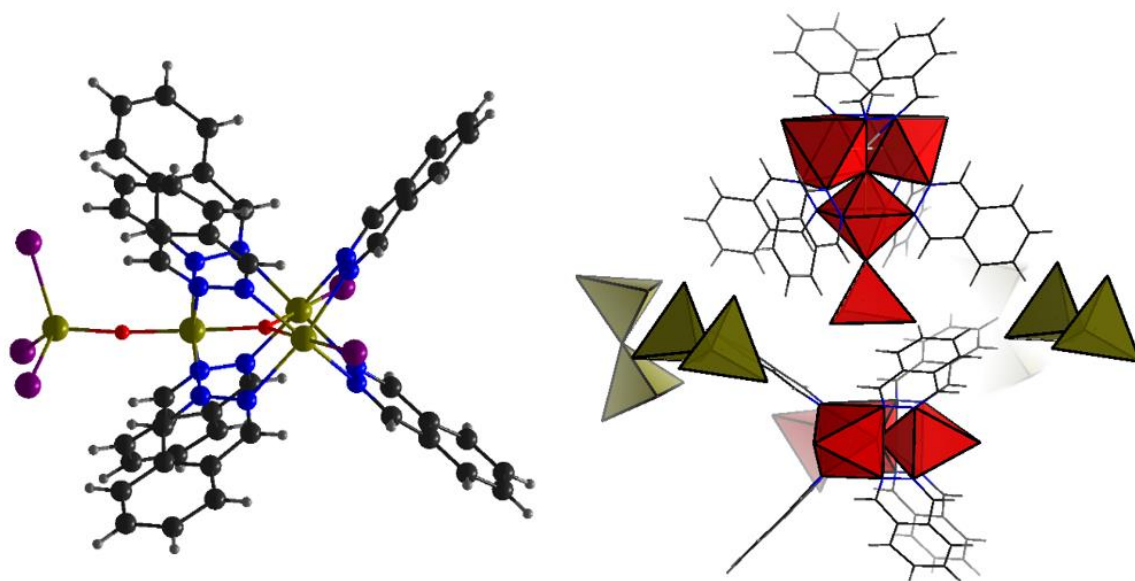


Figure 5.31 Left) ball and stick representation of $[\text{Fe}_3\text{O}(\text{phth})_6(\text{FeBr}_3\text{O})\text{Br}_2]$. Right) Polyhedral representation of the crystal packing structure of $[\text{Fe}_3\text{O}(\text{phth})_6(\text{FeBr}_3\text{O})\text{Br}_2]$

5.3.6 Alcohol-pyridines

Another way of modifying the pyridine ring is by adding second chelation site outside of the main ring. As such, the effect of adding alcohol groups to the ring was investigated.

5.3.6.1 2-pyridinemethanol

The reaction of 2-pyridinemethanol with iron bromide in acetonitrile allowed the formation of a neutral oxo-bridged iron cluster: $\{\text{Fe}_8\}$ ($[\text{Fe}_8\text{O}_4(2\text{-pym})_8\text{Br}_8]$ (**18**), Figure 5.32). Initially this was performed on the automated platform, and later replicated on the bench.

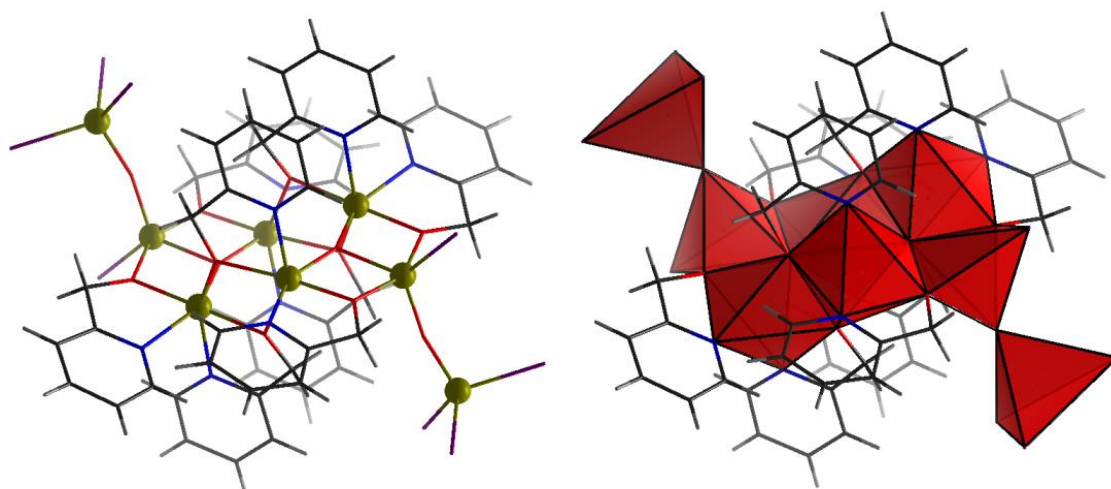


Figure 5.32 Left) Ball and stick representation of $\{\text{Fe}_8\}$. Right) Polyhedral representation of $\{\text{Fe}_8\}$. (Colour scheme: iron atoms= gold, iron polyhedra= red, oxygen = red, bromide=purple, carbon=black, nitrogen=blue, hydrogen=grey)

This compound is formed by two distorted $\{\text{Fe}_3\text{O}\}$ triangles, which are linked via an alkoxide bond resulting from the coordination of pyridine methanol to two of the three iron atoms in each triangle. The triangles themselves are joined by two bridging alkoxide which originate from the same pyridine methanol ligands as the prior two. The third bridging oxygen atom exists as an oxide and likely arises from a water impurity in the solvent used. The iron atom outside the ring of the triangle is attached by a hydroxyl bridge and forms a tetrahedron with three bromide ions (Figure 5.33). This is an unusual example of an iron compound which contains three different coordination geometries, although others have been recognised in the literature.¹⁹⁷

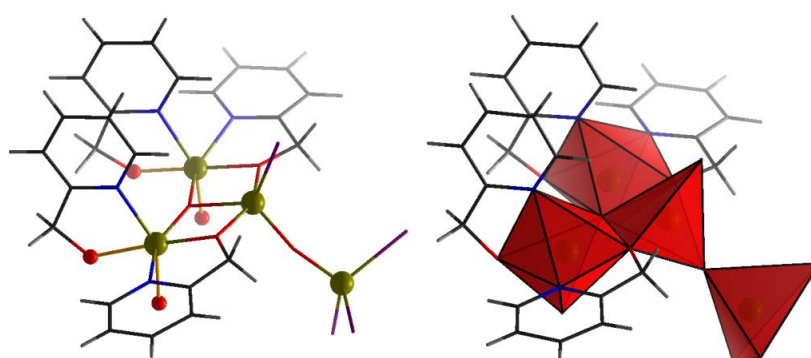


Figure 5.33 Left) Ball and stick representation of the one half of $\{\text{Fe}_8\}$. Bridging oxygen atoms between the two halves of the molecules are shown as balls, whereas those entirely within one half are shown as sticks. (Colour scheme: iron atoms= gold, iron polyhedra= red, oxygen = red, bromide=purple, carbon=black, nitrogen=blue, hydrogen=grey)

Within the ring, the iron atoms bound to two pyridine methanol ligands exhibit an octahedral coordination environment, while the outer iron atom exhibits a tetrahedral environment. The final iron atom, which has 5 ligands attached, exhibits a distorted trigonal bipyramidal coordination geometry (Figure 5.34).

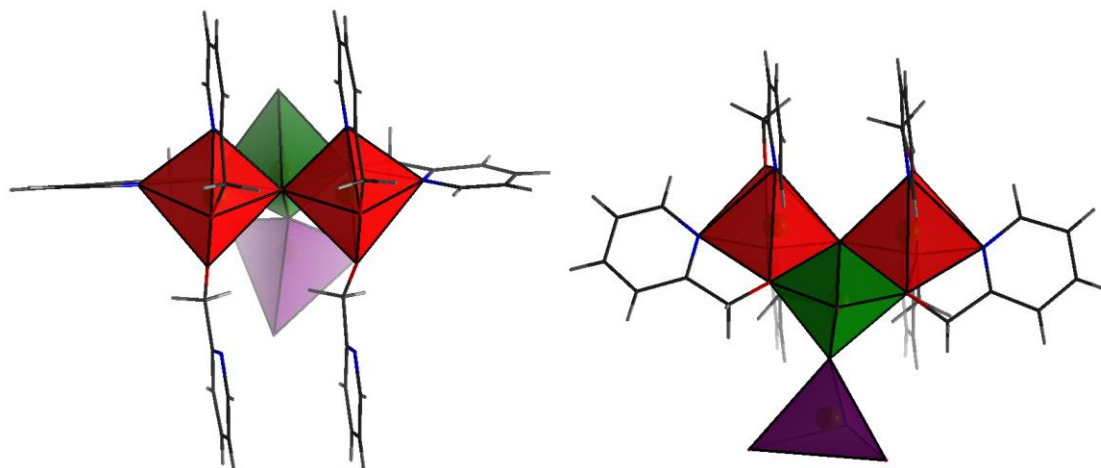


Figure 5.34 Polyhedral representations of the $\{\text{Fe}_4\}$ half unit, which has been colour coded based on coordination geometry. (Colour scheme: Fe octahedra= red, Fe trigonal bipyramids = green, Fe tetrahedra= purple)

5.3.6.2 Chiral $\{\text{Fe}_{17}\}$ using 2-pyridineethanol

The use of 2-pyridineethanol resulted in the largest of the compounds found using functionalised pyridine ligands. The compound, $[\text{Fe}_{17}\text{O}_{16}\text{Br}_4(2\text{-pye})_{12}]^{3+}$ (**19**) (Figure 5.35), is structurally analogous to Fe_{17} mentioned in section 5.3.1, but with the considerable difference that all of the outer -OH- bridges are replaced with the methoxy group from the 2pye ligand. Initially this was performed on the automated platform, and later replicated on the bench. This creates a 6-member ring between the ligand and iron of the outer iron framework, and this reduces the symmetry of the molecule is from T_d to T. This compound is therefore chiral and the crystal structure contains a racemic mixture of both enantiomers.

The enantiomers can be distinguished when looking down one of the C_3 axes. From this direction, one of the four Fe triads can be observed. The ring made by the ligand and iron atom proceeds from the nitrogen of the aromatic ring to the oxygen of the methoxy group. It can be seen that around one of the C_3 axes, each N-C-C-O chain of the three ligands curve in the same direction: either clockwise or

anticlockwise. However, inspection of each of the C_3 axes on one molecule shows that this rotation direction is identical for each axis, i.e. if there is clockwise rotation on one axis, the other three will also rotate clockwise, and likewise in the case of anticlockwise rotation.

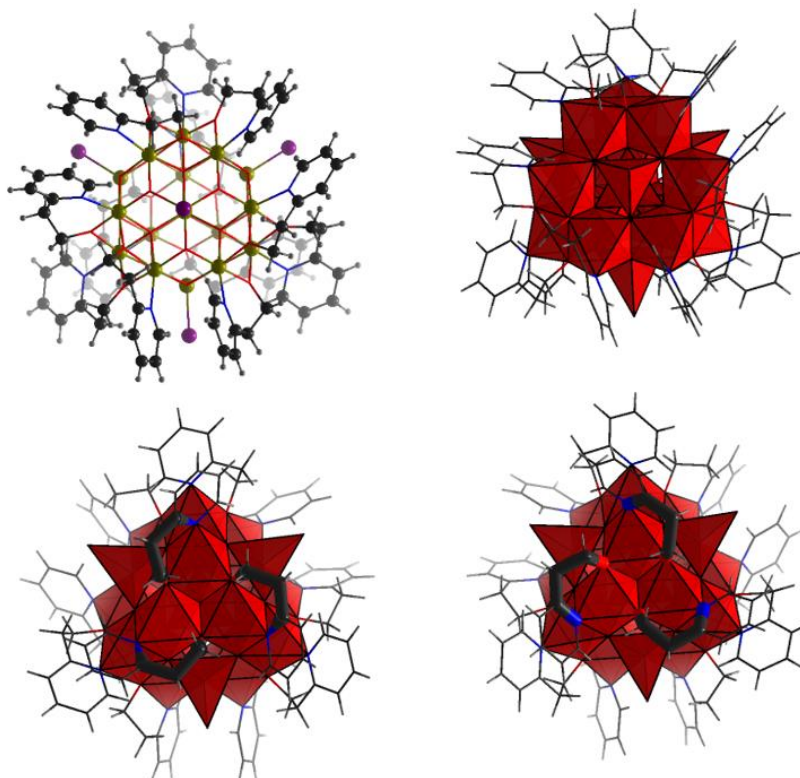


Figure 5.35 Top left) Ball and stick representation of $\{Fe_{17}^*\}$, top right, polyhedral representation of $\{Fe_{17}^*\}$. Bottom left) Enantiomer of $\{Fe_{17}^*\}$ formed by clockwise O->N ring formation around each C_3 rotation axis. Bottom right) Enantiomer of $\{Fe_{17}^*\}$ formed by anticlockwise O->N rotation around each C_3 rotation axis.

5.3.7 Reducing Agents

Because ascorbic acid had been successful in producing new compounds previously, it was used in pyridine based systems which had been diluted in different solvents. It was found that in acetonitrile adding small quantities of ascorbic acid in a diluted reaction resulted only in the original published Fe_{17} . Adding more ascorbic resulted in reduced iron monomers coordinated by pyridine and bromine. However, more interesting compounds were synthesised by changing the solvent or by adding an intermediate amount of ascorbic acid.

5.3.7.1 Chains

By replacing acetonitrile with dichloromethane as solvent and adding ascorbic acid to the reaction between iron bromide and pyridine, the linear chain compound $\sim[\text{Fe}_2(\text{py})_2\text{Br}_2(\text{ox})\text{O}]$ (**20**) (ox=oxalate) is obtained, and shown in Figure 5.36. In this compound, each iron is in an octahedral environment created by two pyridine ligands trans to each other, a di-chelating oxalate compound, and a corner sharing oxide anion. The oxalate anion is created *in situ* by degradation of ascorbic acid. The pathway for this likely proceeds through oxidation of the ascorbate ion, hydrolysis to 2,3-diketogulonic acid and further hydrolysis to oxalic acid.

In each of the iron centred octahedral environments, the Fe-Br bond distances are 2.498 Å and the Fe-N distances are 2.1893 Å and 2.1948 Å. The Fe-O bond distance of the oxide bridge is 1.7824 Å, and the Fe-O-Fe bond angle is slightly bent from linear at 176.86°. There are two Fe-Fe distances based on whether they are separated by the oxo or oxalate bridge, and these are 3.5635 Å and 5.5199 Å, respectively. Finally, the Fe-Fe chain is not totally linear, but instead the iron atoms lie either side of the axis and form an angle of 132.40° in the chain.

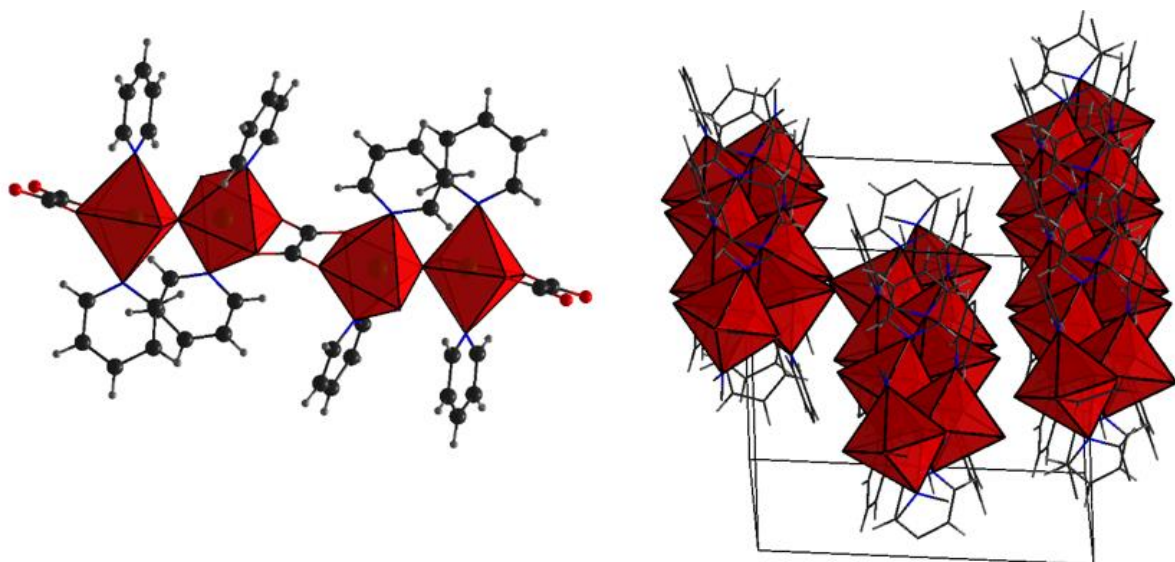


Figure 5.36 Left) polyhedra representation of the repeating unit of the $\{\text{Fe}_2\}$ chain molecule. Right) Polyhedral representation of the $\{\text{Fe}_2\}$ chains within the unit cell.

A separate approach was also taken to create a large Fe_{17} -like cluster by replacing the bridging O^{2-} atoms with S^{2-} . This was done by saturating dry pyridine and dry acetonitrile with H_2S and repeating the experimental conditions. The result of this failed to produce any such large cluster, however, a second iron based chain

molecule, n -[Fe(py)₄(SO₄)] (**21**) was formed, linked by SO₄ groups, as shown in figure 5.37.

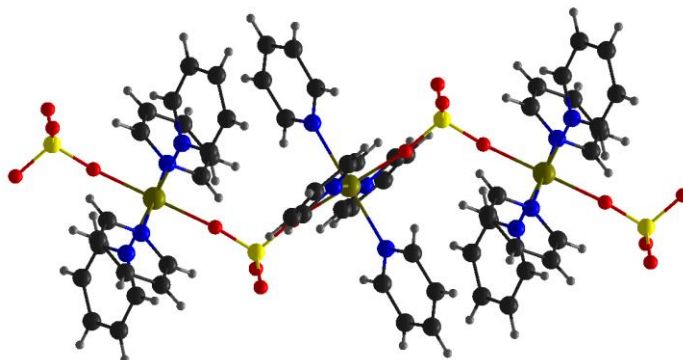


Figure 5.37 Ball and stick representation of n -[Fe(py)₄(SO₄)] chain.

5.3.7.2 Ferric ring molecule: {Fe₁₆}

When performing the reaction in acetonitrile and varying the amount of ascorbic acid used, the compound {Fe₁₆} ([Fe₁₆O₈(ox)₁₆Br₄(py)₁₂]⁴⁻ (**22**), (Figure 5.38) formed and crystallised. Initially this was performed on the automated platform, and later replicated on the bench. This compound is a double stranded ring molecule whose framework is composed of 16 iron centred octahedra which are bridged by oxide ions and oxalate anions, to form a two layered 8-member ring. Bridges between layers consist solely of the oxalate group, whereas each individual layer contains both oxide and oxalate anions.

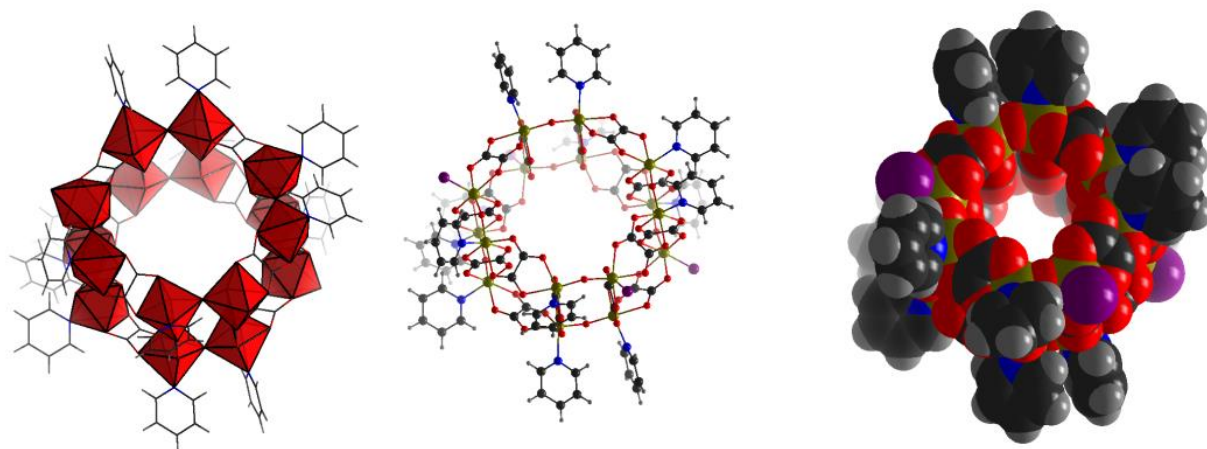


Figure 5.38 Left to right) polyhedral, ball and stick, and space filling representations of {Fe₁₆}

Four different iron coordination environments are present, which form two pairs of mirror related geometries. One pair is formed by one oxide anion at a Fe-O distance of 1.791 Å, a bromide anion at a Fe-Br distance of 2.452 Å and two oxalate anions whose mutually trans O atoms are closer to the iron centre at 2.082 Å and 2.062 Å than those trans to the oxide and bromide at 2.182 Å and 2.144 Å, respectively. The other pair contains a pyridine group in place of the bromide whose Fe-N distance is 2.149 Å, but otherwise contains identical groups, with very similar bond distances. Individuals in each pair are related by being enantiomers, existing in either Δ or Λ configurations as shown in Figure (5.39).

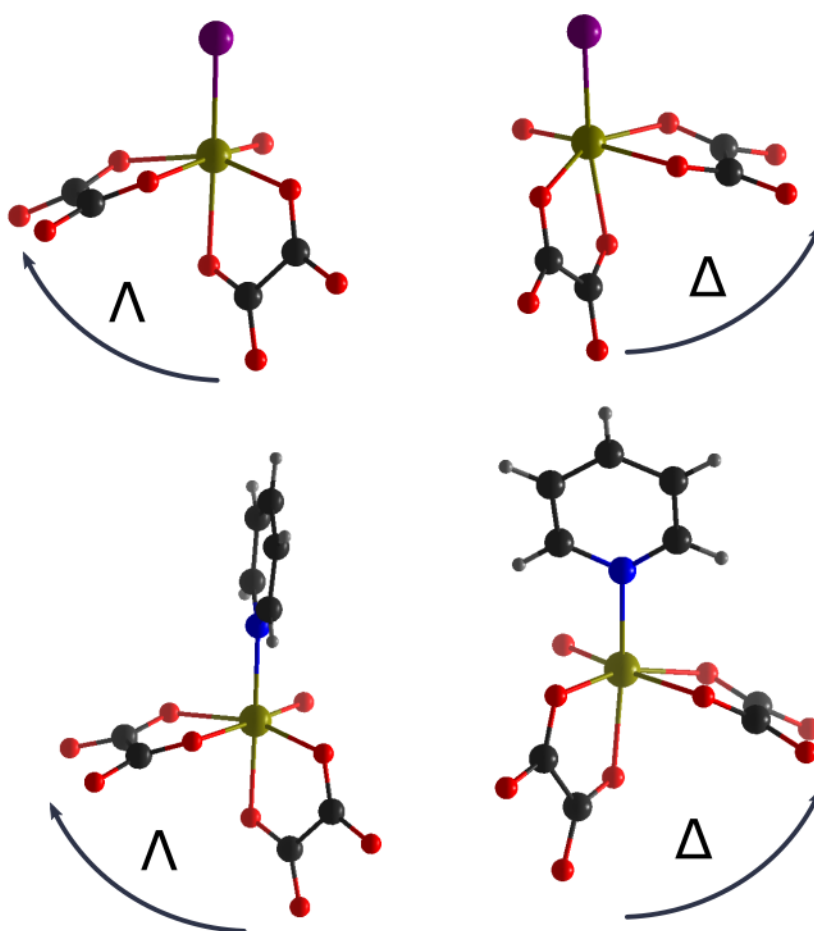


Figure 5.39 Ball and stick representation of the four types of building unit present in $\{\text{Fe}_{16}\}$

A single strand of the ring is composed of three Λ -py octahedra, three Δ -py octahedra, one Λ -Br octahedron and one Δ -Br octahedron. The eight-unit sequence consists of a run of four sequential py octahedra, followed by a Br capped octahedra, two more py octahedra and finally one more Br capped

octahedron. The bonds joining individual octahedra within one ring layer alternate between oxide and oxalate and this has the consequence that Λ and Δ configurations also alternate (Figure 5.40, top). The two strands in the ring both contain this sequence, but rotated upside down and shifted a half cycle with respect to each other (Figure 5.40, bottom). This results in the cluster showing a C_{2h} point group, with the C_2 axis perpendicular to the plane comprised by iso-steriochemically arranged Br capped octahedra.

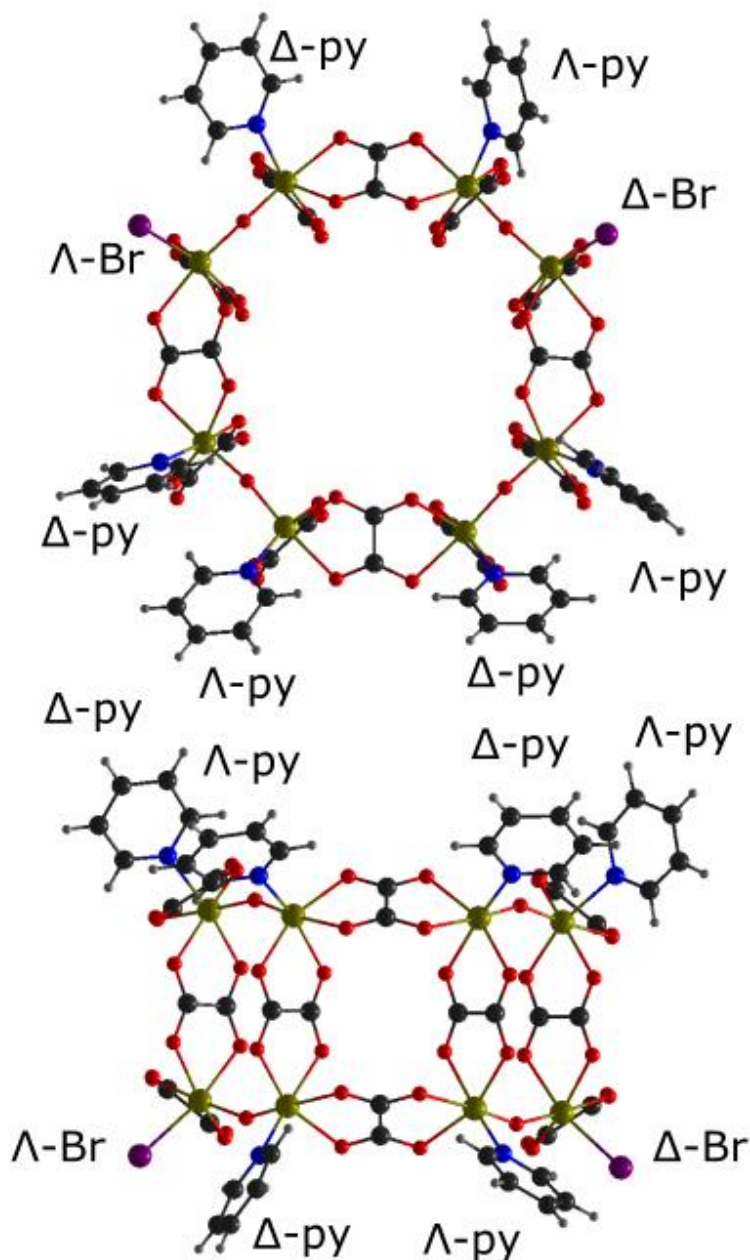


Figure 5.40 Arrangement of the four building units in $\{\text{Fe}_{16}\}$. Top) shown from an angle perpendicular to the plane of the ring. Bottom) shown from an angle parallel with to the plane of the ring.

The eight irons in one strand all lie in the same plane and form a distorted octagon (Figure 5.41), with internal angles between 131.1° and 137.5° . The iron centres are separated by between 3.4610 \AA and 3.4793 \AA by oxo-bridges to form a short edge, and by between 5.3166 \AA and 5.4031 \AA by oxalate-bridges to form long edges. The inter strand Fe-Fe distances, which are all oxalate bridged, are slightly longer than the intra strand Fe-Fe distances and lie between 5.4551 \AA and 4.750 \AA .

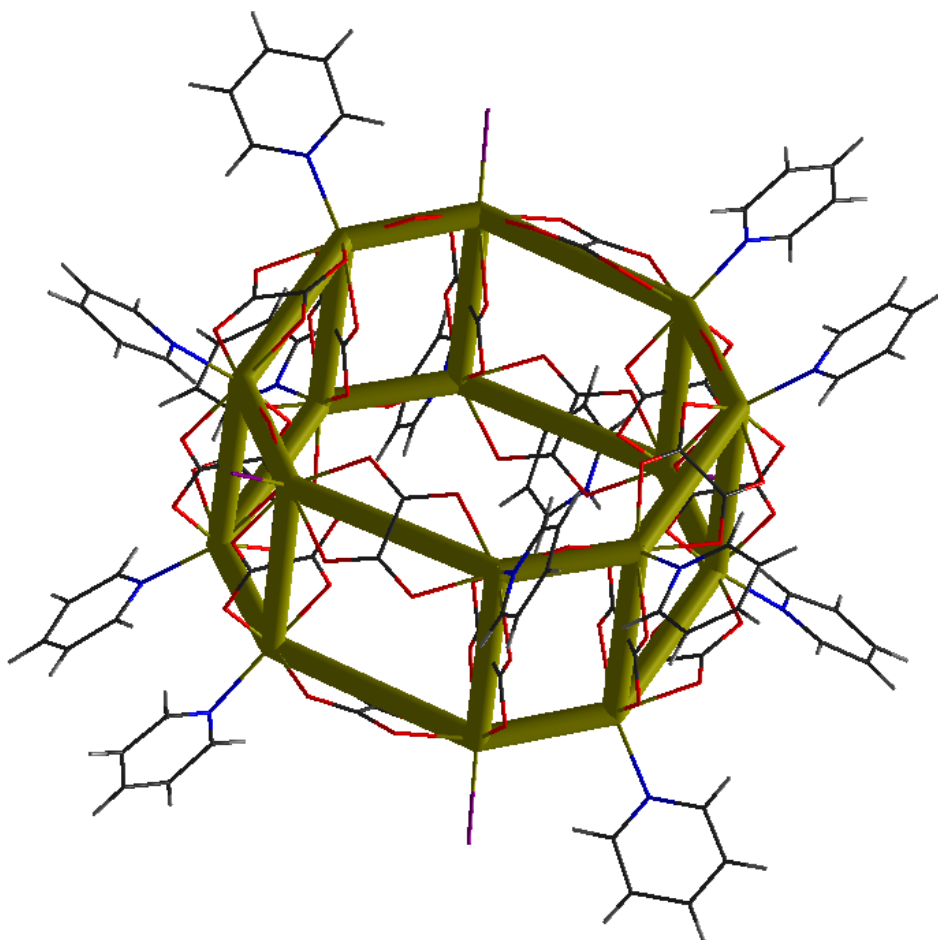


Figure 5.41 Wireframe representation of $\{\text{Fe}_{16}\}$, with the distorted octagonal geometry created by the Fe centres being shown in gold.

Attempts to replace this molecule with replacement of the pyridine with other aromatic bases such as picolines and lutidines were attempted, but no structures could be obtained.

Magnetic Data

Preliminary magnetic susceptibility and low field magnetisation curves were obtained for $\{\text{Fe}_{16}\}$ and are shown below. These indicate the presence of

antiferromagnetic exchange interactions between the Fe centres, however, a complete understanding of these data is currently pending.

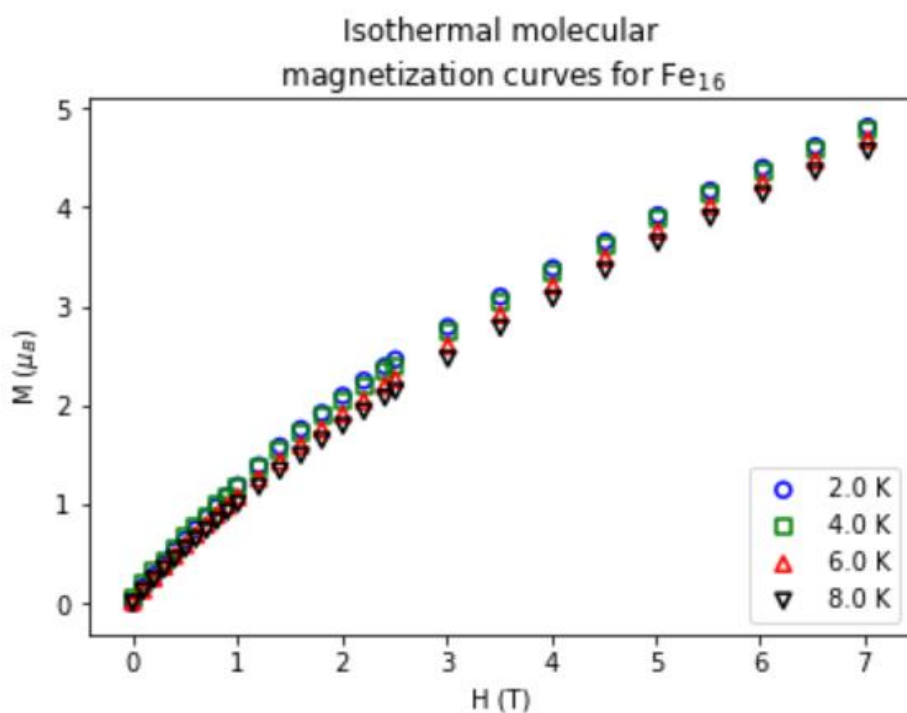


Figure 42. Magnetic susceptibility curves for {Fe₁₆}.

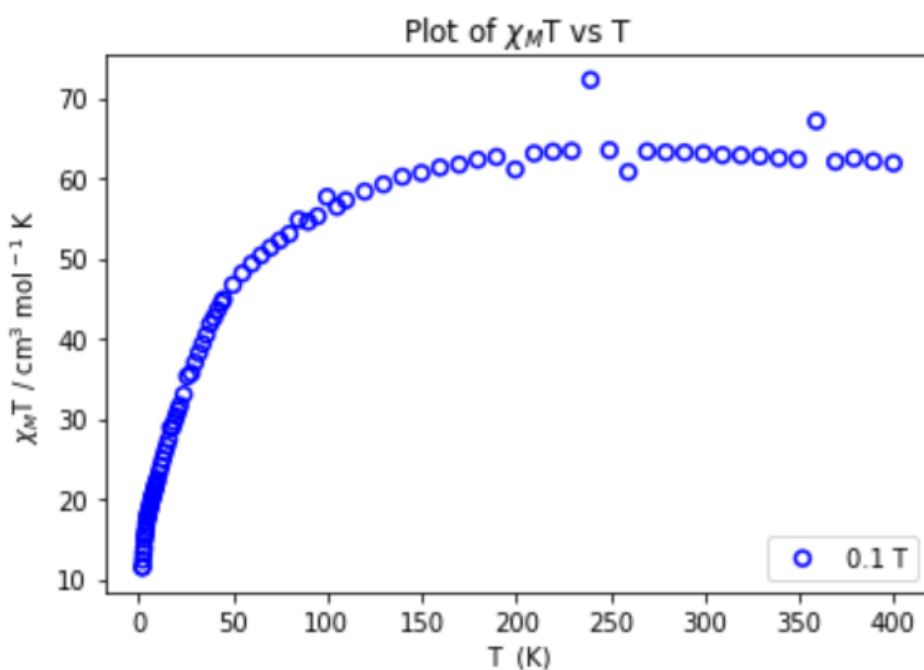


Figure 43. Low-field magnetisation curves for {Fe₃₄}

5.4 Conclusions and Future work

It was seen that cluster discovery by both robotic automation and manual bench synthesis were relatively successful in the discovery of new large iron compounds, although both techniques were seen to have benefits and issues. While it was difficult to build upon the $\{\text{Fe}_{13}\}$ Keggin in water, (producing only an $\{\text{Fe}_1\text{Pb}_3\}$ cluster) discovery of large iron compounds in organic solvents, particularly acetonitrile was very successful. Of key importance in this system was the use of pyridine based molecules to act as ligands and base. These parameters allowed the discovery of the largest iron-oxo aggregates known: $\{\text{Fe}_{30}\}$, $\{\text{Fe}_{34}\}$ and $\{\text{Fe}_{36}\}$, which may have interesting magnetic and electrochemical properties. A summary of each of the iron aggregate frameworks, including $\{\text{Fe}_{17}\}$ is shown in figure 5.33

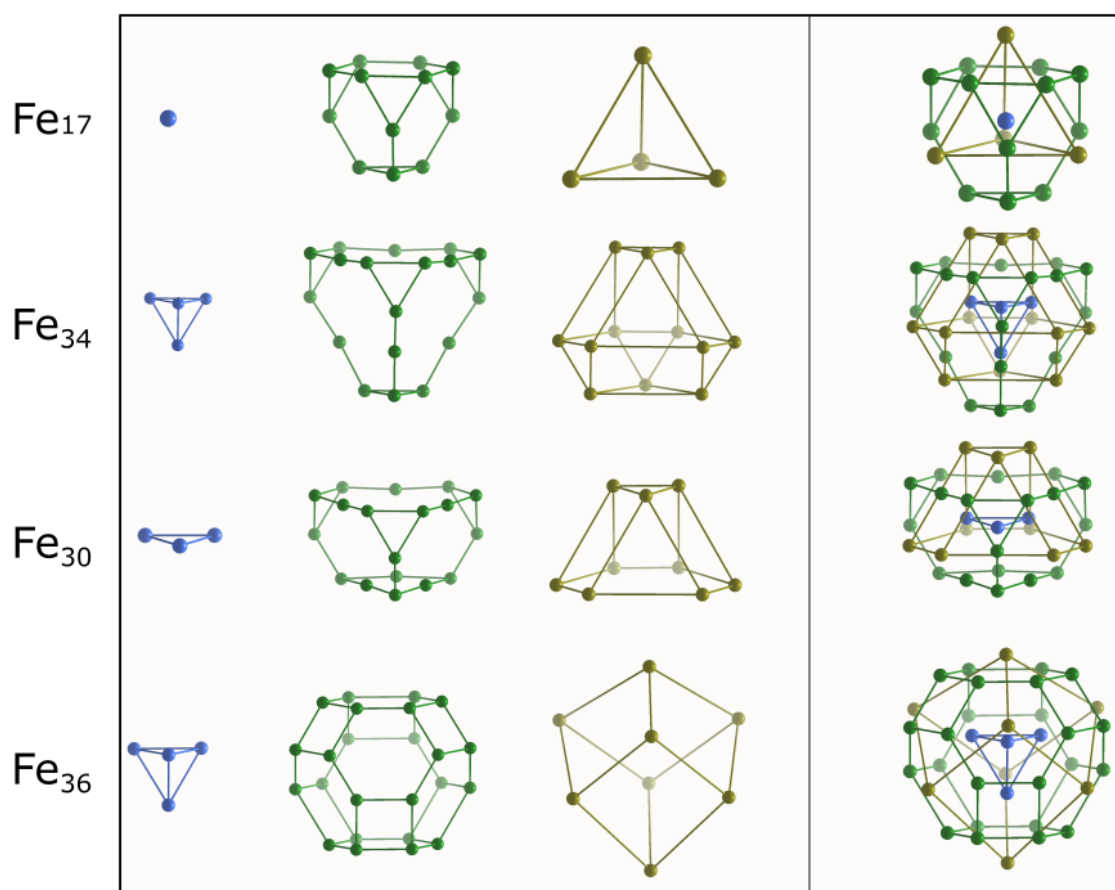


Figure 5.33 Summary of each of the iron aggregate frameworks. Top) $\{\text{Fe}_{17}\}$. Upper Middle) $\{\text{Fe}_{34}\}$. Lower Middle) $\{\text{Fe}_{30}\}$. Bottom) $\{\text{Fe}_{36}\}$

Further, by modifying the functionality of the pyridine ring, to include an alkoxy group, two new compounds $\{\text{Fe}_8\}$ and $\{\text{Fe}_{17}^*\}$ were discovered. Reducing agents

were also seen to cause structural changes in this system, as ascorbic acid was able to decompose into oxalic acid allowing the formation of another iron cluster, $\{\text{Fe}_{16}\}$. The latter three compounds were all discovered using an automated platform, showing the utility of this method. Initially $\{\text{Fe}_{30}\}$, $\{\text{Fe}_{34}\}$ and $\{\text{Fe}_{36}\}$ could not be replicated on the platform due to the inability to find a suitable replacement base for htma, and this greatly hindered efforts to search this system in an automated fashion. Eventually, it was discovered that morpholine could fulfil this role and was successful in allowing the formation of each of these compounds. However, this discovery came too late to allow any search to be done on the automated system. Future work will involve finding conditions continued exploration of aromatic nitrogenous bases as ligands in this system, as this was seen to be able to control the formation and structures of compounds. Additionally, this work did not look in detail at the effect of changing solvent in this system, which may have a large effect on structures that form. Lastly, future work will involve the magnetic characterisation and interpretation of each of these compounds so that they can be compared against others in the literature.

6 Conclusions

Development of a robotic platform to perform multiple inorganic reactions was achieved. This platform used an original design, which allowed the incorporation of a camera to monitor each reaction in real time, which had not previously been seen. Application of this allowed close visual monitoring of reaction and crystallisation progression in many simultaneous inorganic reactions. By using machine learning techniques, crystals were rendered identifiable by their topologies and their shapes, sizes, colours and positions could be recognised relative to walls of the reaction vessel. This technology allowed the platform to be investigated for use as a random number generator using crystal growth as entropy source. It was hypothesised that different chemical processes would affect the quality random number produced, and as such three different reactions were investigated that involved an increasing number of random processes.

Firstly, crystallization of $\text{CuSO}_4 \cdot 5\text{H}_2\text{O}$ was investigated as a process which involved the only one stochastic process (crystallisation), followed by the synthesis and crystallisation of $\{\text{W}_{19}\}$ which involved cluster formation, and finally the synthesis and crystallisation of $\{\text{Co}_4\}$ which involved ligand attachment and cluster formation in addition to crystallisation. A method of image binarization was then developed for conversion of crystal data into binary sequences which involved the size, shape, position and colour of each crystal. In each of the three chemistries investigated, the binary sequences generated passed each test described in the NIST special publications 800 22a at each level. This provided good evidence that the sequences produced were truly random and as such, could be used for generation of true random numbers. However, as no difference between the chemistries was identified, this procedure is not applicable for distinguishing between different stochastic processes present in different reaction systems.

Future work in this project will likely include optimisation of data acquisition process. One useful modification would be to create an artificial ceiling to the platform to provide contrast and allow for easier crystal identification. Additionally, incorporation of a camera with higher resolution would be able to identify crystals earlier and could investigate the random properties of crystal nucleation. Another improvement would be to replace the single tracking camera with an array of cameras for each reaction vial.

Overall, this project has developed a new method for generating true random numbers by observation of crystallisation. In doing so, it has also developed an automated system that can be used for rapid batch screening of inorganic synthetic and crystallisation conditions. It also allows for development of this work in order to study and compare chemical processes in terms of the indeterminacy of their processes. Further, this technology may lead to the application of a modular chemical random number generator for use in cryptographic purposes.

Use of a robotic platform for inorganic cluster discovery was also investigated, and compared against compound discovery by traditional methods. The target compound class was large iron oxide clusters due to their interest as biological mimics and magnetic compounds. Overall, success was seen with both methods, with the discovery of multiple compounds, although, limitations were observed for both.

Using the robotic platform, multiple conditions could be screened in a short period of time. This allowed the discovery of $\{\text{Fe}_{16}\}$, which formed in a narrow window of ascorbic acid concentration, which would likely have been searched manually due to it being at the extremes of the target search region. A further two compounds: chiral $\{\text{Fe}_{17}\}$, $\{\text{Fe}_8\}$ were also discovered due to the ability to rapidly screen reaction conditions while other tasks were being performed. However, the failure to find a solution to handling of solid material for much of the project meant that much effort was used in trying to adapt the synthesis for the new compound $\{\text{Fe}_{34}\}$.

On the other hand, investigation of reaction conditions by traditional manual means led to the discovery of a new Fe-Pb compounds through the breakdown of ascorbic acid, a metal-organic framework, a novel $\{\text{Mo}_{10}\}$ Anderson-like compounds, and three new gigantic iron oxo clusters, $\{\text{Fe}_{30}\}$, $\{\text{Fe}_{34}\}$ and $\{\text{Fe}_{36}\}$. Indeed, several analogues of the latter group were additionally synthesised.

In terms of the chemistry involved, the use of nitrogenous aromatic ligands in organic media to discover new iron-based compounds was very successful, with almost all of the compounds discovered being of this type. The one exception being $\{\text{FePb}_3\text{L}_3\}$ whose trapping ligands were formed by the decomposition of ascorbic acid in water. Lead-iron oxo bridged compounds are rare in the literature, and the discovery of this molecule from the breakdown of ascorbic acid could lead to further discoveries in the biological interaction between lead and ascorbic acid.

For the compounds synthesised in organic media, acetonitrile was found to be very conducive to cluster growth. By this method, it was possible to synthesise the highest nuclearity iron oxo-aggregates known: $\{\text{Fe}_{30}\}$, $\{\text{Fe}_{34}\}$ and $\{\text{Fe}_{36}\}$, simply by changing the R- groups on a pyridine ring and the crystallisation conditions. This leaves great scope for magnetic, electrochemical and potentially catalytic properties to be investigated. Further the structure resembles the biomineral core of the protein ferritin and could be used as a model to investigate properties of this protein. In addition, these structure provides insight into the aggregation processes involved in the mineralisation of iron (oxy)hydroxides, as they are able to grow via an aggregation process to a relatively large size in a water deficient environment. Future study may include time resolved ion mobility mass spectroscopy in order to determine the growth of intermediates leading to the full cluster. There is also the potential for other clusters to form by introducing new ligands to the system. While functionalised ligands tend to produce smaller clusters, this seems a relatively unexplored are of chemistry and future molecular discoveries are likely. Particularly, exploring conditions using other alkyl-substituted pyridine rings may result in even larger clusters being discovered. However, one major hindrance to these kinds of studies is the very low yields obtained with these compounds - often only a few crystals per sample - and work should be done to try to improve this.

Overall, using a robotic system to perform automated inorganic batch reactions allows for both compound discovery, and uses in interdisciplinary fields, such as cryptography.

7 Experimental

7.1 Materials

All reagents and solvents were purchased from Sigma Aldrich Chemical Company Ltd., Fischer Scientific, and Alfa Aesar. Unless otherwise stated, the materials were used without further purification.

7.2 Instrumentation

Single Crystal X-ray Diffraction: Single crystal datasets and unit cells were collected at 150(2) K on a Bruker Apex II Quasar diffractometer equipped with a graphite monochromator (λ ($\text{MoK}\alpha$) = 0.7107 Å). Structure solution and refinement were carried out with SHELXL-97/2013¹⁹⁸ via WINGX¹⁹⁹. Corrections for incident and diffracted beam absorption effects were applied using either analytical or empirical methods.

Mass Spectroscopy: ESI-TWIMS-MS analyses were performed in the positive polarity mode of a Waters Synapt™ G2 HDMS™ Q-ToF equipped with a standard Waters LockSpray Exact Mass Ionization Source (note that LockSpray was not employed for these measurements) and T-Wave™ Ion Mobility cell. Data were analysed using DriftScope 2.2. All data were collected in the positive polarity setting of the mass analyser. Samples were dissolved in methanol and formic acid in a 20:1 ratio at a concentration of approximately 1 ppm and infused through 127 μm ID PEEK tubing to the ESI source via syringe pump at a rate of 10 $\mu\text{L}/\text{min}$. The emitter tip angle was calibrated for optimal sensitivity of the target analytes. The scan range for initial screening experiments ranged between 700 - 3000 m/z with more narrow m/z windows (700 - 2000 m/z, and 2000-3000 m/z) and longer scan times (5 s) employed for higher-quality isotope patterns when required. The spectra in this manuscript are the result of several 5 second individual scans combined over a 10-minute infusion.

Fourier-transform infrared (FT-IR) spectroscopy: The compound was prepared as a powdered sample and measured using a Shimadzu FTIR 8400S Fourier Transformer Infrared Spectrophotometer with attenuated diffraction diamond

cell. Wavenumbers (ν) are given in cm^{-1} ; intensities are denoted as w = weak, m = medium, s = strong.

Thermogravimetric Analysis (TGA): Thermogravimetric analysis was performed on a TA Instruments Q 500 Thermogravimetric Analyzer under dry air flow at a typical heating rate of $10\text{ }^{\circ}\text{C min}^{-1}$ over the temperature range $20 - 800\text{ }^{\circ}\text{C}$.

Elemental Analysis: Fe content were determined by ICP-OES analysis in the following way: 5-10 mg sample material was digested by adding 1mL deionised water and 2 mL conc. HNO_3 to the sample in a digestion beaker. The sample solution was warmed until clear before being allowed to cool and a further 5 mL deionised water added. The resulting solution was transferred quantitatively with washings to an A class 50 mL volumetric flask and made up to the mark with deionised water. A blank sample was also prepared simultaneously to account for any digestion interferences. Carbon, nitrogen and hydrogen content was analysed by the University of Glasgow microanalysis service within the School of Chemistry.

7.3 Method of Crystal Growth

Crystal growth of the metal-oxide complexes was obtained *via* the slow evaporation method. This technique involves filtering the nascent solutions from the reaction mixture into a wide necked conical flask or beaker and the solutions were then left in a controlled temperature environment (18°C) to allow for evaporation. Occasionally, to slow the evaporation rate down, the flask/beaker would be covered either by perforated Parafilm™, or a pierced plastic cap.

7.4 Synthesis of Compounds

7.4.1 Synthesis of $2\text{Na}\cdot[\text{FePb}_3\text{O}(\text{C}_6\text{H}_4\text{O}_7)_3]\cdot 3\text{H}_2\text{O}$ (1)

$\text{Fe}(\text{NO}_3)_3\cdot 9\text{H}_2\text{O}$ (0.169g, 0.418mmol) and $\text{Pb}(\text{NO}_3)_2$ (0.181g, 0.546mmol) were dissolved in deionised water (2.5mL) and ascorbic acid (0.15g, 0.85mmol) was added with stirring, forming a dark purple colour. A solution of Na_2CO_3 (1M) was added dropwise until pH reached 3.5. The solution was filtered and left to crystallise for three weeks. Over this time, the solution turned yellow/beige and beige crystals formed. The yield was 0.15g (60.1%) based on Pb.

7.4.2 Synthesis of $[\text{Fe}_{17}\text{O}_{16}(\text{OH})_{12}(\text{C}_7\text{H}_9\text{N})_{12}\text{Br}_4] \cdot 3\text{Br} \cdot 5(\text{C}_7\text{H}_9\text{N})$ (2)

Anhydrous FeBr_3 (0.164g, 0.415 mmol) was dissolved in 3,4-lutidine (10 mL, 124.1 mmol) forming a dark red/black solution and stirred in a sealed vial for 2 hours. The solution was then filtered and left to crystallise in a vial with a pierced cap at room temperature. Small red needle like crystals appeared after two weeks which were suitable for x-ray. The yield was 0.005g (5.4%) based on Fe. Characteristic FT-IR (powder) bands (cm^{-1}): 3365 (s), 3063 (w), 2777 (w), 2037 (w), 1633 (m), 1605 (s), 1485 (s), 1444 (s), 1217 (m), 1103 (m), 1070 (m), 1039 (s), 1013 (m), 870 (m), 804 (w), 752 (s), 677 (s), 608 (s), 505 (s).

7.4.3 Synthesis of $[\text{Fe}_{17}\text{O}_{16}(\text{OH})_{13}(\text{C}_5\text{H}_5\text{N})_{12}\text{Br}_3] \cdot 3\text{Br} \cdot 2(\text{C}_5\text{H}_5\text{N})$ (3)

Anhydrous FeBr_3 (0.052g, 0.131 mmol) was dissolved in pyridine (6 mL, 74.5 mmol) and ascorbic acid (15mg, 0.085 mmol) was added forming a dark red/black solution and stirred at 50°C in a sealed vial for 2 hours. The solution was then filtered and left to crystallise in a vial with a pierced cap at room temperature. Small red diamond like crystals appeared after two weeks which were suitable for x-ray. The yield was (0.0023g) 9.4% based on Fe. Characteristic FT-IR (powder) bands (cm^{-1}): 1636 (s), 1540 (s), 1486 (s), 1408 (m), 1052 (s), 583 (w), 511 (s)

7.4.4 Synthesis of $[\text{Fe}_{17}\text{O}_{16}(\text{OH})_{12}(\text{H}_2\text{O})_6(\text{C}_5\text{H}_5\text{N})_{12}\text{Br}_2] \cdot [\text{Fe}_{17}\text{O}_{16}(\text{OH})_{12}(\text{H}_2\text{O})_3(\text{C}_5\text{H}_5\text{N})_{12}\text{Br}_3] \cdot 6\text{Br} \cdot 2(\text{C}_5\text{H}_5\text{N})$ (4)

Anhydrous FeBr_3 (0.213g, 0.538 mmol) was dissolved in pyridine (15 mL, 186.22 mmol) and ascorbic acid (5mg, 0.028 mmol) was added forming a dark red/black solution and stirred at 50°C in a sealed vial for 2 hours. The solution was then filtered and left to crystallise in a vial with a pierced cap at room temperature. Small red diamond like crystals appeared after two weeks which were suitable for x-ray. The yield was 0.013g (14.6%) based on Fe. Characteristic FT-IR (powder) bands (cm^{-1}): 3365 (s), 3063 (w), 2777 (w), 2037 (w), 1633 (m), 1605 (s), 1485 (s), 1444 (s), 1217 (m), 1103 (m), 1070 (m), 1039 (s), 1013 (m), 870 (m), 804 (w), 752 (s), 677 (s), 608 (s), 505 (s).

7.4.5 Synthesis of $[\text{Fe}_{34}\text{O}_{38}(\text{OH})_{12}\text{Br}_{12}(\text{C}_5\text{H}_5\text{N})_{18}]\cdot[\text{Br}_6\text{Fe}_2\text{O}]$ (5)

Method 1

Anhydrous FeBr_3 (0.305g, 0.771 mmol) was dissolved in MeCN (15ml) and htma (0.405g, 2.86 mmol) was added. This solution was stirred for 3 minutes before the addition of pyridine (0.3 mL, 3.72 mmol) forming a cloudy dark red/black solution and stirred in a sealed vial for 3 hours. The solution was then filtered, layered with acetone and left to crystallise in a vial with a pierced cap at room temperature. Dark red block crystals appeared after one week which were suitable for x-ray. The yield was 0.012g (9.8%) based on Fe. Elemental analysis: $\text{H}_{90}\text{C}_{90}\text{N}_{18}\text{Fe}_{36}\text{Br}_{18}$, MW = 5688.6.9 g mol^{-1} . Calculated (%): C (19.00), H (1.59), N (4.44), Fe (35.34); found: C (19.01 %) H (1.54%) N (4.32%) Fe (34.31%). Characteristic FT-IR (powder) band (cm^{-1}): 3365 (s), 3063 (w), 2777(w), 2037 (w), 1633 (m), 1605 (s), 1485 (s), 1444 (s), 1217 (m), 1103 (m), 1070 (m), 1039 (s), 1013 (m), 870 (m), 804 (w), 752 (s), 677 (s), 608 (s), 505 (s).

Method 2

Anhydrous FeBr_3 (0.312g, 0.789 mmol) was dissolved in MeCN (15ml) This solution was stirred for 3 minutes before the addition of pyridine (0.30 mL, 3.7 mmol) forming dark red/black solution. Morpholine was then added dropwise until pH 5.0 and the solution was stirred in a sealed vial for 3 hours. The solution was then filtered, layered with acetone and left to crystallise in a vial with a pierced cap at room temperature. Dark red block crystals appeared after one week which were suitable for x-ray. The yield was 0.01g (8.2%) based on Fe. Characteristic FT-IR (powder) bands (cm^{-1}): 3365 (s), 3062 (w), 2775 (w), 2038 (w), 1633 (m), 1605 (s), 1485 (s), 1445 (s), 1217 (m), 1104 (m), 1065 (m), 1039 (s), 1013 (m), 870 (m), 752 (s), 677 (s), 608 (s), 505 (s).

7.4.6 Synthesis of $[\text{Fe}_{34}\text{O}_{38}(\text{OH})_{12}\text{Br}_{12}(\text{C}_5\text{H}_5\text{N})_{18}]\cdot 2\text{Br}$ (6)

Anhydrous FeBr_3 (0.300g, 0.758 mmol) was dissolved in DCM (20mL) and htma (0.506g, 3.571 mmol) was added. This solution was stirred for 3 minutes before the addition of pyridine (0.7 mL, 0.687 mmol) forming a cloudy dark red/black solution and stirred in a sealed vial for 3 hours. The solution was then filtered and left to crystallise in a vial with a pierced cap at room temperature. Small red block

shaped crystals appeared after two weeks which were suitable for x-ray. The yield was 0.015g (12.8%) based on Fe. Characteristic FT-IR (powder) bands (cm^{-1}): 3375 (s), 3063 (w), 2777(w), 1604 (s), 1559 (m), 1485 (s), 1447 (s), 1288 (m), 1103 (m), 1202 (m), 1042 (s), 1008 (m), 976 (m), 964 (w), 795 (s), 658 (s), 630 (s).

7.4.7 Synthesis of $[\text{Fe}_{34}\text{O}_{38}(\text{OH})_{12}\text{Br}_{12}(\text{C}_{12}\text{H}_{11}\text{N})_{18}]\cdot 2\text{Br}$ (7)

Anhydrous FeBr_3 (0.588g, 1.49 mmol) was dissolved in MeCN (25ml) and htma (0.251g, 1.79 mmol) was added. This solution was stirred for 3 minutes before the addition of benzylpyridine (1.0 mL, 6.27 mmol) forming a cloudy dark red/black solution and stirred in a sealed vial for 3 hours. The solution was then filtered and left to crystallise in a vial with a pierced cap at room temperature. Dark red block crystals appeared after two weeks which were x-ray. Yield is unknown due to incomplete characterisation.

7.4.8 Synthesis of $[\text{Fe}_{34}\text{O}_{38}(\text{OH})_{12}\text{Br}_{12}(\text{C}_4\text{H}_4\text{N}_2)_{18}]\cdot 2\text{Br}$ (8)

Anhydrous FeBr_3 (0.520g, 1.31 mmol) was dissolved in MeCN (20ml). This solution was stirred for 1 minute before the addition of pyrimidine (1.5 mL, 19.03 mmol) forming dark red/black solution. The solution was then filtered and left to crystallise in a vial with a pierced cap at room temperature. Black block crystals appeared after three weeks which were suitable for x-ray. The yield was 0.009 g (4.3%) based on Fe.

7.4.9 Synthesis of $[\text{Fe}_{30}\text{O}_{31}(\text{OH})_{16}\text{Br}_9(\text{C}_5\text{H}_5\text{N})_{15}]_{0.9}\cdot[\text{Fe}_{34}\text{O}_{38}(\text{OH})_{12}\text{Br}_{12}(\text{C}_5\text{H}_5\text{N})_{18}]_{0.1}\cdot 9\text{Br}$ (9)

Anhydrous FeBr_3 (0.288, 0.728 mmol) was dissolved in MeCN (20ml) and htma (0.355g, 2.54 mmol) was added. This solution was stirred for 3 minutes before the addition of pyridine (0.6 mL, 0.590 mmol) forming a cloudy dark red/black solution and stirred in a sealed vial for 3 hours. The solution was then filtered and left to crystallise in a vial with a pierced cap at room temperature. Dark red block crystals appeared after two weeks which were suitable for x-ray. The yield was 0.01g (9.47%) based on Fe. Elemental analysis: $\text{H}_{76.5}\text{C}_{76.5}\text{N}_{15.3}\text{Fe}_{30.4}\text{Br}_{12.3}$, MW = 4407.9.9 gmol^{-1} . Calculated (%): C (20.84), H (1.75), N (4.87), Fe (35.12); found:

C (19.49%) H (1.95%) N (4.82%) Fe (34.21%). Characteristic FT-IR (powder) bands (cm^{-1}): 3365 (s), 1633 (m), 1604 (s), 1485 (s), 1446 (s), 1288 (m), 1217 (m), 1042 (m), 1007 (s), 978 (m), 816 (w), 795 (m), 658 (s), 630 (s).

7.4.10 Synthesis of $[\text{Fe}_{30}\text{O}_{31}(\text{OH})_{16}\text{Br}_9(\text{C}_6\text{H}_7\text{N})_{15}]_{0.9}\cdot[\text{Fe}_{34}\text{O}_{38}(\text{OH})_{12}\text{Br}_{12}(\text{C}_6\text{H}_7\text{N})_{18}]_{0.1}\cdot 9\text{Br}$ (10)

Anhydrous FeBr_3 (0.223, 0.564 mmol) was dissolved in MeCN (25ml) and htma (0.405g, 2.86 mmol) was added, followed by addition of BiBr_3 (0.021g, 0.045mmol). This solution was stirred for 3 minutes before the addition of 4-picoline (1.1 mL, 11.30 mmol) forming a cloudy dark red/black solution and stirred in a sealed vial for 3 hours. The solution was then filtered and left to crystallise in a vial with a pierced cap at room temperature. Tiny red hexagonal crystals appeared after one week which were suitable for x-ray. The yield was 0.01g (11.2%) based on Fe. Characteristic FT-IR (powder) bands (cm^{-1}): 3365 (s), 3063 (w), 1633 (m), 1604 (s), 1485 (s), 1446 (s), 1288 (m), 1217 (m), 1042 (m), 1007 (s), 978 (m), 816 (w), 795 (m), 658 (s), 630 (s).

Method 2

Anhydrous FeBr_3 (0.625g, 1.58 mmol) was dissolved in MeCN (25ml) This solution was stirred for 3 minutes before the addition of 4-picoline (1.0 mL, 10.3 mmol) forming dark red/black solution. Morpholine was then added dropwise until pH 5.0 and the solution was stirred in a sealed vial for 3 hours. The solution was then filtered, layered with acetone and left to crystallise in a vial with a pierced cap at room temperature. Tiny red hexagonal crystals appeared after one week which were suitable for x-ray. The yield was approximately 0.011g (12.4%) based on Fe. Characteristic FT-IR bands (cm^{-1}): 3365 (s), 3063 (w), 1633 (m), 1604 (s), 1485 (s), 1446 (s), 1288 (m), 1217 (m), 1042 (m), 1007 (s), 978 (m), 816 (w), 795 (m), 658 (s), 630 (s).

7.4.11 Synthesis of $[\text{Fe}_{36}\text{O}_{30}(\text{OH})_{34}\text{Br}_8(\text{C}_6\text{H}_7\text{N})_{24}]\cdot 6\text{Br}$ (11)

Anhydrous FeBr_3 (0.45, 1.14 mmol) was dissolved in MeCN (30mL) and htma (0.51, 3.64 mmol) was added. This solution was stirred for 3 minutes before the addition of 4-picoline (1.0 mL, 10.28 mmol) forming a cloudy dark red/black solution and

stirred in a sealed vial for 3 hours. The solution was then filtered and left to crystallise in a vial with a pierced cap at room temperature. Tiny red hexagon shaped crystals appeared after one week which were suitable for x-ray. The yield was approximately 0.002g (0.71%) based on Fe. Characteristic FT-IR (powder) bands (cm^{-1}): 3381s, 2986w, 2928w, 2795w, 2718w, 1637s, 1589s, 1506s, 1463m, 1394m, 1309m, 1103s)

7.4.12 Synthesis of $[\text{Fe}_{36}\text{O}_{30}(\text{OH})_{34}\text{Br}_8(\text{C}_7\text{H}_9\text{N})_{24}]\cdot 6\text{Br}$ (12)

Anhydrous FeBr_3 (0.625g, 1.58 mmol) was dissolved in MeCN (25ml) This solution was stirred for 3 minutes before the addition of 3,4-lutidine (1.0 mL, 8.67 mmol) forming dark red/black solution. Morpholine was then added dropwise until pH 5.0 and the solution was stirred in a sealed vial for 3 hours. The solution was then filtered, layered with acetone and left to crystallise in a vial with a pierced cap at room temperature. Dark red block crystals appeared after one week which were suitable for x-ray. The yield was < 0.001g. Insufficient material for further characterisation after XRD analysis.

7.4.13 Synthesis of $[\text{Fe}_{36}\text{O}_{38}(\text{OH})_{12}\text{Br}_{12}(\text{C}_7\text{H}_9\text{N})_{24}]\cdot 6\text{Br}$ (13)

Anhydrous FeBr_3 (0.45, 1.14 mmol) was dissolved in MeCN (30mL) and htma (0.51, 3.64 mmol) was added. This solution was stirred for 3 minutes before the addition of 3,5-lutidine (1 mL, 8.67 mmol) forming a cloudy dark red/black solution and stirred in a sealed vial for 3 hours. The solution was then filtered and left to crystallise in a vial with a pierced cap at room temperature. Tiny red hexagon shaped crystals appeared after one week which were suitable for x-ray. The yield was 0.023g (9.15%) based on Fe. Characteristic FT-IR (powder) bands (cm^{-1}): 3365 (s), 3063 (w), 1633 (m), 1604 (s), 1485 (s), 1446 (s), 1288 (m), 1217 (m), 1042 (m), 1007 (s), 978 (m), 816 (w), 795 (m), 658 (s), 630 (s).

7.4.14 Synthesis of $[\text{Fe}_{36}\text{O}_{38}(\text{OH})_{12}\text{Br}_{12}(\text{C}_7\text{H}_9\text{N})_{24}]\cdot 6\text{Br}$ (14)

Anhydrous FeBr_3 (0.625g, 1.58 mmol) was dissolved in MeCN (25mL) and htma (0.4g, 2.86 mmol) was added. This solution was stirred for 3 minutes before the addition of 4-ethylpyridine (1.0 mL, 8.67 mmol) forming a cloudy dark red/black solution and stirred in a sealed vial for 3 hours. The solution was then filtered and

left to crystallise in a vial with a pierced cap at room temperature. Tiny blue shaped crystals appeared after one week which were suitable for x-ray. The yield was < 0.001g. Insufficient material for further characterisation after XRD analysis.

7.4.15 Synthesis of $[\text{Mo}_{10}\text{O}_{27}(\text{C}_7\text{H}_9\text{N})_7]$ (15)

Anhydrous MoCl_5 (0.185g, 0.677 mmol) was dissolved in MeCN (20ml) and acetone (5ml). This solution was stirred for 1 minute before the addition of 3,4-lutidine (0.8 mL, 6.94 mmol) forming dark red/black solution. The solution was then filtered and left to crystallise in a vial with a pierced cap at room temperature. Light yellow rod shaped crystals appeared after three weeks which were suitable for x-ray. The yield was 0.066g (45.5%) based on Mo.

7.4.16 Synthesis of $[\text{Fe}(\text{C}_4\text{H}_4\text{N}_2)_2\text{Br}_2]$ (16)

Anhydrous FeBr_3 (0.520g, 1.31 mmol) was dissolved in MeCN (20ml). This solution was stirred for 1 minute before the addition of pyrimidine (1.5 mL, 19.03 mmol) forming dark red/black solution. The solution was then filtered and left to crystallise in a vial with a pierced cap at room temperature. Light yellow rod shaped crystals appeared after three weeks which were suitable for x-ray. The yield was 0.147g (37.8%) based on Fe.

7.4.17 Synthesis of $[\text{Fe}_4\text{O}(\text{OH})(\text{C}_8\text{H}_6\text{N}_2)_6\text{Br}_5] \cdot [\text{Br}_6\text{Fe}_2\text{O}] \cdot 5(\text{H}_3\text{C}_2\text{N})$ (17)

Anhydrous FeBr_3 (0.205g, 0.670mmol) was dissolved in acetonitrile (10mL) forming a dark red/block solution. To this phthalazine (0.1g, 0.768 mmol) was added and stirred for 3 hours. The resulting dark red solution was filtered and left to crystals in a vial with a singly pierced cap at room temperature. Black crystals appeared after 7 days. The yield was 0.11g (38.5%) based on Fe.

7.4.18 Synthesis of $[\text{Fe}_8\text{O}_4(\text{C}_6\text{H}_6\text{ON})_8\text{Br}_8]$ (18)

Anhydrous FeBr_3 (0.198g, 0.670mmol) was dissolved in acetonitrile (10mL) forming a dark red/block solution. To this 2-pyridinemethanol (0.1ml, 0.916 mmol) and pyridine (1ml, 12.64mmol) were added and stirred for 3 hours. The resulting dark red solution was filtered and left to crystals in a vial with a singly pierced cap at

room temperature. Black crystals appeared after 7 days. The yield was 0.020g (15.9%) based on Fe.

7.4.19 Synthesis of $[\text{Fe}_{17}\text{O}_{16}(\text{C}_7\text{H}_8\text{ON})_{12}\text{Br}_4]\cdot\text{Br}\cdot(\text{Br}_6\text{Fe}_2\text{O})$ (19)

Anhydrous FeBr_3 (0.139g, 0.351mmol) was dissolved in acetonitrile (7mL) forming a dark red/block solution. To this 2-pyridine ethanol (0.1ml, 0.886 mmol) was added and stirred for 1 hour. The resulting dark red solution was filtered and left to crystals in a vial with a singly pierced cap at room temperature. Black crystals appeared after 5 days. The yield was 0.017g (25.0%) based on Fe. Characteristic FT-IR (powder) bands (cm^{-1}): 3321 (s), 2252 (s), 1604 (s), 1566 (w), 1483 (m), 1440 (s), 1371 (m), 1311 (w), 1161 (s), 1109 (s), 1072 (s), 1047 (s), 875 (w), 785 (s), 684 (w).

7.4.20 Synthesis of $n\text{-}[\text{Fe}_2(\text{C}_5\text{H}_5\text{N})_2\text{Br}_2(\text{C}_2\text{O}_4)\text{O}]$ (20)

Anhydrous FeBr_3 (0.2g, 0.557 mmol) was dissolved in dichloromethane (10ml) and stirred for one hour at room temperature. To this a solution of ascorbic acid in pyridine, (0.3ml, 0.341 M) was added and the resulting solution was stirred for 1 hour at room temperature. The yield was 0.032g (21.5%) based on Fe.

7.4.21 Synthesis of $n\text{-}[\text{Fe}(\text{C}_5\text{H}_5\text{N})_4(\text{SO}_4)]$ (21)

Anhydrous FeBr_3 (0.415g, 1.049mmol) was dissolved in a sample of pyridine which had been saturated with H_2S (9ml). The reaction was stirred for three hours, during which time it turned clear and black. After this, it was filtered left to crystallise at room temperature in a vial with a pierced cap. Large light yellow crystals appeared after 4 weeks. The yield was 0.049g (19.9%) based on Fe.

7.4.22 Synthesis of $[\text{Fe}_{16}\text{O}_8(\text{ox})_{16}\text{Br}_4(\text{py})_{12}]\cdot 4(\text{C}_5\text{H}_6\text{N})\cdot 2(\text{C}_5\text{H}_5\text{N})$ (22)

Method 1

A solution of ascorbic acid in pyridine (0.8ml, 0.287M) was prepared added to a solution of anhydrous FeBr_3 in acetonitrile (10ml, 0.067M), with vigorous stirring on an automated platform. This formed an orange solution, which was filtered left to crystallise at 18°C . Long red-orange crystals then formed after 8 days. The yield

was 0.051g (28.6%) based on Fe. Characteristic FT-IR bands (cm^{-1}): 3000 (w), 1655 (s), 1600 (s), 1485 (m), 1445 (m), 1352 (m), 1309 (m), 1217 (w). 1066 (w), 1043 (w), 1012 (w), 883 (s), 796 (s), 752 (s), 696 (s), 677(s), 638 (s)

Method 2

A solution of ascorbic acid in pyridine (0.8ml, 0.287M) was prepared added to a solution of anhydrous FeBr_3 in acetonitrile (10ml, 0.067M), with vigorous stirring. This formed an orange solution with a pH of 5.15, which was filtered and left to crystallise at 18°C. Long red-orange crystals then formed after 8 days. The yield was 0.024g (11.4%) based on Fe. Characteristic FT-IR bands (cm^{-1}): 3000 (w), 1655 (s), 1600 (s), 1485 (m), 1445 (m), 1352 (m), 1309 (m), 1217 (w). 1066 (w), 1043 (w), 1012 (w), 883 (s), 796 (s), 752 (s), 696 (s), 677(s), 638 (s)

8 Crystallographic Data

Refinement details for the single crystal X-ray diffraction datasets of all new compounds are presented herein. Data reduction was performed using the *Apex2* software package, and structure solution and refinement was carried out using *SHELXL-2018/3*, via *WinGX*. Corrections for incident and diffracted beam absorption effects were applied using the analytical numeric absorption correction of a multifaceted crystal model, or by empirical absorption correction. Structures were solved with a combination of direct methods and difference Fourier syntheses, and refined against *F2* by the full-matrix least-squares technique.

Equations employed:

$$\text{Goodness-of-fit (Goof)} = \left(\sqrt{\frac{\sum w(F_0^2 - F_c^2)^2}{(n-p)}} \right)$$

$$\text{Weighting scheme } w = \frac{1}{[\sigma^2(F_0)^2 + (AP)^2 + (BP)]}$$

$$\text{With } P = \frac{[\max(I_{obs,0}) + 2F_c^2]}{3}$$

p: number of parameters; *n*: number of data; A, B: weighting scheme parameters

$$R1 = \frac{\sum ||F_0| - |F_c||}{\sum |F_0|}$$

$$wR2 = \sqrt{\frac{\sum [w(F_0^2 - F_c^2)^2]}{\sum w(F_0^2)^2}}$$

$$R(\text{int}) = \frac{\sum |F_0^2 - F_c^2(\text{mean})|}{\sum |F_0^2|}$$

Each summation involves reflections for which > 1 symmetry equivalent is averaged.

8.1 $2\text{Na}\cdot[\text{FePb}_3\text{O}(\text{C}_6\text{H}_4\text{O}_7)_3]\cdot 3\text{H}_2\text{O}$ (1)

Identification code	Compound (1): ECL7624	
Empirical formula	C72 H48 Fe4 Na8 O130 Pb12 H18	
Formula weight	5886.7	
Temperature	150(2) K	
Wavelength	0.71073 Å	
Crystal system	Cubic	
Space group	P 21 3	
Unit cell dimensions	a = 15.4102(6) Å	$\alpha = 90^\circ$.
	b = 15.4102(6) Å	$\beta = 90^\circ$.
	c = 15.4102(6) Å	$\gamma = 90^\circ$.
Volume	3659.5(4) Å ³	
Z	4	
Density (calculated)	2.671 Mg/m ³	
Absorption coefficient	14.285 mm ⁻¹	
F(000)	2677	
Crystal size	0.120 x 0.100 x 0.080 mm ³	
Theta range for data collection	2.289 to 25.986°.	
Index ranges	-19 ≤ h ≤ 18, -19 ≤ k ≤ 14, -19 ≤ l ≤ 18	
Reflections collected	28085	
Independent reflections	239693 [R(int) = 0.0517]	
Completeness to theta = 25.242°	99.8 %	
Refinement method	Full-matrix least-squares on F ²	
Data / restraints / parameters	2396 / 6 / 173	
Goodness-of-fit on F ²	1.054	
Final R indices [I > 2σ(I)]	R1 = 0.0264, wR2 = 0.0769	
R indices (all data)	R1 = 0.0276, wR2 = 0.0774	
Absolute structure parameter	0.027(6)	
Extinction coefficient	n/a	
Largest diff. peak and hole	1.666 and -0.972 e.Å ⁻³	

8.2 $[\text{Fe}_{17}\text{O}_{16}(\text{OH})_{12}(\text{C}_7\text{H}_9\text{N})_{12}\text{Br}_4] \cdot 3\text{Br} \cdot 5(\text{C}_7\text{H}_9\text{N})$ (2)

Identification code	Compound 2: ECL4-43-2	
Empirical formula	C484 H608 Br28 Fe68 N64 O112	
Formula weight	15791.63	
Temperature	150(2) K	
Wavelength	0.71073 Å	
Crystal system	Monoclinic	
Space group	P 21/c	
Unit cell dimensions	a = 22.320(4) Å	a = 90°.
	b = 26.063(4) Å	b = 105.597(5)°.
	c = 29.362(5) Å	g = 90°.
Volume	16452(4) Å ³	
Z	4	
Density (calculated)	1.529 Mg/m ³	
Absorption coefficient	3.210 mm ⁻¹	
F(000)	7604	
Crystal size	0.150 x 0.110 x 0.070 mm ³	
Theta range for data collection	0.947 to 21.476°.	
Index ranges	-22 ≤ h ≤ 22, -26 ≤ k ≤ 26, -30 ≤ l ≤ 27	
Reflections collected	57069	
Independent reflections	18513 [R(int) = 0.1416]	
Completeness to theta = 21.476°	98.2 %	
Refinement method	Full-matrix least-squares on F ²	
Data / restraints / parameters	18513 / 0 / 1067	
Goodness-of-fit on F ²	1.040	
Final R indices [I > 2σ(I)]	R1 = 0.1105, wR2 = 0.2858	
R indices (all data)	R1 = 0.2352, wR2 = 0.4122	
Extinction coefficient	n/a	
Largest diff. peak and hole	2.255 and -1.400 e.Å ⁻³	

8.3 $[\text{Fe}_{17}\text{O}_{16}(\text{OH})_{12}(\text{H}_2\text{O})_9(\text{C}_5\text{H}_5\text{N})_{12}\text{Br}_1] \cdot 5\text{Br} \cdot 2(\text{C}_5\text{H}_5\text{N})$ (3)

Identification code	ECL7644
Empirical formula	C580 H472 Br40 Fe136 N96 O296
Formula weight	24313.9
Temperature	150(2) K
Wavelength	0.71073 Å
Crystal system	Monoclinic
Space group	C 2/c
Unit cell dimensions	a = 40.762(4) Å a = 90° . b = 20.6786(19) Å b = 102.563(8)° . c = 28.915(3) Å g = 90° .
Volume	23789(4) Å ³
Z	8
Density (calculated)	1.6971 Mg/m ³
Absorption coefficient	3.763 mm ⁻¹
F(000)	12143
Crystal size	0.100 x 0.070 x 0.040 mm ³
Theta range for data collection	1.024 to 25.999° .
Index ranges	-47<=h<=50, -25<=k<=25, -35<=l<=29
Reflections collected	157835
Independent reflections	23386 [R(int) = 0.1093]
Completeness to theta = 25.242°	100.0 %
Refinement method	Full-matrix least-squares on F ²
Data / restraints / parameters	23386 / 0 / 1201
Goodness-of-fit on F ²	1.065
Final R indices [I>2sigma(I)]	R1 = 0.1104, wR2 = 0.3036
R indices (all data)	R1 = 0.1770, wR2 = 0.3491
Extinction coefficient	n/a
Largest diff. peak and hole	2.765 and -2.401 e.Å ⁻³

8.4 $[\text{Fe}_{17}\text{O}_{16}(\text{OH})_{12}(\text{H}_2\text{O})_6(\text{C}_5\text{H}_5\text{N})_{12}\text{Br}_2] \cdot [\text{Fe}_{17}\text{O}_{16}(\text{OH})_{12}(\text{H}_2\text{O})_3(\text{C}_5\text{H}_5\text{N})_{12}\text{Br}_3] \cdot 9\text{Br} \cdot 5(\text{C}_5\text{H}_5\text{N})$ (4)

Identification code	ECL8591	
Empirical formula	C880 H1424 Br73.6 Fe204 N184 O440	
Formula weight	38895.6	
Temperature	150(2) K	
Wavelength	0.71073 Å	
Crystal system	Monoclinic	
Space group	C 2/c	
Unit cell dimensions	a = 47.852(3) Å	α = 90°.
	b = 28.540(3) Å	β = 116.611(6)°.
	c = 28.468(2) Å	γ = 90°.
Volume	34761(6) Å ³	
Z	6	
Density (calculated)	0.246 Mg/m ³	
Absorption coefficient	0.468 mm ⁻¹	
F(000)	2544	
Crystal size	0.090 x 0.050 x 0.040 mm ³	
Theta range for data collection	0.858 to 25.821°.	
Index ranges	-58 ≤ h ≤ 58, -34 ≤ k ≤ 34, -34 ≤ l ≤ 34	
Reflections collected	240587	
Independent reflections	33232 [R(int) = 0.3471]	
Completeness to theta = 25.242°	100.0 %	
Refinement method	Full-matrix least-squares on F ²	
Data / restraints / parameters	33232 / 0 / 1998	
Goodness-of-fit on F ²	1.100	
Final R indices [I > 2σ(I)]	R1 = 0.1325, wR2 = 0.2869	
R indices (all data)	R1 = 0.3029, wR2 = 0.4032	
Extinction coefficient	n/a	
Largest diff. peak and hole	5.565 and -1.904 e.Å ⁻³	

8.5 $[\text{Fe}_{34}\text{O}_{38}(\text{OH})_{12}\text{Br}_{12}(\text{C}_5\text{H}_5\text{N})_{18}] \cdot (\text{Br}_6\text{Fe}_2\text{O})$ (5)

Identification code	ECL9411
Empirical formula	C90 H102 Br18 Fe36 N18 O51
Formula weight	5700.55
Temperature	150(2) K
Wavelength	0.71073 Å
Crystal system	Triclinic
Space group	P -1
Unit cell dimensions	a = 20.8797(16) Å α = 90.015(6)° . b = 29.111(3) Å β = 90.041(5)° . c = 33.434(3) Å γ = 90.054(5)° .
Volume	20322(3) Å ³
Z	12
Density (calculated)	2.108 Mg/m ³
Absorption coefficient	3.647 mm ⁻¹
F(000)	12504
Crystal size	0.210 x 0.140 x 0.100 mm ³
Theta range for data collection	0.699 to 20.841° .
Index ranges	-20 ≤ h ≤ 16, -28 ≤ k ≤ 28, -33 ≤ l ≤ 33
Reflections collected	108357
Independent reflections	41982 [R(int) = 0.1649]
Completeness to theta = 20.841°	98.4 %
Refinement method	Full-matrix least-squares on F ²
Data / restraints / parameters	41982 / 0 / 2858
Goodness-of-fit on F ²	1.069
Final R indices [I > 2σ(I)]	R1 = 0.1192, wR2 = 0.2862
R indices (all data)	R1 = 0.2724, wR2 = 0.3912
Extinction coefficient	n/a
Largest diff. peak and hole	2.542 and -2.177 e.Å ⁻³

8.6 $[\text{Fe}_{34}\text{O}_{38}(\text{OH})_{12}\text{Br}_{12}(\text{C}_5\text{H}_5\text{N})_{18}]\cdot 2\text{Br}$ (6)

Identification code	ECL9504
Empirical formula	C90 H90 Br12 Fe34 N18 O80
Formula weight	5561.61
Temperature	150(2) K
Wavelength	0.71073 Å
Crystal system	Triclinic
Space group	P -1
Unit cell dimensions	a = 19.2096(14) Å α = 109.960(4)° b = 23.2255(17) Å β = 92.485(4)° c = 28.3559(18) Å γ = 95.321(4)°
Volume	11801.8(15) Å ³
Z	2
Density (calculated)	2.348 Mg/m ³
Absorption coefficient	6.170 mm ⁻¹
F(000)	8100
Crystal size	0.100 x 0.100 x 0.080 mm ³
Theta range for data collection	0.766 to 24.816°
Index ranges	-22 ≤ h ≤ 22, -27 ≤ k ≤ 27, -33 ≤ l ≤ 30
Reflections collected	147786
Independent reflections	40224 [R(int) = 0.1193]
Completeness to theta = 24.816°	98.7 %
Refinement method	Full-matrix least-squares on F ²
Data / restraints / parameters	40224 / 0 / 2198
Goodness-of-fit on F ²	1.051
Final R indices [I > 2σ(I)]	R1 = 0.1012, wR2 = 0.2893
R indices (all data)	R1 = 0.2128, wR2 = 0.3733
Extinction coefficient	n/a
Largest diff. peak and hole	4.081 and -2.896 e.Å ⁻³

8.7 $[\text{Fe}_{34}\text{O}_{38}(\text{OH})_{12}\text{Br}_{12}(\text{C}_{12}\text{H}_{11}\text{N})_{18}]\cdot 2\text{Br}$

Identification code	ECL11355
Empirical formula	C216 H210 Br14 Fe34 N18 O50
Formula weight	6875.45
Temperature	150(2) K
Wavelength	0.71073 Å
Crystal system	Cubic
Space group	P a -3
Unit cell dimensions	a = 40.865(2) Å $\alpha = 90^\circ$. b = 40.865(2) Å $\beta = 90^\circ$. c = 40.865(2) Å $\gamma = 90^\circ$.
Volume	68242(12) Å ³
Z	896
Density (calculated)	3.309 Mg/m ³
Absorption coefficient	17.755 mm ⁻¹
F(000)	61824
Crystal size	0.080 x 0.070 x 0.030 mm ³
Theta range for data collection	0.863 to 14.464°.
Index ranges	-28<=h<=26, -28<=k<=28, -28<=l<=28
Reflections collected	117930
Independent reflections	4151 [R(int) = 0.2780]
Completeness to theta = 14.464°	99.8 %
Refinement method	Full-matrix least-squares on F ²
Data / restraints / parameters	4151 / 0 / 343
Goodness-of-fit on F ²	3.402
Final R indices [I>2sigma(I)]	R1 = 0.2834, wR2 = 0.6320
R indices (all data)	R1 = 0.4271, wR2 = 0.7285
Extinction coefficient	n/a
Largest diff. peak and hole	2.221 and -2.998 e.Å ⁻³

8.8 $[\text{Fe}_{34}\text{O}_{38}(\text{OH})_{12}\text{Br}_{12}(\text{C}_4\text{H}_5\text{N}_2)_{18}]\cdot 2\text{Br}$

Empirical formula	C144 H204 Br14 Fe34 N18 O50	
Formula weight	6004.63	
Temperature	293(2) K	
Wavelength	0.71073 Å	
Crystal system	Triclinic	
Space group	P -1	
Unit cell dimensions	a = 18.557(4) Å	$\alpha = 90.038(6)^\circ$
	b = 18.724(4) Å	$\beta = 96.166(6)^\circ$
	c = 28.063(6) Å	$\gamma = 112.889(5)^\circ$
Volume	8921(3) Å ³	
Z	2	
Density (calculated)	0.973 Mg/m ³	
Absorption coefficient	2.714 mm ⁻¹	
F(000)	2524	
Crystal size	0.170 x 0.105 x 0.090 mm ³	
Theta range for data collection	2.221 to 24.760°.	
Index ranges	-21 ≤ h ≤ 21, -21 ≤ k ≤ 21, -30 ≤ l ≤ 32	
Reflections collected	86106	
Independent reflections	30062 [R(int) = 0.1328]	
Completeness to theta = 24.760°	98.3 %	
Refinement method	Full-matrix least-squares on F ²	
Data / restraints / parameters	30062 / 0 / 1767	
Goodness-of-fit on F ²	1.381	
Final R indices [I > 2σ(I)]	R1 = 0.1505, wR2 = 0.3870	
R indices (all data)	R1 = 0.2640, wR2 = 0.4647	
Extinction coefficient	n/a	
Largest diff. peak and hole	6.897 and -2.022 e.Å ⁻³	

8.9 $[\text{Fe}_{30}\text{O}_{31}(\text{OH})_{16}\text{Br}_9(\text{C}_6\text{H}_7\text{N})_{15}]_{0.9} \cdot [\text{Fe}_{34}\text{O}_{38}(\text{OH})_{12}\text{Br}_{12}(\text{C}_5\text{H}_5\text{N})_{18}]_{0.1} \cdot 2.9\text{Br}$

Identification code	DTL1081	
Empirical formula	C76.5 H76.5 N15.3 Fe30.4 O47.3 Br12.3	
Formula weight	4585.68	
Temperature	150(2) K	
Wavelength	0.71073 Å	
Crystal system	Monoclinic	
Space group	P 21/c	
Unit cell dimensions	a = 17.7759(18) Å	$\alpha = 90^\circ$.
	b = 54.265(5) Å	$\beta = 104.041(6)^\circ$.
	c = 19.1219(19) Å	$\gamma = 90^\circ$.
Volume	17894(3) Å ³	
Z	6	
Density (calculated)	0.385 Mg/m ³	
Absorption coefficient	1.102 mm ⁻¹	
F(000)	1970	
Crystal size	0.200 x 0.180 x 0.090 mm ³	
Theta range for data collection	0.750 to 26.000°.	
Index ranges	-21 ≤ h ≤ 21, -66 ≤ k ≤ 57, -23 ≤ l ≤ 19	
Reflections collected	248699	
Independent reflections	35345 [R(int) = 0.0915]	
Completeness to theta = 25.242°	100.0 %	
Refinement method	Full-matrix least-squares on F ²	
Data / restraints / parameters	35345 / 0 / 1691	
Goodness-of-fit on F ²	1.132	
Final R indices [I > 2σ(I)]	R1 = 0.1220, wR2 = 0.3109	
R indices (all data)	R1 = 0.1989, wR2 = 0.3754	
Extinction coefficient	n/a	
Largest diff. peak and hole	3.127 and -2.743 e.Å ⁻³	

8.10 $[\text{Fe}_{30}\text{O}_{31}(\text{OH})_{16}\text{Br}_9(\text{C}_6\text{H}_7\text{N})_{15}]_{0.9} \cdot [\text{Fe}_{34}\text{O}_{38}(\text{OH})_{12}\text{Br}_{12}(\text{C}_6\text{H}_7\text{N})_{18}]_{0.1} \cdot 2.9\text{Br}$

Identification code	ECL11055
Empirical formula	C88.5 H90.5 N17.3 Fe30.4 Br12.3 O47.3
Formula weight	4785.94
Temperature	150(2) K
Wavelength	0.71073 Å
Crystal system	Triclinic
Space group	P -1
Unit cell dimensions	a = 19.650(4) Å α = 83.389(3)° b = 20.701(4) Å β = 85.881(3)° c = 24.836(5) Å γ = 85.231(3)°
Volume	9981(3) Å ³
Z	131
Density (calculated)	0.764 Mg/m ³
Absorption coefficient	1.981 mm ⁻¹
F(000)	2245
Crystal size	0.115 x 0.085 x 0.050 mm ³
Theta range for data collection	0.827 to 24.764°
Index ranges	-23 ≤ h ≤ 23, -24 ≤ k ≤ 24, -29 ≤ l ≤ 29
Reflections collected	126669
Independent reflections	34105 [R(int) = 0.0994]
Completeness to theta = 24.764°	99.6 %
Refinement method	Full-matrix least-squares on F ²
Data / restraints / parameters	34105 / 0 / 1917
Goodness-of-fit on F ²	1.060
Final R indices [I > 2σ(I)]	R1 = 0.0981, wR2 = 0.2635
R indices (all data)	R1 = 0.1698, wR2 = 0.3262
Extinction coefficient	n/a
Largest diff. peak and hole	8.635 and -2.606 e.Å ⁻³

8.11 $[\text{Fe}_{36}\text{O}_{30}(\text{OH})_{34}(\text{C}_7\text{H}_9\text{N})_{24}\text{Br}_8] \cdot 6\text{Br}$

Identification code	ECL10291
Empirical formula	C168 H250 Br14 Fe36 N24 O64
Formula weight	6758.97
Temperature	150(2) K
Wavelength	0.71073 Å
Crystal system	Tetragonal
Space group	I -4
Unit cell dimensions	a = 22.793(2) Å α = 90° . b = 22.793(2) Å β = 90° . c = 29.389(3) Å γ = 90° .
Volume	15268(3) Å ³
Z	2
Density (calculated)	0.727 Mg/m ³
Absorption coefficient	1.770 mm ⁻¹
F(000)	3294
Crystal size	0.040 x 0.040 x 0.040 mm ³
Theta range for data collection	1.131 to 25.998° .
Index ranges	-28 ≤ h ≤ 28, -27 ≤ k ≤ 28, -36 ≤ l ≤ 35
Reflections collected	110654
Independent reflections	14969 [R(int) = 0.1599]
Completeness to theta = 25.242°	100.0 %
Refinement method	Full-matrix least-squares on F ²
Data / restraints / parameters	14969 / 0 / 618
Goodness-of-fit on F ²	1.357
Final R indices [I > 2σ(I)]	R1 = 0.1353, wR2 = 0.3445
R indices (all data)	R1 = 0.2344, wR2 = 0.4155
Absolute structure parameter	0.534(8)
Extinction coefficient	n/a
Largest diff. peak and hole	3.276 and -3.139 e.Å ⁻³

8.12 $[\text{Fe}_{36}\text{O}_{30}(\text{OH})_{34}(\text{C}_7\text{H}_9\text{N})_{24}\text{Br}_8] \cdot 6\text{Br}$

Identification code	DTL1304	
Empirical formula	C168 H250 Br14 Fe36 N24 O64	
Formula weight	6758.97	
Temperature	150(2) K	
Wavelength	0.71073 Å	
Crystal system	Tetragonal	
Space group	I 4/m	
Unit cell dimensions	a = 26.4575(18) Å	$\alpha = 90^\circ$.
	b = 26.4575(18) Å	$\beta = 90^\circ$.
	c = 37.452(6) Å	$\gamma = 90^\circ$.
Volume	26216(6) Å ³	
Z	2	
Density (calculated)	3.310 Mg/m ³	
Absorption coefficient	17.744 mm ⁻¹	
F(000)	23786	
Crystal size	0.040 x 0.040 x 0.020 mm ³	
Theta range for data collection	0.942 to 24.773°.	
Index ranges	-28 ≤ h ≤ 31, -27 ≤ k ≤ 31, -27 ≤ l ≤ 44	
Reflections collected	87874	
Independent reflections	11435 [R(int) = 0.1545]	
Completeness to theta = 24.773°	99.7 %	
Refinement method	Full-matrix least-squares on F ²	
Data / restraints / parameters	11435 / 0 / 534	
Goodness-of-fit on F ²	1.845	
Final R indices [I > 2σ(I)]	R1 = 0.1986, wR2 = 0.4811	
R indices (all data)	R1 = 0.3107, wR2 = 0.5413	
Extinction coefficient	n/a	
Largest diff. peak and hole	6.886 and -3.672 e.Å ⁻³	

8.13 $[\text{Fe}_{36}\text{O}_{30}(\text{OH})_{34}(\text{C}_6\text{H}_7\text{N})_{24}\text{Br}_8] \cdot 6\text{Br}$

Identification code	ECL10474_2	
Empirical formula	C144 H202 Br14 Fe36 N24 O64	
Formula weight	6422.33	
Temperature	150(2) K	
Wavelength	71.073 pm	
Crystal system	Cubic	
Space group	I -4 3 m	
Unit cell dimensions	a = 2.491(16) pm	$\alpha = 90^\circ$.
	b = 2.491(16) pm	$\beta = 90^\circ$.
	c = 2.491(16) pm	$\gamma = 90^\circ$.
Volume	15.45(1) nm ³	
Z	2	
Density (calculated)	1.468 Mg/m ³	
Absorption coefficient	3.459 mm ⁻¹	
F(000)	6552	
Crystal size	0.040 x 0.040 x 0.020 mm ³	
Theta range for data collection	1.156 to 25.971°.	
Index ranges	-30 ≤ h ≤ 30, -30 ≤ k ≤ 30, -27 ≤ l ≤ 30	
Reflections collected	59609	
Independent reflections	2796 [R(int) = 0.1069]	
Completeness to theta = 25.242°	100.0 %	
Refinement method	Full-matrix least-squares on F ²	
Data / restraints / parameters	2796 / 0 / 144	
Goodness-of-fit on F ²	1.142	
Final R indices [I > 2σ(I)]	R1 = 0.0514, wR2 = 0.1669	
R indices (all data)	R1 = 0.0641, wR2 = 0.1780	
Absolute structure parameter	0.036(8)	
Extinction coefficient	n/a	
Largest diff. peak and hole	1.620 and -3.158 e.Å ⁻³	

8.14 $[\text{Fe}_{36}\text{O}_{30}(\text{OH})_{34}(\text{C}_7\text{H}_9\text{N})_{24}\text{Br}_8] \cdot 6\text{Br}$

Identification code	ECL10903
Empirical formula	C168 H250 Br14 Fe36 N24 O64
Formula weight	6758.17
Temperature	150(2) K
Wavelength	0.71073 Å
Crystal system	Tetragonal
Space group	I -4
Unit cell dimensions	a = 25.432(9) Å $\alpha = 90^\circ$. b = 25.432(9) Å $\beta = 90^\circ$. c = 25.387(10) Å $\gamma = 90^\circ$.
Volume	16420(13) Å ³
Z	2
Density (calculated)	2.178 Mg/m ³
Absorption coefficient	4.876 mm ⁻¹
F(000)	10356
Crystal size	0.040 x 0.040 x 0.030 mm ³
Theta range for data collection	1.132 to 16.726°.
Index ranges	-20 ≤ h ≤ 20, -20 ≤ k ≤ 20, -19 ≤ l ≤ 20
Reflections collected	10703
Independent reflections	4515 [R(int) = 0.1117]
Completeness to theta = 16.726°	99.6 %
Refinement method	Full-matrix least-squares on F ²
Data / restraints / parameters	4515 / 0 / 503
Goodness-of-fit on F ²	1.362
Final R indices [I > 2σ(I)]	R1 = 0.1233, wR2 = 0.3363
R indices (all data)	R1 = 0.2099, wR2 = 0.3976
Absolute structure parameter	0.51(3)
Extinction coefficient	n/a
Largest diff. peak and hole	1.144 and -1.899 e.Å ⁻³

8.15 [Mo₁₀O₂₇(C₅H₅N)₇]

Identification code	ECL9676
Empirical formula	C ₄₉ H ₆₃ Mo ₁₀ N ₇ O ₂₇
Formula weight	2141.465
Temperature	150(2) K
Wavelength	0.71073 Å
Crystal system	Triclinic
Space group	P -1
Unit cell dimensions	a = 12.9552(11) Å α = 79.242(5)° . b = 15.9790(14) Å β = 85.649(5)° . c = 20.2321(16) Å γ = 72.339(5)° .
Volume	3919.9(6) Å ³
Z	2
Density (calculated)	1.814 Mg/m ³
Absorption coefficient	0.644 mm ⁻¹
F(000)	862
Crystal size	0.110 x 0.090 x 0.080 mm ³
Theta range for data collection	1.358 to 26.051° .
Index ranges	-14 ≤ h ≤ 15, -17 ≤ k ≤ 19, -24 ≤ l ≤ 23
Reflections collected	32570
Independent reflections	15077 [R(int) = 0.0736]
Completeness to theta = 25.242°	98.5 %
Refinement method	Full-matrix least-squares on F ²
Data / restraints / parameters	15077 / 0 / 838
Goodness-of-fit on F ²	1.026
Final R indices [I > 2σ(I)]	R1 = 0.0894, wR2 = 0.2487
R indices (all data)	R1 = 0.1251, wR2 = 0.2899
Extinction coefficient	n/a
Largest diff. peak and hole	4.278 and -3.676 e.Å ⁻³

8.16 n-[FeBr₂(C₄H₄N₂)]

Identification code	ECL11163_1	
Empirical formula	C ₄ H ₄ Br ₂ Fe ₁ N ₂	
Formula weight	289.67	
Temperature	150(2) K	
Wavelength	71.073 pm	
Crystal system	Tetragonal	
Space group	I 41	
Unit cell dimensions	a = 7.5621(7) Å	α = 90°.
	b = 7.5621(7) Å	β = 90°.
	c = 20.262(2) Å	γ = 90°.
Volume	1158.68(19) Å ³	
Z	4	
Density (calculated)	2.154 Mg/m ³	
Absorption coefficient	1.172 mm ⁻¹	
F(000)	103	
Crystal size	0.120 x 0.100 x 0.070 mm ³	
Theta range for data collection	2.875 to 25.999°.	
Index ranges	-7 ≤ h ≤ 9, -4 ≤ k ≤ 9, -13 ≤ l ≤ 24	
Reflections collected	1299	
Independent reflections	808 [R(int) = 0.0205]	
Completeness to theta = 25.242°	100.0 %	
Refinement method	Full-matrix least-squares on F ²	
Data / restraints / parameters	808 / 1 / 64	
Goodness-of-fit on F ²	0.998	
Final R indices [I > 2σ(I)]	R1 = 0.0246, wR2 = 0.0487	
R indices (all data)	R1 = 0.0305, wR2 = 0.0509	
Absolute structure parameter	0.10(3)	
Extinction coefficient	n/a	
Largest diff. peak and hole	0.376 and -0.359 e.Å ⁻³	

8.17 $[\text{Fe}_4\text{O}_2\text{Br}_5(\text{C}_8\text{H}_8\text{N}_2)_6] \cdot (\text{Br}_6\text{Fe}_2\text{O}) \cdot 6(\text{C}_2\text{C}_3\text{N})$

Identification code	ECL10363
Empirical formula	C58 H36 Br11 Fe6 N18 O3
Formula weight	2233.06
Temperature	150(2) K
Wavelength	0.71073 Å
Crystal system	Monoclinic
Space group	P 21/n
Unit cell dimensions	a = 32.642(3) Å α = 90° . b = 16.6983(15) Å β = 119.802(4)° . c = 32.701(3) Å γ = 90° .
Volume	15467(2) Å ³
Z	8
Density (calculated)	1.918 Mg/m ³
Absorption coefficient	0.853 mm ⁻¹
F(000)	1058
Crystal size	0.100 x 0.095 x 0.095 mm ³
Theta range for data collection	1.243 to 25.999° .
Index ranges	-38 ≤ h ≤ 40, -20 ≤ k ≤ 20, -40 ≤ l ≤ 40
Reflections collected	120904
Independent reflections	30400 [R(int) = 0.1017]
Completeness to theta = 25.242°	100.0 %
Refinement method	Full-matrix least-squares on F ²
Data / restraints / parameters	30400 / 0 / 1675
Goodness-of-fit on F ²	1.113
Final R indices [I > 2σ(I)]	R1 = 0.0847, wR2 = 0.1950
R indices (all data)	R1 = 0.1418, wR2 = 0.2268
Extinction coefficient	n/a
Largest diff. peak and hole	4.291 and -2.647 e.Å ⁻³

8.18 [Fe₈O₄(C₆H₆NO)₈Br₈]

Identification code	ECLFepm_180619a18
Empirical formula	C ₄₈ H ₄₈ Br ₈ Fe ₈ N ₈ O ₁₂
Formula weight	2015.02
Temperature	150(2) K
Wavelength	0.71073 Å
Crystal system	Monoclinic
Space group	C 2/c
Unit cell dimensions	a = 17.752(7) Å α = 90°. b = 21.347(7) Å β = 94.05(4)°. c = 18.403(9) Å γ = 90°.
Volume	6956(5) Å ³
Z	4
Density (calculated)	1.924 Mg/m ³
Absorption coefficient	6.270 mm ⁻¹
F(000)	3904
Crystal size	0.070 x 0.050 x 0.040 mm ³
Theta range for data collection	1.494 to 24.784°.
Index ranges	-19 ≤ h ≤ 20, -20 ≤ k ≤ 25, -11 ≤ l ≤ 21
Reflections collected	13924
Independent reflections	5891 [R(int) = 0.1810]
Completeness to theta = 24.784°	98.4 %
Refinement method	Full-matrix least-squares on F ²
Data / restraints / parameters	5891 / 0 / 379
Goodness-of-fit on F ²	1.110
Final R indices [I > 2σ(I)]	R1 = 0.0920, wR2 = 0.1943
R indices (all data)	R1 = 0.2418, wR2 = 0.2593
Extinction coefficient	n/a
Largest diff. peak and hole	2.232 and -1.009 e.Å ⁻³

8.19 $[\text{Fe}_{17}\text{O}_{16}(\text{C}_7\text{H}_8\text{ON})_{12}\text{Br}_4] \cdot 3\text{Br} \cdot 0.5(\text{Br}_6\text{Fe}_2\text{O})$

Identification code	ECL10396
Empirical formula	C ₈₄ H ₉₆ Br _{13.50} Fe _{21.33} N ₁₂ O ₂₉
Formula weight	4007.98
Temperature	150(2) K
Wavelength	0.71073 Å
Crystal system	Monoclinic
Space group	P 2 ₁ /n
Unit cell dimensions	a = 21.9939(19) Å α = 90° . b = 25.306(2) Å β = 99.176(4)° . c = 24.548(2) Å γ = 90° .
Volume	13488(2) Å ³
Z	4
Density (calculated)	1.974 Mg/m ³
Absorption coefficient	7.063 mm ⁻¹
F(000)	9224
Crystal size	0.130 x 0.100 x 0.080 mm ³
Theta range for data collection	1.155 to 26.000° .
Index ranges	-27 ≤ h ≤ 26, -31 ≤ k ≤ 31, -30 ≤ l ≤ 25
Reflections collected	144156
Independent reflections	26498 [R(int) = 0.0823]
Completeness to theta = 25.242°	100.0 %
Refinement method	Full-matrix least-squares on F ²
Data / restraints / parameters	26498 / 0 / 1539
Goodness-of-fit on F ²	1.045
Final R indices [I > 2σ(I)]	R1 = 0.0726, wR2 = 0.2012
R indices (all data)	R1 = 0.1273, wR2 = 0.2441
Extinction coefficient	n/a
Largest diff. peak and hole	2.722 and -2.814 e.Å ⁻³

8.20 n-[Fe₂(C₅H₅N)₂Br₂(C₂O₄)O]

Identification code	ECL10614_2	
Empirical formula	C7 H5 Br2 Fe2 N2 O5	
Formula weight	12.41	
Temperature	150(2) K	
Wavelength	0.71073 Å	
Crystal system	Monoclinic	
Space group	C 2/c	
Unit cell dimensions	a = 13.834(6) Å	α = 90°.
	b = 12.210(6) Å	β = 109.672(7)°.
	c = 16.691(8) Å	γ = 90°.
Volume	2655(2) Å ³	
Z	34	
Density (calculated)	0.264 Mg/m ³	
Absorption coefficient	0.650 mm ⁻¹	
F(000)	207	
Crystal size	0.070 x 0.040 x 0.35 mm ³	
Theta range for data collection	2.876 to 25.998°.	
Index ranges	-17<=h<=17, -15<=k<=15, -17<=l<=20	
Reflections collected	8211	
Independent reflections	2587 [R(int) = 0.0381]	
Completeness to theta = 25.242°	98.8 %	
Refinement method	Full-matrix least-squares on F ²	
Data / restraints / parameters	2587 / 0 / 159	
Goodness-of-fit on F ²	1.206	
Final R indices [I>2sigma(I)]	R1 = 0.0906, wR2 = 0.2267	
R indices (all data)	R1 = 0.0995, wR2 = 0.2304	
Extinction coefficient	n/a	
Largest diff. peak and hole	2.611 and -1.362 e.Å ⁻³	

8.21 n-[Fe(C₅H₅N)₄(SO₄)]

Identification code	ECL10784	
Empirical formula	C ₂₀ H ₂₀ Fe ₁ N ₄ O ₄ S ₁	
Formula weight	268.30	
Temperature	150(2) K	
Wavelength	0.71073 Å	
Crystal system	Monoclinic	
Space group	C 2/c	
Unit cell dimensions	a = 18.619(3) Å	α = 90°.
	b = 9.992(2) Å	β = 115.782(7)°.
	c = 11.789(2) Å	γ = 90°.
Volume	1974.9(7) Å ³	
Z	8	
Density (calculated)	1.5749 Mg/m ³	
Absorption coefficient	0.215 mm ⁻¹	
F(000)	142	
Crystal size	0.160 x 0.080 x 0.050 mm ³	
Theta range for data collection	2.373 to 26.000°.	
Index ranges	-21 ≤ h ≤ 16, -6 ≤ k ≤ 12, -12 ≤ l ≤ 14	
Reflections collected	3369	
Independent reflections	1765 [R(int) = 0.0180]	
Completeness to theta = 25.242°	91.3 %	
Refinement method	Full-matrix least-squares on F ²	
Data / restraints / parameters	1765 / 0 / 178	
Goodness-of-fit on F ²	1.060	
Final R indices [I > 2σ(I)]	R1 = 0.0253, wR2 = 0.0632	
R indices (all data)	R1 = 0.0297, wR2 = 0.0657	
Extinction coefficient	n/a	
Largest diff. peak and hole	0.209 and -0.348 e.Å ⁻³	

8.22 $[\text{Fe}_{16}\text{O}_8(\text{C}_2\text{O}_4)_{16}(\text{C}_5\text{H}_5\text{N})_{12}\text{Br}_4] \cdot 4(\text{C}_5\text{H}_6\text{N}) \cdot 4(\text{C}_5\text{H}_5\text{N}) \cdot (\text{C}_2\text{H}_3\text{N})$

Identification code	ECLFEAA_180524A20	
Empirical formula	C136 H114 Br4 Fe16 N22 O72	
Formula weight	4421.73	
Temperature	150(2) K	
Wavelength	0.71073 Å	
Crystal system	Monoclinic	
Space group	P 21/n	
Unit cell dimensions	a = 14.5872(16) Å	$\alpha = 90^\circ$.
	b = 29.389(3) Å	$\beta = 100.949(5)^\circ$.
	c = 19.482(2) Å	$\gamma = 90^\circ$.
Volume	8199.9(16) Å ³	
Z	2	
Density (calculated)	1.791 Mg/m ³	
Absorption coefficient	2.445 mm ⁻¹	
F(000)	4432	
Crystal size	0.100 x 0.050 x 0.050 mm ³	
Theta range for data collection	1.582 to 24.135°.	
Index ranges	-16 ≤ h ≤ 16, -33 ≤ k ≤ 27, -22 ≤ l ≤ 20	
Reflections collected	51219	
Independent reflections	13007 [R(int) = 0.0627]	
Completeness to theta = 24.135°	99.3 %	
Absorption correction	Semi-empirical from equivalents	
Max. and min. transmission	0.745 and 0.615	
Refinement method	Full-matrix least-squares on F ²	
Data / restraints / parameters	13007 / 46 / 1055	
Goodness-of-fit on F ²	1.023	
Final R indices [I > 2σ(I)]	R1 = 0.0564, wR2 = 0.1334	
R indices (all data)	R1 = 0.1094, wR2 = 0.1578	
Extinction coefficient	n/a	
Largest diff. peak and hole	1.17 and -0.87 e.Å ⁻³	

9 References

1. Long, D. L., Tsunashima, R. & Cronin, L. Polyoxometalates: Building blocks for functional nanoscale systems. *Angew. Chemie - Int. Ed.* **49**, 1736-1758 (2010).
2. Kondinski, A. & Parac-Vogt, T. N. Keggin Structure, Quō Vādis? *Front. Chem.* **6**, 1-7 (2018).
3. Sadeghi, O., Zakharov, L. N. & Nyman, M. Aqueous formation and manipulation of the iron-oxo Keggin ion. *Science (80-.)*. **347**, 2013-2017 (2015).
4. Kyung, H., Kim, C., Talkner, P. & Kyun, E. Brownian motion from molecular dynamics. *Chem. Phys.* **375**, 316-326 (2010).
5. Stipčević, M. & Koç, Ç. K. True Random Number Generators. *Open Probl. Math. Comput. Sci.* 275-315 (2014).
6. Combs-Walker, L. A. & Hill, C. L. Use of Excited-State and Ground-State Redox Properties of Polyoxometalates for Selective Transformation of Unactivated Carbon-Hydrogen Centers Remote from the Functional Group in Ketones. *J. Am. Chem. Soc.* **114**, 938-946 (1992).
7. Thouvenot, R., Fournier, M. & Rocchiccioli-deltcheff, C. Catalysis by Polyoxometalates. *J. Chem. Soc. Faraday Trans* **87**, 2829-2835 (1991).
8. Li, M. *et al.* Self-assembled peptide-polyoxometalate hybrid nanospheres: Two in one enhances targeted inhibition of amyloid β -peptide aggregation associated with Alzheimer's disease. *Small* **9**, 3455-3461 (2013).
9. Hu, X. *et al.* A new scheme for rational design and synthesis of polyoxovanadate hybrids with high antitumor activities. *J. Inorg. Biochem.* **193**, 130-132 (2019).
10. Chen, J. J., Symes, M. D. & Cronin, L. Highly reduced and protonated aqueous solutions of [P2W18O62]6- for on-demand hydrogen generation and energy storage. *Nat. Chem.* **10**, 1042-1047 (2018).
11. MacDonald, L. *et al.* Using earth abundant materials for the catalytic

- evolution of hydrogen from electron-coupled proton buffers. *Sustain. Energy Fuels* **1**, 1782-1787 (2017).
12. Busche, C. *et al.* Design and fabrication of memory devices based on nanoscale polyoxometalate clusters. *Nature* **515**, 545-549 (2014).
 13. Clemente-Juan, J. M., Coronado, E. & Gaita-Ariño, A. Magnetic polyoxometalates: From molecular magnetism to molecular spintronics and quantum computing. *Chem. Soc. Rev.* **41**, 7464-7478 (2012).
 14. Richardt, P. J. S., Gable, R. W., Bond, A. M. & Wedd, A. G. Synthesis and redox characterization of the polyoxo anion, γ^* -[S₂W₁₈O₆₂]⁴⁻: A unique fast oxidation pathway determines the characteristic reversible electrochemical behavior of polyoxometalate anions in acidic media. *Inorg. Chem.* **40**, 703-709 (2001).
 15. Miras, H. N., Long, D. & Cronin, L. Exploring Self-Assembly and the Self-Organization of Nanoscale Inorganic Polyoxometalate Clusters. *Adv. Inorg. Chem.* **69**, 1-28 (2017).
 16. Baker, L. C. W. *et al.* Present General Status of Understanding of Heteropoly Electrolytes and a Tracing of Some Major Highlights in the History of Their Elucidation. *Chem. Rev.* **98**, 3-49 (1998).
 17. Nyman, M. & Burns, P. C. A comprehensive comparison of transition-metal and actinyl polyoxometalates. *Chem Soc Rev* **41**, 7354-7367 (2012).
 18. Samangi Abeysinghe, Daniel K. Unruh, and T. Z. F. Keggin-type aluminum nanoclusters: synthesis, structural characterization and environmental implications. *Dalton. Trans.* **52**, 5991-5999 (2012).
 19. La, L. *et al.* Formation of Ti₂₈ Ln Cages, the Highest Nuclearity Polyoxotitanates. *Chem. - A Eur. J.* **18**, 11867-11870 (2012).
 20. Tasiopoulos, A. J., Vinslava, A., Wernsdorfer, W., Abboud, K. A. & Christou, G. Giant Single-Molecule Magnets: A {Mn₈₄} Torus and Its Supramolecular Nanotubes. *Angew. Chemie Int. Ed.* **43**, 2117-2121 (2004).
 21. Kondinski, A. & Monakhov, K. Y. Breaking the Gordian Knot in the Structural Chemistry of Polyoxometalates: Copper(II)-Oxo/Hydroxo Clusters. *Chem.* -

- A Eur. J.* **23**, 7841-7852 (2017).
22. Zheng, X. *et al.* A Gigantic Molecular Wheel of {Gd 140}: A New Member of the Molecular Wheel Family. *J. Am. Chem. Soc.* **130**, 18178-18181 (2017).
 23. Xu, F. *et al.* Correlating the magic numbers of inorganic nanomolecular assemblies with a f Pd 84 g. *Proc. Natl. Acad. Sci.* **109**, 11609-11612 (2012).
 24. Long, D., Burkholder, E., Cronin, L. & Burkholder, E. Polyoxometalate clusters, nanostructures and materials: From self assembly to designer materials and devices. *Chem Soc Rev* **36**, 105-121 (2007).
 25. Hutin, M., Rosnes, M. H., Long, D. L. & Cronin, L. *Polyoxometalates: Synthesis and Structure - From Building Blocks to Emergent Materials. Comprehensive Inorganic Chemistry II (Second Edition): From Elements to Applications 2*, (Elsevier Ltd., 2013).
 26. K. A. Persson, B. Waldwick, P. Lazic, G. C. Prediction of solid-aqueous equilibria: Scheme to combine first-principles calculations of solids with experimental aqueous states. *Phys. Rev. B* **85**, 235438 (2012).
 27. A. Boulay, G. J. T. Cooper, L. C. Directed Assembly of Polyoxometalates across Length Scales: From Macro-Molecules to Microsystems and ICells. in *Polyoxometalate Chemistry: Some recent Trends* 101-153 (2013).
 28. Coe, B. J. & Glenwright, S. J. Trans-effects in octahedral transition metal complexes. *Coord. Chem. Rev.* **203**, 5-80 (2000).
 29. Pope, M. T. Heteropoly and Isopoly Anions as Oxo Complexes and Their reducibility to Mixed-Valence "Blues". *Inorg. Chem.* **11**, 1973-1974 (1972).
 30. Tan, H. Q., Chen, W. L., Liu, D., Li, Y. G. & Wang, E. B. Spontaneous resolution of a new diphosphonate-functionalized polyoxomolybdate. *CrystEngComm* **12**, 4017-4019 (2010).
 31. Müller, A., Beckmann, E., Bögge, H., Schmidtman, M. & Dress, A. Mo₃₆₈. *Angew. Chemie Int. Ed.* **41**, 1162-1167 (2002).
 32. Lipscomb, W. N. The Paratungstate ion. *Inorg. Chem.* **4**, 132-134 (1965).
 33. Lindqvist, I. The structure of the tetramolybdate ion. *Askiv kemi* **2**, 349-355

- (1950).
34. Fuchs, J., Freiwald, W. & Hartl, H. Neubestimmung der Kristallstruktur von Tetrabutylammoniumhexawolframat. *Acta Crystallogr. Sect. B Struct. Crystallogr. Cryst. Chem.* **34**, 1764-1770 (1978).
 35. Nyman, M. *et al.* Solid-state structures and solution behavior of alkali salts of the $[\text{Nb}_6\text{O}_{19}]^{8-}$ Lindqvist ion. *J. Clust. Sci.* **17**, 197-219 (2006).
 36. Pickhard, F. & Hartl, H. Die Kristallstrukturen von $\text{K}_8\text{Ta}_6\text{O}_{19} \cdot 16\text{H}_2\text{O}$ und $\text{K}_7\text{NaTa}_6\text{O}_{19} \cdot 14\text{H}_2\text{O}$. *Zeitschrift für Anorg. und Allg. Chemie* **623**, 1311-1316 (1997).
 37. Batchelor, L. J., Shaw, R., Markey, S. J., Helliwell, M. & McInnes, E. J. L. An all-vanadiuni(III) hexametalate lindqvist structure and its chromium and iron analogues. *Chem. - A Eur. J.* **16**, 5554-5557 (2010).
 38. Chae, H. K., Klemperer, W. G. & Day, V. W. An Organometal Hydroxide Route to $[(\text{C}_5\text{Me}_5)\text{Rh}]_4(\text{V}_6\text{O}_{19})$. *Inorg. Chem.* **28**, 1423-1424 (1989).
 39. Kaziev, G. Z. *et al.* Synthesis and study of aluminum hexamolybdenocobaltate(III) and hexamolybdenochromate(III). *Russ. J. Coord. Chem. Khimiya* **28**, 635-637 (2002).
 40. Marcoux, P. R., Hasenknopf, B., Vaissermann, J. & Gouzerh, P. Developing remote metal binding sites in heteropolymolybdates. *Eur. J. Inorg. Chem.* 2406-2412 (2003).
 41. Evans, H. T. The crystal structures of ammonium and potassium molybdotellurates. *J. Am. Chem. Soc.* **70**, 1291-1292 (1948).
 42. Martin, C. *et al.* Preparation and characterization of 6-molybdocobaltate and 6-molybdoaluminate cobalt salts. Evidence of a new heteropolymolybdate structure. *Inorg. Chem.* **43**, 4636-4644 (2004).
 43. Sazonova, O. I., Rozantsex, G. M., Kholin, Y. V. The State of Tungsten(VI) Ions in Water Solutions. *Russ. J. Coord. Chem.* **43**, 1765-1769 (1998).
 44. Sturdivant, J. H. The Formula of Ammonium Paramolybdate. *J. Am. Chem. Soc.* **59**, 630-631 (1937).

45. Monakhov, K. Y., Gourlaouen, C., Pattacini, R. & Braunstein, P. Heptabismuthate [Bi₇I₂₄]³⁻: A main group element anderson-type structure and its relationships with the polyoxometalates. *Inorg. Chem.* **51**, 1562-1568 (2012).
46. Zhang, Jiangwei; Huang, Yichao; Li, G. & Wei, Y. Recent advances in alkoxylation chemistry of polyoxometalates: From synthetic strategies, structural overviews to functional applications. *Coord. Chem. Rev.* **378**, 395-414 (2019).
47. Marignac, C. M. Recherches sur les acides silicotungstiques, et note sur la constitution de l'acide tungstique. *Ann. chimie physique* **3**, 5-77 (1864).
48. J. F. Keggin. Structure and Formula of 12-phosphotungstic Acid. *Proc. R. Soc. London* **144**, 75-100 (1934).
49. Mialane, P. *et al.* [ϵ -PMo₁₂O₃₆(OH)₄{La(H₂O)₄}]₅⁺: The First ϵ -PMo₁₂O₄₀ Keggin Ion and Its Association with the Two-Electron-Reduced α -PMo₁₂O₄₀ Isomer. *Angew. Chemie (Int. ed.)* **41**, 2398-2401 (2002).
50. Evans, H. T. & Popev, M. T. Reinterpretation of five recent crystal structures of heteropoly and isopoly complexes: divanadododecamolybdophosphate, trivanadododecamolybdophosphate, ' γ -dodecatungstophosphate', the dodecamolybdate-dodecamolybdomolybdate blue complex, and dihydrogen. *Inorg. Chem.* **23**, 501-504 (2005).
51. Sartzi, H., Miras, H. N., Vilà-Nadal, L., Long, D. L. & Cronin, L. Trapping the δ Isomer of the Polyoxometalate-Based Keggin Cluster with a Tripodal Ligand. *Angew. Chemie - Int. Ed.* **54**, 15488-15492 (2015).
52. Rocchiccioli-Deltcheff, C., Fournier, M., Franck, R. & Thouvenot, R. Vibrational Investigations of Polyoxometalates. 2. Evidence for Anion-Anion Interactions in Molybdenum(VI) and Tungsten(VI) Compounds Related to the Keggin Structure. *Inorg. Chem.* **22**, 207-216 (1983).
53. Himeno, S., Takamoto, M., Hoshiba, M., Higuchi, A. & Hashimoto, M. Preparation and Characterization of an α -Keggin-Type [SW₁₂O₄₀]₂-Complex. *Bull. Chem. Soc. Jpn.* **77**, 519-524 (2004).

54. Tucher, J., Nye, L. C., Ivanovic-Burmazovic, I., Notarnicola, A. & Streb, C. Chemical and photochemical functionality of the first molecular bismuth vanadium oxide. *Chem. - A Eur. J.* **18**, 10949-10953 (2012).
55. Chae, H. K., Klemperer, W. G., Loyo, D. E. P., Day, V. W. & Eberspacher, T. A. Synthesis and Structure of a High Nuclearity Oxomolybdenum(V) Complex, [(C5Me5RhIII)8(MoV12O36)(MoVIO4)]²⁺. *Inorg. Chem.* **31**, 3187-3189 (1992).
56. Baker, L. C. W. & McCutcheon, T. P. Heteropoly Salts Containing Cobalt and Hexavalent Tungsten in the Anion. *J. Am. Chem. Soc.* **78**, 4503-4510 (1956).
57. Khan, M. I. *et al.* Cation Inclusion within the Mixed-Valence Polyanion Cluster [(MoVIO3)4Mo12VO28(OH)12]8⁻: Syntheses and Structures of (NH4)7[NaMo16(OH)12O40]·4H2O and (Me2NH2)6[H2Mo16(OH)12O40]. *Angew. Chemie Int. Ed. English* **32**, 1780-1782 (1993).
58. Yamase, T. Isopoly and Heteropoly Compounds of Molybdenum, Tungsten, and Vanadium. *Eur. J. Inorg. Chem.* **2019**, 343-345 (2019).
59. Jia Le, Ya-Guang Chen, C.-J. Z. Formation of [FeW12O40]⁵⁻ under hydrothermal conditions: syntheses, crystal structures, and characterization of [Fe(2,2'-bipy)3]2[HFeW12O40] · 5H2O and (4,4'-H2bipy)6(Hpy)2(H3O)[FeW12O40]3 · 11H2O. *J. Coord. Chem.* **62**, 3810-3818 (2009).
60. Wang, Jing-ping., Ma, Peng-toa., Li, Jie., Niu, J. Hybrid Tungstocuprate [Cu(2,2'-bpy)3]2 H4 [CuW12O40] · 6H2 O Based on Keggin Polyoxoanion [CuW12O40]6⁻ with CuII as Heteroatom. *Chem. Res. Chinese Univ.* **23**, 263-267 (2007).
61. Yan, D. *et al.* Hydrothermal synthesis, structure characterization and catalytic property of a zigzag chain structural cluster compound built on the novel tetra-capped and centered by Ni II. *Inorg. Chem. Commun.* **14**, 1314-1317 (2011).
62. Luo, J. *et al.* Dual Functions of Water in Stabilizing Metal-Pentazolate Hydrates [M (N 5) 2 (H 2 O) 4] · 4H 2 O (M = Mn , Fe , Co , and Zn) High-Energy-Density Materials. **2**, 2-7 (2018).

63. Guo, G., Xu, Y., Cao, J. & Hu, C. An unprecedented vanadoniobate cluster with 'trans-vanadium' bicapped Keggin-type $\{V Nb_{12} O_{40} (VO)_2\}$. *Chem. Commun.* **47**, 9411-9413 (2011).
64. Dutta, A. K. & Ghosh, R. Molecular iron clusters, wheels and cages: Syntheses, structural aesthetics and magnetic properties. *Inorg. Chem. Commun.* **14**, 337-342 (2011).
65. Meng, W., Xu, F. & Xu, W. An Anionic Heptacopper(II) Oxo-Cluster $\{Cu_{II} 7\}$ with an $S = 7/2$ Ground State. *Inorg. Chem.* **55**, 540-542 (2016).
66. Johansson, G., Gullman, L.-O., Kjekshus, A. & Söderquist, R. On the Crystal Structure of Some Basic Aluminium Salts. *Acta Chemica Scandinavica* **14**, 771-773 (1960).
67. Dong, L., Li, X., Cao, J., Chu, W. & Huang, R. An α -Keggin polyoxometalate completely constructed from the late transition metal Co II as poly atom. *Dalt. Trans.* **42**, 1342-1345 (2013).
68. Dong, L., Huang, R., Wei, Y. & Chu, W. A remarkable member of the polyoxometalates: The eight-nickel-capped α -keggin polyoxoazonickelate. *Inorg. Chem.* **48**, 7528-7530 (2009).
69. Izarova, N. V. *et al.* Heteropoly-13-Palladates(II) $[Pd_{II} 13 (As V Ph)_8 O_{32}]^{6-}$ and $[Pd_{II} 13 Se IV 8 O_{32}]^{6-}$. *Inorg. Chem.* **48**, 7504-7506 (2009).
70. Kipra, R. & Mullerbuschbaum, H. Alkaline-earth Oxocuprate(II) with Closed Structural Groups: $BaCuO_2$. *Zeitschrift fur Naturforsch. Sect. B-A J. Chem. Sci.* **32**, 121-123 (1977).
71. Newton, G. N. *et al.* Redox-controlled magnetic $\{Mn_{13}\}$ Keggin systems. *Angew. Chemie - Int. Ed.* **50**, 5716-5720 (2011).
72. Sadeghi, O., Zakharov, L. N. & Nyman, M. Aqueous formation and manipulation of the iron-oxo Keggin ion. **347**, 2013-2017 (2015).
73. Fleet, M. e. The structure of magnetite. *ACTA Crystallogr. Sect. B-Structural Sci.* **37**, 917-920 (1981).
74. F. Marc Michel, Lars Ehm, Sytle M. Antao, Peter L. Lee, Peter J. Chupas,

- Gang Liu, Daniel R. Strongin, M. A. A. & Schoonen, B. L. P. and J. B. P. The Structure of Ferrihydrite, a Nanocrystalline Material. *Science* (80-.). **316**, 1726-1729 (2007).
75. Baumgartner, J. *et al.* Nucleation and growth of magnetite from solution. *Nat. Mater.* **12**, 310-314 (2013).
76. Banfield, J. F., Welch, S. A., Zhang, H., Ebert, T. T. & Penn, R. L. Aggregation-Based and in Growth Microstructure Natural Development Iron Oxyhydroxide Biomineralization Products. *Science* (80-.). **289**, 751-754 (2000).
77. Dawson, B. The structure of the 9(18)-heteropoly anion in potassium 9(18)-tungstophosphate, $K_6(P_2W_{18}O_{62}) \cdot 14H_2O$. *Acta Crystallogr.* **6**, 113-126 (1953).
78. Jansen, S. A., Wang, S. H. & Eddowes, A. D. Stability and acidity contributions of heteropolymetalates: a theoretical study of the Keggin and Dawson ions. *Supramol. Sci.* **4**, 51-58 (1997).
79. Contant, R. & Thouvenot, R. A reinvestigation of isomerism in the Dawson structure: syntheses and ^{183}W NMR structural characterization of three new polyoxotungstates $[X_2W_{18}O_{62}]^{6-}$ ($X=P, As$). *Inorganica Chim. Acta* **212**, 41-50 (1993).
80. Janusson, E., de Kler, N., Vilà-Nadal, L., Long, D.-L. & Cronin, L. Synthesis of polyoxometalate clusters using carbohydrates as reducing agents leads to isomer-selection. *Chem. Commun.* 2-5 (2019). doi:10.1039/C9CC02361E
81. Wu, H. Chemistry of Acids. *J. Biol. Chem.* **43**, 189-220 (1920).
82. Zhang, F. Q. *et al.* On the origin of the relative stability of wells-dawson isomers: A DFT study of α -, β -, γ -, α^* -, β^* -, and γ^* - $[(PO_4)_2W_{18}O_{54}]^{6-}$ anions. *Inorg. Chem.* **50**, 4967-4977 (2011).
83. Rudnick, R. L. and G. S. Composition of the Continental Crust. *Treatise on Geochemistry* **1**, (2003).
84. R. M. Cornell, U. S. *The iron oxides: Structure, Properties, Reactions, Occurrences and Uses.* (2004).

85. Hazen, R. M. & Jeanloz, R. Wüstite (Fe_{1-x}O): A review of its defect structure and physical properties. *Rev. Geophys.* **22**, 37-46 (1984).
86. Qin, X. Y., Kim, J. G. & Lee, J. S. Synthesis and magnetic properties of nanostructured γ -Ni-Fe alloys. *Nanostructured Mater.* **11**, 259-270 (1999).
87. Pauling, L. & Hendricks, S. B. The crystal structures of hematite and corundum. *J. Am. Chem. Soc.* **47**, 781-790 (1925).
88. Bragg, W. H. The Structure of Magnetite and the Spinel. *Nature* **95**, 561 (1915).
89. F. Marc Michel, Lars Ehm, Sylte <. Antao, Peter L. Lee, Peter J. Chupas, Gang Liu, Daniel R. Strongin, Martin A. A. Schoonen, Brian L. Phillips, J. B. P. The Structure of Ferrihydrite, a nanocrystalline material. *Science (80-.)*. **316**, 1726-1729 (2007).
90. Ewing, F. J. The crystal structure of lepidocrocite. *J. Chem. Phys.* **3**, 420-424 (1935).
91. Nazanin Abbaspour, Richard Hurrell, R. K. Review on iron and its importance for human health. *J. Res. Med. Sci.* **19**, 164-174 (2014).
92. Hurrell, R. F. Bioavailability of iron. *Eur. J. Clin. Nutr.* **51**, 4-8 (1997).
93. Kim, M. *et al.* PH-dependent structures of ferritin and apoferritin in solution: Disassembly and reassembly. *Biomacromolecules* **12**, 1629-1640 (2011).
94. Freeman, H. J. Iron deficiency anemia in celiac disease. *World J. Gastroenterology* **21**, 9233-9238 (2015).
95. Hradil, D., Grygar, T., Hradilová, J. & Bezdička, P. Clay and iron oxide pigments in the history of painting. *Appl. Clay Sci.* **22**, 223-236 (2003).
96. O'Grady, P. F. *Thales of Miletus: The Beginnings of Western Science and Philosophy*. (Routledge, 2017).
97. Gregor, C. *et al.* The effect of surface area and crystal structure on the catalytic efficiency of Iron(III) oxide nanoparticles in hydrogen peroxide decomposition. *Eur. J. Inorg. Chem.* 2343-2351 (2010).

98. Chaturvedi, S., Dave, P. N. & Shah, N. K. Applications of nano-catalyst in new era. *J. Saudi Chem. Soc.* **16**, 307-325 (2012).
99. Pinna, F., Fantinel, T., Strukul, G., Benedetti, A. & Pernicone, N. TPR and XRD study of ammonia synthesis catalysts. *Appl. Catal. A Gen.* **149**, 341-351 (1997).
100. Patil, P. R., Krishnamurthy, V. N. & Joshi, S. S. Differential scanning calorimetric study of HTPB based composite propellants in presence of nano ferric oxide. *Propellants, Explos. Pyrotech.* **31**, 442-446 (2006).
101. Tiefenauer, L. X., Kühne, G. & Andres, R. Y. Antibody-Magnetite Nanoparticles: In Vitro Characterization of a Potential Tumor-Specific Contrast Agent for Magnetic Resonance Imaging. *Bioconjug. Chem.* **4**, 347-352 (1993).
102. Pouliquen, D., Le Jeune, J. J., Perdrisot, R., Ermias, A. & Jallet, P. Iron oxide nanoparticles for use as an MRI contrast agent: Pharmacokinetics and metabolism. *Magn. Reson. Imaging* **9**, 275-283 (1991).
103. Gass, I. A., Brechin, E. K. & Evangelisti, M. Cryogenic magnetocaloric effect in the Fe₁₇ molecular nanomagnet. *Polyhedron* **52**, 1177-1180 (2013).
104. Delfs, C. *et al.* Magnetic Properties of an Octanuclear Iron(III) Cation. *Inorg. Chem.* **32**, 3099-3103 (1993).
105. Hershko, C. *et al.* Role of autoimmune gastritis, Helicobacter pylori and celiac disease in refractory or unexplained iron deficiency anemia. *Haematologica* **90**, 585-95 (2005).
106. Beverskog, B. & Puigdomenech, I. Revised Pourbaix diagrams for iron at 25-300 °C. *Corros. Sci.* **38**, 2121-2135 (1996).
107. C. F. Baes, R. E. M. *The Hydrolysis of Cations.* (J. Wiley and Sons, 1976).
108. Jolivet, J. *et al.* Iron oxide chemistry . From molecular clusters to extended solid networks. 481-487 (2004).
109. Jolivet, J. P. *Metal Oxide Chemistry and Synthesis. From Solution to Solid State.* (Wiley, 2000).

110. Hegetschweiler, K., Schmalle, H., Streit, H. M. & Schneider, W. Synthesis and structure of a novel hexanuclear iron(III) complex containing six terminal and twelve bridging groups and one μ_6 -oxo bridge. *Inorg. Chem.* **29**, 3625-3627 (1990).
111. Hegetschweiler, K. *et al.* A Simple, Efficient Route to a μ_6 -Oxo-Centered Hexanuclear Iron(III) Alkoxide Complex: Preparation and Structure of $\text{Na}_2\text{Fe}_6\text{O}(\text{OCH}_3)_{18}\cdot 6\text{CH}_3\text{OH}$. *Inorg. Chem.* **31**, 1299-1302 (1992).
112. Heptanuclear, T. *et al.* Solvothermal Syntheses and Structural Characterizations of Polyoxoalkoxometalates : **11**, (2000).
113. Nachtigall, O. *et al.* 'Super-Lindqvist' Aggregate and Large 3D Interpenetrating Coordination Polymer from Solvothermal Reactions of $[\text{Fe}_2(\text{OtBu})_6]$ with Ethanol. *Angew. Chemie - Int. Ed.* **54**, 10361-10364 (2015).
114. Bino, A., Ardon, M., Lee, D., Spingler, B. & Lippard, S. J. Synthesis and Structure of $[\text{Fe}_{13}\text{O}_4\text{F}_{24}(\text{OMe})_{12}]^{5-}$: The First Open-Shell Keggin Ion. *J. Am. Chem. Soc.* **124**, 4578-4579 (2002).
115. Powell, G. W. *et al.* Building molecular minerals: All ferric pieces of molecular magnetite. *Angew. Chemie - Int. Ed.* **43**, 5772-5775 (2004).
116. Gass, I. A. *et al.* Synthesis and magnetic properties of heptadecametallic Fe (III) clusters. *Polyhedron* **26**, 1835-1837 (2007).
117. Sadeghi, O., Amiri, M., Reinheimer, E. W. & Nyman, M. The Role of Bi^{3+} in Promoting and Stabilizing Iron Oxo Clusters in Strong Acid. *Angew. Chemie - Int. Ed.* **57**, 6247-6250 (2018).
118. Sadeghi, O. *et al.* Chemical Stabilization and Electrochemical Destabilization of the Iron Keggin Ion in Water. *Inorg. Chem.* **55**, 11078-11088 (2016).
119. Zhang, Z. *et al.* Protein-Sized Chiral Fe_{168} Cages with NbO-Type Topology. *J. Am. Chem. Soc.* 14600-14601 (2009).
120. You, J. F., Snyder, B. S. & Holm, R. H. $[\text{Na}_2\text{Fe}_{18}\text{S}_{30}]^{8-}$: A high-nuclearity cyclic cluster generated solely by iron-sulfur bridge bonding. *J. Am. Chem.*

- Soc. **110**, 6589-6591 (1988).
121. Taft, K. L. & Lippard, S. J. Synthesis and Structure of $[\text{Fe}(\text{OMe})_2(\text{O}_2\text{CCH}_2\text{Cl})]_{10}$, a Molecular Ferric Wheel. *J. Am. Chem. Soc.* **112**, 9629-9630 (1990).
122. Caneschi, A., Cornia, A. & Lippard, S. J. A Cyclic Hexairon(III) Complex with an Octahedrally Coordinated Sodium Ion at the Center, an Example of the [12]Metallacrown-6 Structure Type. *Angew. Chemie Int. Ed.* **34**, 467-469 (1995).
123. Gatteschi, D. *et al.* Synthesis, Crystal Structure, Magnetism, and Magnetic Anisotropy of Cyclic Clusters Comprising six Iron(III) Ions and Entrapping Alkaline Ions. *Chem. - A Eur. J.* **2**, 1379-1387 (1996).
124. Abbati, G. L. *et al.* Modulated Magnetic Coupling in Alkoxoiron(III) Rings by Host-Guest Interactions with Alkali Metal Cations. *Inorg. Chem.* **36**, 6443-6446 (1997).
125. Saalfrank, R. W., Bernt, I., Uller, E. & Hampel, F. Template-mediated self assembly of six- and eight-membered iron coronates. *Angew. Chemie. Int. Ed.* **36**, 2482-2485 (1997).
126. Caneschi, A., Cornia, A., Fabretti, A. C. & Gatteschi, D. Structure and magnetic properties of a dodecanuclear twisted-ring iron(III) cluster. *Angew. Chemie - Int. Ed.* **38**, 1295-1297 (1999).
127. Jones, L. F. *et al.* Octametallic and Hexadecametallic Ferric Wheels **. IX, 4318-4321 (2002).
128. Watton, S. P. *et al.* A Cyclic Octadecairon(III) Complex, the Molecular 18-Wheeler. *Angew. Chemie (International Ed. English)* **36**, 2774-2776 (1997).
129. Botezat, O., Van Leusen, J., Kravtsov, V. C., Kögerler, P. & Baca, S. G. Ultralarge 3d/4f Coordination Wheels: From Carboxylate/Amino Alcohol-Supported $\{\text{Fe}_4\text{Ln}_2\}$ to $\{\text{Fe}_{18}\text{Ln}_6\}$ Rings. *Inorg. Chem.* **56**, 1814-1822 (2017).
130. Zhang, Z. M. *et al.* Enantiomerically pure chiral $\{\text{Fe}_{28}\}$ wheels. *Angew. Chemie - Int. Ed.* **48**, 1581-1584 (2009).

131. Zhang, Z. *et al.* Protein-Sized Chiral Fe 168 Cages with NbO-Type Topology H NMR. *J. Am. Chem. Soc.* 14600-14601 (2009).
132. Friedrichs, O. D., Keeffe, O. & Yaghi, O. M. research papers Three-periodic nets and tilings : regular and quasiregular nets research papers. *Acta Cryst. A* 22-27 (2003).
133. Liu, T., Zhang, Y.-J., Wang, Z.-M. & Gao, S. A 64-nuclear cubic cage incorporating propeller-like Fe^{III} apices and HCOO⁻ edges. *J. Am. Chem. Soc.* **130**, 10500-10501 (2008).
134. Beavers, C. M., Prosverin, A. V., Cashion, J. D., Dunbar, K. R. & Richards, A. F. An unprecedented Fe₃₆ phosphonate cage. *Inorg. Chem.* **52**, 1670-1672 (2013).
135. Rathnayake, A. S. *et al.* Site-Specific Metal Chelation Facilitates the Unveiling of Hidden Coordination Sites in an Fe II /Fe III -Seamed Pyrogallol[4]arene Nanocapsule. *J. Am. Chem. Soc.* **140**, 15611-15615 (2018).
136. Chen, W. C. *et al.* Assembly of Fe-substituted Dawson-type nanoscale selenotungstate clusters with photocatalytic H₂ evolution activity. *Chem. Commun.* **50**, 13265-13267 (2014).
137. Botar, B., Kögerler, P. & Hill, C. L. Tetrairon and hexairon hydroxo/acetato clusters stabilized by multiple polyoxometalate scaffolds. Structures, magnetic properties, and chemistry of a dimer and a trimer. *Inorg. Chem.* **46**, 5398-5403 (2007).
138. Lin, S. *et al.* Preparation of polyoxometalates in ionic liquids by ionothermal synthesis. *Dalt. Trans.* **39**, 1740-1744 (2010).
139. Müller, A. *et al.* Generation of cluster capsules (Ih) from decomposition products of a smaller cluster (Keggin-Td) while surviving ones get encapsulated: Species with core-shell topology formed by a fundamental symmetry-driven reaction. *Chem. Commun.* 657-658 (2001).
140. Naseer, R. *et al.* Redox, surface and electrocatalytic properties of layer-by-layer films based upon Fe(III)-substituted crown polyoxometalate [P8W

- 48O184Fe16(OH)28(H 2O)4]20-. *Electrochim. Acta* **134**, 450-458 (2014).
141. Ibrahim, M. *et al.* Tetradecanuclear Iron(III)-Oxo Nanoclusters Stabilized by Trilacunary Heteropolyanions. *Inorg. Chem.* **54**, 6136-6146 (2015).
142. Godin, B. *et al.* Coordination chemistry of the hexavacant tungstophosphate [H 2P2W12O48]12- with FeIII ions: Towards original structures of increasing size and complexity. *Angew. Chemie - Int. Ed.* **44**, 3072-3075 (2005).
143. Whitesides, G. M. Reinventing chemistry. *Angew. Chem. Int. Ed. Engl.* **54**, 3196-209 (2015).
144. Sakiyama, F. Automated Synthesis of Peptides. *R. B. Merrif.* **150**, 178-185 (1965).
145. Alvarado-Urbina, G. *et al.* Automated systems of gene fragments. *Science (80-.)*. **214**, 270-274 (1981).
146. Plante, O. J., Palmacci, E. R. & Seeberger, P. H. Automated solid-phase synthesis of oligosaccharides. *Science (80-.)*. **291**, 1523-127 (2001).
147. Gutte, B. & Merrifield, R. B. The Total Synthesis of an Enzyme with Ribonuclease A Activity. *J. Am. Chem. Soc.* **91**, 501-502 (1969).
148. Kosuri, S. & Church, G. M. Large-scale de novo DNA synthesis: Technologies and applications. *Nat. Methods* **11**, 499-507 (2014).
149. Seeberger, P. H. Automated carbohydrate synthesis to drive chemical glycomics. *Chem. Commun.* 1115-1121 (2003).
150. Naresh, K., Schumacher, F., Hahm, H. S. & Seeberger, P. H. Pushing the limits of automated glycan assembly: Synthesis of a 50mer polymannoside. *Chem. Commun.* **53**, 9085-9088 (2017).
151. Hartman, R. L. Managing solids in microreactors for the upstream continuous processing of fine chemicals. *Org. Process Res. Dev.* **16**, 870-887 (2012).
152. Maurya, R. A., Park, C. P., Lee, J. H. & Kim, D. P. Continuous in situ generation, separation, and reaction of diazomethane in a dual-channel microreactor. *Angew. Chemie - Int. Ed.* **50**, 5952-5955 (2011).

153. Acke, D. R. J. & Stevens, C. V. A HCN-based reaction under microreactor conditions: Industrially feasible and continuous synthesis of 3,4-diamino-1H-isochromen-1-ones. *Green Chem.* **9**, 386-390 (2007).
154. Nagao, I., Ishizaka, T. & Kawanami, H. Rapid production of benzazole derivatives by a high-pressure and high-temperature water microflow chemical process. *Green Chem.* **18**, 3494-3498 (2016).
155. Lin, H., Dai, C., Jamison, T. F. & Jensen, K. F. A Rapid Total Synthesis of Ciprofloxacin Hydrochloride in Continuous Flow. *Angew. Chemie - Int. Ed.* **56**, 8870-8873 (2017).
156. Porta, R., Benaglia, M. & Puglisi, A. Flow Chemistry: Recent Developments in the Synthesis of Pharmaceutical Products. *Org. Process Res. Dev.* **20**, 2-25 (2016).
157. Porwol, L., Henson, A., Kitson, P. J., Long, D. L. & Cronin, L. On the fly multi-modal observation of ligand synthesis and complexation of Cu complexes in flow with 'benchtop' NMR and mass spectrometry. *Inorg. Chem. Front.* **3**, 919-923 (2016).
158. Sans, V. & Cronin, L. Towards dial-a-molecule by integrating continuous flow, analytics and self-optimisation. *Chem. Soc. Rev.* **45**, 2032-2043 (2016).
159. Richmond, C. J. *et al.* A flow-system array for the discovery and scale up of inorganic clusters. *Nat. Chem.* **4**, 1037-1043 (2012).
160. Zang, H. Y. *et al.* Discovery of gigantic molecular nanostructures using a flow reaction array as a search engine. *Nat. Commun.* **5**, 1-8 (2014).
161. Laird, T. Editorial reproducibility of synthetic results. *Org. Process Res. Dev.* **18**, 1259 (2014).
162. Deming, S. N. & Pardue, H. L. An Automated Instrumental System for Fundamental Characterization of Chemical Reactions. *Anal. Chem.* **43**, 192-200 (1971).
163. Legrand, M. & Bolla, P. A fully automatic apparatus for chemical reactions on the laboratory scale. *J. Automat. Chem.* **7**, 31-37 (1985).

164. Suga Wara, T., Kato, S. & Okamoto, S. Development of fully-automated synthesis systems. *J. Automat. Chem.* **16**, 33-42 (1994).
165. Caramelli, D. *et al.* Networking chemical robots for reaction multitasking. *Nat. Commun.* **9**, 1-10 (2018).
166. Dragone, V., Sans, V., Henson, A. B., Granda, J. M. & Cronin, L. An autonomous organic reaction search engine for chemical reactivity. *Nat. Commun.* **8**, 15733 (2017).
167. Ruiz de La Oliva, A., Sans, V., Miras, H. N., Long, D. L. & Cronin, L. Coding the Assembly of Polyoxotungstates with a Programmable Reaction System. *Inorg. Chem.* **56**, 5089-5095 (2017).
168. Steiner, S. *et al.* Organic synthesis in a modular robotic system driven by a chemical programming language. *Science (80-.)*. **363**, (2019).
169. Shannon, C. E. Communication theory of secrecy systems. *Bell Syst. Tech. J.* **28**, 656-715 (1949).
170. Metropolis, N. & Ulam, S. The Monte Carlo Method. *J. Am. Stat. Assoc.* **44**, 335-341 (1949).
171. Genest, C., Lockhart, R. A. & Stephens, M. A. X^2 and the Lottery. *J. R. Stat. Soc. D. Stat.* **51**, 243-257 (2002).
172. Matsumoto, M. Mersenne Twister: A 623-Dimensionally Equidistributed Uniform Pseudo-Random Number Generator Dedicated to the Memory of Nobuo Yoneda. *ACM Trans. Model. Comput. Simul.* **8**, 3-30 (1998).
173. Park, S. K. & Miller, K. W. Random number generators: good ones are hard to find. *Commun. ACM* **31**, 1192-1201 (1988).
174. Rukhin, Andrew; Soto, Juan; Nechvatal, James; Smid, Miles; Barker, E. A *Statistical Test Suite for Random and Pseudorandom Number Generators for Cryptographic Applications*. (Gaithersburg, MD: NIST) (2010).
175. Pimblet, K. A. & Bulmer, M. Random numbers from astronomical imaging. *Publ. Astron. Soc. Aust.* **22**, 1-5 (2005).
176. G.G. Liversidge J.F. Bishop, D.A. Czekai, K. C. C. United States Patent (19)

54. **96**, 62-66 (1980).
177. Martini, G. & Bruno, F. G. True Random Numbers Generation from stationary Stochastic Processes. *2017 Int. Conf. Noise Fluctuations 1-4* (2017).
178. Zhang, Q., Deng, X., Tian, C. & Su, X. Quantum random number generator based on twin beams. *Opt. Lett.* **42**, 895-898 (2017).
179. Petrica, L. FPGA optimized cellular automaton random number generator. *J. Parallel Distrib. Comput.* **111**, 251-259 (2018).
180. De Virgilio, R. & Maccioni, A. Random Query Answering with the Crowd. *J. Data Semant.* **5**, 3-17 (2016).
181. Mcquarrie, D. A. & Gillespie, D. T. Stochastic Theory and Simulations of Chemical Kinetics. *J. Appl. Probab.* **478**, 413-478 (1967).
182. Van den Broeck, C. *Stochastic thermodynamics: A brief introduction. Proceedings of the International School of Physics 'Enrico Fermi'* (2013). doi:10.3254/978-1-61499-278-3-155
183. Symes, M. D. *et al.* Integrated 3D-printed reactionware for chemical synthesis and analysis. *Nat. Chem.* **4**, 349-354 (2012).
184. Yang, E. C. *et al.* Cobalt single-molecule magnet. *J. Appl. Phys.* **91**, 7382-7384 (2002).
185. Anzenhofer, K. & Boer, J. J. D. E. The crystal structure of the basic iron acetate $[\text{Fe}_3\text{CH}_3\text{COO})_6\text{O}\cdot 3\text{H}_2\text{O}] + \text{ClO}_4^-$ (short communication). *Recl. des Trav. Chim. des Pays-Bas* **88**, 286-288 (1969).
186. Norman, R. E., Rose, N. J. & Stenkamp, R. E. Crystal Structure of a Copper Complex of 2-Carboxypentonic Acid; *Dalt. Trans.* 2905-2910 (1987).
187. Löwendahl, L. & Petersson, G. Conversion of dehydroascorbic acid to a branched hexaric acid in neutral and alkaline aqueous solution. *Anal. Biochem.* **72**, 623-628 (1976).
188. Fischer, A. B., Hess, C., Neubauer, T. & Eikmann, T. Testing of chelating agents and vitamins against lead toxicity using mammalian cell cultures. *Analyst* **123**, 55-58 (1998).

189. Sadeghi, A., Bideskan, A. E., Alipour, F., Fazel, A. & Haghiri, H. The effect of ascorbic acid and garlic administration on lead-induced neural damage in rat offspring's hippocampus. *Iran. J. Basic Med. Sci.* **16**, 157-164 (2013).
190. Simon, J. A. & Hudes, E. S. Relationship of ascorbic acid to blood lead levels. *J. Am. Med. Assoc.* **281**, 2289-2293 (1999).
191. Tadashi Suzuki, A. Y. Effect of Dietary Supplementation of Iron and Ascorbic Acid on Lead Toxicity in Rats. *J. Nutr.* **109**, 982-988 (1979).
192. Gass, I. A. *et al.* A cube in a tetrahedron: Microwave-assisted synthesis of an octametallc FeIII cluster. *Inorg. Chem.* **45**, 5281-5283 (2006).
193. Modec, B., Brenčič, J. V. & Giester, G. A decanuclear oxomolybdenum(V,VI) cluster with 4-isopropylpyridine. *Acta Crystallogr. Sect. C Cryst. Struct. Commun.* **57**, 246-247 (2001).
194. Modec, B., Brenčič, J. V., Golič, L. & Daniels, L. M. Oxomolybdenum coordination compounds with alkyl-substituted pyridines. (see abstract). *Polyhedron* **19**, 1407-1414 (2000).
195. Pap, J. S., Kaizer, J., Giorgi, M. & Speier, G. Molecular and electronic structure of a trinuclear oxo-centred Iron(III) complex with trigonal bipyramidal metal sites. *Inorg. Chem. Commun.* **13**, 1069-1073 (2010).
196. Govor, E. V. *et al.* A Redox-Induced Spin-State Cascade in a Mixed-Valent Fe₃(μ₃-O) Triangle. *Angew. Chemie - Int. Ed.* **56**, 582-586 (2017).
197. Shaw, R. *et al.* 1,2,3-Triazolate-bridged tetradecametallic transition metal clusters [M₁₄(L)₆O₆(OMe)₁₈X₆] (M = FeIII, CrIII and VIII/IV) and related compounds: Ground-state spins ranging from S = 0 to S = 25 and spin-enhanced magnetocaloric effect. *Inorg. Chem.* **46**, 4968-4978 (2007).
198. Sheldrick, G. M. A short history of SHELX. *Acta Crystallogr. Sect. A Found. Crystallogr.* **64**, 112-122 (2008).
199. Farrugia, L. J. WinGX and ORTEP for Windows: an update. *J. Appl. Crystallogr.* **45**, 849-854 (2012).